UNIVERSIDAD DE GRANADA

Study of long-range correlations and criticality in neural media and other biological systems

by

Sebastiano de Franciscis

Supervisor

Joaquín Javier Torres Agudo

Departamento de Electromagnetismo y Física de la Matéria

and

Instituto Carlos I de Física Teórica y Computacional

September 2011

"Life is short, and Art long; the opportunity fleeting; experience perilous, and decision difficult"

Hippocrates of Kos (c. 460 BC - 377 BC)

Acknowledgements

Thanks all!!

Contents

List of Figures

List of Tables

Dedicated to my family

Chapter 1

General introduction

> "Does the flap of a butterflys wings in Italy set off a tornado in Spain?"

The study of the nervous system has increased significantly during the second half of the past century, principally due to the advances in molecular biology, electrophysiology, and the development of computational neuroscience. For instance, it has become possible to understand and simulate in detail a large number of complex biophysical processes occurring within a single neuron. However, it is still poorly understood how networks composed by a large number of neurons interconnected by synapses can produce complex cognitions and behaviours.

Understanding the brain is among the most challenging problems to which a physicist can be attracted. As a system with an enormous number of elements (i.e. neurons and synapses), affected by many non-linear dynamical mechanisms, both at cellular and network level, the brain exhibits collective dynamics that in many aspects resemble some of the well studied problems in statistical physics. One of the most interesting collective behaviours recently observed in neural systems is the emergence of critical phenomena. The hallmark of criticality is the appearance of long range spatio-temporal correlations in neural media, that are revealed through the existence of power law distributions, also called *scale free*, for some magnitudes of interest. This critical behaviour has been observed experimentally both at large "whole brain" scale (characterized for instance by the existence of long-range correlations, correlation length divergence and anticorrelated states in the activity of some cortical areas) [9], and at relatively small scale (where cortical circuits exhibit neuronal avalanches, cascades of activity obeying inverse-power-law statistics as well as long-range correlations) [6].

Critical states have raised a great excitement in neuroscience due to the intriguing functional properties they entail. On a small scale, critical neural avalanches have been claim to lead to the optimization of different properties, such as transmission and storage of information, computational capabilities, large network stability and sensitivity to sensory stimuli, to name a few [10]. On the other hand, at large scale, critical spatiotemporal patterns of activity, characterizing the collective dynamics of huge numbers of interacting neurons distributed throughout the cortex, support higher brain functions in humans such as perception, learning and goal directed movement, dynamically adapting them to a varying environment [11, 12], or finally can be the fingerprint of some neural diseases such as epilepsy [13].

The most relevant and still open problems concerning neural critical states are those related with the neuron mechanisms and network structures (i.e. topologies made by neuronal connections) responsible for their emergence and stability. Moreover, the relationships between these elements and the optimal functional properties shared by critical networks are not yet completely understood.

Other intriguing phenomena in system biology that depict critical properties are those related to solid tumour growth, recently matter of an intense debate. Also in this case one has to deal with a system formed by a great number of units, i.e. the cells, with complex nonlinear interactions among them. Experiments have shown that tumours develop as self-affine objects [14], with typical spatiotemporal correlations that are power law distributed [15]. The measure of their associated critical exponents (i.e. the exponents of the power law correlation functions) are highly relevant to understand the essential dynamical process of tumour invasion. Moreover is crucial to find the relationship that exists between exponents values and the mechanisms of tumour cell proliferation, in order to develop therapeutic tools [16].

The aim of this thesis is to investigate, using different mathematical approaches and numerical simulations, the mechanisms responsible for the appearance of critical states in different neural systems, as well as the optimal functional properties emerging in them. Secondly, with the purpose to extend the study of criticality to other classes of system biology, we investigate, in the same framework, the relationships between critical characterization of tumour growth and its fundamental invasion dynamic.

In particular, the main goals of this thesis are:

- Explore the role that activity-dependent synaptic processes in neural networks play on the emergence of critical phenomena, as well as in the robustness of criticality and in the optimization of neural networks functional properties in such critical states (see chapters 5-6).

- Find the relationships between non trivial network topologies with scale free distributions (for both, the node-degree distribution and node-node correlation) and neural network performance (for instance, during the retrieval process of static and dynamical patterns of neural activity) (see chapters 7-8).

- Improve dynamic scaling analysis techniques in the characterization of the main dynamic of self affine solid tumour fronts, and study the relation between tumour cell proliferation mechanisms and the behaviour of fluctuations at the tumour surface (see chapters 10-11).

Structure of the Thesis

The thesis is structured as follows:

In **chapter 2** the concepts of *criticality* and *scale invariance* in the study of complex systems constituted by many identical interacting elements are presented. More precisely, four paradigmatic examples of simple mathematical models or class of models displaying critical properties are described: the 2D Ising model, the Bak Tang Wiesenfeld Sandpile, the Barábasi-Albert Preferential Attachment Network and some discrete models of Self Affine Surface Growth. These models form the basic mathematical framework used in this thesis to study neural media behaviour and tumour growth.

In **chapter 3** useful definitions concerning the biology of neural tissue and some mathematical models used to study its behaviour are introduced. Such basic principles constitute the starting point of the theoretical models developed and studied in this thesis. First, it is briefly described the physiology of the *neurons*, the most important cells of neural tissues, focusing on its "spiking dynamic" (i.e. the generation of action potentials) and on the main mechanisms for signal transmission through the *synapses*, i.e. the functional connections among neurons.

Then, a classical model in theoretical neuroscience is presented, namely the *Hopfield Model*, originally formulated to describe *associative memory*, characteristic of some brain areas. Hopfield model considers the state of each neuron as a binary variable (i.e. silent or generating a signal), and synaptic intensities fixed in time (statics). However, in actual neurons there are many internal biochemical mechanisms modulating in time both the generation of neuron signals and the synaptic transmission. Then a brief description of the *integrate and fire (IF) model*, one of the simplest neuron model implementing membrane potential dynamics, and of the *Tsodyks Model*, that accounts for activity-dependent synaptic strengths (that is, dynamical synapses), is introduced.

In **chapter 4** we describe some relevant experiments performed on neural systems at various scales (single cell, tissue and brain level) and different settings (internal and external potential recordings on cell cultures both *in vitro* and *in vivo*, or Electroencephalogram (EEG) records), in which critical states, characterized by different power law distributions, emerge. In particular, we focus on the experimental settings and methods that use tools from statistical physics, and that show evidences of optimization of some neural functions in such critical states.

In the chapters that follow, the original scientific contributions of this thesis are presented. We start with the study of simple models of neural media and then continue with implementing more realistic and detailed neurons and synapses descriptions.

Thus, in **chapter 5**, we extend the standard Amari-Hopfield neural network model for associative memory adding some biologically justified dynamic rules, that put the system out of equilibrium. The consequence is the emergence of new nonequilibrium phases and critical phase transitions [17]. In the standard Hopfield model, network activity can converge to one of the patterns of activity, previously stored by calibrating the synaptic weights, using for instance the Hebbs rule [18]. However, the activity of actual neural systems does not remain indefinitely in a particular pattern and, in general, it can show a complex dynamical behaviour. To account for that we have generalized the standard model introducing activity dependent synaptic fluctuations, and partial neuron updating, that occasionally silences group of neurons. In this model one can identify additional non-equilibrium phases, in which the network state oscillates irregularly between the various pattern attractors. We have described in detail the second order transition between

the phase of associative memory and the phase characterized by irregular oscillations between attractors. At this transition point, we observed that the network activity presents long range correlations, characterized by fluctuations whose frequencies obey a power law. This kind of criticality is similar to what has been recently observed in the activity of cortical regions. Thus, our study gives some new elements for the understanding of the emergence of critical dynamics in the activity of cortical networks [12].

In **chapter 6** we investigate in deep a recent model for neural media, proposed by Levina, Herrmann and Geisel (LHG) [19], which displays self-organized activity. This model shows power law distributed avalanches of electrical activity, as those recently observed and well characterized in experiments on cortical neural networks [6, 8]. LHG model is constituted by a deterministic sandpile model, where site height mimics the membrane graded potential of each neuron, coupled with the Tsodyks model, that modulates the efficacy of each synaptic strength (i.e. grains redistribution) during an avalanche. In this model, neural dynamic is dissipative and has a loading mechanism for the background synaptic strength, being very similar to some examples of non-conserving self-organization, recently demonstred to lack true criticality [20]. Our purpose has been to explain from a theoretical point of view if the mechanisms of self-organization, such as the Self Organized Criticality (SOC) or non-conservative quasi-Self Organized Criticality (SOqC) can justify the invariance scale observed in neuronal avalanches. With numerical evidences (LHG model simulations) and by means of a theoretical analysis (derived from its mean-field equations) we conclude that LHG model is generally not critical. Therefore, unless the parameters are fine tuned, the dynamics is either sub or supercritical, although the pseudo-critical region in the parameter space is relatively large [21].

In **chapter 7** we introduce and study a simple model of associative memory in a neural network with scale free topology which includes a tunable structure of node-node correlations [22]. Several recent experiments have shown that different regions of the cortex present scale-free functional network topologies [4], with an highly non trivial, inhomogeneous, connective structure [23, 24]. We examined here, both theoretically and by means of numerical simulations, the effect of the correlations between the degrees (i.e. the number of links of each neuron) of nearest neighbour neurons on the behaviour of an Amari-Hopfield neural network with scale-free topology [25]. If the mean nearest neighbours degree function

$k_{nn}(k)$ increases with k, the network is said to be *assortative*, while it is *disassortative* if it decreases. We have constructed this kind of topology using a method recently suggested in [26] on the ensemble of all networks with the chosen node-node correlations that can be considered theoretically. Our main finding is that memory retrieval performance against a general stochastic noise increases with assortativity, mainly because the hubs are the main responsible for the storage of information. The good agreement we have found between the mean-field analysis and Monte Carlo simulations supports both the robustness of the results in terms of neural systems, and the validity of using this method to study the underlying dynamics in correlated networks.

In order to study the computational effects of network structure correlations in more realistic situations, in **chapter 8** we have investigated the emergent behaviour of a network of spiking neurons with a complex topology that includes, as in chapter 7, degree-degree correlations. As a model neuron for nodes, we used the Integrate and Fire mechanism to model neuron membrane dynamics. In networks of spiking neurons different types of synchronization phenomena can emerge. In particular we have focused on the role that degree-degree correlations have on the stability of the fully synchronous state. We also observed that depending on the nature of such correlations some mixture states appear, in which a subpopulation of neurons with synchronous activity and a second one with asynchronous activity coexist. We have found that synchrony among neurons is enhanced when the network is assortative while in disassortative networks the asynchronous state is the rule. Moreover, we stress the importance of local homogeneous subnetworks of neurons on the emergence of local synchronous activity.

In **chapter 9** we make a small introduction to the study of *dynamic scaling*, a theoretical framework recently applied to describe tumour growth fronts [27], that exploits the geometrical features of growing surfaces using different concepts from the theory of stochastic processes and fractal geometry. Following the work by Brú *et al.* [15, 16, 28], there are strong experimental evidences that the fluctuations of solid tumour interfaces have a non-trivial spatiotemporal behaviour, which is the fingerprint of self-affinity. Moreover, tumour interface correlations seem to evolve according to some power laws with robust exponents, belonging to the Molecular Beam Epitaxy/Mullins Herring (MBE/MH) universality class [29]. This type of universality explains the roughening processes in which cells are generated randomly close to surface and then relax towards the highest surface curvature

region. These findings are the starting point of some continuous models in terms of Langevin evolution equations.

In the framework of dynamic scaling analysis for solid tumour fronts, in **chapter 10** we implement and analyze some Langevin surface evolution equations in the radial symmetry case [30]. In fact, most of the proposed models in the literature consider the roughening of a surface on a planar substrate of constant size. A key question here concerns the analysis of the fluctuations of radially growing fronts in terms of dynamic scaling techniques. The problem consists in determine if the models exhibiting radial symmetry, resembling solid tumours fronts growth, belong to the currently known universality classes, or else make part of some new ones. A similar remark applies to the case of one dimensional interfaces with non constant substrate size. We have thus implemented some continuous models in radial symmetry, i.e. Edwards Wilkinson (EW) and Kardar Parisi Zhang (KPZ) equations, finding that they still belong to the respective well-known one dimensional universality classes, at least in the limit of large radius. Then, considering some one dimensional examples with non constant substrate, we have found that systems with growth for dilatation (i.e. with fixed number of discretization points and increasing dx) have a new scaling behaviour, different from the one prescribed by the usual Family-Vicsek *ansatz*, and in the asymptotic limit, the interface is completely uncorrelated. These results calls for a more rigorous study of the limit for a continuous description of microscopically discrete systems.

In **chapter 11** we study the dynamic scaling of surface fluctuations for a lattice-gas (LGCA) model of solid tumour growth. Despite the several models proposed in order to describe solid tumour growth dynamic, the available techniques to check models consistency with experiments are often ambiguous or qualitative, and the problem of models validation by biomedical data is an open challenge. Dynamic fractal scaling, used by Brú *et al.* to characterize tumour front dynamic [28], could be definitively an efficient tool to evaluate tumour models, and interrelate their mathematical assumptions with the relevant involved biological mechanisms. Here we implement a discrete tumour growth LGCA model with diffusive-kinetic dynamics, i.e. cells perform random walks and undergo birth/death processes, originally developed in [31, 32]. Then, we analyze numerically their growing fronts by using fractal scaling analysis. Our study shows that diffusive dynamic induces tumour surface fluctuations to develop according to EW universality observed experimentally [15] and which is not consistent with the MBE/MH universality

class. However linear growth rate of the tumour radius and proliferative activity restricted to the external layer, also found in the same experiments, are recovered. In order to obtain the correct universality we suggest to introduce some adhesive cell-cell interaction mechanism.

Finally the main conclusions of this thesis are presented, focusing on the role that different dynamic mechanisms have in the emergence of critical states for neural systems, and in the performance of their functional properties. In second instance some observation on the validity of dynamic scaling analysis in the characterization of tumour growth dynamic are given. The possible implications of our findings, and also the future research lines that this thesis may suggest, are summarized as well.

Chapter 2

Criticality and scale invariance in physics and biology

"the whole is more than the sum of the parts"

We introduce here some basic ideas regarding the concept of *criticality* and *scale invariance* in the study of complex systems. We describe four paradigmatic examples of simple mathematical models or class of models displaying critical properties that we will use in the rest of the thesis, namely the 2D Ising model, the Bak Tang Wiesenfeld Sandpile model, the Barábasi-Albert Preferential Attachment Network and some discrete models of Self Affine Surface Growth.

2.1 Introduction

In classical mechanics the predictions on the dynamics of a system result by solving the deterministic Newton equations defined for each of its elements. That is, once Newton equations are integrated over time, the system future trajectory is exactly known. Unfortunately, this is not a viable strategy to study systems composed by many elements, as for instance in the study of a gas which is constituted by order of $N_A \sim 10^{23}$ (Avogadro number) molecules. Statistical physics, however, helps us to deal with this problem, and allows to study physical systems with a huge number of identical elements interacting each other with simple rules, and permits the analysis of the macroscopic and collective properties that emerge from

these *microscopic* interactions. To do that, statistical physics uses a probabilistic approach: it tries to make predictions on the probability that a system will evolve to a particular configuration, or state. Thus, the principal strategy of statistical physics consists in extract informations concerning the system behaviour measuring mean values, or higher order moments, like variance, and other different statistical observables, with the use of this probability distribution.

In most of the systems of interest the observed phenomenology cannot be deduced from the dynamics of its single elements, and it is the result of a collective behaviour of all elements: this emergent behaviour is in general **complex** [1]. More precisely, systems with numerous components capable of structured interactions can generate *emergent features*, i.e. phenomena, functions, or effects that cannot be trivially reduced to some properties of the components alone. Instead, these functions describe properties of the system as a whole. In general, complexity is achieved in systems that exhibit a mixture of order and disorder, i.e. regularity and randomness, a property which has a great capacity to generate non trivial emergent phenomena. This is exactly the case of systems configured in a critical state, as we will see next in this chapter.

Complexity is a paradigm not only in the structure and the dynamics of many classic multiparticle physical systems, like gases, but also it appears in "live matter". In biology, different systems consisting of many identical interacting elements, as neurons in neural network, cells in tumours or bacteria in colonies, have a complex dynamics which displays collective behaviours in the form of spatiotemporal correlations [33, 34], pattern formation [35–37] or synchronization phenomena [38]. Starting from the 50's of the past century with the Turing seminal paper "The Chemical Basis of Morphogenesis" on a reaction-diffusion system for morphogenesis [39], the modelling of biological systems has been turned out to be one of the paradigmatic fields of application of statistical physics [40–42]. One of the most intriguing properties observed in biological system in the last 30 years is the appearance of long-range spatial and temporal correlations in physiological signal recordings [1, 43], in spatiotemporal dynamics [6, 28], or in structure formation [14, 44]. Such long range correlations are characterized by different statistical observables that exhibit a **power law**, or **scale free**, distribution $P(z)$, i.e.:

$$P(z) \propto z^{\gamma};$$

---

[1]In general, complex systems are characterized by the existence of highly non-linear processes involved in their dynamics and high sensitivity to initial conditions.

where $P(z)$ is the probability distribution of the quantity z taken in consideration (i.e. being space and/or time) and γ is an exponent characterizing the long range behaviour of $P(z)$.

As an illustrative example of scale free distributed correlations, let's consider the case of the heartbeat time series measured in electrocardiography (ECG) recordings from subjects with heart disease [1] (see figure 2.1). It is possible to define, as a statistical observable, the interbeat time interval $B(n)$, that is the time interval between the n-th and the $n + 1$-th heart pulse. The mean interbeat fluctuation function $F(n') \equiv \langle |B(n + n') - B(n)| \rangle_n$ (where $\langle \cdot \rangle_n$ means the mean value over the whole beat time series) increases with n as $F(n) \propto n^\gamma$, with $\gamma \sim 0.5$, while for healthy subjects this function is flat with $\gamma = 0$, as depicted in figure 2.2. Long range behaviour analysis, also called **scaling analysis**, could give several indications about the particular mechanisms governing such system dynamics. Concerning the time series of $F(n)$, the exponent value $\gamma = 0$, observed in normal subjects, indicates anticorrelation properties, consistent with neurophysiological feedback processes that "kicks" heart rate away from extreme values. On the contrary, $\gamma = 0.5$ is the typical exponent resulting from the trajectory of a random walker, produced by a "step by step" summation of uncorrelated random variables [45], and gives the evidence of a different types of correlations between the interbeat intervals, in which the heart lacks any mechanisms of beat rate self-regulation.

The peculiar scale-free distributed function, characterized by a power law, described in the former example, has been found in a great variety of biological systems, and characterizes, for instance, the size of neural activity bursts [6, 46, 47], the structure of functional brain topology [4] or the shape of bacterial colonies [48]. Power law distributed spatiotemporal correlations emerge essentially in two situations: at the exact point of a continuous (second order) transition between two different macroscopic phases or in spontaneuos, self-organizing, non equilibrium critical states.

In **Equilibrium Statistical Mechanics** [49, 50] it is possible to define, for some systems, an Hamiltonian, or energy functional, which depends on the microscopic states of the system. Their **macroscopic equilibrium stationary states** are related to the minima of the free-energy potential, which can be derived from the Hamiltonian by using standard statistical mechanics tools. This potential allows to study the influence that the different external parameters (e.g. temperature, pressure and driving forces) have on the equilibrium states. Let us consider a
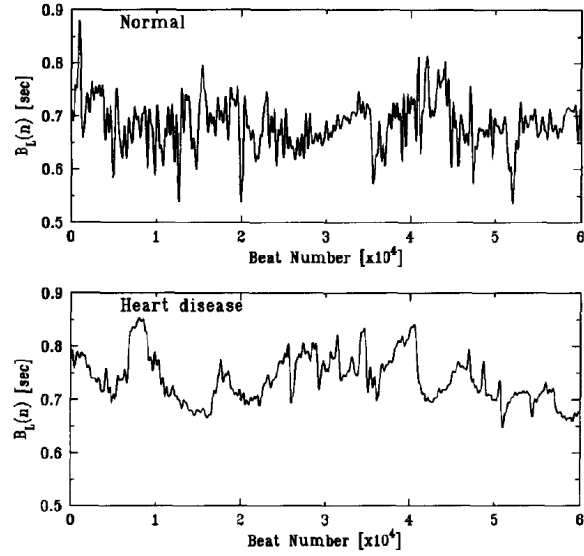
FIGURE 2.1: Interbeat intervals $B(n)$ series for an healthy subject (Top) and for a patient with severe cardiac disease (dilated cardiomyopathy). The healthy heartbeat time series shows more complex fluctuations compared to the diseased heart pattern (reprinted from [1]).
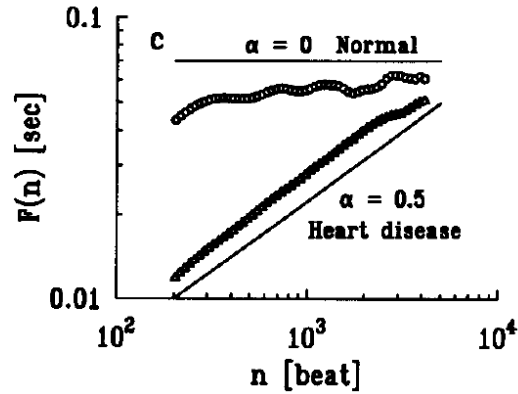
FIGURE 2.2: Log-log plot of $F(n)$ versus n calculated from data in figure 2.1. The two lines with slope $\alpha = 0$ and $\alpha = 0.5$ correspond to *"1/f"* noise and *"brown noise"* respectively (reprinted from [1]).

system of N elements characterized by the state variables $\{a_1(\vec{r}_1, t), \cdots, a_N(\vec{r}_n, t)\}$, where the state of i-th element, at time t and position $\vec{r}_i$, is characterized by the value of $a_i(\vec{r}_i, t)$. When the system reaches a well defined macroscopic equilibrium state, i.e. a minimum of the free-energy, it can be characterized by the mean value of one or more statistical observables, derived from the Hamiltonian. In this equilibrium state, spatial and temporal correlations among the state variables $a_i(\vec{r}_i, t)$

decay rapidly, as an exponential function:

$$\langle a_i(\vec{r}_1, t) a_j(\vec{r}_j, t') \rangle \propto e^{-\chi(|\vec{r}_i - \vec{r}_j|, |t - t'|)},$$

where $\chi(|\vec{r}_i - \vec{r}_j|, |t - t'|)$ is a $1st$ order polynomial with non negative coefficients. On the other hand, power law distributions emerge in phase transitions between two different macroscopic states, in general constituted by an ordered phase and a disordered one. Each phase is characterized by an observable, or *order parameter*, that changes its value when it approaches the transition point between the macroscopic phases. When the order parameter change continuously from a non zero value in the ordered phase to 0 in the disordered one, a **second order phase transition** occurs.

Let us consider for example the 2D Ising model [51, 52], describing the ferromagnetic interactions between N binary spins, with state variables $\sigma_i \in \{-1, 1\}$, placed in the nodes of a square lattice, under the effect of a thermal bath with temperature T. In this system, considering as a order parameter the global magnetization $M \equiv \frac{1}{N} \sum_{i=1}^{N} \sigma_i$, one can observe a second order phase transition between an ordered "Ferromagnetic" phase, dominated by the deterministic spin-spin interaction, with $M \neq 0$, and a disordered "Paramagnetic" phase, with $M = 0$, in which the dynamic is dominated by stochastic fluctuations induced by the thermal bath (see section 2.2).

Close to a second order transition the system is said to be in a **critical state**, and the respective transition point is called **critical point**. While a local perturbation has only localized effects in a stable phase, close to a critical point it propagates throughout the whole system, because its effect decays algebraically instead of exponentially. Although the Ising model considers only nearest neighbour interactions, very near the critical point there is a non zero correlation between every pairs of spins in the system, as if they had an effective interaction mutually influencing each other: this is the intrinsic meaning of a critical state. Thus, when one sets the system, tuning conveniently its relevant parameters, exactly or very close to the transition point, spatial correlations will decay with a large queue, power law shaped [53], that is

$$\langle a_i(\vec{r}_i, t) a_j(\vec{r}_j, t) \rangle \propto |\vec{r}_i - \vec{r}_j|^{-\alpha}$$

More generally, systems in a critical state are characterized by **scale invariance**, or scale free behaviour, i.e. they have the same appearance at any spatial and temporal scale. Mathematically, this feature is described by functions, like correlation functions or probability distributions, dominated by power laws:

$$f(x) = Ax^{-\alpha}.$$

Scale invariance could be easily visualized if one change the variable x to ζx in $f(x)$, resulting:

$$g(x) \equiv f(\zeta x) = (A\zeta^{-\alpha})x^{-\alpha}, \qquad (2.1)$$

so that, for any value of the scaling factor ζ and the exponent α, $g(x)$ has the same form that $f(x)$, with a multiplicative factor scaled by $\zeta^{-\alpha}$. Alternatively, one can say that the relative change $f(x)/f(\zeta x) = \zeta^{\alpha}$ has no dependence on x; thus it does not exist any characteristic scale in the phenomena depicted by the function $f(x)$. On the other hand, scale invariance implies a functional decay qualitatively prolongated, i.e. algebraically shaped. But is this the only class of functions that accomplish with the scale invariance criteria? To answer that, one can look for a general distribution function $p(x)$ that satisfy the following property:

$$p(bx) = g(b)p(x),$$

for any b. If the scale of x is increased (or decreased) by a factor b, the shape of $p(x)$ must remains unchanged, apart from an overall multiplicative constant $g(b)$. It can be easily demonstrate that the only and unique solution of this problem is a power law function [54]. Mathematically speaking, one can say that a scale free function $p(x)$ with exponent $-\alpha$ is an **homogeneous function** of degree $-\alpha$, having the property

$$p(\lambda x) = \lambda^{-\alpha}p(x).$$

On the other hand, scale invariance is not present in phenomena controlled by an exponential function, like $e^{-x/\xi}$. Here the function decays quickly, and the scaling $x \to \zeta x$ changes the **correlation length** ξ (that measures the characteristic scale of the decay) by a factor ζ. In practical cases, power law behaviour strictly occurs only in a finite range for the distance, time or other variables, due to the finite size of the real systems. Therefore and in order to check the consistence of scale invariance hypothesis, in numerical studies of complex systems it is necessary to perform a finite size analysis that estimates the increase of such finite range when

the size of the system changes.

There is another class of systems displaying criticality with scale free behaviour in which the attractor of their dynamic is exactly at the critical point, i.e., it achieves there a stationary non-equilibrium state characterized by the existence of long-range correlations. In this case, we deal with the so called **Self Organized Criticality** (SOC) phenomena. During SOC dynamics a system spontaneously settles in the critical state, without the need of any parameter tuning, and thus one can always observe power law distributions in the relevant macroscopic observables. On the contrary, ordinary criticality (non self organized) emerges by fine tuning of some external parameter (e.g. the temperature in the Ising model) necessary in order to put the system close to a second order phase transition. For the systems displaying SOC is not possible to define an Hamiltonian, so the stationary states are **non equilibrium stationary states**, and usually are studied using **Non Equilibrium Statistical Mechanics** techniques [55].

The first attempt to model a SOC mechanism was made by Bak, Tang and Wiesefeld in 1987 with a simple model of sandpile dynamics on a plane surface. In this model the grains of sand fall at random positions on the surface, and a column of piled grains topples on their neighbours when exceeds a certain height, inducing chain reactions of topplings, or *avalanches* [56] (see section 2.3). In this model the avalanche sizes and avalanche time durations are power law distributed, with well defined exponents, and the system achieves this state without the need of any parameter fine tuning.

Power law distributions appear often also in the analysis of self assembled structures, i.e. in the connectivity distributions of complex network, or in the statistic of spatiotemporal correlations of growing surfaces. Networks with scale free degree distributions are observed in nature, as in the neural network of the worm *Caenorhabditis Elegans* [57], in metabolic networks [58], geological formations [59], and artificial systems, as in the World Wide Web connection topology [58, 60]. It has been reported that systems implemented in a scale free network improve the synchronization among their elements and stability, mainly due to the role played by the few nodes with high connectivity, the so called *hubs* [61]. Specific characteristics of scale free networks can only depend on the generative mechanisms used to create them and on the particular dynamic of nodes (see chapter 6). One famous generative process for scale free topology is the *preferential attachment mechanism*, described in section 2.4.

Geometric structures in which each subpart is a scaled copy of the whole are

ubiquitous in nature, and are the consequence of a subtle interplay between random and deterministic processes at small scales. The result is the emergence of long range correlated structures, called *self affine surfaces*, in which macroscopic coherence is generated from a microscopic short range dynamic. One can think, for example, about geological formations [59] or snowflake deposition surfaces. In industrial processes self affine surfaces are observed in the growth of thin films by molecular beam epitaxy [27]. Also this class of phenomena are related with a SOC mechanism that induces these systems to evolve with a kind of structure placed in the frontier between a flat, homogeneous surface, and an extremely rough one dominated by noise without any spatial correlation nor pattern.

At this point one can ask: "Why critical behaviour is so interesting, in particular when observed in biological systems?" One can try to address this question by pointing out the differences between correlations in equilibrium phases and non equilibrium critical states. In an ordered phase all the microscopic elements are identically and strongly correlated while in a disordered one, dominated by stochastic fluctuations or deterministic chaotic oscillations, their mutual correlations are null. In both phases, any little external perturbation or drift produces little effects on short scale, and the system quickly returns to the original equilibrium state. Only in the critical state, which occurs when the system moves from an ordered to a disordered equilibrium phase or *vice versa*, correlations are long tailed, power law distributed, and have a substantial role at every scale. Thus a critical system, situated in a rocky/wobbly position between order and disorder, becomes extremely susceptible and reactive in response to any small external handling, noise or perturbation.

This general property results to be extremely relevant when one deals with biological systems, because it allows for the optimization of their main functions. For example, one can think on cognitive tasks (memory storage and processing) in the case of neural structures (see for instance chapters 5-7), or regarding tumour growth on invasion processes and survival against host environment (see chapters 10-11).

In order to give an appropriate description of the main mechanisms in which critical states and structures with power law correlations emerge (i.e. phase transitions, self organized criticality and self organized assembly of structures) we briefly describe next four paradigmatic models or class of models displaying criticality, that represent the essential structure of the biological system models studied in this thesis: the 2D Ising Model, the Bak Tang Wiesenfeld Sandpile Model, the

Barabási-Albert Preferential Attachment Algorithm and some discrete models of Self Affine Surface Growth.

2.2   2D Ising Model

Ising Model was formulated and studied firstly in 1920 by Wilhelm Lenz and Ernst Ising [62] in order to study the *ferromagnetism* in solids produced by magnetic spin interactions. The two dimensional version of this model is constituted by a system of N binary spin variables $\sigma_i \in \{-1, 1\}$ placed in a square lattice of size $L \times L$ ($L = \sqrt{N}$). Each spin interacts with its nearest neighbours by mean of an exchange energy term J, and the whole system is driven by an external magnetic field h. The configurational energy of the system is described by the Hamiltonian:

$$H = -\frac{1}{2}J \sum_{<i,j>} \sigma_i \sigma_j - h \sum_{i=1}^{N} \sigma_i$$

where $< i, j >$ means that the sum is extended only over pairs of nearest neighbour spins. In statistical mechanics, once the Hamiltonian is formulated, one obtains all the relevant information about the system at an equilibrium state, characterized by a temperature T, by studying the partition function:

$$Z = \sum_{\vec{\sigma}} \exp^{-(H(\vec{\sigma})/k_B T)}.$$

The partition function is a sum over all the possible configurations of the probability to have the system in a particular configuration $\vec{\sigma} = \{\sigma_1, ..., \sigma_N\}$, which is assumed to follow the Boltzmann distribution:

$$P(\vec{\sigma}) = e^{-(H(\vec{\sigma})/k_B T)}.$$

Here k_B is the Boltzmann constant. Using the partition function, one can study the equilibrium states of the system, by minimizing the related free-energy potential F, i.e.

$$F = -k_B T \log Z$$

The two-dimensional square lattice version of Ising model has been solved analytically in the zero field case $h = 0$ by Lars Onsager in 1944 [51]. Considering
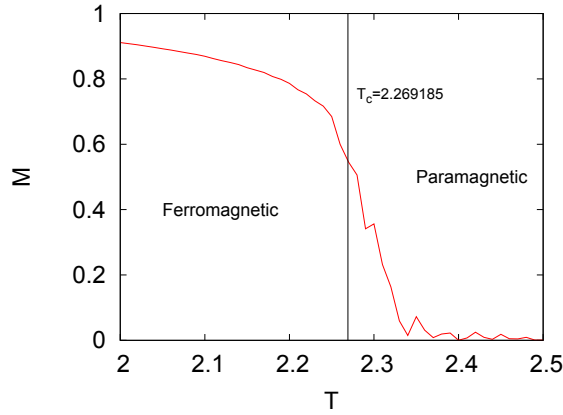
FIGURE 2.3: Global magnetization M versus temperature T, for a 2D Ising model with $N = 1600$ spins and linear dimension $L = 400$. Here is possible to notice the second order phase transition, with a continuous change in M between the ordered ferromagnetic phase, with $M \neq 0$, and the disordered paramagnetic one, with $M = 0$. The difference between actual critical temperature, placed around ~ 2.35 and the theoretical prediction $T_c = \frac{2}{\ln(1+\sqrt{2})} \simeq 2.27$ is due to a finite system size effect.

as order parameter the global magnetization $M \equiv \frac{1}{N} \sum_{i=1}^{N} \sigma_i$, the system presents a continuous phase transition between a ferromagnetic phase, where $M \neq 0$ and a paramagnetic phase, where $M = 0$ (as depicted in figure 2.3). The transition point of this transition is obtained at a critical temperature T_c given by:

$$\frac{k_B T_c}{J} = \frac{2}{\ln(1 + \sqrt{2})}$$

which implies $T_c \simeq 2.27$ for $J = k_B = 1$. Close to the transition point various physical quantities, that depend on T, M, h or on the spatial distance among spin pairs, either vanish or diverge in the form of power laws with well defined exponents [63]. For example, global magnetization M, specific heat $C_h \equiv \frac{\partial^2 H}{\partial T^2}\Big|_{h=0}$ and magnetic susceptibility $\chi \equiv \frac{\partial M}{\partial h}\Big|_{h=0}$ behave in the limit $T \to T_c$ as

$$C \propto (T_c - T)^{-\alpha}$$
$$M \propto (T_c - T)^{\beta} \quad (T \preceq T_c)$$
$$\chi \propto |T_c - T|^{-\gamma},$$

with $\alpha = 0$ (corresponding to a logarithmic divergence), $\beta = 1/8$ and $\gamma = 7/4$. In the paramagnetic phase, the spin-spin correlation function decays exponentially:

$$C(\vec{r}) = \langle \sigma(\vec{r}_i) \sigma(\vec{r}_j) \rangle_{\{ij:(\vec{r}_i - \vec{r}_j) = \vec{r}\}} \propto e^{-|\vec{r}_i - \vec{r}_j|/\xi},$$

where ξ is the typical *correlation length*. On the other hand, near the transition point ξ diverges with the temperature as:

$$\xi \propto |T_c - T|^{-\nu}$$

with $\nu = 1$, and as a consequence $C(\vec{r})$ spans over the whole system with an effective long range interaction with a power law decay:

$$C(\vec{r}) \propto |\vec{r}|^{-\eta},$$

with $\eta = 1/4$. Analytically, ξ and $C(\vec{r})$ can be derived by Fourier transform of correlation function, namely $\tilde{C}(\vec{k}) = \int d\vec{r} C(\vec{r}) \exp^{i\vec{k}\cdot\vec{r}}$, that can be approximated by the Ornstein-Zernike formula [49]:

$$\tilde{C}(\vec{k}) \propto \frac{1}{k^2 + \xi^{-2}}.$$

Some examples of functions displaying power law scaling in the 2D Ising model are shown in figure 2.4. When the system is far from the transition point, it has a finite typical correlation length ξ, which is a measure of the typical size of clusters with aligned spins, while at the transition point this length diverges, and the system shows clusters with aligned spins of all sizes. More intuitively, one can appreciate the graphical meaning of scale free behaviour looking to the different configurations of the Ising model depicted in figure 2.5: close to T_c the system has always the same appearance at any scale of the picture, i.e. we can zoom in or zoom out the picture without appreciate any difference in the structure. Summing up, in Ising model one observes that:

- Close to the ferromagnetic/paramagnetic transition, different macroscopically measurable physical quantities have a scale free (power law) behavior

- Such macroscopic observables are homogeneous functions of the macroscopic external parameters h and $t \equiv |T - T_c|$

- An analytical formulation of the observables can be obtained from the partition function Z, i.e.:

$$C = k_B \left. \frac{\partial^2 T^2 \log Z}{\partial T^2} \right|_{h=0} \qquad M = k_B T \left. \frac{\partial \log Z}{\partial h} \right|_{h=0}$$
$$\chi = k_B T \left. \frac{\partial^2 \log Z}{\partial h^2} \right|_{h=0} \qquad \tilde{C}(0) = (k_B T)^2 \left. \frac{\partial^2 \log Z}{\partial h^2} \right|_{h=0}.$$
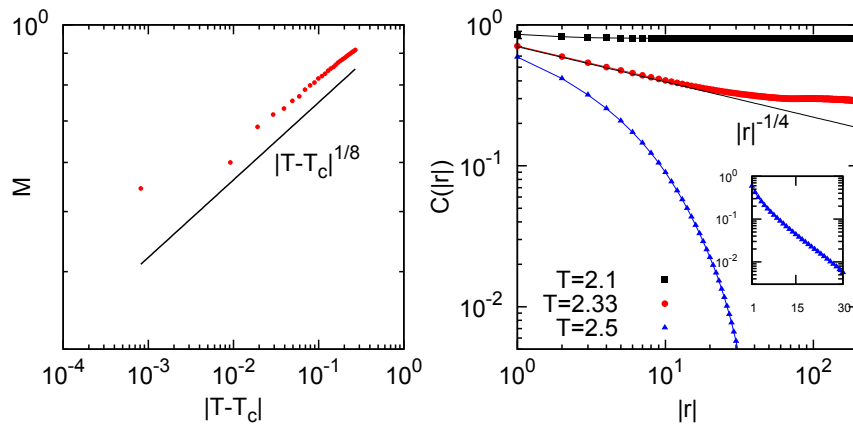
FIGURE 2.4: Left: global magnetization M versus $|T - T_c|$ for a 2D Ising model. Close to the transition it diverges as $M = |T - T_c|^{1/8}$. Right: spin-spin correlation function versus distance, measured in a log-log plot with subcritical (paramagnetic), critical and supercritical (ferromagnetic) temperature. In the ferromagnetic phase almost all spins are aligned, and the spin pairs have same correlations at each scale. On the contrary, in the paramagnetic phase correlations decay exponentially with a typical correlation length, as one can verify from its linear behaviour in the semilogarithmic inset plot. Close to the critical point, at $T = 2.33$, correlations have a power law decay with exponent $\eta = -1/4$. System parameters are the same of figure 2.3.

At this point one could deduce that the different power law behaviour at the critical point for all these statistical quantities are somewhat related each other. In fact, it can be easily demonstrated that their critical exponents satisfy the relations [27]:

$$\alpha + 2\beta + \gamma = 2 \quad \gamma = \nu(2 - \eta) \quad 2 - \alpha = d\nu,$$

where d is the dimension of the system ($d = 2$ for the case described here).

Often a number of systems with different dynamics, i.e. microscopic rules among their elements, share the same set of values for the critical exponents. As a matter of fact, defining coherently an unique set of independent order parameters, one can find just a few different set of critical values among thousands of different systems. For example, all fluids with different chemical composition have the same critical exponents at the liquid-gas critical point. In addition, they match exactly the critical exponents of the ferromagnetic/paramagnetic phase transition in a 3D Ising model [50]. Thus, in this group of phenomena and models, although the microscopic dynamics is different (especially for different kind of systems), the critical behaviour is identical. This phenomenon is known as **universality**, and the common set of critical exponents defines an **Universality Class**. Systems

grouped in the same universality class have the same long range properties, which characterize their common critical and collective behaviour. Universality is a prediction of the *renormalization group theory* of phase transitions, firstly introduced by Kadanoff in the 60's of the past century [64] which states that the thermodynamic properties of a system near a critical point depend only on a small number of features, such as the embedded geometry dimension and the symmetries of the system, and are insensitive to the underlying microscopic properties of the system. Thus, universality is a very powerful concept, because it allows to predict the critical behavior of a system, and classify the relevant essence of its diverging correlations in few classes, just by identifying system symmetries.
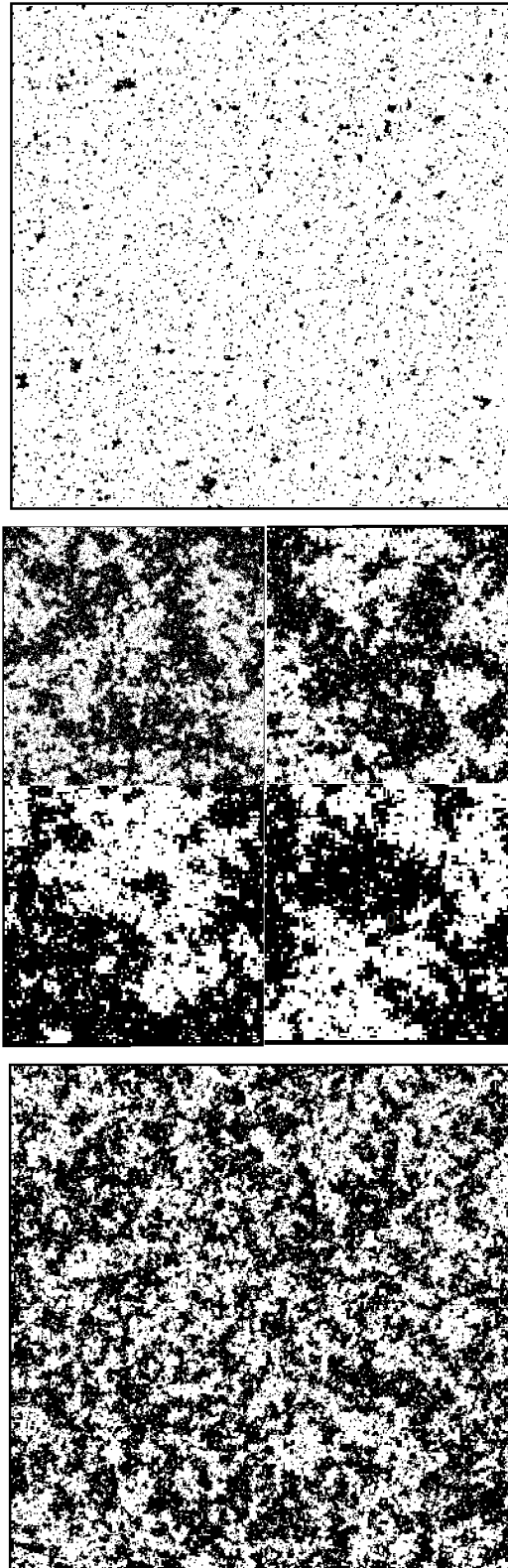
FIGURE 2.5: 2D Ising model in ferromagnetic (subcritical) ($T = 2.1$, left), almost critical ($T = 2.33$, middle) and paramagnetic (supercritical) state ($T = 2.5$, right). Note that the picture in the middle is composed by four panels. They correspond, in clockwise order, starting in the up-left panel to the original size $L = 400$, and to $\times 4$, $\times 9$ and $\times 16$ zooms, respectively.

2.3   Bak Tang Wiesenfeld Sandpile Model

At the end of the 80's of the past century Per Bak, Chao Tang and Kurt Wiesenfeld presented in two seminal papers [56, 65] a dynamical system, inspired by a pile of sand, which displays Self Organized Criticality. In the original model at each time step a grain of sand is placed on a plane (discretized by a 2D square lattice) at a random position. Then, when the height of a pile $z_{i,j}$ reaches the threshold $z_{th} = 4$, it topples its grains on the nearest neighbours, generating eventually a successive sequence of topplings, also called *avalanche*. More precisely, the system is governed by three main dynamical processes, described by the following rules:

1. **Driving**: A randomly chosen site (i, j) in the 2D square lattice receives one single grain:
$$z_{i,j} \to z_{i,j} + 1.$$
   This driving step is repeated until at some site the height of a pile becomes unstable and topples.

2. **Toppling**: When a site fulfills the condition $z_{i,j} = z_{th} = 4$, all its grains are equally distributed to each of its nearest neighbours in order to recover stability, that is

$$
\begin{aligned}
z_{i,j} &\to z_{i,j} - 4 \\
z_{i\pm 1, j\pm 1} &\to z_{i\pm 1, j\pm 1} + 1.
\end{aligned}
$$

   A simple sketch of a grain deposition with toppling is depicted in figure 2.6. If one toppling destabilizes one or more nearest neighbour sites, by increasing their heights up to the threshold, then another toppling will be generated, involving their neighboring sites, and so on until all the grains on the lattice become stable again with $z_{ij} < z_{th} \; \forall i, j$. During this avalanche process the driving step is retained.

3. **Dissipation**: The grains toppled out of the lattice, due to the toppling of an unstable site at the border, are lost.

In figure 2.7 is represented one example of avalanche process, starting from a single site in the center of the lattice which had just reached the threshold height by driving. Note that the dynamical rules for this sandpile are extraordinary simple,
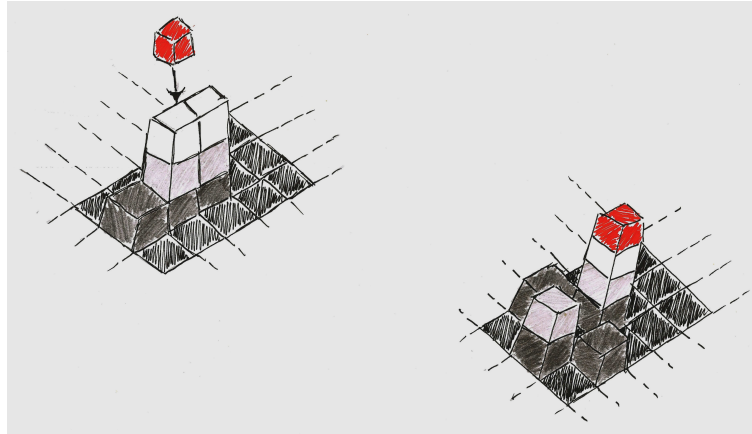
FIGURE 2.6: Scheme of a grain deposition in the site with critical height $z = 3$ (left), enhancing toppling, with deposition of one grain in each one of its four nearest neighbours sites (right). After the first toppling, initiated by a grain deposition in the centric pile, the pile on the right becomes unstable, and will topple in the following step.

but the underlying behavior is extremely complex. Thus, sandpile dynamic is another example in which complexity and collective behaviors emerge from simple microscopic interactions. In fact, the distribution of avalanche sizes (the number of sites toppling during a single avalanche process) between two driving events, and of avalanche lifetimes (the number of steps in which an avalanche is spreading) are power laws with exponents $\tau = 1.13(3)$ and $\tau_t = 1.16(3)$ respectively, as it is depicted in figure 2.8.

Self organized criticality can be always associated with a regular continuous, second order transition between an active and an absorbing state (i.e. without activity) for a dynamical system [66]. The local dynamics of the system depends on a type of *memory*, which in the sandpile case is related with the existence of a non zero threshold. Also in this case, in order to visualize the active/absorbing phase transition one can use as order parameter the density $\rho = \frac{1}{Nz_{th}} \sum_{i,j} z_{i,j}$ of grains in the system. Now eliminating both external driving and dissipation, and considering periodic boundary conditions, one obtains a system with conserved energy, or equivalently constant ρ. The second order phase transition between the dynamical active phase, with non zero probability of persistent dynamic, and the absorbing phase, where the probability to obtain a configuration with asymptotic non zero dynamics is null, results at $\rho = 1$. *Vice versa* in order to transform a conventional active/absorbing phase transition to SOC, is necessary to couple the local dynamics of the system into the driving and dissipation processes.

The relevant order parameters, like ρ, associated with the phase transition are
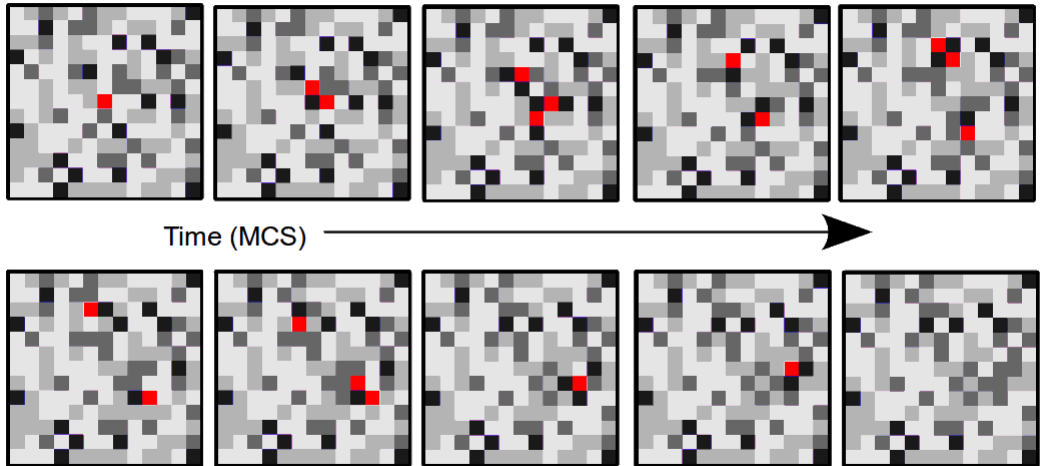
FIGURE 2.7: Avalanche of size $s = 17$ and time duration $t = 9$ generated in a 2D BTW model. Subthreshold sites height is indicated by grey scale, i.e. $(black, white) \rightarrow (0, 3)$, while red sites corresponds to unstable sites with $z_{i,j} = z_{th} = 4$.
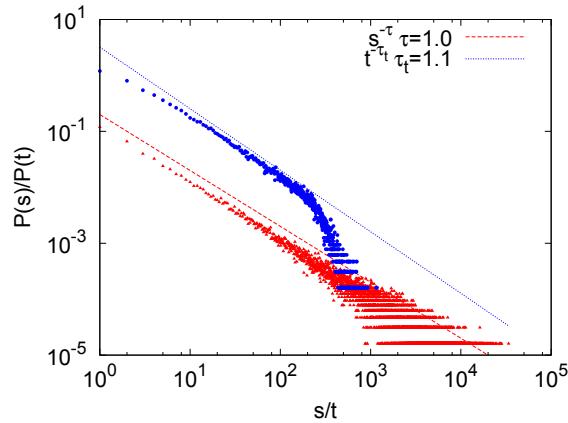
FIGURE 2.8: Log-log plot of avalanche size $P(s)$ and avalanche lifetime $P(t)$ distribution (shifted on y axis for a better visualization), for a 2D BTW model in a square lattice of linear size $L = 80$. Both distributions have a typical power law shape with exponents $\tau \simeq \tau_t \simeq 1$.

controlled by the drive, in a way that does not make explicit reference to ρ [66]. One example is the *extremal dynamics*, implemented in the Sneppen model [67] for species evolution, that restricts activity to the least stable element in the system, thereby tuning the order parameter itself to zero. On the other hand, the sandpile model involves slow driving, in which the interaction with the environment is contingent on the presence or absence of activity in the system, linked to order parameter *via* the absorbing-state phase transition. To locally ensure the conservation of energy, the driving process is retained during an avalanche. This

implies an infinite separation of time scales among the typical avalanche lifetime T_{ava} and the time between two driving perturbations T_{drv}, i.e. $\frac{T_{ava}}{T_{drv}} \to 0$. On the other hand, energy is conserved globally by mean of the dissipation of toppling grains at the open boundaries.

In order to understand how the SOC state emerges, is useful to follow in detail the dynamics of the system. Let's consider as initial state a configuration in which there are no grains in the system. In each driving event ρ is increased a fixed amount $d\rho$. At the first stages of the system evolution, energy density is not large enough and driving events trigger only a few site activations; moreover, the first avalanches cannot propagate a long distance, and activity decays exponentially fast to zero. In this situation, the system is in a *subcritical regime*. Driving goes on until ρ is large enough so that any perturbation triggers a reaction and all avalanches spread over the whole system, being the boundaries the only limit for them. Now there is a characteristic size (and activity density) for these events which scales with the size of the system, which is now in a *supercritical regime*. However, when activity reaches the border during large events, energy is dissipated and ρ decreases a (non-fixed) quantity $d\rho$. As energy is lowered, as it is the case during an avalanche, the system enters again in a subcritical regime. Then, a driving is performed and the cycle starts again. Thus, after an initial transient, ρ is maintained around a specific value $\tilde{\rho}$, which coincide with the critical value for absorbing phase transition ρ_c. In this way, the SOC regime is obtained for any set of relevant system parameters values, while in a standard critical point there is only one set of values for the parameters which makes the system critical [68]. Although, as commented before, the driving parameter is actually dynamic, that is, it evolves each time a driving event occurs, depending in a hidden way from the order parameter. In other words, for a predefined choice of the rest of parameters, the dynamic parameter is driven towards its critical value without any apparent fine external tuning of it, and the critical point is an attractor of the dynamics. In this scenario any stochastic fluctuations disappears in the thermodynamic limit, which is a very striking point in characterizing and discriminating SOC from similar non-conserved cases, called *self organized* quasi *criticality* (SOqC), where the distribution of order parameter fluctuations remains broad, even in the thermodynamic limit [20]. In chapter 5 we have studied in deep the emergence of Self Organized Quasi Criticality for a neural network model with non-conserved synaptic intensities (the so called dynamic synapses, see chapter 3 for further details), producing (pseudo)critical avalanche dynamics.

2.4 Barabási-Albert preferential attachment network model

Networks with scale free node degree distributions are widely observed in natural and man-made systems, including neural networks [57], protein-protein interaction networks [58], the world wide web and some social networks [60]. In such networks the most notable characteristic is the existence of a non neglecting probability for nodes with a degree that greatly exceeds the mean degree with respect to the case of Gaussian distributed networks. Scale free networks are thus characterized by power law degree distribution, which presents relatively few nodes with large connectivity, the so called hubs, and many nodes with poor connectivity. It has been reported that these networks have optimal properties in enhancing node-node interactions. In fact, the average distance between two nodes in the network, i.e. the minimum number of links connecting two nodes, is very small compared with that of an highly ordered network such as a regular lattice [69]. This feature of scale-free networks allows for local and global synchronization and for an efficient flow of information between the different nodes of the network [70–72]. On the other hand, scale free topologies are also optimally stable against random node failures, due to the presence of the hubs which guarantees the compactness of the whole network. However, a degree dependent attack to these highly connected nodes can destroy the whole network [73].

One of the most famous generative models for scale free topologies is the so called **Barabási-Albert preferential attachment network model**. Although the first use of a preferential attachment mechanism was reported by Udny Yule in 1925, its mathematical treatment was opaque due to the lack of appropriate tools for analyzing stochastic processes. Albert-László Barabási and Réka Albert rediscovered independently this network model in 1999 [60]. In general, the mechanisms proposed to generate these networks are constituted by a linking process among a fixed number N of nodes that accomplishes a degree distribution, chosen *a priori*. The Barabási-Albert (BA) model is able to generate scale free networks in systems with increasing size, by mean of a local attachment rule applied to the new incoming nodes. Their paper, with more than 8000 cites up to now, generated a great stimulus in the scientific community, that oriented its attention on the fascinating topic of network topology and related applications. BA mechanism, in fact, constitutes a minimal evolutive algorithm that reply the actual mechanisms

by which natural networks self assembly. The BA network is generated with the following rules:

1. **The initial configuration** is made by a small number m_0 of nodes, each one with at least one link, randomly connected each other.

2. **Growth step**: at every time step a new node with $m \leq m_0$ links is added to the network.

3. **Preferential attachment step**: the new node links to m different nodes, already present in the system, with a probability of connection to node i, $\Pi(k_i)$, which depends on the connectivity k_i of that node:

$$\Pi(k_i) = \frac{k_i}{\sum_j k_j}.$$

Then, heavily linked nodes, the so called **hubs**, tend to quickly accumulate even more links, while nodes with only a few links are unlikely to be chosen as the destination for a new link. The new nodes have thus a preference to attach themselves to the already heavily linked nodes, as one can see in the sketch 2.9. It can be easily demonstrated that the asymptotic degree distribution reached by the system is:

$$P(k) \propto k^{-\gamma},$$

with $\gamma = 2.9 \pm 0.1$, as it is shown in figure 2.10.

One example of scale free topology obtained with preferential attachment generative algorithm is depicted in figure 2.11. Growth and preferential attachment ingredients are necessary in order to obtain a stable scale free distribution: eliminating one of them implies that the final distribution will be respectively exponential or fully connected. On the other hand, changing some relevant parameters or details from these two simple rules, scale free distributions are always obtained. For example, choosing the number of new links m randomly will not change neither the distribution shape and its exponent γ, and modifying the dependence of $\Pi(k_i)$ with $k_i + c$ (with $c > 0$), the resulting distribution is still scale free with an exponent $\gamma = 2 + \frac{m_0 + c}{m}$. Scale-free networks created by mean of a generalization of such preferential attachment process emerge in topological phase transitions between heterogeneous (Gaussian distributed) networks and homogeneous ones
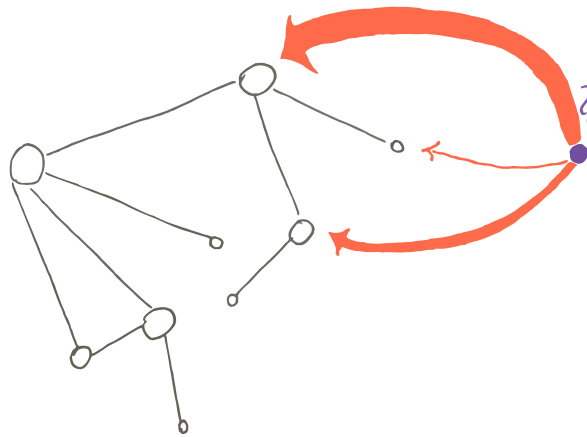
FIGURE 2.9: Preferential attachment mechanism. A new incoming node, colored in blue, has a probability to link with one of the preexistent nodes in the network, i.e. the red arrows, which is proportional to their degree.
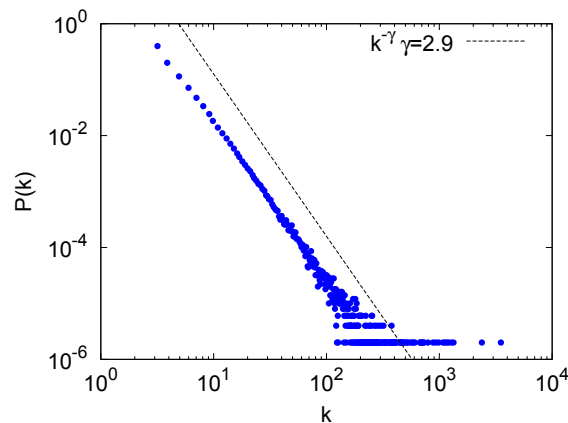
FIGURE 2.10: Log-log plot of the degree distribution $P(k)$ versus k, calculated from the Barabási-Albert preferential attachment network model with $5 \cdot 10^5$ steps (new incoming nodes), $m_0 = 5$, $m = 3$, and an uniform network as initial topology with $k = 2$. The resulting connectivity distribution is compared with a power-law line of slope $\gamma = 2.9$.

(fully connected) [74] as well as in a broad region of the parameters space, resembling the SOC phenomenology [60, 75].

The BA has very intriguing properties due to the short mean distance between nodes and the high tendency to clustering (i.e. to form groups of nodes very interconnected). These features can be revealed respectively by measuring the *mean shortest path length* and the *clustering coefficient*. The first is defined as the mean distance, measured in number of links, among any pair of nodes in the network, while the second is the number of links between all the pairs of nodes
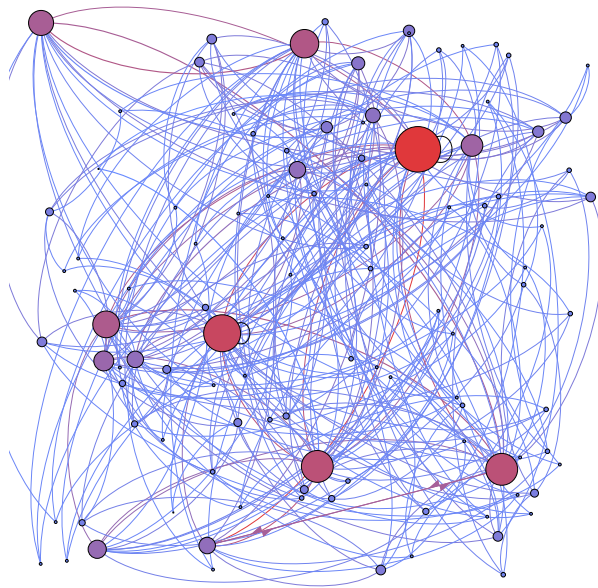
FIGURE 2.11: Scale free topology from a Barabási-Albert attachment network model with 10^2 steps (that is, new incoming nodes), $m_0 = 5$, $m = 3$, and an uniform network as initial topology with $k = 2$. Node size and color are associated with their degree ranging from small and blue (poorly connected nodes) to big and red (high connected nodes).

that are neighbours of a certain third one, divided by the number of all possible links between pairs of neighbours. For a node i, there are $k_i(k_i - 1)$ links that could exist among the nodes within the neighbourhood, and therefore the local clustering coefficient is given by:

$$C_i = \frac{|\{\#links\,(j,k):\; j, k\; neighbours\; of\; i\;\}|}{k_i(k_i - 1)},$$

and the global clustering will be

$$\bar{C} = \sum_i C_i.$$

Clustering coefficient per node degree distribution defined as $C(k) \equiv \langle C_i \rangle_{\{i:\, k_i = k\}}$ decreases as the node degree increases, and also follows a power law, i.e. $C(k) = k^{-1}$. That means that the low-degree nodes belong to very dense sub-graphs and

those sub-graphs are connected to each other through hubs. Consider, for instance, a social network in which nodes are people and links are acquaintance relationships between people. It is easy to see that people tend to form communities, i.e., small groups in which everyone knows everyone (one can think of such community as a complete graph). In addition, the members of a community also have a few acquaintance relationships to people outside that community. Some people, however, are so related to other people (e.g. politicians) that they are connected to a large number of communities. Those people may be considered the hubs responsible for the so called "small world" phenomenon. In fact, BA networks are part of the *small world networks* family, generally characterized by short average path length and high clustering [76], with some of these features in common with random and regular (e.g. square lattice) networks. For instance, on regular networks, like ordered lattices, the mean shortest path length and the clustering are both high, while in totally random topologies, like Erdös Rényi random graph [77], one finds low short path length and a poor clustering. In the BA model instead the average path length is short, eventually shorter than in a random graph and, at the same time, clustering coefficient is significantly higher than for random networks. Thus, BA networks are in the middle between ordered and disordered topology configurations, and this ensures an efficient communication between each pair of nodes together with a good cluster separation. These features could be useful, for instance, for neural networks that perform dynamics that include sequentially ordered and/or spatially located tasks [4, 22, 78].

2.5 Self affine surface growth, dynamic scaling, discrete and continuous Langevin models

The spontaneous generation of fractal interfaces or fronts has been observed in many natural processes [27, 79], and *fractal geometry* is the mathematical tool that allows to understand some of their morphological properties and dynamic mechanisms. The main assumption made in such framework is that these interfaces exhibit *self similarity*, namely, their statistical properties do not change under isotropic scale variations. The lack of any characteristic length is a common property of fractal objects, and an important feature of physical systems close to a critical point, as we have already explained in section 2.1. On the other hand, **dynamic scaling** deals with interfaces that roughen in space and time and that can

be described by means of a continuous, **self-affine**, function, which are invariant under anisotropic spatial scaling. A self-affine surface, or interface, is represented by its height function $h(\vec{r}, t)$, i.e. the height of the surface over the substrate point of coordinates $\vec{r}$ at time t. The self-affine height function has the following scaling properties:

$$h(\lambda \vec{r}, t) \sim \lambda^{\alpha} h(\vec{r}, t)$$
$$h(\vec{r}, \lambda t) \sim \lambda^{\beta} h(\vec{r}, t).$$

Here $\alpha, \beta \neq 1$ determine the anisotropic scale transformation. α is the *roughness exponent*, that describes the morphological characteristic of the interface, β the *growth exponent*, which controls its time evolution, and $z = \alpha/\beta$ the *dynamic exponent*, which governs the spreading velocity of the parallel correlation length, i.e. $\xi(t) \propto t^{\frac{1}{z}}$. Scaling analysis considers the interface dynamic as a stochastic process, and study the evolution of its spatiotemporal fluctuations. Due to the self-affine character of the interface, fluctuations display power-law behaviours. Let's consider for instance a surface in dimension $1+1$ (one spatial and one temporal), whose evolution is described by the height function $h(x, t)$. Its fluctuations can be characterized by means of the *interface width*:

$$W(L, t) \equiv \left\langle \left[\left(h(x, t) - \bar{h}(t) \right)^2 \right]_L \right\rangle^{1/2},$$

where $\bar{h}(t) = [h]_L (t) \equiv \frac{1}{L} \int_0^L h(x, t) dx$ is the mean height of the interface, whose fluctuations are averaged over the whole system of size L (or can be calculated averaging on every subsystem with window size $l \ll L$) and over different realizations of the experiment or model as denoted by $\langle \rangle$. Another statistical observable, often considered, is the *height-height correlation function* $C(l, t)$ given by:

$$C(l, t) = \left\langle \left[\left(h(x, t) - h(x + l, t) \right)^2 \right]_L \right\rangle,$$

that can be used to study the small-scale fluctuations of size l (see figure 2.12). Finally, the *power spectra*

$$S(k, t) \equiv \left\langle \hat{h}(k, t) \hat{h}(-k, t) \right\rangle,$$

where

$$\hat{h}(k, t) = L^{-1/2} \sum_x [h(x, t) - \bar{h}(t)] \exp(ikx),$$
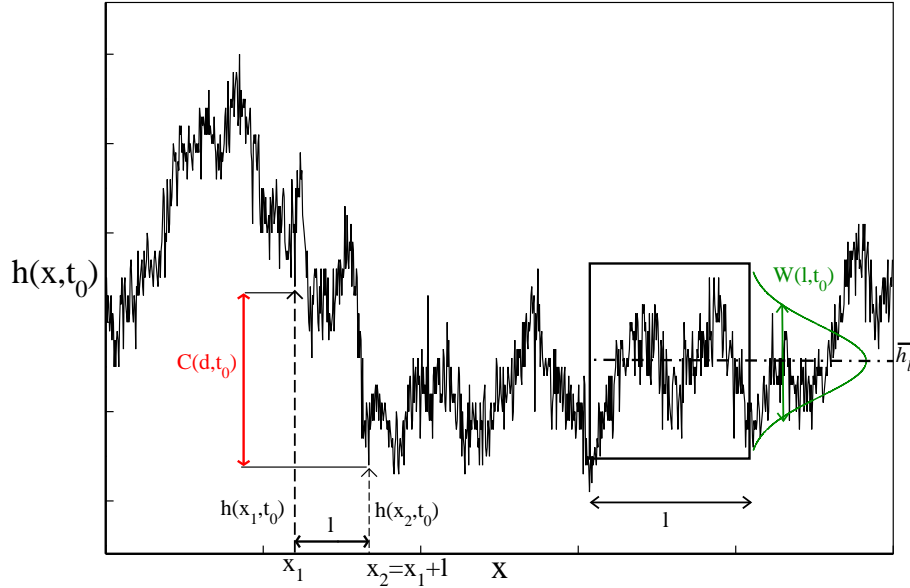
FIGURE 2.12: The correlation function $C(l,t) = \left\langle (h(x_1,t) - h(x_2 = x_1 + l, t))^2 \right\rangle$ is defined as the mean square height difference among all pairs of surface points $(x, y = h(x,t))$ placed at a distance d from x. The local surface width $W(l,t)$ is the mean of the local variances of $h(x,t)$, calculated around a mean height $\bar{h}_l$ over a domain of fixed size l.

describes the scaling behavior of the Fourier modes for the interface and obeys the following relationships:

$$C(l,t) \sim \int_{2\pi/L}^{\pi/a} \frac{dk}{2\pi} [1 - \cos(kl)] S(k,t) \quad ,$$

$$W^2(L,t) = \int \frac{dk}{2\pi} S(k,t) \quad .$$

(2.2)

These statistical observables completely describe the class of scale invariance for the spatiotemporal fluctuations of a self-affine interface, displaying typical power laws with exponents that depend on α, β, and z. For example, the typical behaviour of $W(L,t)$ follows the scaling *Ansatz*

$$W(L,t) = L^\alpha f(L/\zeta(t)), \quad f(u) \sim \begin{cases} u^\alpha & \text{if } u \gg 1 \\ \text{const} & \text{if } u \ll 1. \end{cases}$$

The function $f(u)$ is the so-called *scaling function* which captures the change between a non stationary regime, where correlation length $\xi(t)$ has not reach yet the window size L, and a stationary regime, when finally $\xi(t)$ spreads over the whole window size considered. Similarly, the power spectra scales as

$$S(k,t) = k^{-(2\alpha+1)}s(kt^{1/z}), \quad s(u) \sim \begin{cases} \text{const} & \text{if} & u \gg 1 \\ u^{2\alpha+1} & \text{if} & u \ll 1, \end{cases}$$

while the scaling of the correlation function $C(l,t)$ can be computed using (2.2), resulting

$$\sqrt{C(l,t)} = t^{\beta}g(l/\zeta(t)), \quad g(u) \sim \begin{cases} u & \text{if} \quad u \ll 1 \\ \text{const} & \text{if} \quad u \gg 1. \end{cases}$$

The aim of the dynamic scaling procedure is to perform a classification of growth processes into a few universality classes, determined by the values of the critical exponents, in order to develop general tools to establish their asymptotic behaviour.

In order to account for these roughening and self-affine properties, a number of discrete and continuous growth models have been proposed. For instance, a class of discrete models considers the surface growth as the result of both particle deposition and relaxation processes: each time step one particle falls down on the surface at a random substrate coordinate and then, according to the local geometry, eventually relaxes moving at one of the neighbour positions. Such models are defined with the *solid-on-solid* (SOS) hypothesis, by which no surface overhangs or bulk vacancies are allowed [2]. One of the simplest examples is the *Family model*, which has the following rules:

- **Deposition**: each time step one particle is deposited on the surface at a random substrate coordinate.

- **Relaxation**: an incoming particle relaxes on the neighbour site with the local minima. After this relaxation the particle cannot move anymore.

The critical exponents found for this model are $\alpha = (2-d)/2$ and $z = 2$, where d is the dimension of the substrate. Similarly in the *Wolf Villain* (WV) model the deposited particle relaxes to the site with the maximum number of bonds, or coordination number. On the other hand, in the *Das Sarma-Tamboranea* (DT) model, the deposited particle can relax to a randomly chosen neighbour site with a
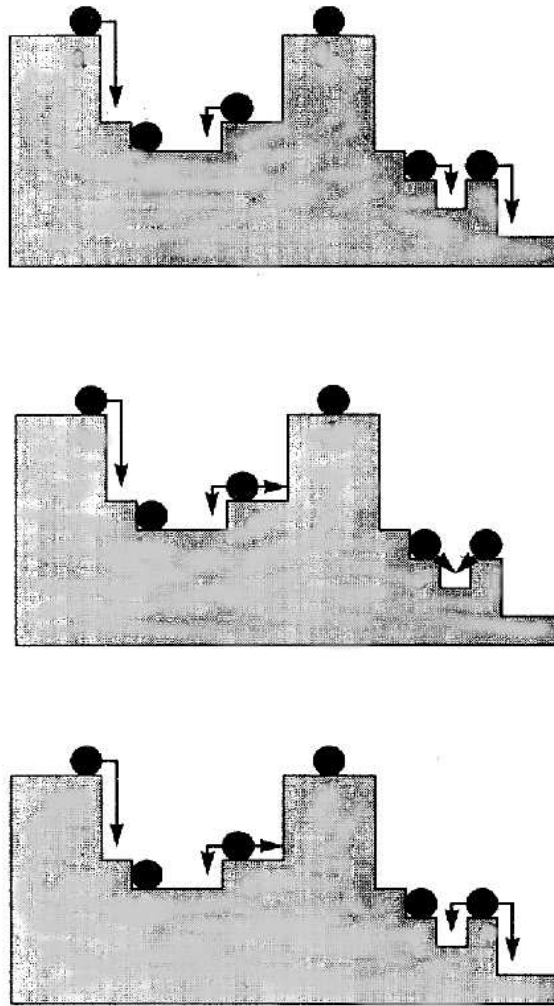
FIGURE 2.13: Schematic configurations defining the growth rules for the different SOS models described, in $d = 1$ dimension. From top to bottom: the Family model, where particle relax to the local minima, the Wolf-Villain model, with relaxation to local maximum bonds site, and the Das Sarma-Tamborenea model, in which particles with lateral bonds cannot relax. Reprinted from [2].

higher number of bonds (not necessarily the maximum one) only if the deposition site has no lateral bonds, as depicted in figure 2.13. Both WT and DT models have the scaling behavior characterized by $\alpha = (4 - d)/2$ and $z = 4$, at least for $d = 1$, even if in DT model the asymptotic regime is still unclear [2].

Different surface roughening processes can be described and generated also by *perimeter growth rules*, for instance in the three version of *Eden model* (Eden A, Eden B and Eden C), first implemented and studied in the 60's of the past century to simulate the growth of solid tumors [80]. Eden model considers particles in a square lattice. In the first version, each time step a single perimeter site (i.e. a site

adjacent to the particles in the surface) is filled with equal probability. In version B each perimeter site is filled with a probability proportional to the bonds it has with the surface. Finally in version C a particle of the surface is chosen randomly and then a new particle is placed in one of the adjacent empty sites with the same probability. Contrary to the models with relaxation dynamics, here surface overhangs and bulk vacancies could be present. For $d = 1$ all the versions of the Eden model have exponents $\alpha = 1/2$ and $z = 3/2$, and until now the dependence of the universality class on d for $d > 1$ has not yet been addressed.

In order to study the universality classes, that associate the roughening and self-affine properties of different particles models into the main dynamic processes characterized by their critical exponents, a number of continuous models have been proposed. In the continuum setting and under the assumption of linear symmetry, these models are usually written in terms of a Langevin-like equation, namely

$$\frac{\partial h(\vec{r}, t)}{\partial t} = F + G(h(\vec{r}, t)) + \eta(\vec{r}, t), \tag{2.3}$$

where $h(\vec{r}, t)$ stands for the surface height function, G is a generic function of $\vec{r}$, t, $h(\vec{r}, t)$ and its spatial derivatives, F is a driving force term and $\eta(\vec{r}, t)$ is the noise term which accounts for the roughening of the front. The physical meaning of each of these terms is the following: F is the mean rate of particle deposition or creation over the surface $h(\vec{r}, t)$, the functional G represents the local dynamic processes which adjust the shape of the surface by a relaxation process or preferential growth (like in the Eden model), and also it is involved in the shaping of both the short-time and the steady state properties of the growing interface. The noise term $\eta(\vec{r}, t)$ accounts for the stochastic fluctuations in the deposition rate and in the relaxation dynamics, and it is mainly a consequence of the average on the microscopic degrees of freedom, represented by each single particle dynamics. There are different types of noise that influence the critical features of surface growth, but in our case the noise used to study all the discrete particle models above described is a *white noise*, characterized by its first two moments, i.e.

$$\langle \eta(\vec{r}, t) \rangle = 0 \quad \left\langle \eta(\vec{r}, t) \eta(\vec{r'}, t') \right\rangle = 2A\delta^d(\vec{r} - \vec{r'})\delta(t - t'),$$

where A is the amplitude of the autocorrelation. In practice, such noise is implemented by choosing at each time step and for each position $\vec{r}$ a random number extracted from a Gaussian distribution with mean $\mu = 0$ and variance $\sigma^2 = A$.

In the case of deposition-relaxation processes, the most general continuum

equation which preserves the surface mass conservation and the symmetries of translational invariance along the growth direction and rotational invariance in the substrate plane, is:

$$\frac{\partial h}{\partial t} = \nu_2 \nabla^2 h - \lambda_4 \nabla^4 h + \lambda_{2,2} \nabla^2 (\nabla h)^2 + \lambda_{1,3} \nabla h (\nabla h)^3 + F + \eta(\vec{r}, t),$$

where ν_2, $\lambda_{2,2}$, $\lambda_{1,3}$ and λ_4 are the macroscopic growth coefficients. Without the SOS hypothesis, e.g. in the perimeter growth models, the Langevin equation with the leading order is the Kardar-Parisi-Zhang (KPZ) equation:

$$\frac{\partial h}{\partial t} = \nu_2 \nabla^2 h + \lambda_2 (\nabla h)^2 + F + \eta(\vec{r}, t),$$

Using Fourier transformation or the dynamical renormalization group (DRG) techniques, one can theoretically derive the values of the scaling exponents, resulting that the asymptotic dynamic is determined by the dominant relaxation terms with non zero coefficients. The hierarchy for the different terms is $\lambda_2 > \nu_2 > \lambda_{1,3} > \lambda_{2,2} > \lambda_4$. In this way, one can reduce the surface roughening behavior of many different discrete particle models in few universality classes (represented by Langevin equations) containing their essential dynamics, as it is summarized in table 2.1.

	$G(\vec{x}, h, t)$	α	β	z
EW (Family Model and asymptotic WV)	$\nu_2 \nabla^2 h$	$\frac{2-d}{2}$	$\frac{2-d}{4}$	2
KPZ (A, B and C Eden models with $d = 1$)	$\lambda_2 \nabla^2 h$	$\frac{1}{2}$	$\frac{1}{3}$	$\frac{3}{2}$
MBE (WV and DT models with $d = 1$)	$-\lambda_4 \nabla^4 h$	$\frac{4-d}{2}$	$\frac{4-d}{8}$	4

TABLE 2.1: Universality classes defined by the deterministic relaxation term $G(\vec{x}, h, t)$ of the corresponding Langevin equation (2.3). The value of critical exponents α, β and z, depends on the geometrical dimension d of the surface.

Chapter 3

Mathematical models of neuron and synapse dynamics

In this chapter a brief description of the physiology of *neurons*, the most important cells of neural tissues, and of the *synapses*, that constitute the mechanisms by which they communicate each other, is introduced. We also present the *Integrate and Fire Model* (IF), one of the simplest neuron models implementing *membrane potential dynamic*, and of the *Tsodyks Model*, which describes the so called *dynamical synapses*. Finally a brief description of a classic model in theoretical neuroscience, namely the *Hopfield Model*, originally formulated to describe the phenomena of *associative memory* displayed in some brain areas, is given.

3.1 Neuron physiology and dynamics

In superior animals the nervous system receives information from the external environment through senses and then organizes and coordinates the actions by mean of the transmission of motor signals to the different parts the body. The nervous system is therefore responsible of the individual adaptation in a changing environment, which is a crucial mechanism for the survival of the species. Nervous system is constituted by specialized cells, called neurons, which are organized in two different structures [81]:

- **The Central Nervous System (CNS)**, constituted by the brain and the spinal chord, where neurons, structured in a very sophisticated network, process the huge amount of information coming from the external environment through the senses.

- **The Peripheral Nervous System (PNS)**, constituted by cranial and spinal nerves, that represent the pathways that allow communication and interchange of information between the CNS and the rest of the body and *vice versa* by mean, respectively, of the motor nerve fibers and the somatic sensory nerve fibers.

Animal brains are thus essentially networks composed by a great number of interconnected neurons. In such networks, each neuron receives a number of input signals from other neurons through some specialized junctions, the *synapses*. A neuron processes the input signal by modulating its own internal state, that depends essentially on the level of its *membrane potential*. Neuron membrane potential changes in response to *ionic currents* flowing across the membrane. The different ions flow through voltage dependent or specific ligands (i.e. *neurotransmitters*) dependent channels.

The anatomy of a typical neuron is constituted by the following parts (see in figure 3.1):

- A central cell body or **soma** that houses the cell nucleus and most of the genetic expression and synthetic machinery for elaborating the proteins, lipids, sugars and others constituents of cytoplasm environment. In the cell membrane membrane, moreover, there are communication sites between the extracellular medium and the interior of the cell constituted by specific transmembrane macromolecules that control the level of the membrane potential and ion concentrations, as the voltage and ligand activated ionic channels and the ionic pumps.

- The *receiving pole* consists of wide branching tree-like extensions of the soma membrane, known as **dendrites**, and arises in vertebrate directly from the cell body. Each one of such poles is closely joined to the *output pole* of another neuron. These junctions are called **synapses**.

- The output pole, called **axon**, arises as a single branch structure from the soma. Axon membrane allows for the conduction of the propagating neuron
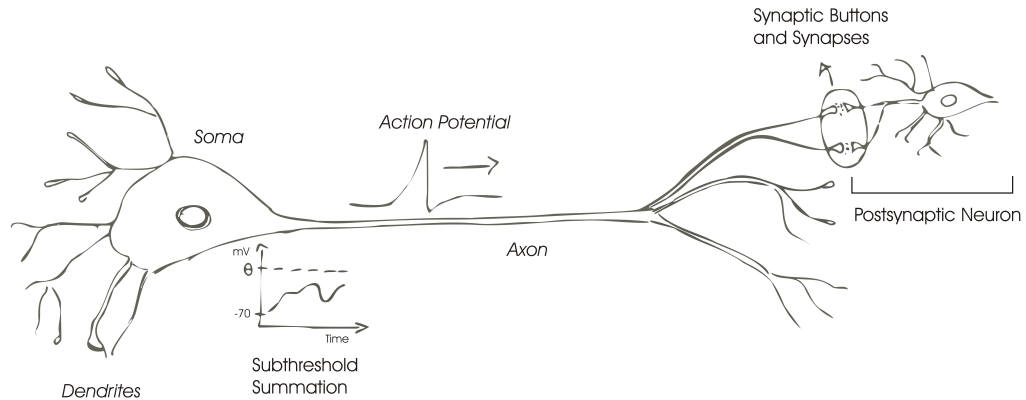
FIGURE 3.1: Schematic representation of a neuron. In the central body, or *soma*, neuron integrates the changes in membrane potential that are produced, by synaptic inputs coming from presynaptic neurons, in the *dendritic* terminations. Then when membrane potential reaches the threshold potential, neurons generate an action potential wave that propagates from the soma to the terminal branches through the axon. At the end of terminal axon branches, in the synaptic buttons, action potential is transducted, i.e. it produces an output in the form of a change in postsynaptic neuron membrane potential, by mean of different synaptic biochemical mechanisms.

electrical signals, called **action potentials** (AP), which are generated in the *Hillock* of the soma and travel towards the synaptic junctions. An action potential, also called *spike*, lies in a rapid change in voltage across the membrane, and constitutes the way a neuron "speaks" to others neurons. In the axon terminations, i.e. the so called **synaptic buttons**, an action potential from a **presynaptic neuron** is transducted, evoking a change in membrane potential of the linked **postsynaptic neuron**.

The synapses, that transduce neurons action potential in the synaptic button, could be classified essentially in two different types, depending on the nature of the mechanisms involved [82], which are schematized in figure 3.2:

- **Electrical synapses**. In these synapses, presynaptic and postsynaptic membrane are joined by specific protein structures, called gap junctions, which form channels that connect the cytoplasm of both cells. When a neural signal (action potential) comes to the gap junction, it depolarizes (or hyperpolarizes) the membrane which induces the opening of the channels and the diffusion of ions through them from one neuron to another. Ion flux,

depending on the difference between presynaptic and postsynaptic neuron membrane potentials, triggers a change in postsynaptic membrane potential.

- **Chemical synapses**, which are mediated by *chemical messengers*, called **neurotransmitters**. These are released from the presynaptic neuron into the synaptic cleft (i.e. the narrow space between the membranes of the pre- and post-synaptic cells) each time an AP arrives to the synaptic button. Once they are released, these neurotransmitters diffuse and activate ionic channels in the postsynaptic neuron. In a chemical synapse there is not physical contact among the neurons. Signal transmission there occurs as follows: when a presynaptic action potential arrives to the synapse, it produces the opening of some neurotransmitter filled vesicles near the membrane. Vesicles exocytosis causes the release and diffusion of a large amount of neurotransmitters in the intersynaptic space. The released neurotransmitters have affinity for certain molecular receptors in the postsynaptic membrane and, after binding to them, induce the opening of specific ionic channels. The last finally produces the depolarization (or hypepolarization) of the postsynaptic membrane. Then, the released vesicles in the presynaptic neuron are replaced by others which are in some reserve pool of vesicles, located relatively far from the membrane.

  Chemical synapses efficacy have then a dependence on neurons activity. In fact, spiking frequency modules the quantity of released neurotransmitters, which is also influenced by vesicles/neurotransmitters recycling mechanisms, with a characteristic time τ_{rec}. Moreover, the arrival of action potentials regulates the influx of Ca^{+2} in the synaptic button, which enhances the probability of releasing a vesicle [83]. The result is a phenomenon known as **synaptic plasticity**, that is described and modeled in section 3.3.

3.1.1   Action potential generation

The main properties of membrane potential dynamic and action potential generation, described in figure 3.3, are the following:

- **Linear subthreshold summation**. When the neuron is in a resting state, its membrane potential, also called *graded potential*, is hyperpolarized, typically around $-70\ mV$. The membrane ionic currents generated from the
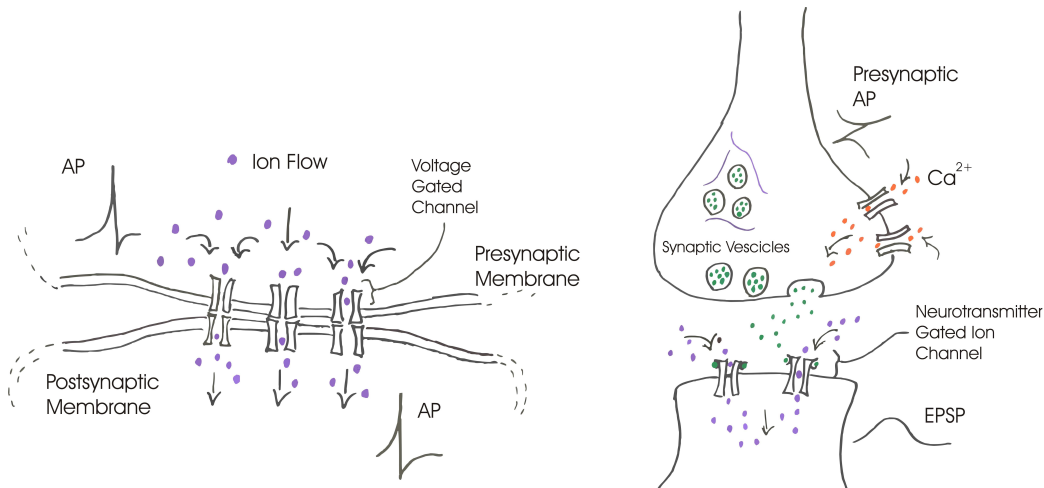
FIGURE 3.2: Scheme showing the differences during signal transmission between electrical synapses (right) and chemical synapses (left). Signal transmission in electrical synapses is a passive mechanism in which ions can quickly diffuse between presynaptic and postsynaptic neurons through the gap junctions. In chemical synapses signal transmission occurs as the result of different biophysics mechanisms, which occur sequentially in different time scales, and which generate an excitatory (or inhibitory) postsynaptic potential, namely, EPSP (or IPSP for inhibitory synapses)

different synapses in the dendritic terminations contribute to module this potential. Such contributions are linearly summed in the soma, until the graded potential reaches a threshold value, namely the *threshold potential*, and the neuron then generates an action potential.

- **Positive and negative contributions to membrane potential**. The chemical synapses, depending on the type of neurotransmitters and receptors in postsynaptic neurons, can be *excitatory*, increasing the postsynaptic membrane potential (producing an Excitatory Post Synaptic Potential, or EPSP), or *inhibitory*, i.e. decreasing it (Inhibitory Post Synaptic Potential, or IPSP).

- **All or none spike generation**. The generation of an action potential is a **threshold process**, thus only when the membrane potential reaches the threshold potential, a depolarizing wave, the *action potential*, is produced in the soma termination of neuron axon, i.e. the axon Hillock. Action potential is generated by a fast depolarization of the membrane potential from $-70\ mV$ to $+30\ mV$, and propagates maintaining its shape, amplitude and velocity towards neuron synaptic terminations through the axon [84]. On
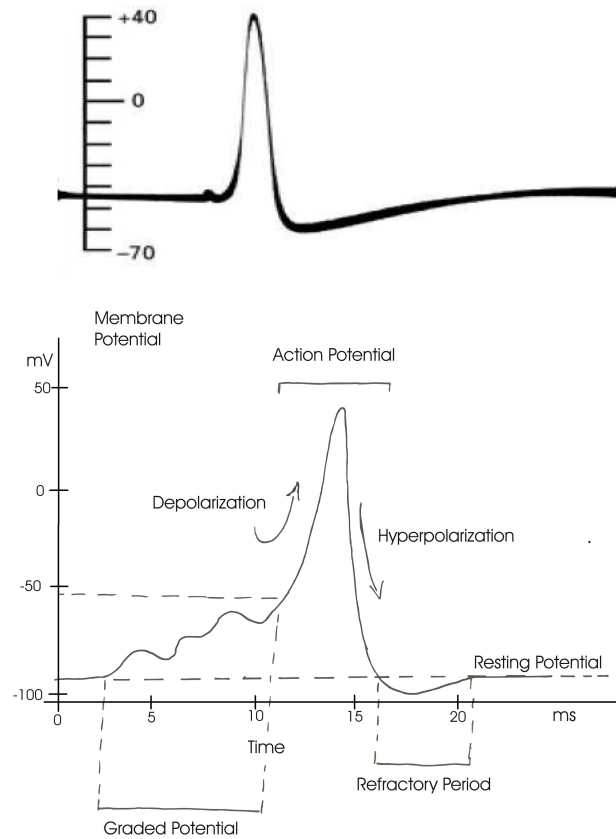
FIGURE 3.3: Top: First published intracellular recording of an AP, obtained in 1939 by Hodgkin and Huxley from the squid giant axon. The vertical scale indicates, in millivolts, the potential of the internal electrode used to perform the recording. Adapted from [3]. Bottom: Scheme showing the changes of the membrane potential in the soma, during the generation of an AP. Membrane potential linearly sums excitatory and inhibitory input contributions, until the threshold potential value is reached. Then, it rapidly depolarizes, generating an AP which propagates through the axon. Finally it repolarizes and becomes insensitive to any input for a time interval called refractory period.

the contrary, when membrane potential is subthreshold no signal can be transmitted to the synapses. Action potential propagation in the axon also depends on the ionic currents flowing across the membrane through ionic channels (the most common being sodium, potassium, calcium and chloride channels) which modulate the active (voltage dependent) and passive (capacitive and voltage independent) electrical properties of the cell membrane.

- **Refractory period**. After a spike is emitted, the membrane potential can not integrate any contribution from synapses during a period of time called *refractory period*. Refractory period is the characteristic time necessary to recover the membrane resting potential state.
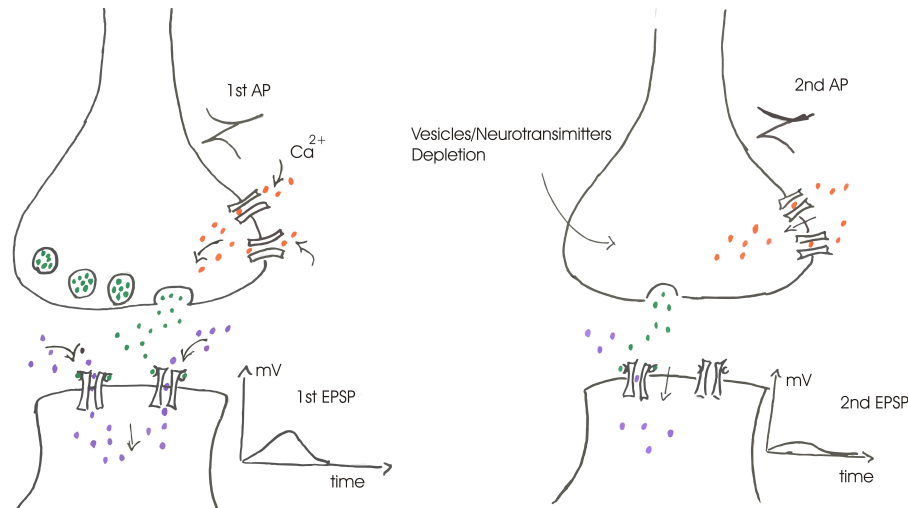
FIGURE 3.4: Scheme of the basic mechanism of STD. Left: A first AP induces, via an influx of Ca^{+2} into the cell, the fusion of a certain number of vesicles with the membrane, and the release of their neurotransmitters into the synaptic cleft. The binding of the neurotransmitters to the postsynaptic receptors causes a flux of extracellular ions into the postsynaptic cell which induces an EPSP. Right: After a relatively short period of time, a second AP arrives at the presynaptic terminal. Since the neuron needs some time to replace the released vesicles near the membrane, the amount of neurotransmitter released will be lower than in the case of the first AP. As a consequence, a smaller number of postsynaptic receptors will open, and the EPSP will be smaller in amplitude than the first one.

3.2 The integrate and fire neuron model

The integrate and fire (IF) model constitutes the simplest paradigm of the threshold-firing neuron mechanism. It was introduced by Lapicque in 1907 [85] as a simple model which presents the most basic features of actual subthreshold membrane potential dynamics. The model has the form of a single linear differential equation defining the dynamics of the membrane potential $V(t)$ with a threshold condition for spike generation, that is:

$$\tau \frac{dV(t)}{dt} = -\left[V(t) - V_r\right] + R_m I(t). \tag{3.1}$$

Here $I(t)$ is the input current that models the contributions to the membrane potential due to presynaptic inputs and R_m is the membrane resistance. The negative term on the right-hand side is the so called *leakage* term that accounts for the ion flow across passive channels, and it tends to reset the potential to the rest value with characteristic time τ.

In addition the model includes an auxiliary condition which states that, when

the membrane potential exceeds the threshold V_{th}, an AP is generated and the membrane potential is reset to a resting value V_r in which the neuron, for a short period of time τ_{ref}, i.e. the refractory period, is insensitive to any additional input. The simplicity of this model implies that only a few realistic neural features are reproduced, such as tonic spiking and integrating capacities. However the simplicity of the model implies some advantages from a theoretical point of view, since in many cases one can analytically solve the dynamics of networks of IF neurons, or at least to find approximate solutions by employing mean-field techniques. For instance, if the input current is sufficiently simple, it is possible to find adequate solutions which allow to compute magnitudes of interest, such as the mean firing rate or the coefficient of variation of the neural activity [86]. On the other hand, the IF model can be easily extended to include more biophysically realistic features, such as neural adaptation, bursting activity, resonance properties, or spike latency, to name a few [87, 88]. In addition, the parameters employed in the basic IF model are physiologically meaningful (such as the membrane resistance R_m, the refractory time τ_{ref}, or the membrane threshold V_{th}) and therefore they can be measured directly in experiments. For all these reasons, the IF neuron model is one of the most studied and used in the computational neuroscience literature. Coupled IF neurons systems have been studied on different classes of networks. The IF coupled equations for a N-neurons network can be written as:

$$\tau \frac{dV_i(t)}{dt} = -\left(V_i(t) - V_r\right) + R_m \left(I_i^{net}(t) + I_i^{ext}\right) \qquad \forall i \in \{1, \ldots, N\}$$

where $I_i^{net}(t)$ is the sum of all synaptic currents arriving to neuron i from other neurons in the network. Synaptic currents are the sum of the spikes contributions arriving at different synapses. One of the easiest way to model these spike contributions is with the use of delta functions:

$$R_m I_i^{net}(t) = \tau \sum_{j=1}^{N} J_{ij} a_{ij} \sum_k \delta(t - t_j^k).$$

Here a_{ij} is the i, j-th element of *adjacency matrix* ($a_{ij} = 1$ if exists a synapse from neuron j to i, $a_{ij} = 0$ if not), J_{ij} is the postsynaptic potential (PSP) amplitude (or efficacy), while the second sum represents a sum over different spikes arriving at synapse j, at time $t = t_j^k$, where t_j^k is the emission time of k-th spike at neuron j. PSP amplitudes J_{ij} are positive for excitatory synapses, and negative for inhibitory ones. External synapse contributions, from other neuron layers (outside

the network considered) or from the senses, are modelled by $I_i^{ext}(t)$, that in general is implemented as a constant term, a Gaussian variable or a Poisson process [86].

With this model it has been reported a wide range of behaviours, ranging, for instance, from totally asynchronous to global synchronous activity states, depending on the balance between excitatory and inhibitory synapses, and also on the membrane time constant τ and on the external input currents I_i^{ext} [89]. Also the properties of the underlying topology of networks of IF neurons has shown to have influence on the emergent features of such type of synchronization states [90–92]. Finally and very recently, it has been reported some intriguing behaviour in networks of IF neurons with non-conservative couplings (which includes the case of static [93] and dynamic synapses [21, 94]) as, for instance, the appearance of Self Organized Criticality (SOC) with avalanches of spikes in the network power-law distributed [6], and the existence of SOC events with subthreshold UP/DOWN transitions [94] (see also section 4.4).

3.3 Basic model of chemical synapses: Tsodyks Model

Synaptic strength can vary dynamically on short time scales depending on the presynaptic spiking activity [95]. Synapses presenting such activity-dependent dynamics are also known as *dynamic synapses*, and can be described by two complementary mechanisms, short-term facilitation (STF) and short-term depression (STD):

- In STF, high frequency spiking enhances vesicles release, due to the influx of Ca^{2+} ions into the synaptic button through voltage-sensitive channels just after the arrival of each presynaptic spike. Calcium concentration activates a set of calcium-sensitive proteins attached to the vesicles. Then these proteins change shape, causing the membranes of some "docked" vesicles to fuse with the membrane of the presynaptic cell, thereby opening the vesicles and releasing their neurotransmitter contents into the synaptic cleft [83]. Thus higher concentration of Ca^{2+}, due to residual cytosolic calcium produced by immediate past spiking activity, see figure 3.5, facilitates the neurotransmitter vesicle depletion, and by this mechanism the postsynaptic response increases for successive spikes [96].
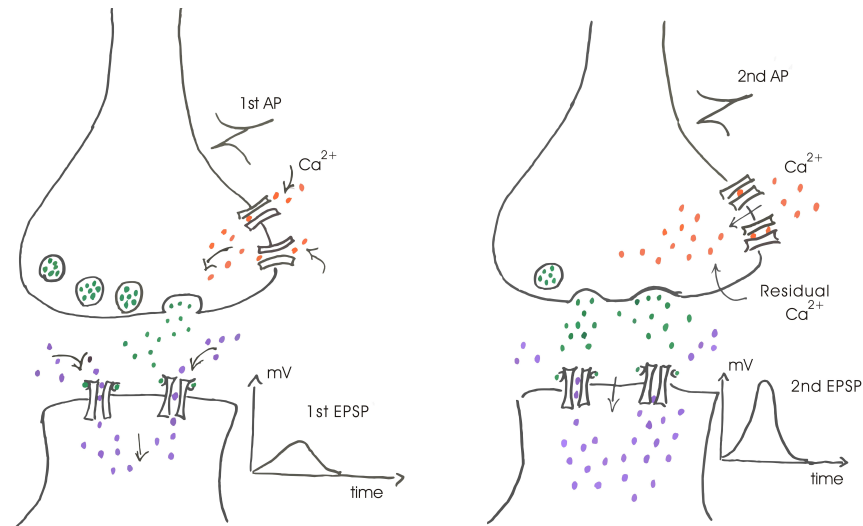
FIGURE 3.5: Scheme of the mechanism of STF. Left: A first AP induces, via the influx of Ca^{2+} into the cell, the fusion of a certain number of vesicles and the release of their neurotransmitters into the synaptic cleft. The binding of the neurotransmitters to the postsynaptic receptors causes a flux of extracellular ions into the postsynaptic cell, and this induces an EPSP. Right: After a relatively short period of time, a second AP arrives at the presynaptic terminal. This induces a new influx of extracellular Ca^{2+} into the presynaptic terminal, which still houses a residual amount of Ca^{2+} from the first AP. Since the concentration of presynaptic Ca^{2+} is larger than before, a higher amount of neurotransmitter will be released, and as a consequence this second EPSP will be larger than the first one.

- In STD, fast presynaptic spiking activity induces a weakening in the postsynaptic response, due to a partial depletion of synaptic vesicles and neurotransmitters in the synaptic button, as one can see in figure 3.4. This occurs due to the recovering process of the synaptic vesicles (whose dynamic has a characteristic time τ_{rec}), which are released into the synaptic cleft in response to a presynaptic AP (see figure 3.6).

The dynamic of the synapses is thus affected by some activity-dependent mechanisms that produce non-linear effects in the postsynaptic response. Synapses can be dominated by depression effect, when the probability to release a vesicle is high, or by facilitation, for low values of vescicle release probability. For intermediate values of U, one can find an optimal spiking frequency enhancing synaptic strength [97], see figure 3.6. Short-term depression plays an important role in several emerging phenomena in the brain, such as selective attention [98], cortical gain control [97], and has been introduced in different neural models to describe the collective switching dynamic between high and low neural activity levels [94, 99], the so called UP/DOWN transitions (for details see section 4.4), the enhancing of the

stability of SOC (or *quasi*-SOC) neural states [21], or spike coincidence detection [100], to name a few. STD is also responsible for the complex switching behavior between activity patterns observed in neural network models with depressing and facilitating synapses [101, 102], while synaptic facilitation is involved in the precise detection of bursts of action potentials [103, 104], and in the efficient transmission of temporal correlations between spike trains arriving from different synapses [105].

One of the most important theoretical approaches to model dynamic synapses is the phenomenological model presented in [95], the so called Tsodyks model, which considers that the state of a synapse between a presynaptic neuron j and a postsynaptic neuron i is governed by the following system of three differential equations,

$$\frac{dx_j(t)}{dt} = \frac{z_j(t)}{\tau_{rec}} - U_j(t)x_j(t)\delta(t - t_j^{sp})$$

$$\frac{dy_j(t)}{dt} = -\frac{y_j(t)}{\tau_{in}} + U_j(t)x_j(t)\delta(t - t_j^{sp}) \tag{3.2}$$

$$\frac{dz_j(t)}{dt} = \frac{y_j(t)}{\tau_{in}} - \frac{z_j(t)}{\tau_{rec}},$$

where $x_j(t), y_j(t), z_j(t)$ are dynamical variables that represent the fraction of neurotransmitters in a *recovered, active* and *inactive* state[1], respectively, and the delta functions consider that a spiking event reaches the synapse at time $t = t_j^{sp}$. Here, τ_{in} is the typical time for inactivation of postsynaptic receptors and τ_{rec} is the typical time for neurotransmitters recovery process in the presynaptic neuron. The variable $U_j(t)$ in this phenomenological model is defined as

$$U_j(t) \equiv u_j(t)(1 - U_{SE}) + U_{SE}$$

and represents then the maximum fraction of neurotransmitters that can be activated, both by the arrival of a presynaptic spike, included in the term U_{SE}, and by means of facilitating mechanisms, i.e. $u_j(t)(1 - U_{SE})$, where $u_j(t)$ is a dynamical variable which takes into account the influx of calcium ions into the presynaptic neuron near the synapse through voltage-sensitive ion channels [83] (see figure

---

[1]Neurotransmitters in a recovered state are those in the vesicles that refill the ready releasable pool, i.e. the set of vescicles of the presynaptic button very close to the membrane. Active neurotransmitters are those which have been released and can produce a postsynaptic response, while inactive neurotransmitters are the remaining, in such a way that $x(t) + y(t) + z(t) = 1$.
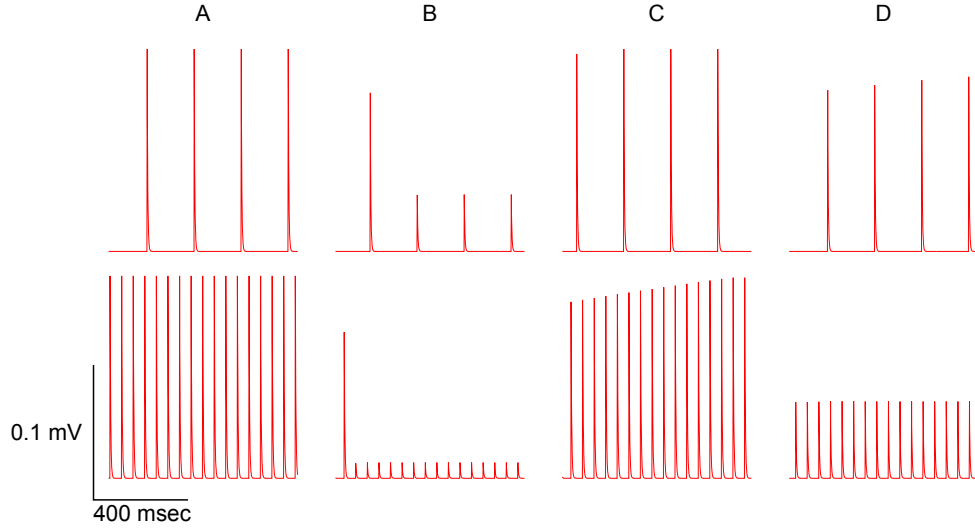
FIGURE 3.6: Simulated train of EPSPs generated in a single synapse after the arrival of a train of presynaptic spikes at frequency of 5 Hz (top panels) and 20 Hz (bottom panels), when the synapse is *static* (A), and *dynamic* with only a depressing mechanism (B) and with depressing and facilitating mechanisms (C and D). The synapse parameters were $U_{SE} = 0.02$ and $\tau_{rec} = \tau_{fac} = 0$ for panel (A), $U_{SE} = 0.3$, $\tau_{rec} = 600ms, \tau_{fac} = 0$ for panel (B), $U_{SE} = 0.02$, $\tau_{rec} = 10ms, \tau_{fac} = 6s$ for panel (C) and $U_{SE} = 0.02$, $\tau_{rec} = 100ms, \tau_{fac} = 6s$ for panel (D).

3.2). Its dynamic is described by:

$$\frac{du_j(t)}{dt} = \frac{U_{SE} - u_j(t)}{\tau_{fac}} + U_{SE}[1 - u_j(t)]\delta(t - t_j^{sp}). \qquad (3.3)$$

In the limit of $\tau_{fac} \to 0$ the resting value $U_j(t) = U_{SE} \forall t$ is obtained, suppressing all the STF effects, and recovering a pure depressing synapse (if $\tau_{rec} > 0$) or a static synapse (if $\tau_{rec} = 0$).

Equations (3.2) constitute a close phenomenological description of activity dependent short-term synaptic mechanisms. Some of the main functional properties of STD and STF can be understood via the former equations. In order to understand that, one may assume, for instance, a presynaptic excitatory neuron, firing APs periodically (being Δt the time interval between two successive presynaptic spikes and $f \equiv 1/\Delta t$ the corresponding presynaptic firing rate), connected to a postsynaptic one via a depressing synapse (that is, with $\tau_{rec} > 0$ and $\tau_{fac} = 0$). In this simple situation, analytical solutions of the model can be obtained easily [106]. Figure 3.6 shows that the effect of repetitive presynaptic stimulation in

the presence of STD is a decrease of the EPSP, until a stationary EPSC value is reached. This effect is observed in experimental *in vitro* recordings, and numerical simulations of the model presented above nicely fits such behavior [95]. A straightforward consequence is that this filtering effect depends on the presynaptic firing rate, in such a way that higher firing rates induce stronger decreases of the EPSP. A similar effect can be obtained also by increasing the value of τ_{rec} (which is a measure of the mean time employed by the synapses in refilling with neurotransmitters vescicles the ready releasable pool) instead of the presynaptic firing rate. Therefore, STD provides a synapse-level mechanism to control the gain of postsynaptic responses in an activity dependent manner [107]. On the other hand, the inclusion of STF induces an increment in the postsynaptic response under repetitive presynaptic stimuli. This can be seen by setting $\tau_{rec} > 0$ and $\tau_{fac} > 0$ in the model and analyzing the effect of a presynaptic periodic stimulation in the EPSC in the presence of STD and STF. The particular stationary value of the postsynaptic response depends on the presynaptic firing rate and/or the facilitation time constant τ_{fac}. When both STD and STF mechanisms are considered together, a competition between the two a priori opposite tendencies can occur. In this particular situation, a maximum value of the postsynaptic response is obtained for certain value of the presynaptic firing rate, as the figure 3.6 (panel D) shows.

3.4   Collective behavior in neural networks: associative memory and synaptic reverberations

In the previous sections we have seen how neuron and synapse dynamics includes several non linear mechanisms occurring at different spatial and temporal scales. For example, one can mention the feedback interactions among ion fluxes and membrane channels in membrane potential integration, the all or none spiking generation process, the traveling dynamic of the action potential through the axon, and finally the synaptic plasticity mechanisms affecting synapses transmission. In addition the actual neural systems are structured in large networks, in general, with a complex topology. The cerebral cortex of the human brain, for example, contains roughly $15-33$ billions of neurons [108] linked with up to 10^4 synaptic connections each [109]. However, human brain is continuously receiving, processing

and reacting in an appropriate way to a large amount of external stimuli, producing a lot of different behaviours and phenomenologies that cannot be considered as the result of a simple sum of the contributions of its components, neurons and synapses. Thus the brain must be considered indeed as a paradigm of **complex system** (in the meaning of section 2.1).

Many efforts have been made in the last decades to develop mathematical and computational models able to reproduce the different properties of the brain. Although the realization of a complete model reproducing the whole behavior of a brain is a very difficult task, and nowadays it is still a far aim, one can elaborate simple models focusing their attention just on few features, for example neural signal integration, network topology or synaptic dynamic, and observe the role they have on a particular kind of network phenomena. One classic example is the Hopfield Attractor Neural Network (HNN) (see section 3.4.1 for details). In the Hopfield network, nodes corresponds to neurons and links represent synapses. The state of a neuron is described by a binary variable (i.e. corresponding to silent and spiking states), and synaptic intensities are fixed in time and weighted according to some prescription (in the original model the so called *Hebb rule* [18]) which allows the network to store information in the form of a set of given patterns of neurons activity. In fact, these patterns become attractors of the dynamic, so that the network is able to retrieve the stored pattern which is close to its initial condition. This process, known as **associative memory**, can be considered as a suitable representation of the memory and recall processes observed in the brain [110].

Associative memory phenomenon has been extensively studied in the literature [110–112], and could be considered as the mechanism by which neural networks are able to retrieve a particular memory by simply presenting as an input incomplete or partial information of such memory. By mean of such mechanism one can recover, for instance, the memory of a known familiar face, or more in general an image or a word previously "learned". Although an image can be seen only in some details, or a word can be heard from different voices, with some wrong accent, one recovers always the same detailed and precise associate mental representations of them. Moreover, even when the input disappears, it is possible to retain such representations for a certain period of time in the consciousness, encoding them in the activity pattern of certain brain subsystem.

One of the first experimental works that suggested the central role of the neural

network synaptic structure in the storage and in the recovering of visual representations was performed by Miyashita *et al.* [113–115]. The goal of their experiments were to recognize in some neural structures of monkeys the mental representations of visual stimuli. In a first training phase, some couples of images have been presented to the monkeys. Successively, the monkeys performed an image recognition test, trying to recognize correctly the couple of images previously learned. At the same time extracellular spiking activity of single neurons, located in a small zone of the anterior ventral temporal cortex (AVT) were recorded. Such neurons resulted to have an activity strongly dependent with the images proposed during the test, even within in the delay period before the presentation of the second image. More precisely, single neurons, during the delay period, are active only in response to some couples of stimulus-(correct)response images, while the activity of whole group of neurons resulted to mark different fingerprints for each image pairs. Miyashita experiments allows the following conclusions [115]:

- In the anterior ventral temporal cortex (AVT), where neurons forms highly interconnected networks, is possible to observe self sustained, long lasting, neurons activity patterns. These patterns, also called *reverberations*, as well as the activities of each single neuron constituting them, depend on the first image presented (i.e. the initial stimulus). The reverberations can be considered as internal representation of the stimulus.

- The reverberations are not single-neuron features because single neurons cannot maintain selective activity rates. On the contrary the internal representations are distributed, that is, many neurons are involved in the representation of each memory, and different representations can share some active neurons.

- The internal representations can be considered as attractors of network dynamics. In fact they are insensitive to color, size or angular orientation of stimulus, thus they can be recalled with partial or distorted inputs [116]. Moreover, in some experimental settings, different stimuli leads to the same internal representation [117].

These conclusions strongly support the idea that the internal representations of memories depend essentially on the network structure and the synapse strength distributions, as previously argued by Hebb [18] in his works on the physiological

bases of learning. Hebb proposed a learning rule which, each time an input is presented to a neural network, establishes the relation between the reinforcement of a synapse and the level of correlation in the activity of the two neurons linked by such synapse. That is, reiterative activity is able to induce long-term plastic modifications which lead to specific changes in the synaptic response. Synaptic reinforcements induced by neural activity have been measured in a wide variety of experiments, both *in vivo* and *in vitro*, as well as in psychophysical experiments [118–120].

Associative memory constitutes a typical example of emergent large-scale phenomena induced by cooperation between microscopic elements, i.e. neurons and synapses. As mentioned above, the first mathematical model which demonstrated the plausibility of associative memory is the Hopfield model (also known as Amari-Hopfield model because was developed independently by Amari [121] and Hopfield [110]) which we will describe with more detail in the next section.

3.4.1 The Amari-Hopfield Neural Network Model

In the 80's Hopfield [110] formulated a neural network model that included the hypothesis of Hebbian learning in order to study associative memory. The model consists in a network composed by N binary neurons, i.e. the state of i-th neuron can assume only two values $s_i \in \{+1, -1\}$, that represent respectively neuron at the resting potential and emitting an action potential. The state of the whole network is described by a N component vector $\vec{S} = \{s_1, \ldots, s_N\}$. The original model considers in addition a **fully connected topology** network, where each neuron i is connected with all the other neurons, and receives as input from j-th neuron the quantity $w_{ij}s_j$, where w_{ij} is a constant representing the **weights** of the synapse between j-th presynaptic and i-th postsynaptic neuron. According to the linear subthreshold summation principle for neuron graded potential [84], all the inputs reaching the i-th neuron are merely summed in its **local field potential**, $h_i(\vec{S})$, defined as:

$$h_i(\vec{S}) = \sum_{j \neq i} w_{ij}s_j - \theta_i,$$

where θ_i is the threshold potential for the generation of an action potential. The local field potential induces s_j to assume its same sign. From the physical point of view $h_i(\vec{S})$ represents the energy per neuron in the network, and allows to define, when all the synapse strengths are symmetric, i.e. $w_{ij} = w_{ji} \quad \forall i, j$, a Hamiltonian

of the system, very similar to that of the Ising model (described in Section 2.2), that can be written as:

$$H = -\frac{1}{2}\sum_i h_i(\vec{S}) = -\frac{1}{2}\sum_{i,j\neq i} w_{ij}s_i s_j + \sum_i \theta_i s_i. \tag{3.4}$$

The evolution of the probability distribution for the network configuration $\vec{S}$, i.e. $P_t(\vec{S})$, can be described in term of the following Master Equation:

$$P_{t+1}(\vec{S}) = \sum_{\vec{S'}} \bar{T}(\vec{S'} \to \vec{S}) P_t(\vec{S'}), \tag{3.5}$$

with transition probability from state $\vec{S'}$ to $\vec{S}$ given by

$$\bar{T}(\vec{S'} \to \vec{S}) = \varphi\left[\beta\left(H(\vec{S'}) - H(\vec{S})\right)\right].$$

Here the parameter $\beta \equiv 1/T$, being T a "temperature" parameter which defines the level of noise in the network, due to the different sources of intrinsic stochastic fluctuations, for example, affecting the generation of APs or the recycling mechanism of the released vesicles in the synaptic cleft. $\varphi(x)$ is a generic function of the temperature and the energy gap between the old configuration $\vec{S'}$ and the new one $\vec{S}$, which we assume to satisfy the detailed balance condition, i.e. $\Phi(x) = e^{-x}\Phi(-x)$. In the deterministic limit $T \to 0$ (that is $\beta \to +\infty$) neural network state always reaches a minimum of the associated Hamiltonian $H(\vec{S})$, so that $\varphi(x)$ has to fulfill the conditions $\varphi(x \to +\infty) \to 1$ and $\varphi(x \to -\infty) \to 0$.

Let's define in the model, as previously mentioned in section 3.4 an activity pattern, or memory, as a particular configuration of the system $\vec{\xi} \equiv \{\xi_i, \ldots, \xi_N\}$, with $\xi_i \in \{-1, 1\}$ $\forall i$. In order to store P memories in the network, i.e. $\left\{\vec{\xi^\nu}\right\}_{\nu=1\ldots P}$, the connection weights must be defined using for instance a **hebbian learning rule**:

$$w_{ij} = \frac{1}{N}\sum_{\nu=1}^{P} \xi_i^\nu \xi_j^\nu \qquad \theta_i = -\sum_{\nu=1}^{P} \xi_i^\nu u^\nu, \tag{3.6}$$

where $\vec{u} = \left\{u^1, \ldots, u^P\right\}$ is a P components constant vector, representing the contributions to the threshold potential of the different patterns. This particular choice allows for the appearance of the associative memory property [18]. In fact, via this rule, the activity patterns are thus stored in the synaptic weights w_{ij}, that are reinforced by a positive quantity $\delta = \xi_i^\nu \xi_j^\nu > 0$ when a certain pattern ν contemplates both neurons i and j in the same state, and are weakened when

the same are in different states, with $\delta = \xi_i^\nu \xi_j^\nu < 0$. Moreover, the hebbian rule establishes symmetric weights, i.e. $w_{ij} = w_{ji} \forall i, j$, that is a necessary condition in order to define the Hamiltonian of the system. Due to this symmetry, each stored memory yields the appearance of two attractor in the dynamics of the system, one associated with the corresponding activity pattern $\vec{\xi^\mu}$, and the other with the *antipattern* $-\vec{\xi^\mu} = \{-\xi_1^\mu, \ldots, -\xi_N^\mu\}$. Due to this association between stored activity patterns and dynamical attractors, Hopfield-like models are commonly denoted as Attractor Neural Networks (ANN). At this point one can ask: *in what sense can we say that an ANN exhibits the property of associative memory?*

Let's consider a case with weak noise, i.e. low T, and few stored patterns, or small memory load $\alpha = P/N$. In addition we define the overlap function of network configurations $\vec{S}$ with pattern μ as

$$m^\mu(\vec{S}) \equiv \frac{1}{N} \sum_{i=1}^{N} \xi_i^\mu s_i$$

If the initial condition of the network $\vec{S'}$ close to the pattern configuration $\vec{\xi^\nu}$, $m^\mu(\vec{S}) \gg 0$, the network will evolve toward such a memory, being the state $\vec{\xi^\nu}$ the attractor for network dynamics. In other words, when one starts with a configuration similar to a particular activity pattern μ (e.g. giving to the network a partial or distorted pattern as initial input), the system will rapidly move to the basin of attraction of such stored pattern, recovering the previously learned information. The dynamics of model has been implemented essentially with two different neurons updating protocols: parallel updating, also called *Little dynamics*, and randomly sequential updating, i.e. *Glauber dynamics*. In both cases the network converges to one of the pointwise memory attractors, at least at $T = 0$.

The Hopfield model can be analytically solved within the statistical mechanics theory for spin-glasses using a mean-field *replica trick* [122–124]. This mean-field treatment allows to characterize for instance the phases of the system, the stability of such phases, or the maximum storage capacity α_{max}, i.e. the maximum number of patterns that can be recovered efficiently at a certain temperature. In this approach the steady states are obtained by solving the following fixed-point

set of equations:

$$
\begin{aligned}
m^\nu &= \left\langle \left\langle \xi^\nu \tanh\left[\beta(r\alpha)^{1/2}z + \hat{m}\cdot\hat{\xi}\right]\right\rangle_\xi \right\rangle_z \\
q &= \left\langle \left\langle \tanh^2\left[\beta(r\alpha)^{1/2}z + \hat{m}\cdot\hat{\xi}\right]\right\rangle_\xi \right\rangle_z \\
r &= q\left[1 - \beta(1-q)\right]^{-2},
\end{aligned}
$$

where $\langle\ldots\rangle_\xi$ indicates the average over the quenched disorder, i.e. over the distribution of the discrete values of the ξ^ν's, and $\langle\ldots\rangle_z$ indicates the average over a normal variable z. The vectors $\hat{m} \equiv \{m^1, \cdots, m^s\}$ and $\hat{\xi} \equiv \{\xi^1, \cdots, \xi^s\}$ have s components each, corresponding to the *condensed patterns*, i.e. the patterns with a macrscopic non zero overlap in the thermodynamic limit $N \to +\infty$. The former equations depend on three macroscopic observables, or order parameters:

$$
\begin{aligned}
\hat{m} &\equiv \frac{1}{N}\left\langle \sum_i \hat{\xi}_i \overline{s_i} \right\rangle_\xi \\
r &\equiv \frac{1}{\alpha}\left\langle \sum_{m^\mu \notin \hat{m}} \overline{(m^\mu)^2} \right\rangle_\xi \\
q &\equiv \frac{1}{N}\left\langle \sum_i \overline{s_i}^2 \right\rangle_\xi,
\end{aligned}
$$

where $\overline{(\ldots)}$ denotes the mean over the ensemble, i.e. over the Boltzmann distribution $P(\vec{S})$[2]. The order parameter r sums up the rest of *non condensed patterns*, while q is a measure of the persistence of the system in a particular state. The limit cases are $q = 0$, when all the neurons fluctuates randomly in time, and $q = 1$, where each neuron stays in only one state during the whole dynamic.

A global picture of the network phases in the diagram $(T, \alpha = P/N)$ is reported in figure 3.7, where one can observe:

- The "Memory Recover", or Ferromagnetic, phase (MR), corresponding to the region below T_C line, where the stable solutions of equations 3.7 have $\hat{m}, r, q \neq 0$. These solutions, that in this phase are the absolute minima of the free energy, are essentially the so called Mattis states, or memory configurations, where $\hat{m}$ has just one non-zero component m^ν, that is only, the overlap with a given pattern $\vec{\xi}^\nu$ is non zero. In this phase then the network exhibits associative memory.

---

[2]If the system is ergodic, as is the replica symmetric solution, this average is equivalent to the temporal average.
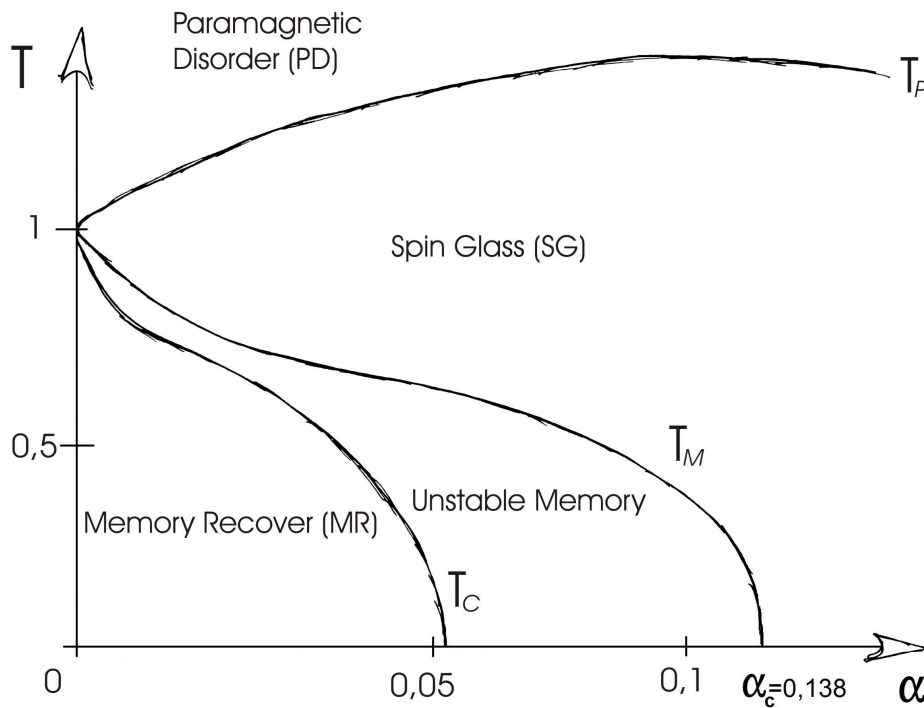
FIGURE 3.7: Phase diagram of the Hopfield model as a function of temperature T and memory load $\alpha = P/N$. Above a critical load $\alpha_c = 0.138$, the network cannot recover any stored pattern, and assumes only the Spin Glass phase or the Paramagnetic Disordered phase (for high T).

- "Spin Glass" phase (SG), corresponding to the region between T_M and $T_P = 1 + \sqrt{\alpha}$ lines, where $\hat{m} = 0$ and $r, q \neq 0$. Here new absolute minima in the free energy landscape emerge, corresponding to "spurious" states, in which the network does not have a macroscopic overlap with any previously stored pattern. Thus, the system is not able to recover any memory. Note that even in the deterministic case, at $T = 0$, there is a critical load parameter $\alpha_c = 0.138$, upon that associative memory fails.

- "Unstable Memory" phase, corresponding to the region between T_C and T_M lines, where "spurious" Spin Glass states are still the absolute minima, but MR solutions appears as local minima, lowering their energy value until T_C line, that marks the first order transition between SG and MR.

- "Paramagnetic Disordered phase" (PD) phase, corresponding to the region over T_P. Here $\hat{m} = r = q = 0$, and the dynamic of the system is disordered and completely dominated by thermal noise.

Although the steady state of the general model defined above represents an equilibrium system in the sense of the statistical mechanics, some nonequilibrium versions of such model can be studied by using for instance effective hamiltonians or different mean field approaches. Some interesting situations, such as the presence of fast synaptic mechanisms (that mimics synaptic plasticity) which strongly alters the dynamics of the system, fall into this class of nonequilibrium frameworks. In this case, the phase diagram will change qualitatively, with the emergence of new no equilibrium dynamic phases, chaotic switching among memory patterns and criticality (see chapter 5 and [17, 125] for further details).

There are several qualitative differences between the IF coupled neurons model and the Hopfield model. In the IF neuron equation (3.1), there are some non linearities, consisting for example in the threshold firing process, and the interaction that firing has with potential dissipation due to the leakage term. Such on linearities allow for a disordered dynamic in a IF neurons network, even in the completely deterministic case, i.e. using a non stochastic external input [91]. Moreover, in the IF equation (3.1) it is possible to add different specific sources of noise, biologically well defined, as for example considering a probabilistic synaptic efficacy dynamics [94], or a stochastic fluctuating external current input [19, 94]. Neuron updating in an IF neurons network emerges in a natural way, and is not necessary to postulate any arbitrarily chosen scheme. This last property results to be particularly useful in the study of synchronize/asynchronous states [89]. On the other hand, in the Hopfield model neuron dynamics for $T \neq 0$ is intrinsically stochastic. In other words, noise, which is controlled by temperature parameter T, constitutes a general source of fluctuations, that accounts for all the fluctuations associated to the many different biochemical processes implied in spiking generation and synaptic transmission mechanisms. In addition, neuron updating protocol in Monte Carlo simulations, is not determined from the model and is not possible to associate it to any biological mechanism. In some cases different updating rules could produce extremely different dynamical behaviours, related both to equilibrium and non equilibrium stationary states, in particular when one considers non linear variation of Hopfield original model [17, 125]. Finally, while in Hopfield model neurons binary states are symmetric respect to the dynamics, allowing for the implicit appearance of antipatterns, in the more realistic IF networks, leakage term, resting value V_r and refractory period τ_{ref} produce in the single neuron dynamics an asymmetry between firing and not firing state.

Summing up, in this thesis we mainly focus the attention on the effect of chemical synapses on neural networks performance in a broad range of experimentally observed phenomenology (see chapter 4), consisting for example in chaotic, critical oscillations among two different subthreshold levels (section 4.4), switching between different memories (see section 3.4 and chapter 5), and in critical (or *quasi* critical) neuronal avalanches (section 4.3 and chapter 6). The idea is that non linear adaptive mechanisms involved in synaptic plasticity, coupled with the all-or-none action potential threshold processes, are the key ingredients in order to have stable *quasi* critical avalanches (see chapter 6), or in other cases persistent critical switching among different network attractors (see chapter 5). The difference between the generation of well time separated neuronal avalanches and persistent attractor switching depends on the role of external stochastic fluctuations/perturbations and on neurons updating.

Chapter 4

Evidence of criticality in neural systems

In this chapter we describe some experiments performed on neural systems at single cell, tissue and brain level, where some distributions of interest, describing the emergent properties of these systems, show power-law behaviour. Although there is still a strong debate on the possibility to rigorously relate the appearance of scale free distributions found here with criticality, nevertheless these systems are good examples of biosystems with *critical* (or *pseudocritical*) properties that allows for the optimization of their main functions.

4.1   Scale free brain functional network

The hypothesis of large scale correlations in neural systems was firstly tested by Eguíluz et al [4], which designed an experiment for the measure of anatomical spatial correlations in human brain activity by mean of Functional Magnetic Resonance Imaging (FMRI). FMRI is a type of specialized magnetic resonance imaging scan, that measures the Blood-Oxygen-Level Dependence (BOLD), related to neural activity in the brain. In fact, supposing that active neurons increase their oxygen intake and consumption, this technique exploits the different magnetic properties of oxygenated and deoxygenated hemoglobin, that is the oxygen carrier in the blood. A schematic representation of the experimental method is shown in figure 4.1.

In these experiments FMRI signals are recorded from subjects performing some
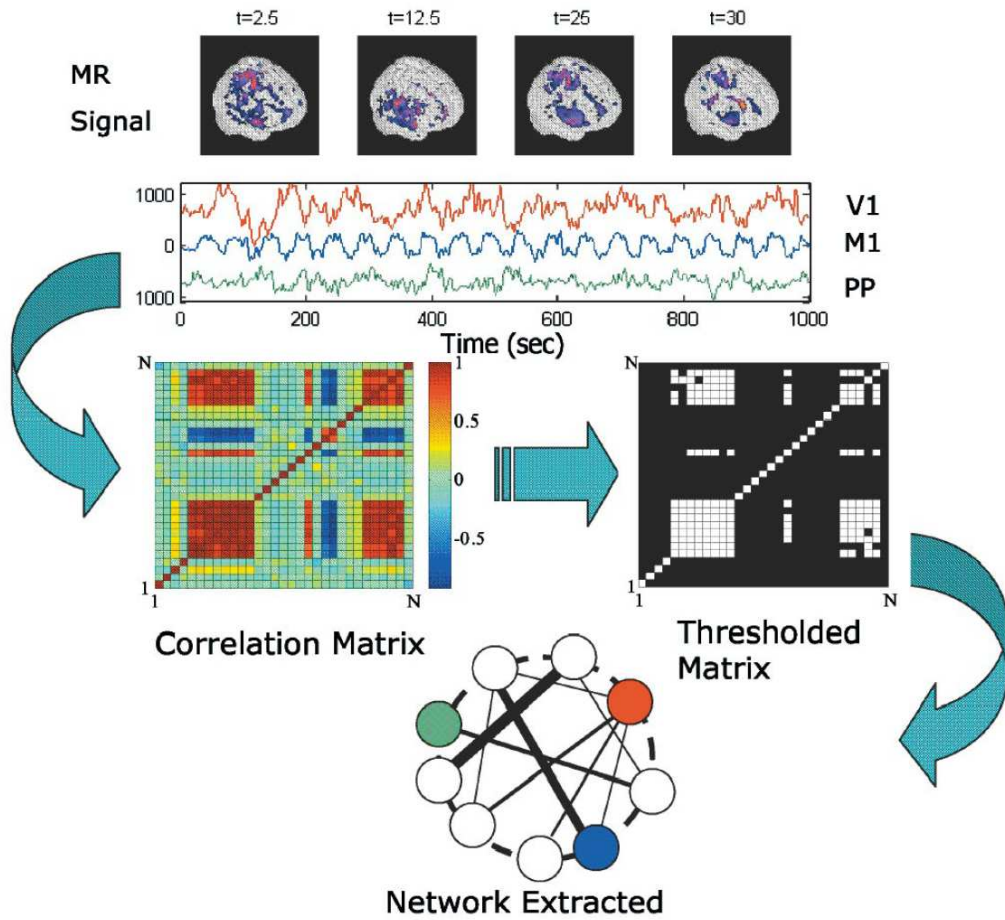
FIGURE 4.1: Methodology used to extract functional networks from FMRI brain signals. The correlation matrix among the different voxels (i.e the nodes of the functional network) is calculated using formula 4.1. Then, a functional network is defined by linking nodes with a correlation higher than a chosen threshold r_{th}. (Top) four images representing snapshots of activity and three traces which correspond to selected voxels from visual (V1), motor (M1) and posterio-parietal (PP) cortices (Reprinted from [4]).

kind of simple actions, like listening music or finger tapping. Brain activity $V(x, t)$ is measured in $36 \times 64 \times 64$ brain sites, the so called "voxels", of dimension $3 \times 3,475 \times 3,475 \ mm^3$. Then, a voxel-voxel functional correlation matrix $\bar{R}$ is constructed, where the matrix element corresponding to the voxel pair (x_1, x_2) is:

$$r(x_1, x_2) \equiv \frac{\langle V(x_1, t)V(x_2, t) \rangle - \langle V(x_1, t) \rangle \langle V(x_2, t) \rangle}{\sigma(V(x_1, t))\sigma(V(x_2, t))}. \tag{4.1}$$

Here $\langle \cdot \rangle$ represents a temporal average and $\sigma^2(V(x)) \equiv \langle V(x, t)^2 \rangle - \langle V(x, t) \rangle^2$. Finally, one obtains a kind of *functional topology* of the voxel elements by considering that two voxels i and j are connected if $r(x_i, x_j) > r_{th}$, being r_{th} a threshold valued properly chosen. Functional topology not necessarily reflects the real connection
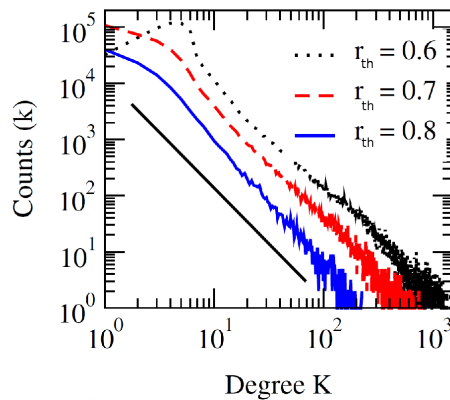
FIGURE 4.2: Log-log plot of the degree distribution $P(k)$ for the functional topology obtained for different values of the threshold r_{th} in the correlation matrix. Each curve has been averaged from 22 networks extracted from 7 individuals. The straight line illustrates a decay of k^{-2}, compatible with all the curves (reprinted from [4]).

structure of the brain, nevertheless it stress out the spatial correlations that the brain develops among its various subcomponent activities in order to accomplish the different tasks performed in the experiments.

Such topology results to have a scale free distribution $P(k) \propto k^{-\gamma}$, with exponent $\gamma \simeq -2$, very robust under parameter, subject and task variations, as it is depicted in figure 4.2. In addition, clustering coefficient and average path length (defined in section 2.4) are significantly higher than those for a random network, which implies that the resulting functional topology is *small world*. This result is highly relevant because small world networks are known to show resistance to failure, facility for synchronization, and fast signal processing both in neural system models [126] and experiments [127].

As it is shown in the bottom panel of figure 4.3, there is a positive correlation between the degrees of adjacent nodes. Such positive degree-degree correlation, called *assortative mixing*, indicates a hierarchical structure among the node degrees which connect the nodes with similar degree. Such correlations have interesting properties on memory capacity and stability [22], as we demonstrate in chapter 7.

4.2   Is the resting brain state critical?

Magnetic resonance and Electroencephalogram (ECG) low frequency fluctuations were shown to be correlated across widely spatially separated but functionally related brain regions in subjects at rest [128]. Brain resting state can be defined
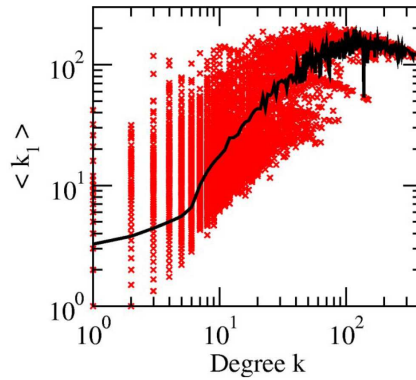
FIGURE 4.3: Log-log plot of a neighboring node degree versus degree which illustrates the assortative feature. Symbols represents individual data and continuous lines depict the average values for nodes with the same degree. Subjects were the same used for the data in figure 4.2 with $r_{th} = 0.6$ (reprinted from [4]).

as the state in which there is no explicit brain input or output and the overall brain activity fluctuates around a baseline value. In different experiments these fluctuations, corresponding to the neuronal baseline or idle activity of the brain, exhibit long range correlations with the power spectrum of frequencies f decaying as $1/f^{\beta}$ [129, 130]. On the other hand, observations on anatomical and functional connectivity [4, 23] depict some indications of dense local correlations with few long-range links, that is, scale free connectivity distribution with assortative features [1]. Coexistence of large positively correlated domains with equally large anticorrelated ones has been also observed [131].

Fraiman *et al* [5] analyzed different statistical functions of the brain functional topology, obtained from the BOLD correlation matrix (4.1) and compared them with the respective ones obtained in a simple 2D Ising model (see section 2.2). The result of this study shows that experimental distributions have an excellent overlap with the ones obtained from the model close the critical temperature. In figures 4.4-4.5 one can observe the effective degree distribution and the mean nearest-neighbor degree distribution measured in both model and experiments. In addition, this work shows that the correlations distribution is centered around zero, indicating a symmetry between distributions of correlated and anticorrelated regions (see [131] for details). It is remarkable how a very simple Ising model tuned at critical point in an elemental geometry, i.e. a square lattice, is able to replicate different long range properties actually measured in the brain, supporting and promoting the idea of a critical state as the brain default functional state. The idea

---

[1]Assortativity indicates the tendency for the nodes to be connected with nodes with similar degree, for details see section 2.4 and chapter 7
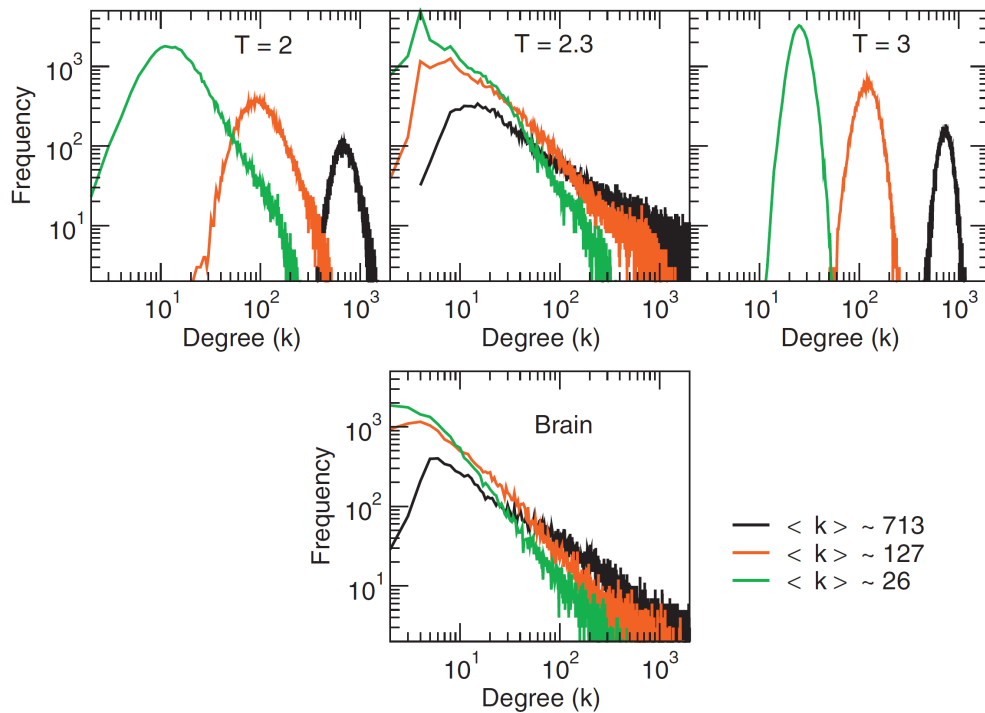
FIGURE 4.4: Log-log plot of degree distribution for positively correlated networks. Top three panels depict the degree distribution for the Ising networks at $T = 2$, $T = 2.3$, and $T = 3$ for three representative values of $\langle k \rangle = 26$, 127, and 713. Bottom panel: degree distribution for positively correlated brain network for the same three values of $\langle k \rangle$ (reprinted from [5]).

of criticality in the resting brain state is supported by our analysis of a variation of the Hopfield model, implemented with the introduction of a synaptic plasticity mechanism, as reported in chapter 5. In this model, at the point of transition between regular and chaotic behaviour, i.e. at the onset of criticality, the network wanders irregularly among memory attractors. In such state the network has the optimal sensitivity to sensory stimuli, and is able to recover a stored memory pattern even with a little stimulus [22, 132]. This last indicates the relevant role of criticality in the optimization of the brain response to a broad range of external stimuli, necessary for the evolution and the survival of superior animals [11].
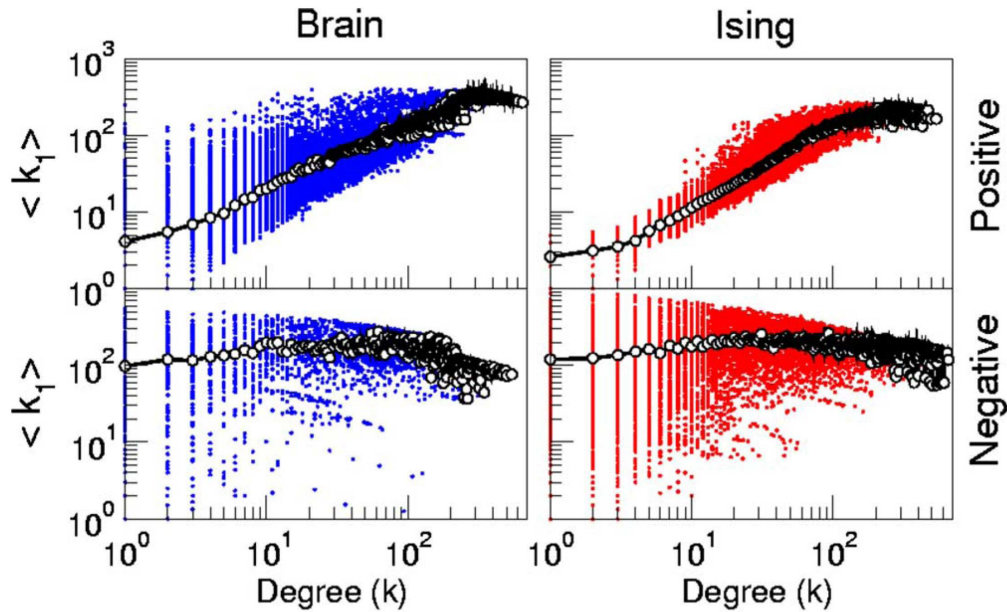
FIGURE 4.5: Log-log plot of the nearest-neighbor degree, $\langle k_1 \rangle$, as a function of own degree k for the two type of networks extracted from the brain (left) and from the Ising model at T_c (right) (reprinted from [5]).

4.3 Self Organized Criticality in Neural Avalanches (or at least *Quasi-SOC*)

Recent experiments on neural tissues have claimed not only a critical behaviour in neural systems, but a proper SOC characterization (for details about Self Organized Criticality, see section 2.3). Under a theoretical point of view one can investigate the emergence of SOC in neural systems by studying in deep neuron and synapse dynamics. As commented in section 3.2, one of the simplest realistic description for neuron AP generation is the so called integration and fire mechanism. In this model a neuron, which receives all the information in terms of presynaptic inputs, modules its membrane graded potential until a certain threshold is overcome; then the neuron "fires" its output in the form of an action potential. After that, it resets the membrane potential to some resting state. A single neuron firing event can eventually trigger additional firings in its postsynaptic neurons connected through synapses, and therefore the spiking activity propagates to other different parts of the system in the form of an *avalanche*, as depicted in figure 4.6. In experiments, this kind of activity can be measured by the local-field potential (LFP), that takes into account the electrical current flowing from all the synapses within a volume of tissue, and thus represents the level of neurons synchronous

time (4 ms frames) ⟶
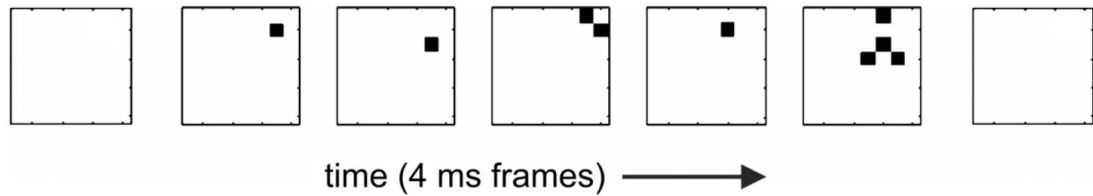
FIGURE 4.6: Example of a typical avalanche of neural activity. Each black dot correspond to an electrode in firing state, i.e. measuring a LFP larger than a determined threshold. In this avalanche the spatial size is 9 and the temporal duration, or the number of time frames, is 5. Please note how this kind of activity reminds to avalanches measured in BTW sand pile model, described in section 2.3 (reprinted from [6]).

activity of the zone under study. The first experimental studies that have defined and measured neural avalanches have been reported by Beggs *et al* [6, 8], both on *in vivo* (slices of rat cortex placed in a cold, oxygenated solution of the cerebrospinal fluid) and *in vitro* (organotypic cultures bathed into a culture medium) samples of somatosensory cortex. They collected LFPs signals by means of square 8x8 electrode arrays (60 electrodes separated by a distance of $200\mu m$), as depicted in figure 4.7. In general, the electrode size used to measure LFP on neural tissues is able only to catch the mean behaviour of a large group of neurons, that is, each electrode records the activity of a group of neurons placed around its location; thus from these experiments it is possible to extract useful information on the mesoscopic dynamic of the system [2]. In later works the same kind of experiments have been performed on 512 electrodes arrays [133], extending in space and time the observation of avalanches, and confirming with more confidence the main results.

In all these experiments, activity is not induced by external stimuli, but is spontaneously generated by fluctuations in the density of ions in the medium in which the samples are immersed. At a rough large time scale, the spatiotemporal activation patterns, as the ones depicted in the second panel of figure 4.7, show all neurons firing in a synchronized way. However, if the temporal resolution is increased, more complex patterns arise (see lower panel of the right part of figure 4.7). Such patterns suggest a consecutive, more than synchronized, activation of neurons, similar to a *chain reaction*. The set of activation events occurring between two periods of silence is defined as a **neuronal avalanche**. Numerical

---

[2]Nevertheless, in this section, as well as in chapter 6 we will use the term "neuron" to indicate one "electrode" of the array

simulations of a network of integrate and fire neurons (see section 3.2) [125] exhibits characteristics similar to those observed in a typical SOC system [56, 93], that is

- **An accumulation period** for the single neuron, during which it collects the incoming information in the form of depolarization of membrane potential. Throughout this period, the site remains inactive.

- **The existence of a threshold for the accumulated potential**. Once it is exceeded, the site turns into an active unit.

- **A separation of time scales**. The time between the spontaneous activation of a site, i.e. the triggering of avalanches, is of the order of seconds, while the burst-propagation of activity lasts only a few milliseconds.

This mechanism, which better represents the behaviour of neurons of an in vitro sample connected by chemical synapses, resembles the dynamic of a SOC sandpile, described in section 2.3.
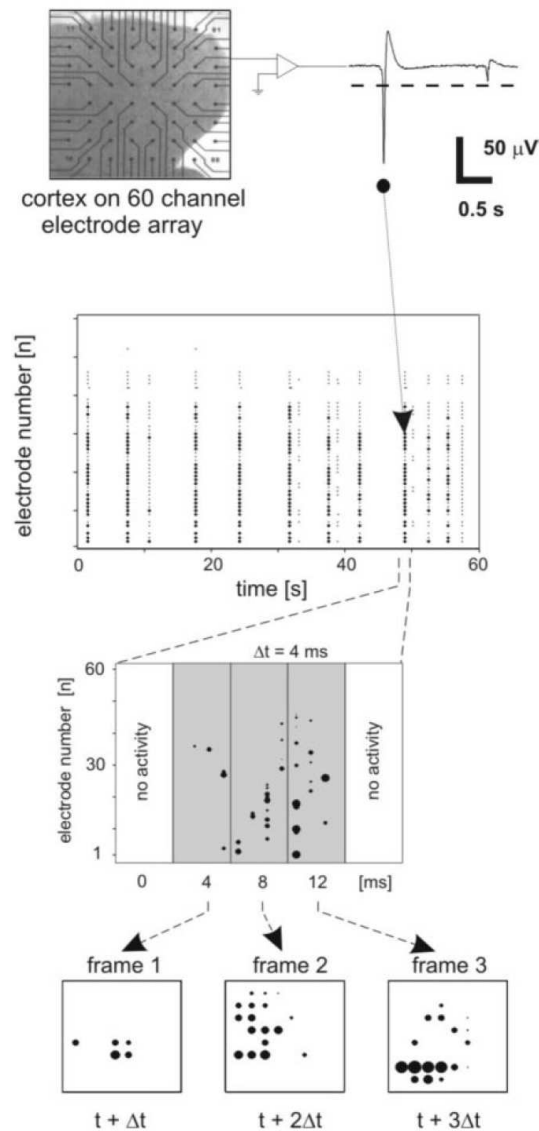
FIGURE 4.7: Experimental setting of the experiments of Beggs and Plenz [6], measuring neural avalanches on *in vitro* and *in vivo* samples. Top panel: Local Field Potential (LFP) signals (right) recorded in a 8x8 electrode array (left). Electrode is considered in firing state when its LFP reaches a chosen threshold. Middle panels: at a large temporal scale of observation, in the order of seconds, the whole activity is characterized by synchronous firing, followed by large intervals of silence. In a finer temporal scale, in the order of milliseconds, each synchronous collective firing results to be an avalanche of successive firings. Bottom panel: avalanches have different temporal duration (i.e. number of time frames) and spatial sizes (the number of neurons firing in an avalanche)(reprinted from [6]).

The relevant observables associated with neuronal avalanches are their size s, i.e., the number of firing electrodes or equivalently the total amount of millivolts μV registered during an avalanche, and their lifetime, measured in number t of time bins Δt used to discretize the record of activity. For both $P(s)$ and $P(t)$, a power law shape with mean field critical exponents, i.e. $\tau = 3/2$ and $\tau_t = 2$, have been reported [134] (see figure 4.8). The exponent associated with avalanche size distribution is very robust under different experimental settings, and its value corresponds to the one obtained in the mean field description of SOC models [20].

This result is not surprising, because it have been found in such networks connections between neurons separated a long distance, both functional and anatomical [127, 135]. Such connections blur the differences between local and global structures (as in small-world networks), and confers the system the mean-field feature [76]. The reported probability distributions have a cutoff which depends on the total number of electrodes and on the inter-electrode distance; the larger is the system, the higher is the value of the cutoff. Taking into account that a mean-field avalanche in a sandpile can be translated into a branching process [20], a study of the branching ratio, defined here as the fraction of active electrodes in a time bin per each active electrode of the previous time bin, has been performed [136]. This ratio was found to be $c = 1.04(19)$, very close to the value $c_{cbp} = 1$ obtained for a critical branching process. Finally in order to understand the stability of the network activity and of the power law avalanche size distribution, network excitability has been increased, with the use of a picrotoxin, a blocker of inhibitory synapses receptors. In this case, the power law behavior was destroyed and the distribution of event sizes changed to a bimodal distribution, where network activity was dominated either by very small or very large events, typical of epileptic behaviour. The peak corresponding to small events still decays with a power law but with a slope considerably lower than $3/2$ [6]. Summing up, in the experiments performed by Beggs *et al.*, neuronal avalanches were characterized by means of three different findings:

- The propagation of synchronized LFP activity is described by a power law.

- The slope of this power law, as well as the branching parameter, indicates that the mechanism underlying these avalanches is a critical branching process.
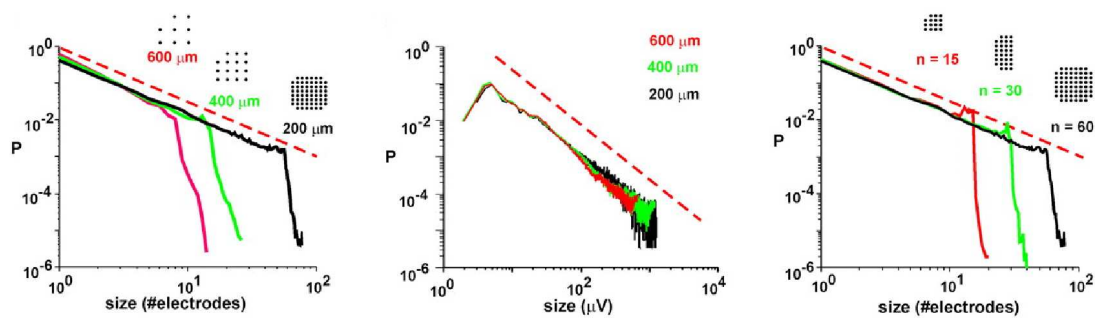
FIGURE 4.8: Characteristic probability distributions of avalanche in the experiments reported in [6]. Exponents for neuronal avalanche sizes is $-3/2$. Left: The slope value is independent on the array size and the interelectrode distance (IED). Icons indicate resampled arrays at $IED = 200, 400,$ and $600\mu m$. Middle: Resampled power laws for summed LFP values (same arrays as in Left). Right: The cutoff point of the power law is determined by the number of electrodes in the array ($n = 15, 30, 60$; $IED = 200m$). Broken line in red indicates slope of $-3/2$.

- Pharmacological experiments suggest that a critical branching process optimizes information transmission while preserving stability in cortical networks.

As a consequence, one can conclude that the self sustained, power law distributed, activity places the examined neural tissues at the edge of stability, which implies an efficient transmission of information and, at the same time, guarantees some stability under pathological conditions, as for instance during epileptic seizures.

In order to study in details the emergence of power law distributed avalanches and the robustness such activity, in the chapter 6 we implement a biologically motivated neural network of IF neurons with a Tsodyks dynamic for synaptic plasticity [125]. Our study shows that critical avalanches result to be robust under a broad variation of internal and external environmental conditions (i.e. in an extended zone of relevant parameters space). Thus neural critical avalanche phenomenology has to be considered not as produced by SOC, but rather by a more stable, dissipative self-organized quasi criticality (SOqC) dynamics (see chapter 6 for further details and conclusions).

4.4 Up/Down cortical transitions and criticality

Experiments of LFP and multiarray electrode recordings in different neural media show two preferred neuron membrane potentials, both subthreshold for the generation of an action potential. These two levels, depending from the kind of neural system observed, could be stable, i.e., once placed the neuron potential in either state it will remain there with no additional stimulation, or metastable, which can be induced by brief depolarizations and last for some period of time before the membrane potential spontaneously returns to its resting state. In some cases the neuron membrane potential presents bistability, and could switch between the two levels with a self consistent dynamic mechanism. Such kind of subthreshold states are called **Up** and **Down** states. Figure 4.9 shows a typical example of up down switching for two different single neuron records. Usually, membrane potential fluctuations around the Up state are of higher amplitude, whereas the Down state is relatively free of noise. Up/Down transitions can be observed both in single neuron dynamic and in collective bunch of neurons, oscillating in a synchronized or coordinated way [137, 138]. There are two main hypotesis on the regulating mechanism for up down transitions: the first considers that neurons may exhibit two state behaviour because of their intrinsic excitability, while the second states that there is a network mechanism involved, which essentially is based on a dynamic balance of excitatory and inhibitory currents [139, 140].

Following the second hypotesis, in cells possessing no intrinsic bistability, bistable networks may produce Up/Down transitions. Several models of cortical circuits have made an attempt to describe this network behaviour considering a population of excitatory neurons and a population of inhibitory neurons mutually connected. It has been reported that the stable level of activity in both the Up and Down states is determined by a balance between the mutual excitation among excitatory neurons and the feedback inhibition generated by the inhibitory population [141]. Creation of a stable Up state at moderate membrane potentials is achieved by balancing excitation with inhibition from interneurons. This mechanism can readily be altered to generate rhythmic transitions between excited and quiet states of the network. To achieve this, the Up and Down states must both be made to be transiently stable. However, recent biophysically realistic network models employ synaptic depression to destabilize it with time and generate Up/Down transitions [99, 142]. Periodic re-entry into the Up state is achieved by postulating a stochastic mechanism that randomly triggers a transition to the excited network state
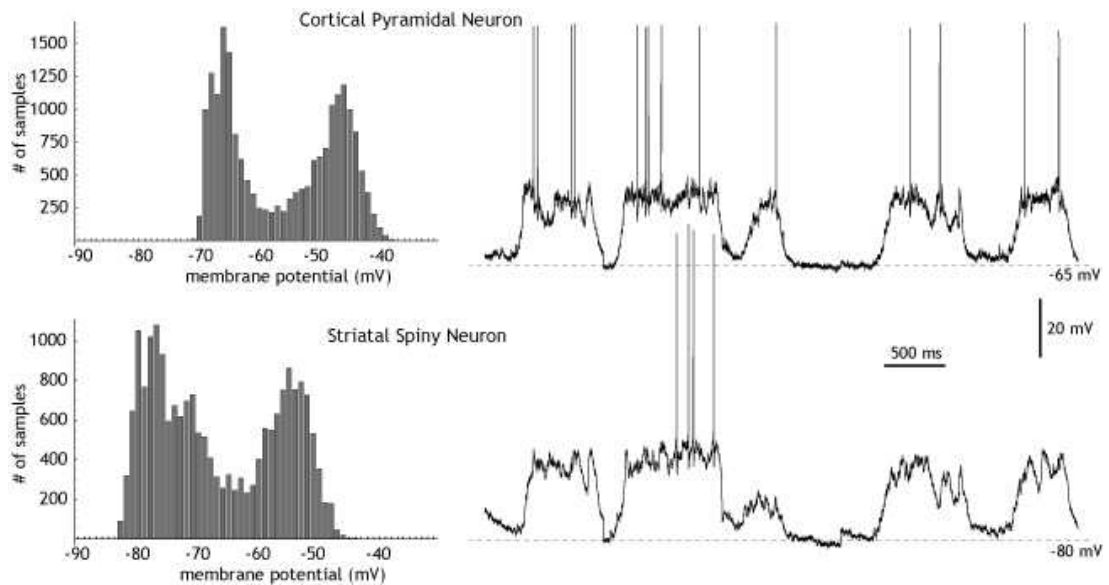
FIGURE 4.9: (Right) Neuron membrane potential recordings shows typical examples of Up/Down transitions on a striatal spiny neuron, and for a cortical pyramidal cell in layer V, recorded simultaneously. The histograms to the left show the amount of time the cell spends at each value of membrane potential. Both cells toggle between two preferred membrane potentials, one very hyperpolarized, the Down state, and one more depolarized, the Up state. In both cells, the Up state is only a few millivolts from the action potential threshold (reprinted from Scholarpedia *http://www.scholarpedia.org/article/Up and down states*).

from time to time.

An intriguing connection between Up/Down oscillation and criticality has been argued by Fujisawa *et al.* [7], which studied the statistical properties of some intracellular recordings from hippocampal CA3 pyramidal cells *ex vivo*. In this work, they measure the Significant Depolarizing Shift (SDS) in neuron membrane potential, i.e. the time in which the neuron is in the UP state, and characterize with SDS duration and spike rate five neuronal internal states, ranging from a silent Down state (I) to a permanently bursting Up state (V). Multiple recordings from adjacent neurons revealed that the neuron internal states were coherent, indicating that the internal state of any given cell in a local network could represent the whole network state. Repeated stimulation of single neurons leads over time to transitions to different internal states in both the stimulated neuron and neighboring neurons. In particular, most of the transitions occurs between state IV, characterized for Up/Down oscillations, and state V. Thus, single cell activation is sufficient to shift the state of the entire local network, indicating some evidences of extreme susceptibility in response to an external stimulus. In state IV, both SDS and Inter Spike Interval (ISI) distributions show power law behaviour, as
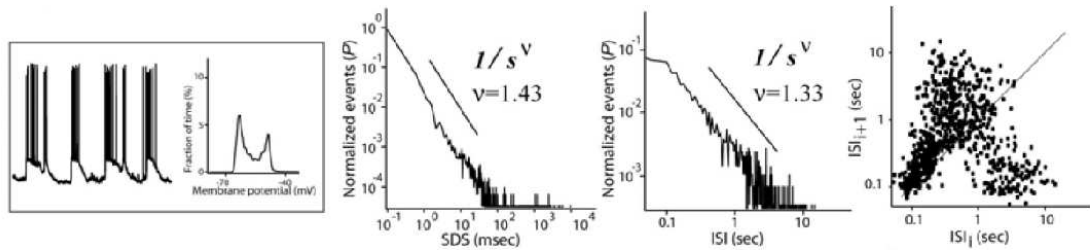
FIGURE 4.10: Characterization of the internal state IV in the Fujisawa *et al.* experiments [7]. Left panel show representative Up Down oscillation waveforms and their membrane potential histograms. The middle-left panel indicates the frequency of the SDS duration. State IV shows a scale free $1/s^\nu$ structure with $\nu = 1.43$. The middle right histogram indicate the frequency of inter-spike intervals (ISIs), also scale free distributed with $\nu = 1.33$. The right panel indicates first-return maps of ISIs, in which ISIs are plotted against the next ISIs. State IV shows a typical bell-shaped distribution, indicative of deterministic chaos (reprinted from [7]).

it is depicted in figure 4.10. Moreover, the ISI return map has a typical bell-shaped structure, indicative of deterministic chaos, which suggests the existence of a non-linear chaotic process that controls spike generation sequences [143]. In conclusion, these results give us different hints for a critical behaviour of Up/Down oscillations. Remarkably scale free behaviour seems to emerge from a collective dynamic, more than from the individual neuron fluctuations. In fact, SDS durations observed in individual neurons usually has a multi-peaked distribution, with peak frequencies varying from cell to cell, suggesting that the dynamics of membrane fluctuations is multistable and diverse at the single cell level. Since the responsiveness to external stimuli depends on internal states, the balanced input conductance is the mechanism that regulates network performance during information processing. For this reason Fujisawa *et al.* proposed a simple model in which the input conductance generated by network activity is plastic, thereby achieving self-sustained multistability of the internal states. In their system, neurons are modelled with a Hodgkin-Huxley equation for membrane potential, with an input conductance dependent on the global network activity, which is moving in a bistable potential. This model has shown Up/Down transitions with statistical properties similar to the ones observed in their experiments. We have studied a similar critical switching among different network activity patterns in chapter 5 for an ANN model exploring a different hypothesis, namely, we have considered the possibility that the strength of individual synapses could be modulated stochastically with a probability that depends on the actual level of activity in the network, i.e. a mechanism that resemble activity-dependent synaptic plasticity

[125]. Similarly to the experiments performed in [7] we have also observed power law distributions for the time of permanence in a certain activity pattern and studied the biophysical conditions for the emergence of such behaviour.

Chapter 5

Nonequilibrium Phases and Criticality in an Attractor Neural Network model

In this chapter we present and study a model of excitable media constituted by an attractor neural network (ANN) with occasionally quiet nodes (i.e. considering partial system updating) and with connection weights that vary with activity on a short time scale. The network global activity shows spontaneous (i.e., even in the absence of stimuli) unstable dynamics, nonequilibrium phases- including one in which the global activity wanders irregularly among attractors - and $1/f$ *noise* as the system falls into the most irregular behavior. The combined effect of dynamic connection weights and partial node updating on resilience results in an efficient search in the model attractors space that can explain the origin of similar behavior observed in some experiments on neural systems. By extensive computer simulation we also address a previously conjectured relation between observed power law distributions and the possible occurrence of a "critical state" during functionality of (e.g.) cortical networks, and describe the precise nature of such critical noise in the model.

5.1   Introduction

As we have already introduced in chapter 3, a neural network is said to have *attractors* when it can autonomously change its state, characterized by the pattern

of activity, in order to converge in time towards one particular region of phase space (e.g., a single fix point, a trajectory or a chaotic "strage attractor"). Thus once the system reaches its attractor, it remains there permanently, and is resilent to perturbations. Following psychological observations [18] and the formal works of Amit [144] and Hopfield [110], this concept has been popular two decades ago as a mathematical tool to explore the fundamentals of brain tasks attributed to cooperation between many neurons. According to the, say, *standard model* [122–124], patterns of information, corresponding to sets of the nodes activity, are stored in a way that affects the intensities of the edges, representing the synapses, which follows an heterogeneous weights distribution. The global activity may then converge towards one of the given patterns when starting with a degraded version of it. That is, the system exhibits resilience which causes *associative memory*, a property of some brain regions, that are able to store mental representations of the objects of perception (for example visual images), by mean of patterns of neural activity, and subsequently recover them under partial stimulation. Such mechanism is common to humans (one can think for example to the process of recognizing a childhood friend we have not seen for dozens of years) and extensively demonstrated in experiments on primates [113–115] (see section 3.4), results to be difficult to be efficiently emulated with computers.

However neural networks, and more in general the systems of interest in nature do much more than just choosing one out of a set of patterns and staying in its neighborhood, see for example the phenomenologies described in [46, 145, 146]. For example, signals from the heart and cortical neural activities have been successfully interpreted using non-linear dynamics theory [147], and the Hopfield standard model has been generalized along biologically motivated lines that endow it with even more interesting behavior [148, 149]. In particular, it was shown that one may capture some of the observed shaky mechanisms and instabilities by taking into account two features that seem to characterize generically excitable media [150], namely, assuming both rapid activity-dependent fluctuations of the edge weights and the existence of nodes that are reluctant to a change of state during a time interval after the last change. It is remarkable that incorporating these simple mechanisms into the standard model has allowed one to recreate [151] the transient dynamics of activity as observed in experiments concerning the locust odor representation [146]. Instead of just associative memory, one may readily identify in this experiment, as in most of the available observations e.g., the ones mentioned in the previous paragraph a kind of continuous and irregular wandering

among attractors, say, *roaming dynamics*.

In this chapter, we describe in detail model phenomenology bearing relevance to situations with spontaneously unstable dynamics associated to excitability. By extensive computer simulations, we show both first and second order phase transitions, characterize the nature of different *nonequilibrium phases* [55] that occur as one modifies the system parameters, study the details of the network activity dynamics, and determine the conditions in which long-range correlations and non-Gaussian noise emerge. This results in a systematic study that adds up to recent efforts trying to understand the origin of the observed relation between certain statistical criticality and dynamically critical functionality in neuroscience [4, 9, 21, 152, 153]. Our study here complements analytical study of the simplest limits of the same model in [151] and related exploratory numerical studies therein.

5.2   Definition of model

We first consider the standard Hopfield Attractor Neural Network (ANN) model, as described in section 3.4.1, in which the consequences of the activity changes of each node (neuron) above some defined threshold may be sketched by means of a binary variable: $s_i = \pm 1$, $i = 1, \ldots, N$. This is known to suffice in practice to investigate the main effects of cooperation in different network contexts [58, 69, 154]. The topology structure considered is one of the most simplest, i.e. the fully connected one, where every neuron is connected with all the rests in the system. Each node receives a signal, called local field, $h_i(\vec{S}) = \sum_{j \neq i} w_{ij} s_j$, where $\vec{S} = \{s_i\}$ stands for the global activity and w_{ij} is the weight of the connection between nodes i and j, i.e. the synapse strength. In the problems of interest, one may typically single out P patterns of activity, namely, $\{\xi_i^\mu = \pm 1\}$ with $\mu = 1, \ldots P$, that have some special relevance. The weights then follow accordingly to the Hebbs superposition rule $w_{ij} = \frac{1}{N} \sum_{\mu=1}^{P} \xi_i^\mu \xi_j^\mu$. This is one of the simplest conditions that transforms the special P patterns into attractors of dynamics [18, 123]. In our study we implement on the Hopfield ANN model the following two novel elements for the dynamics, that attempt to model with simply rules important aspects of neurons and synapses mechanisms:

Partial Neuron Updating
Classic ANN models have been extensively analyzed and studied both in the case of

parallel updating (or Little dynamics), where at each Monte Carlo Step (MCS) the whole N neurons system is updated, and sequential updating (or Glauber dynamics), where each MCS only one randomly chosen neuron is updated. However the former updating rules, in addition to fully connected structure and instantaneous velocity of synapses, are not supported by any realistic assumption on network dynamics. Actually neurons do not update their state in an ordered sequence or group. As a matter of fact there are many internal effects influencing neuron updating, like connection structure and impulse velocity along the axon, refractory times, variability in neuron thresholds, stochastic fluctuations in membrane currents and potential or in neurotransmitters dynamics, as well as collective properties, like extended connection structure, impulse velocity along the axon and its branching structure. We can mention for example, regarding asynchronous neurons updating, the experiments on neural systems in which groups of the so called silent neurons, i.e. some neurons that keep inactive during a specific network task, are detected [155].

Thus we generalize the idea of neuron updating in our model, defining the the transition rate for the master equation (3.5) as:

$$\mathbf{T}\left(\vec{S} \to \vec{S'}\right) = \sum_{\mathbf{x}} p_n(\mathbf{x}) \prod_{\{i|x_i=1\}} \mathcal{T}_n\left(s_i \to s'_i\right) \prod_{\{i|x_i=0\}} \delta_{s_i,s'_i}. \qquad (5.1)$$

Here, $\mathbf{x}$ is an operational set of binary indexes fixed to 1 at n sites chosen at each time according to distribution $p_n(\mathbf{x})$, and to zero at the other $N - n$ sites. The choice (5.1) simply states that one (only) updates simultaneously the selected n nodes. The corresponding elementary rate is

$$\mathcal{T}_n\left(s_i \to s'_i\right) = \varphi\left(s_i \to s'_i\right)\left[1 + \left(\delta_{s'_i,-s_i} - 1\right)\delta_{n,1}\right], \qquad (5.2)$$

where we consider the choice:

$$\varphi(s_i \to s'_i) = \frac{1}{2}\left\{1 + \tanh[-s_i\beta h_i(\vec{S})]\right\}. \qquad (5.3)$$

In other words during the dynamics we update at each Monte Carlo step only a fraction $\rho = n/N$ of the neurons (with $1 < n < N$), randomly chosen. It has been demonstrated that the an Hopfield network at $T = 0$ reaches always a fixed point with any kind of block updating [156]. However our *partial updating*, even at very low T, produces a different non equilibrium behaviour when some fast fluctuations in local fields, depending on the network activity, are introduced [151], as we will

see next.

Time-dependent connection weights

As we argued in chapter 3, synaptic mechanism, that encodes the transmission of information from presynaptic to postsynaptic neuron, is very elaborate, and the biochemical processes involved in it generally are not stationary, thus transmission capability or connection strength are variable in time [96, 98, 103, 104]. We focus our attention on short term synaptic plasticity mechanism, described in section 3.1, where synaptic strength changes in response to the number of vesicles and thus of neurotransmitters ready to be released by the advent of an action potential out in the synaptic cleft, and thus is modulated by spiking frequency. Continuous firing activity produces a negative effect on synapse strength, namely synaptic depression, when spiking frequency overcomes the recovery time for vesicles, but in some cases it generates also positive effect, i.e. the synaptic facilitation, because in consecutive action potentials, neurotransmitters release is enhanced by the rest of Ca^{2+} ions, produced by the previous spike event, and still remaining in the button. Short term neural plasticity at synaptic level (synaptic depression and facilitation) plays a central role in memory storage, retrieving, transmission of information and computation [97].

One possible choice to study the effect of such synaptic fluctuations is to assume the state of synapses at time $\bar{t}$ as

$$\overline{w}_{ij} = \epsilon_j w_{ij}. \tag{5.4}$$

where ϵ_j is a stochastic variable distributed according to a time-dependent conditional probability distribution given the network history $\vec{S}(\bar{t} - t)$ until time $\bar{t}$, that is $P_{\bar{t}}(\epsilon_j|\vec{S}(\bar{t} - t))$. In the limit of fast synaptic changes, when ϵ_j varies in a time scale infinitely smaller than the one governing $\vec{S}$ changes, it reaches some steady-state, namely $P_{st}(\epsilon_j|\vec{S}(\bar{t}))$ (see [102, 151] for the general formalism). Here, we consider the choice

$$P_{st}(\epsilon_j|\vec{S}) = \zeta_j(\vec{S})\delta(\epsilon_j - \Phi) + [1 - \zeta_j(\vec{S})]\delta(\epsilon_j - 1). \tag{5.5}$$

This assumes that with some probability $\zeta_j(\vec{S})$ (which depends on the actual network state) the synaptic intensities are multiplied by an amount Φ which induces a kind of fatigue or *depression* of the synaptic transmission for $-1 < \Phi < 1$, and an enhancement or *facilitation* for $\Phi > 1$. In standard attractor neural networks,

the memory states are stable fixed points for the dynamics in some regions of the phase diagram. The dependence of the probability of depression or facilitation on the current neuron state tries to mimic activity-dependent synaptic depression and facilitation on real neural media.

We suppose that the average neuronal mean firing rate in that steady-state is proportional to the overlap of the network state with the retrieved pattern and, therefore, that the probability for a synapse to be depressed increases when the system approaches to one of the memory pattern. Roughly speaking, the more the network configuration get close to a memory pattern, the long is the time it remains in that configuration. This implies to consider $\zeta_j(\vec{S}) = \zeta[\vec{m}(\vec{S})]$. A suitable choice can be a normalized monotonic increasing function of the overlap vector $\vec{m}(\vec{S}) \equiv \{m^1(\vec{S}), \ldots, m^P(\vec{S})\}$ with $m^\nu(\vec{S}) = \frac{1}{N} \sum_{i=1}^{N} s_i \xi_i^\nu$, for instance,

$$\zeta[\vec{m}(\vec{S})] = \frac{1}{1 + P/N} \sum_{\mu=1}^{P} [m^\mu(\vec{S})]^2, \tag{5.6}$$

where we put the factor $\frac{1}{1+\frac{P}{N}}$ to have a correct $\zeta[\vec{m}]$ normalization. For random patterns and under a standard mean-field approach $s_j \approx \langle s_j \rangle$, which is valid for extended systems with long-range interactions, as in our case. Thus the effective synaptic weights are [102]:

$$\overline{w}_{ij} = [1 - (1 - \Phi)\zeta(\vec{m})]w_{ij}. \tag{5.7}$$

For simplicity, we shall be concerned only with mutually orthogonal patterns. This is achieved in practice setting every node in ξ_i^μ for all μ equal to $+1$ or -1 independently with the same probability, so that $\xi^\mu \cdot \xi^\nu \simeq 0$ for any $\mu \neq \nu$ in a large system [1]. Then, under some restrictions which strictly require also the limit $\rho \to 0$ (see [102] for technical details), the conditions so far stated may be taken into account by assuming *effective* weights:

$$\bar{w}_{ij} = \left\{ 1 - \frac{1 - \Phi}{2} \left[\zeta(\vec{m}) + \zeta(\vec{m}^i) \right] \right\} w_{ij}, \tag{5.8}$$

where the components of $\vec{m}^i$ are $m^\mu(\mathbf{s}) - 2s_i\xi_i^\mu N^{-1}$. We shall consider in the following this simplified version of our model which coincides with the general case for any $\rho > 0$ after averaging $\bar{w}_{ij} = \epsilon_j w_{ij}$ over the stationary noise distribution

---

[1] Assuming specific sets of P correlated patterns, which is of great practical interest, is beyond the scope of the study presented here that intentionally understates this model detail

$P_{\text{st}}(\epsilon_j|\vec{S})$. As a matter of fact, (5.8) may formally be viewed as any learning pre-scription, w_{ij}, which is affected by a multiplicative noise -with correlations built due to the dependence on $\vec{m}$. Recently, connections that are roughly of this type were recently shown to induce sort of criticality in neural population dynamics [157]. Simulations and theoretical analysis have shown different emergent behaviors depending on the relevant parameters Φ and ρ. For instance, with negative Φ and small ρ the system has the well know associative memory property and recovers a given pattern, while beyond a value ρ_{crit} emerges a chaotic behavior with irregular jumps between the stored patterns. Transitions between static and dynamic phases are obtained in some cases also when one tunes the depression parameter Φ with fixed ρ [17], including in the limit of $\rho = 1$ (parallel updating) [158]. In the next section we give a systematic definition and characterization of classic static and emergent phases and of some parametric phase diagrams, in which one can observe how the system can change among different regimes tuning the relevant dynamic parameters (Φ and ρ).

5.3 Phases and diagrams

A main observation concerns the nature of the phases exhibited as one varies the noise parameter, Φ, the fraction of active nodes, ρ, the temperature T, and the load parameter $\alpha = P/N$. It turns out convenient to monitor the time evolution of various order parameters [124], that we define essentially with some modifications to the original Hopfield order parameters, see equation (3.7). in particular, we define

$$M = \langle|\overline{m^*}|\rangle = \frac{1}{N}\left\langle\left|\overline{\sum_i \xi_i^* s_i}\right|\right\rangle, \tag{5.9}$$

where the asterisk is the value of μ that identifies the pattern having the largest squared overlap, $(m^*)^2$, and $\overline{(\cdots)}$ and $\langle\cdots\rangle$ stand, respectively, for averages over time and over independent realizations of the experiment (i.e., changing both the initial conditions and the set of the particular stored patterns). The set of the other overlaps, m^μ with $\mu \neq *$, may be characterized by:

$$R = \frac{1}{1+\alpha}\left\langle\overline{\sum_{\mu\neq*}(m^\mu)^2}\right\rangle, \tag{5.10}$$

where the sum is over all patterns excluding the one in equation (5.9). We also monitor the global activity by means of

$$Q = \frac{1}{N} \left\langle \sum_i \overline{s_i}^2 \right\rangle. \tag{5.11}$$

In the standard case $\Phi = 1$, for uncorrelated patterns, the system shows three phases [124, 159]:

(Ph$_1$) *Memory phase*, in which the system evolves towards one of the given patterns, often known as *pure* or *Mattis states*. The stationary state corresponds to maximum overlap with the particular pattern, so that M is large while R is small in the stationary state, namely, $R \sim \mathcal{O}\left[(P-1)/(N+P)\right]$. One also has that $Q \simeq 1$ near $T = 0$. (This case is illustrated by the two top graphs in figure 1.)

(Ph$_2$) *Mixture phase*, in which a large system converges to a mixture of pure states, so that it exhibits some order but not associative memory. Therefore, one may have several relatively large overlaps, which induces that $0 < M < 1$ with a lower bound - due to finite size - of order of $1/\sqrt{N}$, while $0 < R < (1+\alpha)^{-1}$ with a lower bound of order of $(P-1)/(N+P)$. Also, $Q \simeq 1$ near $T = 0$.

(Ph$_3$) *Disordered phase,* in which the system remains completely disordered as dominated by thermal noise. Then, all the overlaps oscillate around zero, so that $M \sim \mathcal{O}(1/\sqrt{N})$ and R is of order $(P-1)/(N+P)$, and $Q \simeq 0$ in the stationary state.

These cases correspond, respectively, to the familiar ferromagnetic, spin glass and paramagnetic phases that are well characterized in studies of equilibrium magnetic models.

The behavior of our system is more complex than suggested by this picture, however. A main novelty for $\Phi \neq 1$ is that, as illustrated in figure 5.1, the system exhibits different types of dynamic behavior that cannot be fitted to the above ones. That is, one observes that dynamics may eventually destabilize and irregular jumping - among attractors as well as from one pattern to its negative (*antipattern*) - occurs. The observed behavior suggests to define the following dynamic scenarios, say, *nonequilibrium phases* that do not occur in the standard model:
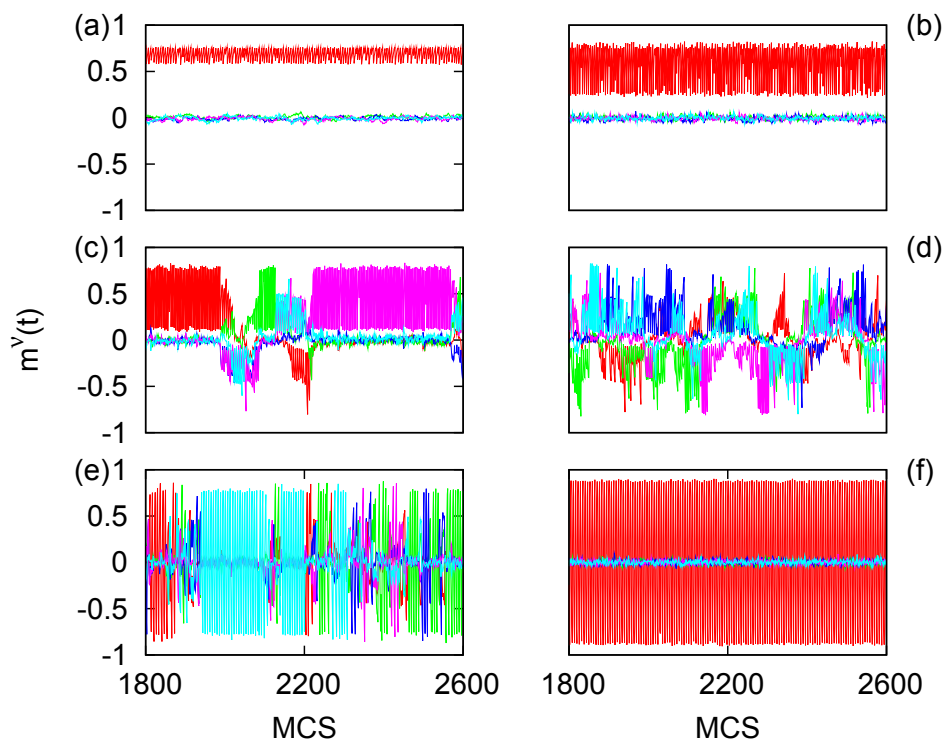
FIGURE 5.1: The overlap functions $m^\nu(t)$ showing typical different behaviors for $N = 1600$ nodes, $P = 5$ patterns, noise parameter $\Phi = -0.5$, temperature $T = 0.01$ and, from top to bottom: associative memory as in $\mathbf{Ph}_1$ at (a) $\rho = 0.10$ (left) and (b) $\rho = 0.30$ (right); irregular roaming among patterns at (c) $\rho = 0.375$ (left) and (d) $\rho = 0.40$ (right) as in $\mathbf{Ph}_4$; eventual jumping between patterns after a set of oscillations between a pattern and its negative (*antipattern*) as in $\mathbf{Ph}_5$ at (e) $\rho = 0.50$ (left); and pure pattern-antipattern oscillations as in $\mathbf{Ph}_6$ at (f) $\rho = 0.60$.

($\mathbf{Ph}_4$) *Irregular roaming* in which the activity keeps randomly visiting the basins of attraction corresponding to different patterns. (This is the case in figures 5.1(c) and 5.1(d)).

($\mathbf{Ph}_5$) Irregular roaming as for $\mathbf{Ph}_4$ but eventually interrupted at random during some time by oscillations between a pattern and its antipattern. (This occurs in figure 5.1(e)).

($\mathbf{Ph}_6$) Pure *pattern-antipattern oscillations*. (As in figure 5.1(f)).

These three genuine nonequilibrium cases correspond to $Q \simeq 0$ and $M \simeq 0$ (due to orthogonality). Case $\mathbf{Ph}_6$ also has $R \simeq 0$ (revealing the symmetry of oscillations), while both $\mathbf{Ph}_4$ and $\mathbf{Ph}_5$ have $R \neq 0$. In order to properly characterize these dynamic cases, we shall monitor latter the statistics of the itinerant trajectory.
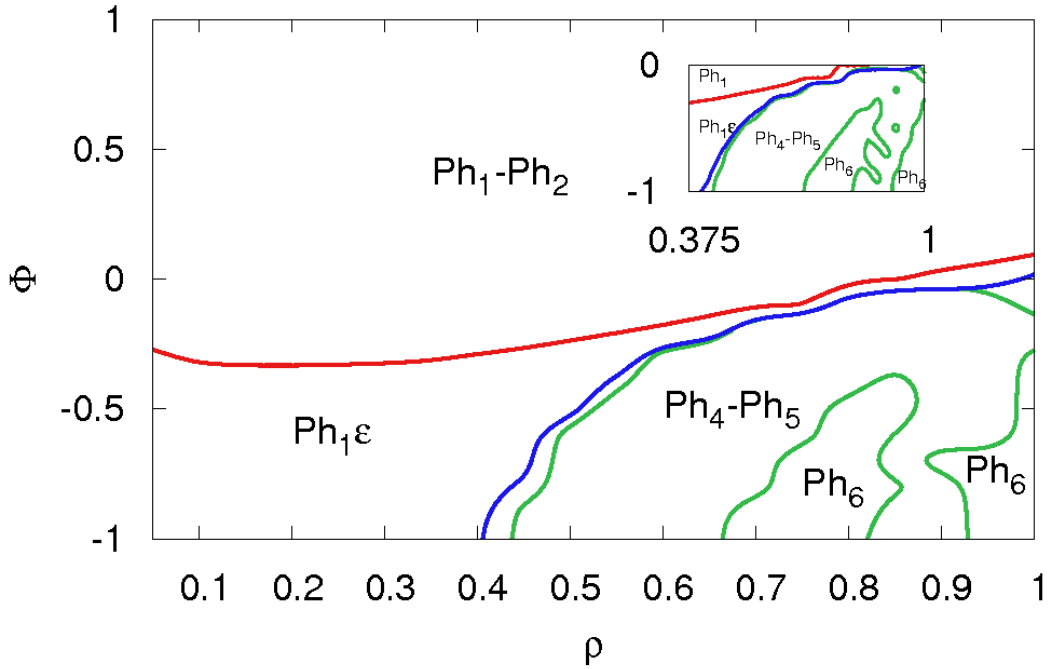
FIGURE 5.2: Nonequilibrium phase diagram (Φ, ρ) at low temperature. This was obtained for $N = 1600$, $P = 5$ and $T = 0.1$ from detailed analysis of all the order parameter functions. The top (blue) line is for $M = 0.8$. This leaves the equilibrium phases above, where $\mathbf{Ph_1}$ occurs with probability 0.87 and $\mathbf{Ph_2}$ otherwise. To the bottom, the next (violet) line - leaving also $\mathbf{Ph_1}\epsilon$ above - is for $M = 0.5$. The next (green) lines comprise an inverted-U shaped region in which $R > 0.18$. The inset shows the roaming region in more detail.

The different behaviors are better observed and interpreted at very low temperature. As shown in figure 5.2, the disordered phase $\mathbf{Ph_3}$ is not observed at the chosen (low) temperature, while the ordered, ferromagnetic and spin-glass phases then occur for any Φ as far as ρ is not too large. That is, one may have familiar order as in equilibrium -practically independently (over a wide range) of the noise affecting the connections- as far as only a relatively small fraction of nodes are simultaneously active [102]. However, one observes small fluctuations or dispersion with time around the mean value M, and that the amplitude of this kind of "error" increases as one lowers Φ and increases ρ. This effect, which is evident when one compares the two top panels in figure 5.1, led us to indicate a zone $\mathbf{Ph_1}\epsilon$ around the region for $\Phi < 0$ and $\rho \lesssim 0.5$. It is worth to distinguish this zone which reveals how the ferromagnetic phase $\mathbf{Ph_1}$ has resilience, i.e., a remarkable stability of the attractor to large fluctuations. These increase monotonously with increasing ρ and/or decreasing further Φ, and it finally results in jumping to other attractors
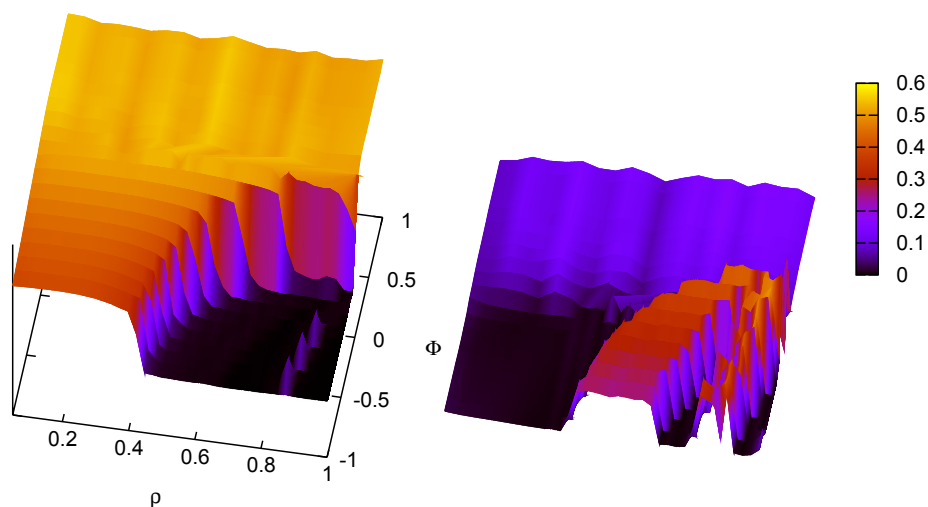
FIGURE 5.3: $M(\Phi, \rho)$ (left) and $R(\Phi, \rho)$ (right; same axes but not shown for clarity) for $N = 1600$, $P = 5$, and $T = 0.1$. There is coexistence of $\mathbf{Ph}_1$ and $\mathbf{Ph}_2$ for $\Phi > 0$, while the latter phase does not show up for $\Phi < 0$ and memory then occurs but as $\mathbf{Ph}_1\epsilon$ (see the main text) at sufficiently low ρ.

(as in the two middle graphs in figure 5.1) when more than one half of the nodes are simultaneously active. This is the origin of the genuine nonequilibrium cases $\mathbf{Ph}_4$, $\mathbf{Ph}_5$ and $\mathbf{Ph}_6$. In fact, as shown in figure 5.2, one observes the onset of irregular roaming with $R \neq 0$ and $M = 0$ for $\Phi < 0$ and ρ between 0.4 and 0.6.

The above picture and figure 5.2 follow from a detailed combined analysis of functions $M(\Phi, \rho)$, $R(\Phi, \rho)$ and $Q(\Phi, \rho)$ as illustrated in figure 5.3. This also shows that two main types of phase transitions between equilibrium and nonequilibrium phases occur (see figure 5.4). There is a second-order or continuous transition, as one maintains $\Phi < 0$ at a constant value, from the memory phase with large "error", i.e., $\mathbf{Ph}_1\epsilon$, to the irregular roaming phase $\mathbf{Ph}_4$. Then, at least near $T = 0$, one also observes a first-order or discontinuous transition (figure 5.4) as ρ is maintained constant, from the memory phase to the irregular roaming with pattern-antipattern oscillations, namely, $\mathbf{Ph}_5$. Furthermore, it is noticeable here that, as illustrated in figure 5.5, the transition region depends on the value of $\alpha = P/N$, that is, the critical value of ρ increases somewhat with decreasing α for finite N, and it seems to go to $\rho \simeq 0.5$ as $N \to \infty$ for finite α and T.
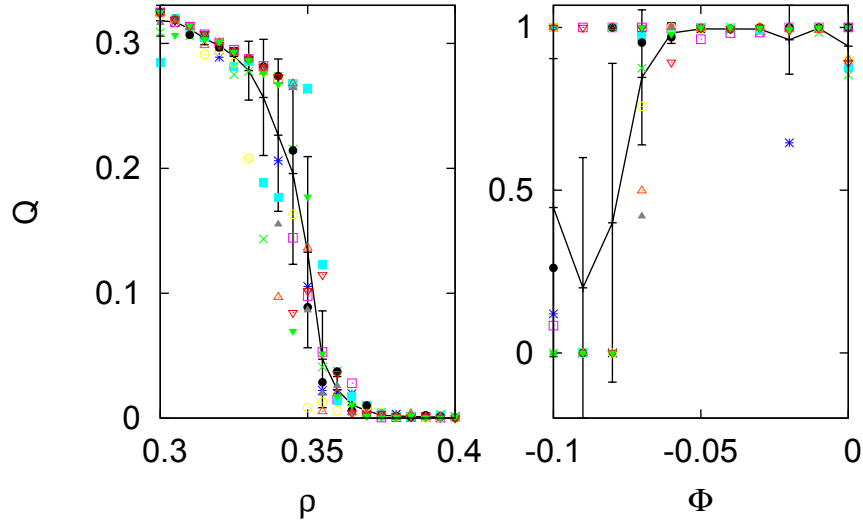
FIGURE 5.4: Left: Second-order phase transition between $\mathbf{Ph_1}\epsilon$ and $\mathbf{Ph_4}$ around $\rho \simeq 0.37$ when $\Phi = -0.8$. Right: First-order phase transition between $\mathbf{Ph_1}$ and $\mathbf{Ph_5}$ around $\Phi \simeq -0.1$ when $\rho = 0.8$. Both plots are for $N = 1600$, $P = 5$, and $T = 0.01$. Note that different realizations using a different seed produce here different values corresponding to the different symbols; the mean of all the realizations is represented by a solid curve.

The rare shape of the roaming region in plane (Φ, ρ) for $P = 5$, which shows in detail the inset of figure 5.2, is roughly the same as the one obtained analytically when $P = 1$ for the change of sign of the Lyapunov exponent in a closely related model (figure 2 in Ref.[55]). This confirms the general observation during our MC experiments of kind of chaos within the inverted-U region which is delimited in figure 5.2 by the green lines. That is, one should endow a chaotic character to the roaming region. That similarity also reinforces the reliability of our measures of order, and it shows how robust the model here is in relation to the dynamically irregular behavior. It also follows, in particular, that the model parameter P is irrelevant to this qualitative behavior, at least as far as not too many patterns are stored.

The "phases" $\mathbf{Ph_4}$ and $\mathbf{Ph_5}$, e.g., cases (d) and (e) in figure 5.1, cannot be discriminated on the basis of M, R and Q only. The top panel in figure 5.6 illustrates how these functions change with ρ for fixed Φ at low temperature. The bottom panel shows some overlap functions time series, depicting the dynamic transition from irregular roaming in $\mathbf{Ph_4}$ to the more regular behavior in $\mathbf{Ph_5}$ as
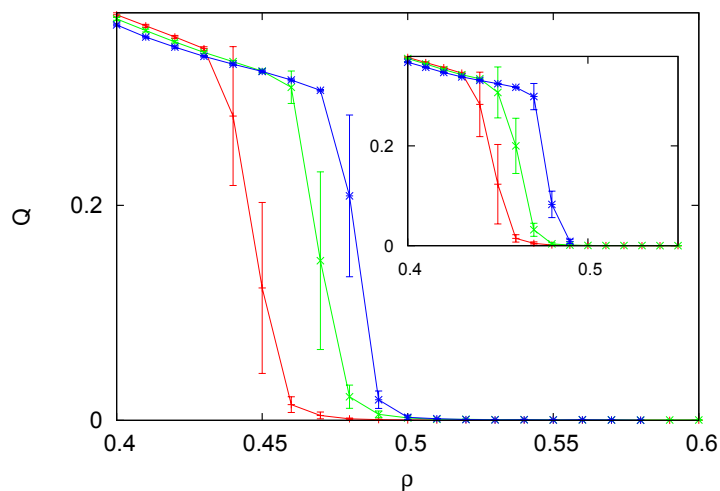
FIGURE 5.5: The second-order phase transition on the left of figure 5.4. For the same system as in this figure, the main graph here shows data for $P = 5$ and $N = 1600$, 3200 and 6400, respectively from left to right in the middle of the Q value. The inset is for the same values of N but $P = 5$, 10 and 20, respectively, i.e., same value of α.

a consequence of increasing the amplitude of fluctuations around the attractor as the fraction ρ of active nodes is increased during time evolution. As indicated in figure 5.2, the separation between the memory phase $\mathbf{Ph_1}$ or $\mathbf{Ph_1}\epsilon$ and the nonequilibrium cases is clear cut, while again it results more difficult to discriminate numerically the region $\mathbf{Ph_6}$ of pure pattern–antipattern oscillations (where $M = R = 0$) out of the $\mathbf{Ph_4}$–$\mathbf{Ph_5}$ chaotic region (where $M = Q = 0$ with $R \neq 0$). In any case, however, our finding concerning this agrees with the analytical result in a related case [150].

5.4   The onset of irregularity

The above section shows that the most intriguing behavior is when the system activity becomes irregular, e.g., as one crosses the second–order transition from the memory phase region to the nonequilibrium behavior —either at $\mathbf{Ph_4}$ with irregular roaming among attractors or at $\mathbf{Ph_5}$ where this may be randomly interrupted by series of pattern-antipattern oscillations. Figure 5.7 illustrates an aspect of this transition. In addition to the time evolution of some of the overlaps (right panels), which indicates where the activity is at each moment, this shows (left panels)
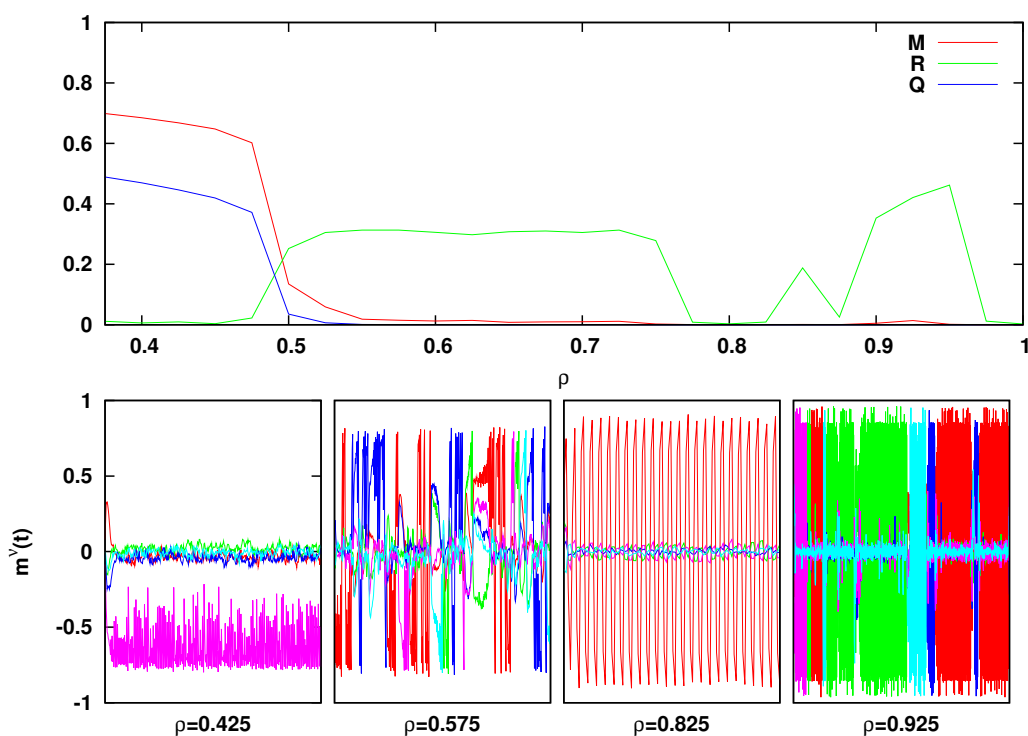
FIGURE 5.6: Upper panel: Functions $M(\rho)$, $R(\rho)$ and $Q(\rho)$ for $\Phi = -0.7$, $T = 0.1$, $N = 1600$ and $P = 5$. Bottom panels: Time series for the overlap functions $m^\nu(t)$ in the same case. The value of ρ is increased here during time evolution as indicated by the horizontal axis in the upper panel. Different colours correspond in this graph to different values of ν.

the signal $h_i(t)$ that can sometimes be monitored in experiments. As a matter of fact, this may be compared, for instance, with electrical signals measured in single neurons - as well as more delocalized, local fields - in the cortex and hippocampus of rats, and with Magnetoencephalogram (MEG) signals and recordings for single neuron action potentials.

It thus seems it would be most interesting to characterize more quantitatively how the model signal transforms while performing the relevant transitions. That is, when moving from the case of random fluctuations around a constant value in the memory phase, to the case in which the amplitude of the fluctuations increases and eventually switches to the negative of the original value, and finally reaches the case in which the frequency of switching and all the other variables become fully irregular in $\mathbf{Ph_4}$ and $\mathbf{Ph_5}$. With this aim, we studied in detail the distribution of times of permanence in an interval around significative values of h. More specifically, in order to extract the relevant information in the case of quite different signals such as those in figure 5.7, it turned out convenient to compute
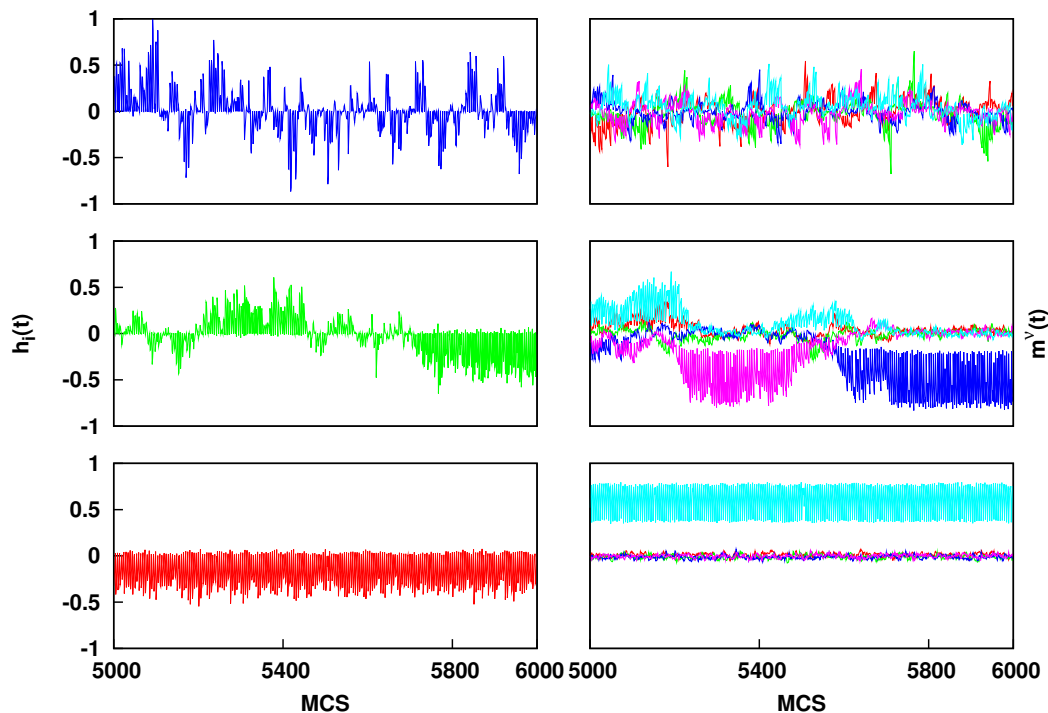
FIGURE 5.7: The local signal or field $h(t)$ on a typical neuron (left panels) and five overlaps $m^\nu(t)$ (right panels) indicated with different colours for a system with $N = 1600$, $P = 20$, $\Phi = -0.80$, $T = 0.01$ and, respectively from top to bottom, $\rho = 0.225$, 0.325 (near the transition point), and 0.425.

the distribution of time intervals, say $\Delta\tau$, in which the signal continuously stays in any of two ranges either $h(t) > h_0$ or $h(t) < -h_0$. The cutoff h_0 intends to suppress the smallest fluctuations, which correspond to non–significative noise; this is achieved here in practice for $h_0 \in [0.05, 0.1]$. We thus observe, after averaging over the network, time and different experiments that the interesting behavior requires relatively large systems, so that it does not occur for, say, $N = 400$ and $P = 5$ while it already becomes evident for, e.g., $N = 6400$ and $P = 40$. The most interesting fact from this study is that the exponent β in a power law fit $\Delta\tau^{-\beta}$ monotonously increases with size from $\beta \simeq 1$ for $N = 800$ and $P = 10$ in a way that might indicate a tendency of β to 1.5–2 (though our data never reached this regime). These facts are illustrated in the following figures.

The left panel in figure 5.8 shows a changeover from a general exponential behavior to a power law behavior near the interesting second–order phase transition. Analysis of the Fourier spectra reveals a similar situation, i.e., changeover from exponential to power law behavior, concerning both the signal $h(t)$ (right pannel in figure 5.8) and the overlap function $m(t)$. Figure 5.8 is a definite evidence for
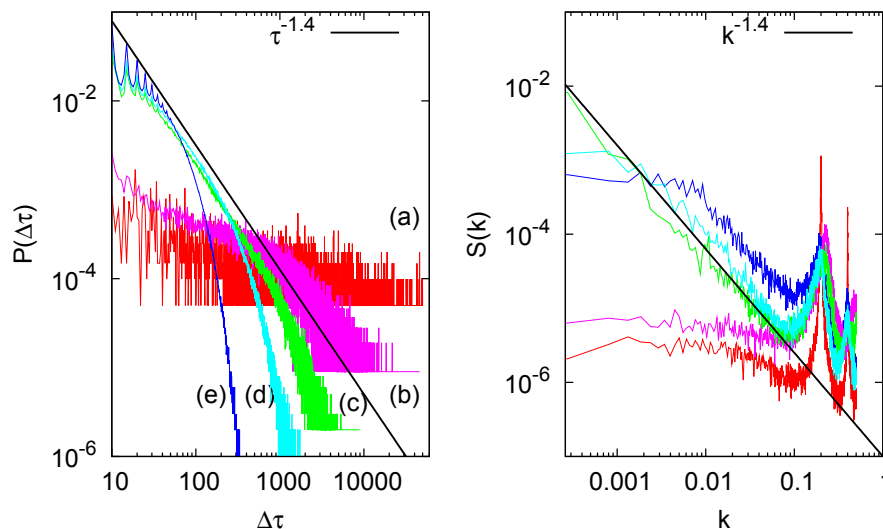
FIGURE 5.8: Logarithmic plots. Left: Distribution of time intervals in which the signal continuously stays in any of the two ranges either $h(t) > h_0$ or $h(t) < -h_0$, with $h_0 = 0.1$, when $N = 1600$, $P = 20$, $\Phi = -0.8$ and $T = 0.01$, for the sub–critical cases $\rho = 0.225$ (a) —a practically horizontal signal in the $\mathbf{Ph}_1$ phase— and 0.3 (b), the super–critical cases $\rho = 0.35$ (d) and 0.425 (e) —an exponential behavior in the $\mathbf{Ph}_4$ phase—, and the near–critical case $\rho = 0.325$ (c). The latter, near–critical case approximately follows the dotted line $\Delta\tau^{-\beta}$ with $\beta = 1.4$ for a large time interval. Each case corresponds to an average over 50 neurons and 20 independent systems running for 10^5 MCS. Right: Power spectra of $h(t)$ for the same cases as in the left pannel using runs with 4×10^5 MCS. The power law is illustrated with a dotted line.

statistical criticality as one approaches the relevant transition. On the other hand, figure 5.9 shows how the system activity close to the transition between the memory equilibrium phase$\mathbf{Ph}_1$ and the irregular behavior in $\mathbf{Ph}_4$ tends to follow the power law distribution over a larger range as one increases the size N for fixed P, which decreases α. However, we observed that β does not depend on N, namely, the same value $\beta = 1.4$ is obtained when $P = 20$ for $N = 1600$, 3200 and 6400.

5.5   System performance at the edge of chaos

Once the different emergent nonequilibrium phases in the system have been fully described in the previous sections, we have explored here the performance of the
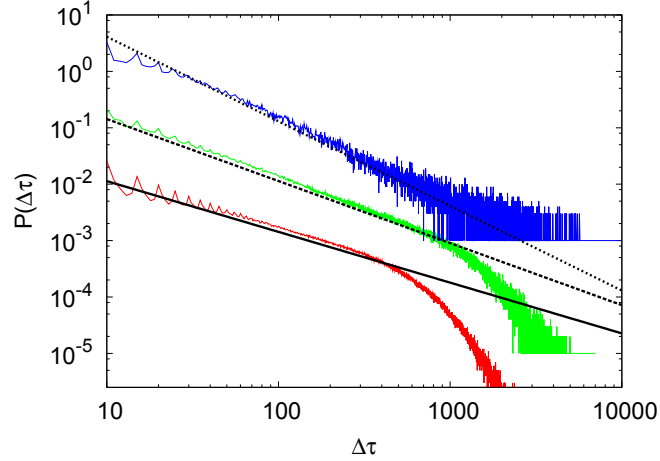
FIGURE 5.9: The same as in fig.5.8, but for $h_0 = 0.05$, to show the effect of varying the size N at fixed $\alpha = P/N = 0.003125$ and $\rho = 0.375$. From bottom to top, the data —corresponding to an average over 50 neurons and 10 independent systems— are for $N = 1600$ and 3.5×10^6 MCS (red), $N = 3200$ and 6×10^5 MCS (green), and $N = 6400$ and 8×10^4 MCS (blue), respectively. (For clarity purposes, there is a vertical translation of the data points.) Both the exponent β in $\Delta\tau^{-\beta}$ as well as the cutoff at which this power law fails clearly increase as N is increased.

system during some information processing tasks. As previously discussed in section 2.1 and in chapter 4, a system close to criticality is able to perform optimally different tasks due to its high sensitivity to any small perturbation. On the other hand, different theoretical works have shown the emergence of a high computational capacity in systems at the edge of chaos [160, 161], i.e. at the onset of a chaotic dynamical behaviour. In our model, we have characterized a second order transition between the memory equilibrium phase $\mathbf{Ph}_1$ and the chaotic irregular phase $\mathbf{Ph}_4$, which implies that the critical point is at the same time the onset for chaotic behaviour. To investigate if our system presents these optimal computational abilities at the edge of chaos, we have investigated its performance during the retrieval of stored patterns under small external stimuli close to this transition. We proceed as follow: first we have stimulated a particular neuron i with an external current of amplitude δ and duration t_{per} MCS associated with a randomly chosen memory pattern each $t_{int} = 300$ MCS (see figure 5.10), so that its corresponding local field is

$$h_i(\mathbf{s}, t_0 + t) = \sum_{j \neq i} \bar{w}_{ij} s_j(t_0 + t) + \delta \xi_i^\mu \qquad \forall i \quad t \in [1, t_{per}].$$

Second, we computed the overlap of the network activity with the stimulated
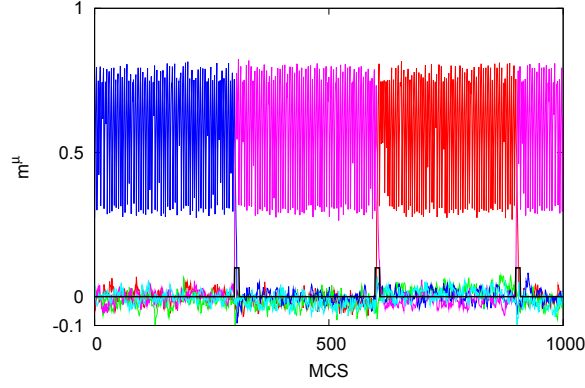
FIGURE 5.10: Overlap functions $m^\mu(t)$ for a network of $N = 1600$ nodes, $P = 5$ patterns, $\Phi = -0.8$, $\rho = 0.275$ and temperature $T = 0.01$, with an external stimulation of amplitude $\delta = 0.1$ and duration $t_{per} = 10$. Black curve represents the memory input applied to local fields. In this case memory input corresponds always to the actual retrieved pattern.

pattern μ^* during the interval t_{int} (which is a measure of the performance of the system to retrieve this pattern) as well as the overlaps with the non-stimulated patterns, respectively

$$
\begin{aligned}
M_{st} &\equiv \langle |m^{\mu^*}| \rangle_{t_{int}} \\
M_{no-st} &\equiv \frac{1}{P-1} \langle \sum_{\nu \neq \mu^*} |m^\nu| \rangle_{t_{int}}.
\end{aligned}
$$

In addition, we have compared the retrieval performance close to the transition **Ph$_1$-Ph$_4$** (with tuning parameter ρ), with the one obtained in an ordinary second order ferromagnetic-paramagnetic phase transition (with tuning parameter T) of the classic Hopfield model (i.e. with $\Phi = 1$).

Implementing different stimulation protocols to networks close to these transitions, we observed and concluded the following:

- Retrieval performance is efficient, in general, for high δ and t_{per}, in the whole **Ph$_1$** region, being $M_{st} \sim M$ and $M_{no-st} \ll M$. Decreasing the intensity and/or duration of the stimulous, the retrieval is still optimal close to the **Ph$_1$-Ph$_4$** transition (see left panels of figure 5.11).

- Assuming different stimulation protocols such that the product $\delta \times t_{per}$ remains constant, network retrieval performance is better for low δ and large duration t_{per} compared to stimulation with high δ and short t_{per} (compare A-left and B-left panels in figure 5.11).

- In the ferromagnetic-paramagnetic transition retrieval performance is always worse than the one relative to **Ph₁-Ph₄** transition (compare in figure 5.11 the panels A, B, C), result that demonstrates the positive role of the onset of chaos for pattern retrieval tasks.
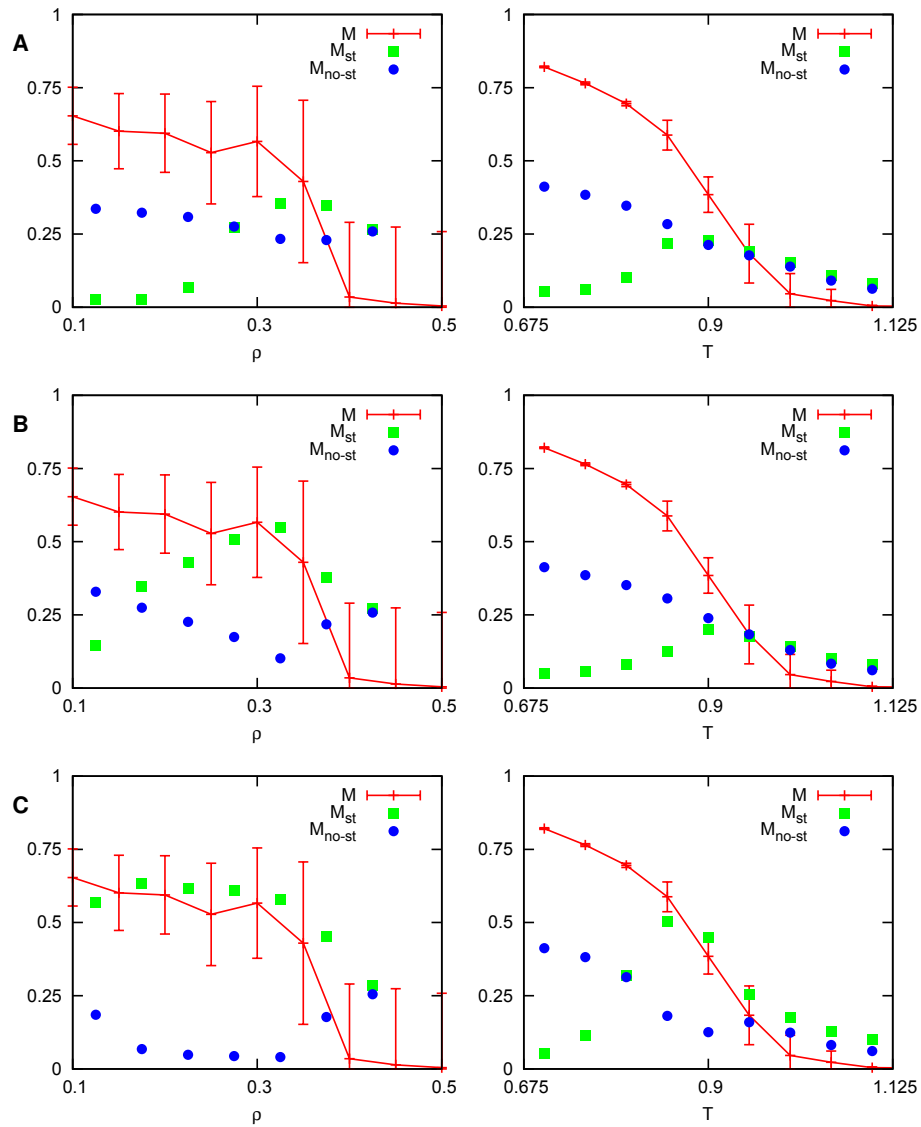
FIGURE 5.11: Mean overlap function with stimulated M_{st} and non stimulated M_{nost} patterns, for a **Ph₁-Ph₄** transition (network of $N = 1600$ nodes, $P = 5$ patterns, $\Phi = 0.8$ and $T = 0.01$, left panels) and a ferromagnetic-paramagnetic transition in the correspondent classical Hopfield network (obtained for $\Phi = 1$ and $\rho = 1$, right panels), with different stimulation protocols. Panels A: $\delta = 0.1$ and $t_{per} = 5$. Panels B: $\delta = 0.5$ and $t_{per} = 1$. Panels C: $\delta = 0.1$ and $t_{per} = 10$. Red curves corresponds to the overlap M with the condensed pattern, as defined in formula 5.9, in absence of stimulation.

5.6   Final discussion

Chemical reactions diffusing on a surface, forest fires with constant ignition of trees, parts of the nervous system vigorously reacting to weak stimuli, and the heart enduring tachycardia are paradigms of *excitable systems*, out of many cases in mathematics, physics, chemistry and biology; see [162, 163], for instance. Despite obvious differences, these systems share some characteristics. They comprise spatially distributed "excitable" units connected to each other and cooperating to allow for the propagation of signals without being gradually damped by friction. The simplest realization of the relevant excitability consists in assuming that each element has a threshold and a refractory time between consecutive responses. In order to deal with a setting which is both realistic and mathematically convenient, one may suppose the system is networked with occasionally quiet nodes and connection weights that vary with activity on short–time scales. As a matter of fact, experimental observations reveal rest states stable against small perturbations, which correspond to the silent nodes here, and rapid varying strength of connections, either facilitating or impeding transmission, which temporarily affect thresholds and may also induce time lags during response. Furthermore, it is known that such nonequilibrium setting induces dynamic instabilities and attractors [150, 164]. On the other hand, we believe it is likely that this modeling of excitable media may in fact be related to the one by means of partial differential equations such as when the simple FitzHugh-Nagumo neuron model [165, 166] is used to represent each unit.

With this motivation, we have studied a neural excitable media by extensive computer simulations of a discrete time model with an updated rule which generalizes the Hopfield–like standard case. The resulting phenomenology as described here is expected to describe the basic behavior in a number of apparently diverse man–made and natural excitable systems. In particular, we explicitly show how the model exhibits in the absence of stimuli highly unstable dynamics when a sufficiently large fraction ρ of nodes are synchronized and for certain values of a noise parameter Φ that controls the noise within the connections strength. We also illustrate how these instabilities induce the occurrence of novel, first and second order nonequilibrium phases. One of these happens to be most interesting as it describes the global activity wandering irregularly among a number of attractors, details strongly depending on the values of ρ and Φ. In particular, one may tune an efficient search in the model attractors space which is sensible to assume it may

be at the origin of phenomenology previously described for neural, genetic and ill–condensed matter systems. There is also definite evidence of non–Gaussian, $1/f$ *noise* when the system is tuned into this irregular behavior, which may explain recent experimental observations of criticality and power law distributions in cortical networks.

Additionally, we remark how the mechanism behind the irregular jumping from one pattern to the other is well understood in the model. That is, the relevant instabilities are to be directly associated to the effective local fields that one may write as

$$h_i^{\text{eff}} \approx [1 - (1 - \Phi)\zeta(m)] \sum_{j \neq i} \omega_{ij} s_j \tag{5.12}$$

for large N, i.e., neglecting terms of order N^{-1}. After some manipulation, one may write this more explicitly as

$$h_i^{\text{eff}} = h_i^{\text{Hebb}} - \eta \sum_{\mu} \xi_i^{\mu}(m^{\mu})^3 - \eta \sum_{(\mu \neq \nu)} \xi_i^{\mu} m^{\mu}(m^{\nu})^2. \tag{5.13}$$

Here, h_i^{Hebb} stands for the energy per neuron in the standard model, $\eta = (1 - \Phi)/(1 + \alpha)$, and the last sum is over all pairs of different indexes μ and ν. As discussed above, h_i^{Hebb} tends to drive the system activity near the attractor associated to one of the stored patterns. Together with the second term in equation (5.13), this sums up to $\sum_{\mu} \xi_i^{\mu} m^{\mu}[1 - \eta(m^{\mu})^2]$ which, depending on the value of η, induces instabilities and irregular behavior of the overlaps dynamics similar to those in a cubic map [167]. The third term in (5.13), on the other hand, may be written as $-\eta \sum_{\nu} m^{\nu} h_i^{\nu}$ with $h_i^{\nu} = \sum_{\mu \neq \nu} m^{\mu} \xi_i^{\mu} m^{\nu}$. Given that ν differs from μ here, this only includes asymmetric terms $\xi_i^{\mu} m^{\nu}$ similar to those that characterize the local fields for asymmetric learning rules, namely, $\hat{h}_i = \sum_{\mu} \xi_i^{\mu} m^{\mu+1}$, which are often used to stored and retrieve ordered sequences of patterns [111, 168]. It is sensible to assume, therefore, that this term is most efficient in the present case in inducing transitions among patterns. Unlike for asymmetric learning [111], however, the destabilization here does not induce any order nor predictability in the sequence of visited patterns. On the other hand, we have also demonstrated that this general emergent behaviour allows a better response of the system to some external changing input. These results could explain the ability of actual neural systems to efficiently process information arriving from other different areas or to process continuously changing stimuli from the senses.

Chapter 6

Self-organization without conservation: Are neuronal avalanches generically critical?

Recent experiments on cortical neural networks have revealed the existence of well-defined *avalanches* of electrical activity. Such avalanches have been claimed to be generically scale-invariant - *i.e.* power law distributed - with many exciting implications in Neuroscience. Recently, a self-organized model has been proposed by Levina, Herrmann and Geisel to justify such an empirical finding. Given that (i) neural dynamics is dissipative and (ii) there is a loading mechanism "charging" progressively the background synaptic strength, this model/dynamics is very similar in spirit to forest-fire and earthquake models, archetypal examples of non-conserving self-organization, which have been recently shown to lack true criticality. In this chapter we show that cortical neural networks obeying (i) and (ii) are not generically critical; unless parameters are fine tuned, their dynamics is either sub- or super-critical, even if the pseudo-critical region is relatively broad. This conclusion seems to be in agreement with the most recent experimental observations. The main implication of our work is that, if future experimental research on cortical networks were to support that truly critical avalanches are the norm and not the exception, then one should look for more elaborate (adaptive/evolutionary) explanations, beyond simple self-organization, to account for this.

6.1 Introduction and outlook

6.1.1 Generic scale invariance

In contrast to what occurs for standard criticality, where a control parameter needs to be carefully tuned to observe scale invariance, certain phenomena as earthquakes, solar flares, avalanches of vortices in type II superconductors, or rainfall, to name but a few, exhibit generic power-laws, - *i.e.* they lie generically at a critical point without any apparent need for parameter fine tuning [56, 66, 169]. Ever since the concept of *self-organized criticality* [56, 169] was proposed to account for phenomena like these, it has generated a lot of excitement, and countless applications to almost every possible field of research have been developed. Underpinning the necessary and sufficient conditions for a given system to self-organize to a critical point is still a key challenge.

In this context, it has been established from a general viewpoint that *conserving dynamics* (i.e. that in which some quantity is conserved along the system evolution) is a crucial ingredient to generate true self-organized criticality in slowly driven systems, see section 2.3 and [20, 170]. In this way, non-conserving self-organized systems have been shown *not* to be truly scale-invariant (see [20] and references therein). While sandpiles, ricepiles, and other prototypical self-organized models are examples of conserving self-organizing systems, forest-fire and earthquake automata are two examples of non-conserving models. They both were claimed historically to self-organize to a critical point and they both were shown afterwards to lack true scale-invariant behavior [20]. The main reason for this is, in a nutshell, that non-conserving systems combine driving (loading) and dissipation, and this suffices to keep the system "hovering around" a critical point separating an active from a quiescent or absorbing phase (driving slowly pushes the system into the active phase and dissipative takes it back to the absorbing phase). But, in order to have the system lying exactly *at* the critical point requires of an exact cancellation between dissipation and driving (loading) to achieve a critical steady state; such a perfect balance can only be achieved by parameter fine tuning, and then the system cannot be properly called "self-organized".

This mechanism of (non-conserving) self-organization has been termed self-organized quasi-criticality (SOqC) [20] to underline the conceptual differences with truly scale-invariant, (conserving) self-organized criticality (SOC) [56, 66, 169].

From now on, we shall use the acronym SOqC to refer to non-conserving self-organized systems, and shall keep the term SOC for self-organized conserved systems.

SOqC may explain the "approximate scale invariance" (with apparent power-law behavior extending for a few decades) observed in many real systems as those mentioned above (earthquakes and forest fires) but, strictly speaking, it fails to explain true scale-invariance. SOqC systems require some degree of parameter tuning to lie sufficiently close to criticality. For a much more detailed explanation of the SOqC mechanism and its differences with SOC, we refer the reader to [20].

6.1.2   Scale invariance in neuronal avalanches?

Neuronal avalanches were first reported by Beggs and Plenz, who analyzed *in vitro* cortical neural networks using slices of rat cortex as well as cultured networks [6, 8, 10, 171]. More recently, neuronal avalanches have been observed also *in vivo* [46, 47]. In all these cases, cortical neurons form dense networks which, under adequate conditions, are able to spontaneously generate electrical activity. The associated *local field potentials* can be recorded by using multielectrode arrays [6, 8]. Each electrode in the array monitors the electrical activity of a local group of neurons [1]. According to Beggs and Plenz [6, 8, 10, 171] activity appears in the form of "avalanches", i.e. localized activity is generated spontaneously at some electrode and propagates to other ones in a cascade process which occurs at a much faster timescale (tens of milliseconds) than that of the quiescent periods between avalanches (typically of the order of seconds). Previous experimental research in cultured networks had identified the existence of spontaneously generated *synchronized bursts* of activity (involving synchronous activation of many neurons), followed by silent periods of variable duration [70, 72, 145, 173] (theoretical work has been done to explain such a coherent or synchronous behavior, see for instance, [174, 175]). The main breakthrough by Beggs and Plenz in [6, 8] was to enhance the resolution and bring the internal structure of "synchronized" bursting events to light. In other words, the apparently synchronous activation of many neurons required for a synchronized burst corresponds to a sequence of neuron activations, i.e., a neuronal avalanche, which generates spatio-temporal patterns of activation confined between two consecutive periods of quiescence.

---

[1]which for convenience can be thought of as a unique "effective" neuron; a review of the involved experimental techniques and methods can be found in [172]

Experimental measurements of avalanches can be performed, and the distribution of quantities as *i)* the avalanche size s (i.e. the number of electrodes at which a non-vanishing signal is detected during an avalanche) and *ii)* the avalanche lifetime, t, can be recorded, see section 4.3. What is relevant for us here is that, according to Beggs and Plenz, avalanches seem to be generically scale invariant [6, 8, 10, 171]; in particular, avalanche sizes, s, and times t are distributed as:

$$P(s) \sim s^{-3/2}\mathcal{F}(s/s_c), \qquad P(t) \sim t^{-2}\mathcal{G}(t/t_c) \qquad (6.1)$$

respectively, where $\mathcal{F}$ and $\mathcal{G}$ are two cut-off functions; the cutoff s_c grows in a scale invariant way as a function of system-size: the larger the system the larger the cutoff, providing evidence for finite size scaling. The cut-off t_c appears at very small times, so the evidence for scale invariance is much larger for s than for t.

These results have been claimed to be robust across days, samples, and pharmacological variations of the culture medium [6, 8, 10, 171]. The exponent values in equations (6.1) coincide with their mean-field counterparts for avalanches in sandpiles (the prototypical examples of self-organized criticality) [134]. Mean-field exponents do not come as a surprise: given the highly entangled structure of the underlying network (which has been reported to have the *small-world property* [127, 135]) mean-field behavior is to be expected for critical phenomena occurring on it [69].

Finally, recalling that, at a mean-field level, avalanche dynamics can be interpreted as a *branching process* [136, 176], an empirical study of the branching ratio, σ, (defined as the fraction of active electrodes per active electrode at the previous time bin) was performed in [6, 8, 136]. It was found that the value of σ measured for avalanches started from one single electrode is very close to unity, in agreement with the critical value of marginally propagating branching processes, $\sigma_c = 1$.

From these results, it has been claimed that cortical neural networks are generically critical, i.e. scale-invariant, and that they reach such a critical state in a "self-organized" way [6, 8]. Scale invariance in the propagation of neural activity has raised a great deal of interest and excitement in Neuroscience. For instance, critical neural avalanches have been claim to lead to [6, 8, 173]:

- optimal transmission and storage of information [6, 8, 10, 136, 171],

- optimal computational capabilities [177],

- large network stability[160],

- maximal sensitivity to sensory stimuli [11, 132], etc.

Let us caution that discrepant results, i.e. non-critical neuronal avalanches, have also been recently reported in the literature. For instance, measurements of cortical local-field-potentials were performed by Bédard *et al.* [178] using parietal cat cortex. None of the features reported by Beggs and Plenz [6, 8] was observed for such a network; not only the observed behavior was not critical, but it was not even possible to observe clean-cut avalanches. It was argued that the absence of scale-free avalanches could stem from fundamental differences between the considered cortex regions used in [178] and in [6, 8]. Moreover, in a recent review paper, Pasquale *et al.* [179] report on different empirical types of avalanche distributions: critical, subcritical, or super-critical, depending on various factors. These authors conclude that critical avalanches can indeed emerge, but they are more the exception that the rule.

6.1.3 Goals and outlook

The main goal of this chapter is to elucidate from a theoretical viewpoint whether neuronal avalanches are truly critical or not. Or, more precisely, to understand whether self-organizing mechanisms (such as those of SOC or SOqC) can justify the findings for neuronal avalanches. To this purpose, we rely extensively on a model for neuronal avalanches, proposed recently by Levina, Herrmann and Geisel [19]. The model is a self-organized one, including integrate-and-fire neurons and short-term synaptic plasticity. It has been claimed, both analytically and numerically, to back the existence of generically (strictly) critical neuronal avalanches in a very broad region of parameter space [19].

The key observation, which motivated the present work, is the fact that local conservation laws, such as those required to have truly critical self-organized (SOC) behavior, are not present in neural networks in any obvious way. In fact the information coming from action potential, is transmitted to postsynaptic neurons, by mean of several transduction biochemical mechanisms acting in synaptic button: such processes are highly no linear, and do not allow for any kind of potential and/or ionic current conservation, see section 3.1. Thus if cortical networks are represented as an electrical circuit, perfect transmission without loss

of energy is an unrealistic idealization and, analogously, if they are modeled as networks of dynamical synapses, there also exist dissipative or "leakage" phenomena. In summary, *no quantity is strictly conserved in neural signal transmission.* Reasonably enough, the Levina, Herrmann and Geisel (LHG) model [19] is also a non-conserving one (see below).

Therefore, the existence of critical neuronal avalanches (both experimentally and in the LHG model) seems to be in contradiction with the general conclusion in [20], i.e. the lack of true criticality in non-conserving systems. In this way, a rationalization of neuronal avalanches would only be possible, at most, in terms of self-organized *quasi-criticality* (SOqC) and not in terms of *strict criticality* as suggested in [19].

Following the steps in [20], here we shall underline the analogies and differences between the model by Levina *et al.* and other non-conserving self-organized models such as those for earthquakes or forest fires. We shall show that the LHG model is *not* generically critical: it can be either critical, subcritical or supercritical depending on parameter values; fine tuning is required to achieve strict scale-invariance. Still, the model is capable of generating, for a relatively wide parameter range, pseudo-critical avalanches with associated truncated power-laws which can suffice to explain empirical observations.

This conclusion, *i.e.* the lack of true criticality, is expected to apply not only to the model in [19], but also to empirical neuronal avalanches. It suggests that if neuronal avalanches turned out to be truly critical, the ultimate reason for that should be looked for in some type of adaptive/evolutionary mechanism [180] or in homeostatic processes [181], but cannot be generically ascribed to plain self-organization.

The rest of the chapter is structured as follows. In section 6.2, we present the self-organized model proposed by Levina *et al.* for neuronal avalanches. A discussion of its main properties appears in sections 6.3 (numerical) and 6.4 (analytical). Then, in section 6.5, we put this model under the general framework of self-organized quasi-criticality introduced in [20] by deriving explicitly a Langevin equation from its microscopic rules, emphasizing the lack of true generic criticality. Finally, the main conclusions and a critical discussion of recent experimental results are presented.

6.2   The Levina-Herrmann-Geisel (LHG) model

Aimed at understanding the origin of power-law distributed cortical avalanches, Levina, Herrmann, and Geisel (LHG) [19] proposed a variation of the well-known Markram-Tsodyks model of chemical synapses [175]. Such a model had been already extensively used to reproduce the dynamics of synchronized bursting events (also called "population spikes") [175].

Consider a *fully connected network* of N **integrate-and-fire neurons** each of them characterized by its local (membrane) potential, V_i, with

$$0 \leq V_i \leq V_{max}. \tag{6.2}$$

Neurons i and j (with $i \neq j$) are connected by a synapse of strength J_{ij}. This can be thought of as the amount of available neurotransmitters or, more generally, "synaptic resources", for such a connection.

In the original Markram-Tsodyks model [175], together with V_i and J_{ij}, there is a third variable, $u_{i,j}$, representing the fraction of neurotransmitters which is actually released every time a pulse is transmitted between i and j. Its dynamics can be used to implement synaptic facilitation (see, for instance,[182]); but, aimed at keeping the model as simple as possible, and following LHG [19], we fix $u_{i,j} = u$ to be a constant.

The simplified Markram-Tsodyks or LHG dynamics is defined by the following equations:

$$\begin{cases} \dfrac{\partial V_i}{\partial t} = & I^{ext}\delta(t - t^i_{driv}) + \sum_{j=1}^{N-1}\dfrac{uJ_{i,j}}{N-1}\delta(t - t^j_{sp}) - V_{max}\delta(t - t^i_{sp}) \\[3mm] \dfrac{\partial J_{i,j}}{\partial t} = & \dfrac{1}{\tau_J}\left(\dfrac{\alpha}{u} - J_{i,j}\right) - uJ_{i,j}\delta(t - t^j_{sp}). \end{cases} \tag{6.3}$$

The different terms in equations (6.3) are as follows:

- *Driving*: I^{ext} is the amplitude of an external random input which operates at discrete times t^i_{driv} on i. Driving impulses can be introduced at a fixed rate h. Alternatively, slow-driving ($h \to \infty$) can be implemented by switching I^{ext} on if and only if all potentials are below threshold.

- *Firing*: $-V_{max}\delta(t - t^i_{sp})$; if the potential at i overcomes the threshold, V_{max}, at time t^i_{sp}, the neuron spikes, and it is reset to

$$V_i(t^i_{sp}) \to V_i(t^i_{sp}) - V_{max};$$ (6.4)

  otherwise, nothing happens.

- *Integration*: $\sum_{j=1}^{N-1} \frac{uJ_{i,j}}{N-1}\delta(t - t^j_{sp})$; the (post-synaptic) neuron i integrates signals of amplitude $uJ_{i,j}/(N-1)$ from each spiking (pre-synaptic) neuron j. A non-vanishing delay between the time of discharge and the time of integration in neighboring neurons could also be introduced, without affecting significantly the results.

- *Synaptic depression*: $-uJ_{i,j}\delta(t - t^j_{sp})$; after each discharge involving the (pre-synaptic) neuron j all synaptic strengths J_{ij} (where i runs over all post-synaptic neurons) diminish by a fraction u.

- *Synaptic recovery*: $\frac{1}{\tau_J}\left(\frac{\alpha}{u} - J_{i,j}\right)$; synapses recover to some target value, $J_{ij} = J = \alpha/u$, on a timescale determined by the recovery time, τ_J.

Observe that the only sources of stochasticity are the initial condition and the external driving process, while the avalanche dynamics is purely deterministic. Also, the set of equations above can be implemented on any generic network topology; here (following LHG) we will mostly restrict ourselves to fully connected networks, even if results for random networks and two-dimensional lattices are also briefly discussed.

6.3   Model analysis

6.3.1   Static limit

Let us first discuss the *static limit* of the model in which the synaptic recovery rate is so fast (i.e $\tau_J \to 0$) that $J_{i,j}$ can be taken as a constant for all pairs i, j and for all times: $J_{i,j} = J = \alpha^{static}/u$. In such a case (keeping u fixed), α^{static} acts as a control parameter [183, 184]. Observe that, in the limit in which $\alpha^{static} \to V_{max}$, the model becomes conserving: each spiking neuron reduces its potential by V_{max} and each of its $(N-1)$ neighbors is increased by $V_{max}/(N-1)$ (integration term

in equations (6.3)).

Once the system has reached its steady state, it is possible to assume that the values of V are uniformly distributed in the interval $[\epsilon, V_{max} - \epsilon]$ with $\epsilon \to 0$ when $N \to \infty$. This assumption parallels what is done in a similar analysis of related self-organized systems such as earthquake models [185] and can be numerically verified to hold with good accuracy (see section 6.6). This implies that, fixing (without loss of generality) $V_{max} = 1$, in the large system-size limit, a randomly chosen neuron can be in any possible state with uniform probability. Thus, upon receiving a discharge of size $uJ/(N-1)$, it becomes over threshold with probability $uJ/(N-1)$. Hence, viewing the propagation of activity within avalanches as a *branching process* with branching rate $uJ/(N-1)$ and $N-1$ neighbors per neuron, the average avalanche size $\langle s \rangle$ can be written as the sum of an infinite geometric series [176]

$$\langle s \rangle = \frac{1}{1 - (N-1)\ uJ/(N-1)} = \frac{1}{1 - uJ}. \tag{6.5}$$

Observe that this expression is valid only for $uJ < 1$. The model critical point can be identified by the presence of a divergence in equation (6.5); this occurs at the conserving limit $\alpha_c^{static} = 1$, in agreement with what happens in other models of SOC (like sandpiles) which are critical only in the case of conserving dynamics.

For $\alpha^{static} > 1$ (i.e. above the conserving limit) the potential at each site grows unboundedly (i.e. there is no stationary state) with perennial activity (generating an "explosive" super-critical phase) while, for $\alpha^{static} < 1$, the process is dissipative on average, i.e. the total potential is reduced at every spike and avalanches die after a characteristic time (sub-critical phase). Thus, in summary, as already discussed in the literature [183, 184], *the static version of the LHG model exhibits a standard (absorbing) phase transition separating a sub-critical from a super-critical phase.*

Let us remark that, for finite systems, the critical point has size-dependent corrections. It is only in the infinite size limit, in which driving and dissipation vanish, that $\alpha_c^{static} = uJ_c = 1$. Actually, for any finite system, $\epsilon \neq 0$, and additional finite-size terms need to be included in the calculation above. This is a consequence of the fact that, in order to achieve a steady state for finite systems, some form of dissipation needs to be present to compensate the non-vanishing driving, I^{ext}, entailing $\alpha_c^{static}(N) < \alpha_c^{static}(N \to \infty) = 1$ (see Table 1 where numerical estimates for the critical point location are reported; details of the computational procedure are reported in the forthcoming section).

N	300	500	700	1000	2000	3000	...	∞
α_c^{static}	0.92(1)	0.93(1)	0.94(1)	0.95(1)	0.96(1)	0.97(1)	...	1

TABLE 6.1: Location of the critical point α_c^{static} as a function of the system size N, as obtained in computer simulations of the *static* model ($\tau_J \to 0$). The critical point location does not depend on the way the system is driven, i.e. on I^{ext}.

6.3.2   Dynamic model

Let us now turn back to the full *dynamic* model. Observe that:

- The equation for $J_{i,j}$ in equations (6.3) includes a loading mechanism (analogous to those reported in [20] for earthquake and forest-fire models) or "synaptic recovery mechanism" which counterbalances the effect of synaptic depression in the absence of spikes: the "background field" J_{ij} increases steadily towards its target value α/u. Note that in contrast with models of forest fires or earthquake automata, in which the "loading mechanism" (see [20]) acts only between avalanches, the recovery dynamics of J occurs also during avalanches, at a finite timescale controlled by τ_J.

- In the limit in which $u\langle J_{i,j}\rangle \to V_{max} \quad \forall(i,j)$, where $\langle.\rangle$ stands for steady-state time averages, conservation is recovered *on average*. In analogy with the static model, the dynamics becomes non-stationary above such a limit: loading overcomes dissipation and potential fields grow unboundedly.

In the case in which I_{ext} drives the system slowly we are in the presence of the main ingredients characteristic of non-conserving self-organized models, as described generically in [20]:

1. separation of (driving and dynamics) timescales,

2. dissipative dynamics (provided that $u\langle J_{i,j}\rangle < V_{max}$), and

3. loading mechanism, increasing the average value of the "background field" J_{ij}.

Prior to delving into further analytical calculations, which are left for Section 6.4, let us present in the rest of this section computational results obtained for equations (6.3).

6.3.2.1 Numerical analyses

Numerical integration of equations (6.3) becomes very costly as the number of components grows, limiting the maximum system size (up to $N = 3000$ in the present study). Observe that, owing to the presence of δ-functions, equations (6.3) is an "impulsive dynamics" equation and thus, caution must be paid when integrating it numerically not to miss delta peaks when discretizing.

The system is initialized with arbitrary (random) values of $V_i \in [0, V_{max}]$ and $J_{i,j} \in [0,1] \quad \forall (i,j)$. We keep α as a control parameter and fix parameter values mostly as in [19]: $u = 0.2$, $V_{max} = 1$ and $\tau_J = 10N$.

Let us remark that the choice $\tau_J = 10N$ [19] might be not very realistic from a neuro-scientific point of view; i.e. it is not clear whether the synaptic recovery rate should depend on the total number of connections of the corresponding neuron or not. Observe that N is the number of synapses per neuron, therefore in principle, it could be the case that, if a given neuron has limited resources, the recovery rate per synapse depends on the total number of synapses. But also the opposite could be true; i.e. the recovery time of a given synapse could depend only on its local properties and not on those of its corresponding neuron. This is a neuro-scientific issue that is beyond the scope of the present chapter and that we prefer not to enter here. Anyhow, we have verified that our results are not significantly affected by such a choice; for example, we have also considered values of τ fixed for any N and checked the robustness of our results. We work in the slow driving limit, i.e. we drive the system with an input, I_{ext} at a randomly chosen site if and only if all potentials are below threshold. The sequence of activity generated therefrom constitutes an avalanche. We have used two different N-dependences for I^{ext}: (i) $I^{ext} = 7.5 \times N^{-1}$, and (ii) $I^{ext} = N^{-0.6467}$; both of them engineered to comply with the scaling form $I^{ext} \sim N^{-w}$ considered by Levina *et al.*, and to reproduce the value $I^{ext} = 0.025$ for $N = 300$ used in simulations in [19]. Results are mostly insensitive to the choice of I^{ext}.

Running computer simulations of equations (6.3) with this set of parameters, a steady state for both V_i and $J_{i,j}$ is eventually reached, after an initial transient. In such a regime, driving events generate avalanches of activity. figure 6.1 shows time series in the steady state for the network-averaged value of $uJ_{i,j}$, $u\bar{J}$, with

$$\bar{J}(t) \equiv \sum_{i,j,\ i\neq j} \frac{J_{i,j}(t)}{N(N-1)}. \tag{6.6}$$
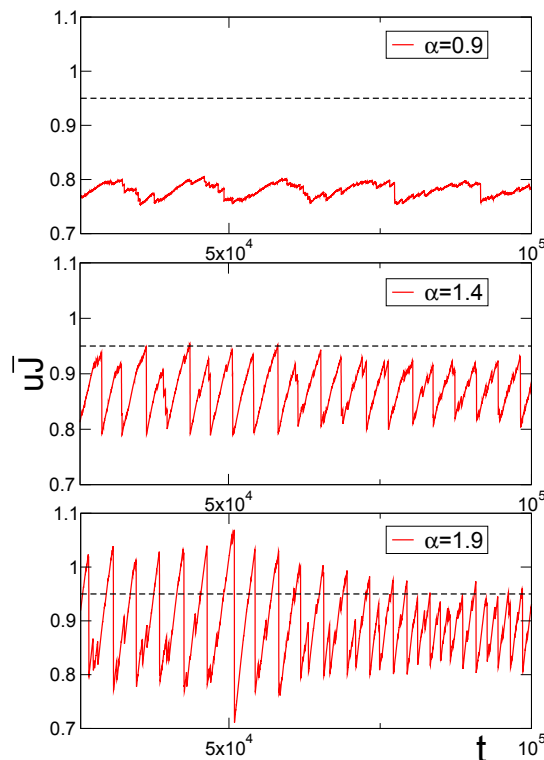
FIGURE 6.1: Time evolution of $u\bar{J}$ and the number of spiking neurons for $\alpha = 0.9$ subcritical (up), $\alpha = 1.4$ critical (center), and $\alpha = 1.9$ supercritical (down), in simulations with $N = 1000$. It is only above the critical point of the dynamical model that $u\bar{J}$ goes beyond the critical point of the static model for the considered system size, $\alpha_c^{static} = 0.95(1)$ (dashed line).

Results correspond to $N = 1000$ and three different values of α, 0.9, 1.4 and 1.9. Large avalanches (which are much more frequent in the supercritical phases) correspond to abrupt falls in $u\bar{J}$, while in between avalanches $u\bar{J}$ grows linearly in time owing to the external driving.

Observe the intermittent response of the system in all cases: peaks of activity of various sizes appear in all cases; note also the "quasi-periodic" behavior in all the three cases (similar quasi-periodic behavior had already been described for the Markram-Tsodyks model [101]).

In order to determine the critical point, in figure 6.2(left) we show the associated avalanche-size distributions for the same three values of α. All of them show, for small values of s a power-law decay, with exponent close to 1.5; for $\alpha = 0.9$ (subcritical) there is an exponential cut-off while for $\alpha = 1.9$ (supercritical) there is a "bump" for large size values, which defines a characteristic scale. In the intermediate case, $\alpha = 1.4$ there is also an exponential cut-off but, upon increasing system size, it shifts progressively to the right in a scale invariant way, as corresponds to a critical point. This is illustrated in figure 6.2(right) where critical
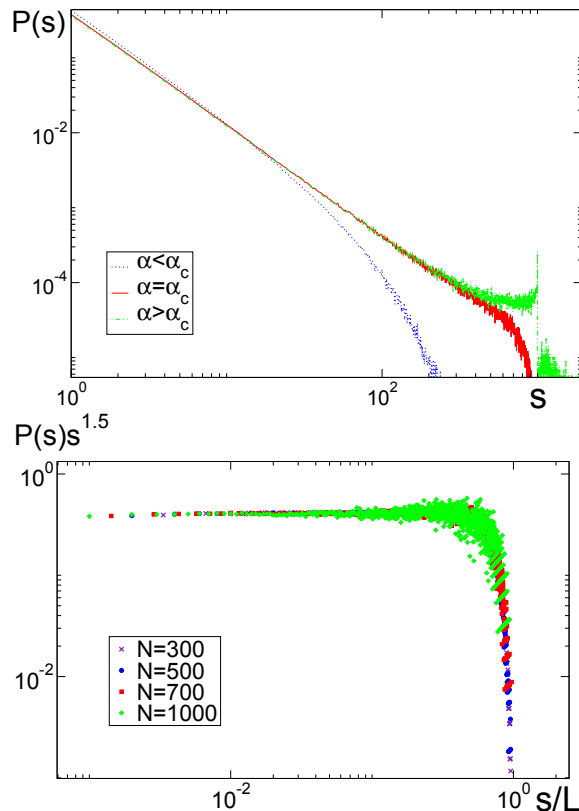
FIGURE 6.2: Top: Avalanche-size distribution of the LHG model for $N = 1000$ and three different values of α, 0.9, 1.4 and 1.9 (slightly below, at, and slightly above the critical point, respectively). Bottom: Rescaled avalanche-size distribution showing good finite size scaling. This implies that the cut-off for the critical value (see Left) shifts progressively to the right, in a scale invariant way, upon enlarging the system size.

distributions (i.e. for $\alpha = 1.4$) for various system-sizes have been collapsed into a unique scale-invariant curve.

In figure 6.3(top) we plot the distributions of $u\bar{J}$ for different values of α, obtained by sampling values of $\bar{J}$ all along the dynamics. Observe the progressive broadening and displacement to the right upon increasing α. Figure 6.3(bottom) illustrates the presence of strong finite size effects; in particular, for the critical point $\alpha = 1.4$, we see that the distribution of $\bar{J}$ moves progressively to the right. The main observation to be made is that these distributions *do not* converge to narrower ones upon enlarging system size. Similar broad distributions are typical of non-conserving self-organized models, for which delta-peaked distributions are *not* obtained even if the infinite-size limit is taken [20]. This means that the dynamical model does not correspond to the static one with some fixed "effective" or averaged value of $\bar{J}$, but to a *dynamical convolution* of different values of $\bar{J}$,
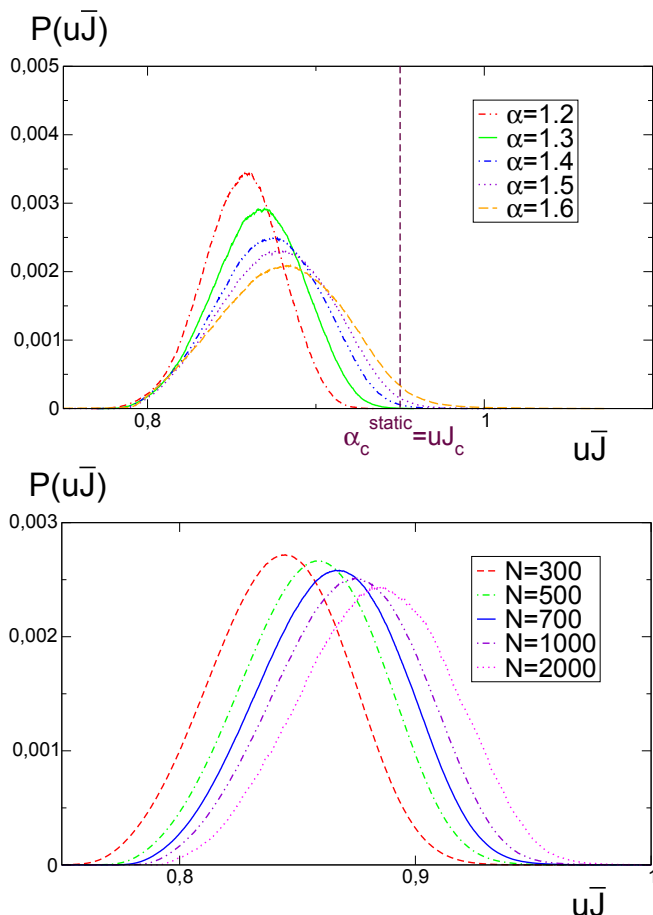
FIGURE 6.3: Top: Probability distribution of $u\bar{J}$ for a system size $N = 1000$ and different values of α. Only for $\alpha > \alpha_c = 1.4(1)$, the right tail of the distribution extends beyond the critical value of the static model $\alpha_c^{static}(N = 1000) = uJ_c = 0.95$. Bottom: $P(u\bar{J})$ at the critical point, $\alpha_c = 1.4$, for different system sizes; the width of the distribution does *not* decay with increasing system size and, therefore, this distribution is *not* delta-peaked in the thermodynamic limit. This reflects the fact that, for sufficiently large values of α the system hovers around the critical point alternating subcritical and supercritical regimes. For smaller values of α the system is always subcritical.

distributed in some interval $[\bar{J}_{min}(\alpha), \bar{J}_{max}(\alpha)]$, with weights given by the distributions above. The probability of finding the system at any point out of such an interval $[\bar{J}_{min}(\alpha), \bar{J}_{max}(\alpha)]$ is zero (within numerical precision).

As illustrated in figure 6.4 we have verified that for $u\langle\bar{J}\rangle > 1$ (which occurs for large values of α; in particular, for $\alpha \to \infty$ when $N \to \infty$ limit), the loading mechanism dominates over the discharging one (synaptic depression), and the potential grows unboundedly with never ceasing activity; this is a non-stationary supercritical or *explosive phase*, analogous to the one reported for the static version of the model.

Finally, we have also computed the average value of J *at spike*, i.e. right
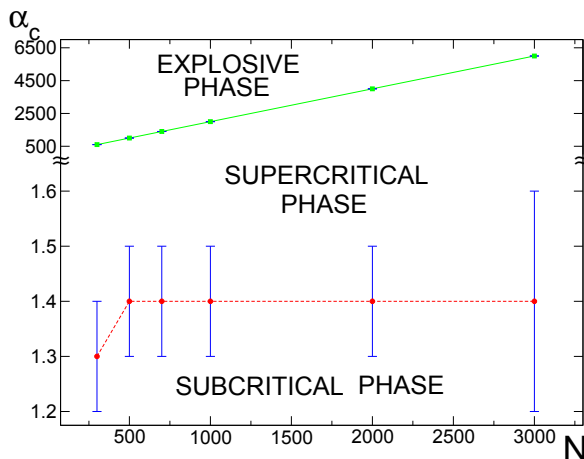
FIGURE 6.4: Phase diagram for the LHG model for different system sizes. Observe the presence of a critical line separating an active (supercritical) from an absorbing (subcritical) phase. Also, for large values of α a non-stationary or "explosive" phase (in which potentials grow unboundedly) exists.

before the corresponding pre-synaptic neuron fires and before the value of J is diminished (see figure 6.5). This quantity, that we call J_{sp}, appears in the analytical approach to be discussed below. Observe in figure 6.5, in analogy with the histograms above, the existence of broad distributions whose width does not decrease significantly upon enlarging system-size. Analyzing the highly non-trivial structure of these (multi-peaked) histograms is beyond the scope of this section, but let us just mention that similar histograms with various peaks appear in related non-conserving model of SOqC [185]. Note also that they extend beyond $uJ_{sp} = 1$, even if their average is close to unity.

6.3.2.2 Characterization of criticality

Perusal of either figure 6.1 or figure 6.3(top) leads to the important observation that it is only for values of α above the critical point ($\alpha_c \approx 1.4$) that the support of the distribution of $u\bar{J}$ extends beyond the (N-dependent) critical point of the static limit, i.e. that $u\bar{J}_{max} \geq \alpha_c^{static}(N)$ (see figure 6.3(up)). For $\alpha < \alpha_c$ the dynamics is subcritical at every time (i.e. $u\bar{J}_{max}(N)$ is always below the threshold of the static model, $\alpha_c^{static}(N)$), and hence avalanche distributions, being a dynamical convolution of avalanches with instantaneous subcritical parameters, are subcritical. Instead, for $\alpha > \alpha_c$, $u\bar{J}_{max} > \alpha_c^{static}(N)$, and one can observe instantaneous values of the average synaptic strength, $\bar{J}$, above the static model
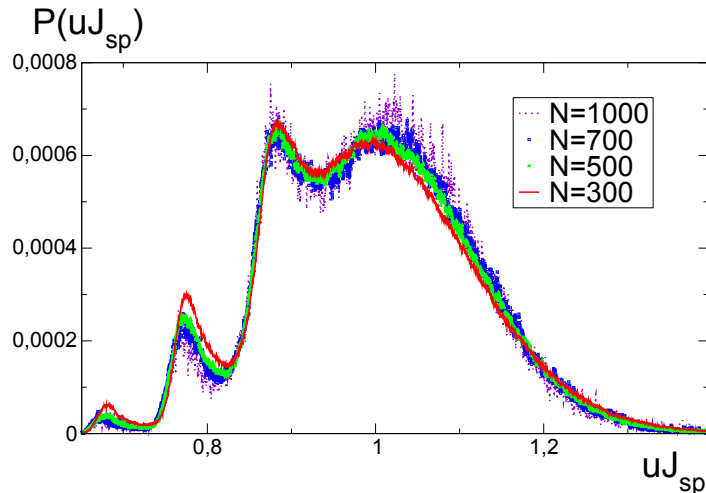
FIGURE 6.5: Probability distribution of values of uJ computed *at spike*, i.e. at their local maxima, just before being depressed. Curves correspond to different system sizes (from 300 to 1000) and fixed α, $\alpha = 4 > \alpha_c$, i.e. in the supercritical phase. Observe the broad distribution, whose width does not decrease significantly upon enlarging system-size. Similar broad histograms, typical of SOqC systems, are obtained for other values of α.

critical point, giving raise to instantaneous super-critical dynamics and system-wide propagation (observe that, in a fully connected topology, any site/neuron can be reached within one time-step). Then, during the avalanche, owing to the term $-uJ_{ij}\delta(t - t_{sp}^j)$ in the second equation of equations (6.3), $u\bar{J}$ decreases, and the system moves progressively from the supercritical regime to the subcritical one. This, in turn, becomes supercritical again upon recovering/loading. This cyclical shifting (analogous to the one for SOqC as described in [20]) provides a dynamical mechanism for the generation of a broad distribution of avalanche sizes in the steady state.

Thus, it is only for $\alpha > \alpha_c$ that arbitrarily large avalanches appear, and *the critical point of the dynamical model corresponds, for any system size, to the value of α for which the maximum of the support of the distribution of values of $\bar{J}$, $\bar{J}_{max}$, coincides with the critical point of the static model:*

$$u\bar{J}_{max} = \alpha_c^{static} = uJ_c. \tag{6.7}$$

figure 6.6(left) illustrates the coincidence (within numerical resolution) of the critical line for the static model, $uJ_c(N)$, and the maximum of the support of the distribution of $\bar{J}$ at the critical point of the dynamical model for various system
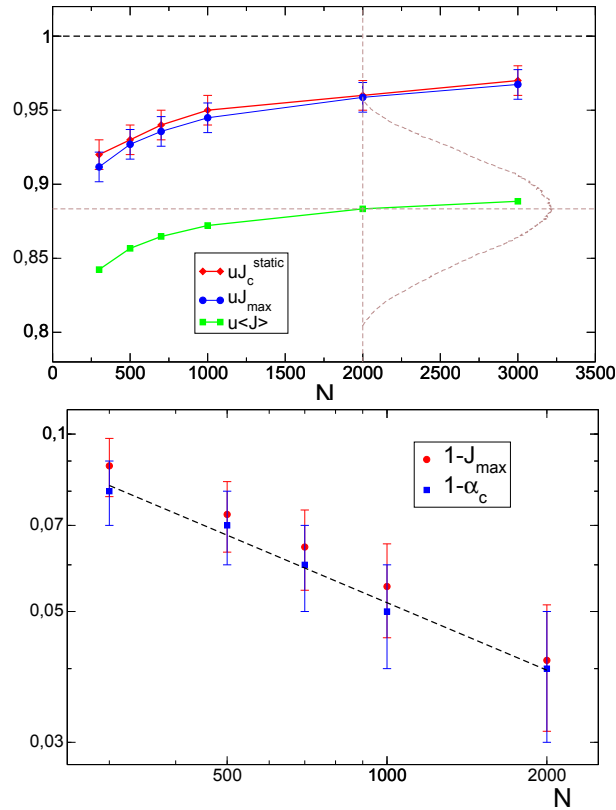
FIGURE 6.6: Top: Critical value of J, J_c, in the static model (upper curve), maximum of the support of the distribution of $\bar{J}$, J_{max}, in the dynamic model (central curve), and average value of $\bar{J}$, i.e. $\langle \bar{J} \rangle$ at the critical point (lower curve). Note that this last curve lies in the subcritical region: $\langle \bar{J} \rangle$ is not equal to 1 at the critical point. The dashed bell-shaped curve represents in a sketchy way the $\bar{J}$-probability distribution for $N = 2000$; its height is unrelated to the x-coordinate in the main graph; the peak is located around 0.88 (in coincidence with the $\langle \bar{J} \rangle$ curve), while the upper tail of the distribution "touches" the vertical line, around 0.95 (i.e. at the corresponding point in the J_{max} curve). Bottom: Scaling of the distance to the infinite-size critical point (i.e. 1) in both the static and the dynamic LHG model as a function of the system size. As predicted by the general theory for non-conserving self-organized models, they both are power-laws with an exponent close to 1/3 (dashed line).

sizes. The small deviation between the two curves stems from the binning procedure employed to determine $\bar{J}_{max}$.

The average value of $\bar{J}$ at the critical point is also plot in figure 6.6(left) for illustration: at criticality, the average value is always far below unity, i.e. far below the conserving limit. Even in the infinite size limit, this curve remains below 1 (as a consequence of the fact that the maximum of the distribution converges to 1 and the distribution is not a delta-function).

Using our numerical estimates of the critical point as a function of N (taken
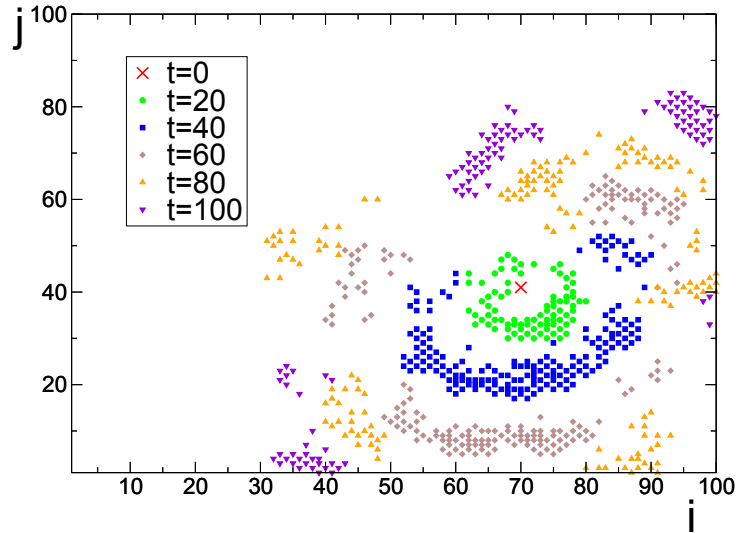
FIGURE 6.7: Propagation of activity as a function of time in a two-dimensional $(100 * 100)$ implementation of the LHG model, for $\alpha = 2$, in the supercritical phase.

from figure 6.6(left)) we have shown (see figure 6.6(right)) that the critical point converges to unity as $1 - u\bar{J}_{max}(N) \sim N^{-0.36(6)}$. The same property holds for the static model, for which we obtain $1 - uJ_c(N)) \sim N^{-0.36(6)}$. This illustrates that the progressive shifting of the distributions in figure 6.3(bottom) to the right occurs at the same pace as that of the critical point of the static model, in such a way that our estimate of the critical point, α_c, is hardly sensitive to finite-size effects: for every studied system size, we obtain $\alpha_c(N) \approx 1.4(1)$ as illustrated in figure 6.4.

Using the absorbing state picture of non-conserving self-organized systems, which predicts scaling to be controlled by a *dynamical percolation* critical point, we made the quantitative prediction that, for generic SOqC systems, the finite-size correction to the critical point should scale with system size as $N^{-1/3}$ (see [20] and Section 5 below). In our case,

$$u\bar{J}_{max}(N \to \infty) - u\bar{J}_{max}(N) \sim N^{-1/3}, \qquad (6.8)$$

in agreement with the numerical estimates (see the dashed line in figure 6.6(right)). This supports the validity of the theoretical framework presented in [20] to account for the present model: the critical behavior of neural avalanches is controlled by a *dynamical percolation* critical point.

Before finishing this section, let us briefly present some results for the LHG

model implemented on different type of topologies. In particular, we have numerically studied a version with a finite connectivity (random neighbors) as well as a two-dimensional lattice. In both cases, we find sub-critical and super-critical phases separated by a critical point, as in the fully connected lattice.

For the random neighbor case, some details, as the way the cut-offs scale with system size, are different, but the main results are as in the fully connected case.

For the two-dimensional lattice, figure 6.7 illustrates the evolution of an avalanche of activity for a particular value of α (in the supercritical regime). Observe the presence of a noisy wave of activity propagating outward from the seed; similar avalanches cannot be visualized in the fully connected case where activity reaches all sites in a single time-step. The waves shown in figure 6.7 resemble very much the ones observed in the retina (which is an almost two-dimensional network) before maturation [186] and, more importantly for the discussion here: they are fully analogous to supercritical waves appearing in

- other non-conserving self-organized systems as forest-fires and

- the dynamical percolation theory in the supercritical regime.

This observation confirms, once again, the very close relationship between the LHG model and the theory of SOqC [20].

In summary, the LHG model is a representative of the class of non-conserving self-organized systems or SOqC, in which, as shown in a previous work [20], exhibits a conventional critical point separating a subcritical from a supercritical phase. Criticality is controlled by the maximum of the support distribution of $\bar{J}$, $\bar{J}_{max}$, and not by its average value. This is in accordance with the general criterion for criticality in SOqC systems put forward in [20]: criticality emerges when the temporarily changing background field, $\bar{J}$, overlaps with the active phase of the underlying (static) absorbing state phase transition [20]. This result is of relevance for the analytical approach in the next section

6.4   Analytical results

The main conclusion of the previous section, i.e. the need to fine tune α to observe true criticality, seems to be in disagreement with the one presented in [19] for the LHG model. There it was claimed, relying on a mean-field calculation, that all

values of α in the interval $[1, \infty[$ are strictly critical. Using the hindsight gained from the results above, it is not difficult to find where the problem lies, as we show in what follows.

Let us first construct (following LHG) a balance equation for the static limit of the model. Calling Δ^{isi} the inter-spike interval (time between two consecutive spikes of *a given neuron*) and Δ^{iai} the inter-avalanche interval (time between two consecutive avalanches, started at *any neuron*), the average number of avalanches between two spikes of the same neuron, $\langle M \rangle$, is

$$\langle M \rangle = \frac{\Delta^{isi}}{\Delta^{iai}}. \tag{6.9}$$

Obviously, Δ^{iai} has to be inversely proportional to I^{ext}: if the external driving is reduced by a factor r the average time to generate an avalanche grows by a factor r. Levina *et al.* [19] actually showed that

$$\Delta^{iai} = \frac{V_{max} - \epsilon(N)}{I^{ext}}, \tag{6.10}$$

where, as above, $\epsilon(N)$ vanishes for $N \to \infty$. Focusing on a single neuron, in the steady state, it must obey the following balance equation

$$V_{max} = \frac{I^{ext}}{N} \Delta^{isi} + \frac{uJ}{N-1} \langle s \rangle \langle M \rangle, \tag{6.11}$$

which equates the potential decrease for each spike (l.h.s. term) to the total potential increase between two consecutive spikes; this comes from two possible sources: (1) the average loading owing to external driving between two consecutive spikes (first term in the r.h.s.) and (2) the average charging from avalanches (second term). Note that $N - 1$ is the number of neighbors of a given neuron and $\langle s \rangle$ is the averaged avalanche size. Fixing $V_{max} = 1$, $\epsilon(N) = 0$, and plugging equation (6.9) and equation (6.10) into equation (6.11), one readily obtains

$$\frac{N}{\Delta^{isi} I^{ext}} \propto uJ \langle s \rangle \tag{6.12}$$

for large values of N.

In the *static case*, $\langle s \rangle$ is given by equation (6.5), so Δ^{isi} can be expressed as a function of J, N and I^{ext}. We have numerically verified that the resulting balance equation holds.

On the other hand, in the *dynamical case*, J is not a constant and we do not

have a simple expression for $\langle s \rangle$. The authors of [19] assume that the average avalanche size can still be written using equation (6.5) but replacing uJ by $u\langle J_{sp} \rangle$. In particular, it is hypothesized that avalanches can be effectively described as static avalanches with an effective branching rate given by the average branching ratio *at spike* (i.e. the synapses which are about to spike are the ones controlling the branching process of activity); this is:

$$\langle s \rangle = \frac{1}{1 - u\langle J_{sp} \rangle}. \tag{6.13}$$

This equality is expected to hold in the infinite system-size limit and for infinitely large avalanches (where the law of large numbers applies) in which case, the average of sampled values of J_{sp} along sufficiently large avalanches can be safely replaced by $\langle J_{sp} \rangle$. In any case, it can be valid for only for branching ratios up to 1 (for which the geometric series converges). Substituting equation (6.13) into equation (6.12) LHG readily obtain

$$u\langle J_{sp} \rangle = \frac{N^2 - \Delta^{isi} I^{ext} N}{N^2 + \Delta^{isi} I^{ext}} \tag{6.14}$$

which, trivially, is smaller or, at most, equal to 1. From this, one concludes that the effective branching process is either subcritical or critical, but cannot be supercritical. Two comments are in order:

The first one is that equation (6.12) is valid if and only if $u\langle J_{sp} \rangle$ is not larger than 1, hence, the calculation above does not exclude the existence of other (supercritical) solutions, for which equation (6.12) would not hold. Actually, as illustrated in the numerics, for any finite system, an exploding phase, with branching ratio larger than unity, does exist (as a mater of fact, given a fixed value of α, depending on how the "loading" constant τ_J is scaled with system size, i.e. depending on how fast is the recovery of synapses, one can shift the location of the critical point and enlarge or reduce the size of the supercritical region).

The second one is as follows: the main approximation of the calculation above is the replacement of the average of sampled values of J_{sp} along any sufficiently large avalanche by $\langle J_{sp} \rangle$. If, during avalanche propagation, the uncovering of values of J_{sp} from $P(J_{sp})$ (which is depicted in figure 6.5 for a particular value of α) occurred in a random, *uncorrelated*, way then the process would be what is called in the literature a "branching process in a random environment" [176]. Such a process turns out to be controlled by the average value of the random branching ratio [176]. In such a case, the calculation would be exact and, for any value of α for which the average branching ratio is unity, the process would be critical.

However, the uncovering of values of J_{sp} in the LHG model exhibits *strong correlations*. J_{sp} fluctuates around the central value $uJ_{sp} = 1$ in a rather correlated way. This is illustrated in figure 6.8, where we plot a return map for of uJ_{sp} averaged along each single avalanche. Notice that the return map is not structureless as would correspond to a random process. Instead, the system is progressively charged towards large values of the synaptic intensity and, afterwards, it gets suddenly discharged, starting a new cycle. In this way, the true dynamics of the system consists of a continuous alternation of supercritical (where most of the J_{sp} take values above 1), and subcritical dynamics: individual avalanches are either subcritical (average branching ratio smaller than 1) or supercritical (average branching ratio above 1), and hence the resulting avalanche-size distribution is a complex one (not a simple power-law). This is illustrated in figure (6.9) which shows the avalanche size distribution for different system sizes and $\alpha = 4$ which lies in the supercritical phase (the rest of parameters are as in figure 6.5). Even if the averages of uJ_{sp} (as calculated from figure 6.5) are very close to 1 for all sizes, the curves in figure 6.5 show a bump at large avalanche-sizes, reflecting the presence of many supercritical avalanches. This effect does not decrease upon increasing system size, even if the bump moves progressively to larger values as the system size is increased. Similarly, correlations are also responsible for the shift from the predicted mean-field critical point $\alpha = 1$ to the actual one $\alpha_c \approx 1.4$.

In conclusion: even if the branching ratio turns out to be always very close to unity for any value of $\alpha \geq \alpha_c$, the avalanche-size distributions are not generically pure power-laws. In the supercritical phase there are bumps revealing its non-truly scale-invariant nature. This conclusion is in agreement with the general scenario for non-conserving self-organized systems introduced in [20].

As a final remark, we want to emphasize that the results by Levina *et al.* are mostly correct: the branching ratio is actually equal to unity in a broad region of parameter space (in the infinitely large system size limit). However, as explained above, this "marginality" of the averaged branching ratio does not exactly correspond generically to true scale invariance.

The main virtue of the LHG model is that, even if not generically critical, it generates a rather broad "pseudo-critical" region, exhibiting partial power-laws. The ultimate reason for this is rooted in the extremely slow loading (recovering) process of the background field (synaptic strength), which occurs during avalanches. This is to be compared with the more abrupt loading in forest-fire and earthquake models, which occurs between avalanches. This more abrupt loading
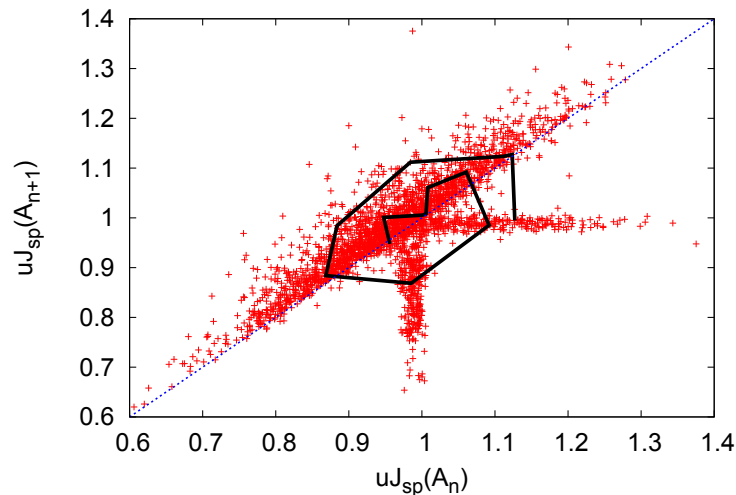
FIGURE 6.8: Return map for uJ_{sp} averaged along two consecutive avalanches A_n and A_{n+1} in the supercritical regime. The broken line joints (clockwise) 20 consecutive points of the map to illustrate the temporal structure of the charging-discharging cycle. The non-trivial structure of the map reflects the presence of strong correlations: the system typically moves up in a few steps along the main diagonal (see the broken line) then, after reaching the supercritical regime $uJ_{sp} > 1$, a large avalanche is produced, and the system returns back to the subcritical regime $uJ_{sp} < 1$, to start a new charging-discharging cycle. The diagonal dashed-line, $uJ_{sp}(A_{n+1}) = uJ_{sp}(A_n)$, is plotted as a guide to the eye.

induces excursions around the critical point to be broader than their counterparts in the LHG model. This is particularly true in the (probably unrealistic) case in which τ_J diverges with system size.

6.5 A simple absorbing-state Langevin equation approach

In order to have a more explicit connection between the LHG model and the family of SOqC models and theory discussed in [20], in this Section we construct a Langevin equation for the LHG model, which includes absorbing states (and is therefore a natural extension of the Langevin theory for SOC, as introduced in [66, 187–191]) and turns out to be almost identical to the general Langevin theory for SOqC systems (as introduced in [20]).

For the sake of simplicity, and without loss of generality, let us consider homogeneous initial conditions for all V_i and $J_{i,j}$, i.e. $V_i = V \ \ \forall i$ and $J_{i,j} = J \ \ \forall i, j$, and
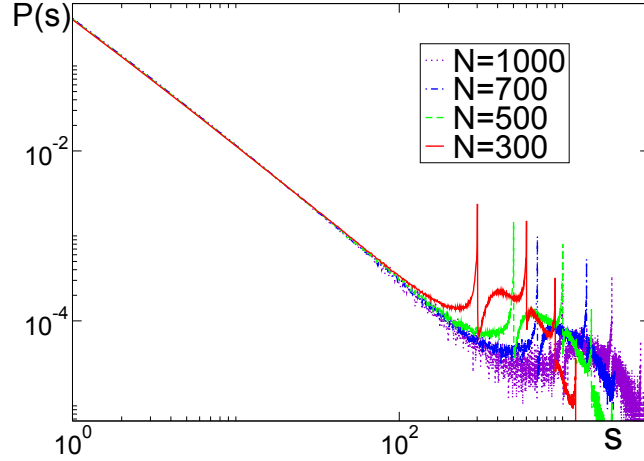
FIGURE 6.9: Avalanche size distribution for $\alpha = 4$ (rest of parameters, as in plots above) and different system sizes (as in figure 6.5) Observe the presence of bumps, which do not disappear by increasing system size. This illustrates the existence of a supercritical phase in the LHG model.

also, $I^{ext} = 0$. Under these conditions, and given the deterministic character of the dynamics, all neurons evolve synchronously and equations (6.3) can be simply rewritten as:

$$\begin{cases} \partial_t V = [uJ - V_{max}]\,\delta(t - t_{sp}) \\ \partial_t J = \dfrac{1}{\tau_J}\left(\dfrac{\alpha}{u} - J\right) - uJ\delta(t - t_{sp}). \end{cases} \tag{6.15}$$

where t_{sp} are the firing times. Let us remark that in order to treat the more general heterogenous case it suffices to keep sub-indexes in the different variables.

The spike terms, proportional to $\delta(t - t_{sp})$, can be alternatively written as

$$\delta(t - t_{sp}) \to \rho \equiv \Theta(V - V_{max}), \tag{6.16}$$

where $\Theta(x)$ is the Heaviside step function (we take the convention $\Theta(0) = 0$); i.e. spike terms operate only whenever the potential is above threshold, implying that the *activity variable*, ρ, is non-zero only in such a case. Thus:

$$\begin{cases} \partial_t V = [uJ - V_{max}]\,\rho \\ \partial_t J = \dfrac{1}{\tau_J}\left(\dfrac{\alpha_J}{u} - J\right) - uJ\rho. \end{cases} \tag{6.17}$$

Further analytical progress can be achieved by regularizing the step-function in equation (6.16) as a hyperbolic-tangent:

$$\rho \approx \frac{1}{2}\left(1 + \tanh\left[\beta\left(V - V_{max}\right)\right]\right), \tag{6.18}$$

which is a good approximation provided that $\beta \gg 1$. Inverting equation (6.18):

$$V = \frac{\text{arctanh}(2\rho - 1) + V_{max}}{\beta} \qquad (6.19)$$

and, taking derivatives on both sides,

$$\partial_t V = \frac{1}{2\beta} \frac{\partial_t \rho}{\rho(1-\rho)}, \qquad (6.20)$$

which is well-defined provided $\rho \in]0, 1[$. Let us underline that the forthcoming equations are also valid at $\rho = 0$, where activity ceases. Using this, equations (6.17) can be rewritten as:

$$\begin{cases} \partial_t \rho = & 2\beta (uJ - V_{max}) \rho^2 (1 - \rho) \\ \partial_t J = & \frac{1}{\tau_J} \left(\frac{\alpha_J}{u} - J \right) - uJ\rho \end{cases} \qquad (6.21)$$

which, omitting higher order terms, reduces to:

$$\begin{cases} \partial_t \rho = & 2\beta uJ\rho^2 - 2\beta V_{max}\rho^2 \\ \partial_t J = & \frac{1}{\tau_J} \left(\frac{\alpha_J}{u} - J \right) - uJ\rho. \end{cases} \qquad (6.22)$$

Renaming variables as: $2\beta V_{max} \to b$, $2\beta u \to w$, $J \to \phi$, $\frac{1}{\tau_J} \to \gamma$, $\alpha_J/u \to \phi_c$, and $u \to w_2$, one obtains:

$$\begin{cases} \partial_t \rho = & w\phi\rho^2 - b\rho^2 \\ \partial_t \phi = & \gamma (\phi_c - \phi) - w_2\phi\rho. \end{cases} \qquad (6.23)$$

The equation for ρ is a typical mean-field equation for a system with absorbing states (i.e. all dynamics ceases when $\rho = 0$). It includes a coupling term with the background field ϕ: the larger the background the more activity is created. In the simplest possible theory of SOqC (see [20]), such a coupling is linear in ρ, but the effect of both types of coupling can be argued to be qualitatively identical. On the other hand, the second equation is identical to the mean-field background equation for SOqC systems: the presence of activity reduces the background field while the loading mechanism, acting independently of activity, increases it.

Except for the coupling term which is quadratic in ρ, these mean-field equations are identical to the ones proposed in [20] to describe non-conserving self-organized models at a mean-field level. Also, in analogy with SOqC systems, when slow driving is switched on, i.e. $I^{ext} \neq 0$, activity can be spontaneously created, even

if $\rho = 0$, generating avalanches of activity. Moreover, if some sort of stochasticity (and hence heterogeneity) is introduced into the dynamics, then it can be easily seen that:

- a noise term, proportional to $\sqrt{\rho}$, needs to be added to the first equation,

- a diffusion term accounting for the coupling with nearest neighbors, and

- a linear-coupling term is perturbatively generated in the activity equation (and, thus, the quadratic-coupling becomes a higher order term).

Therefore, after including fluctuations and omitting higher order terms, the final set of stochastic equations that we have derived is identical to the one of *dynamical percolation* [192] in the presence of a "loading mechanism", i.e. to that of SOqC systems as described in [20].

This heuristic mapping between the LHG model and the general theory of SOqC, justifies from an analytical viewpoint all the findings in previous sections (including the quantitative prediction for the finite-size scaling of $(1 - uJ_{max}(N))$) and firmly places the LHG model in the class of self-organized quasi-critical models, lacking true generic scale-invariance.

6.6 Synchronization and oscillatory properties

Synchronization was studied in the self-organized criticality literature as a possible mechanism, alternative to conserving dynamics, leading to generic scale invariance [93, 193]. Even though such a suggestion turned out not to be true [20], let us explore here the oscillatory and synchronization properties observed in numerical simulations of the LHG model. With this aim, we compute the power-spectra, $S(f)$, for the time series of J shown in figure 6.1 (as well as for other values of α). In all cases, as illustrated in figure 6.10, the spectra exhibit peaks at some characteristic frequencies, f. Closer inspection reveals that the maximum peak appears at a characteristic frequency, f_c, which we have verified to be inversely proportional to $\langle \Delta^{isi} \rangle$. This indicates that the typical time needed for a neuron to overcome threshold and spike again introduces a characteristic scale into the system, entailing periodicity. Observe also that the power-spectra exhibit fat tails, with exponent k^{-2}, characteristic of sawtooth profiles with linear increases.
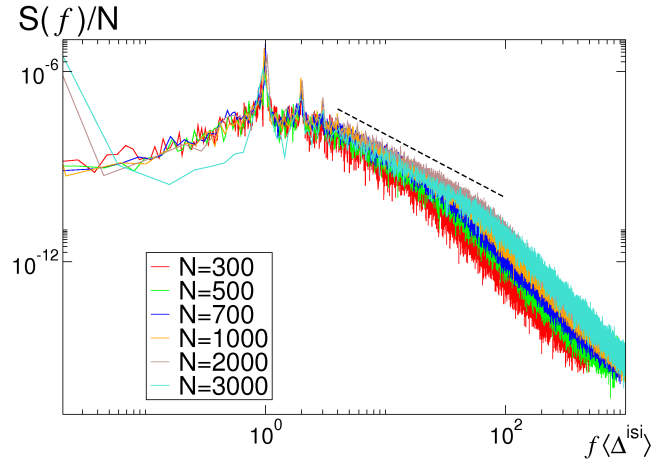
FIGURE 6.10: Power spectrum of the LHG model for $\alpha = 2$ (i.e. supercritical). Frequencies f are plotted rescaled by a factor $\langle \Delta^{isi} \rangle$. Note the presence of peaks, at $f \propto \langle \Delta^{isi} \rangle^{-1}$, coexisting with fat tails. The tail decay k^{-2} (dashed line) is characteristic of sawtooth profiles (*i.e.* with linear increases).

The previous numerical analysis can also be done for the static model, with almost identical results: the origin of the periodic behavior lies in the charging/discharging cycle of potentials, V, and is not crucially affected by the synaptic strengths being fixed or not.

Given that individual neurons oscillate with a certain periodicity, let us study (in analogy with other analyses of non-conserving self-organized systems) the synchronization (or absence of it) between different units (either neurons or synapses).

In order to quantify synchronization, we use bins of size $2 \cdot 10^{-7}$ (for V) and 10^{-6} (for J), and consider as an order parameter the fraction of neurons/synapses which are synchronized, i.e. which lie in the same discrete bin, divided by the number of occupied bins. Such a parameter becomes arbitrarily small for a large enough random system and is 1 in the case of perfect synchronization. If the total number of elements into a multiply occupied bin is N_s and the number of bins is N_b, the value of the synchronization order parameter, ϕ, is

$$\phi_V \sim \frac{N_s/N}{N_b} \qquad\qquad \phi_J \sim \frac{N_s/N(N-1)}{N_b} \qquad\qquad (6.24)$$

for neurons (V) and synapses (J), respectively. By monitoring ϕ_V, we observe that the potentials in the system converge to a totally un-synchronized state ($\phi_V \sim 10^{-5}$). This is in agreement with the uniform distribution of values of V employed in analytical arguments above.

On the other hand, by measuring ϕ_J we observe that it rapidly converges to a

stationary state value, $N_b = N$, reflecting a perfect synchronization of the different synapses of any given neuron, j, i.e. $J_{ij} = J_{kj}$ for any values of i and k: *all the synapses J_{ij} emerging from of a given (pre-synaptic) neuron, j, converge to a common state.* This can be easily understood using the following argument. The dynamics of J_{ij} and $J_{k,j}$ are controlled by the same equation

$$\frac{\partial J_{l,j}}{\partial t} = \frac{1}{\tau_J}\left(\frac{\alpha}{u} - J_{l,j}\right) - uJ_{l,j}\eta(t),\tag{6.25}$$

where l is either i or k and $\eta(t)$ is a (positive) noise, accounting for the spikes of (pre-synaptic) neuron j, which is obviously common to all synapses of j. Subtracting equation (6.25) for k from equation (6.25) for i we obtain that the difference, $\Delta = J_{ij} - J_{kj}$ evolves as

$$\frac{\partial \Delta}{\partial t} = -\Delta[\frac{1}{\tau_J} + u\eta(t)],\tag{6.26}$$

which, given the positivity of τ_J, u and η, entails a negative Lyapunov exponent and, hence, convergence to the synchronous state, $J_{i,j} = J_{k,j}$ – *i.e.* all synapses emerging from a given pre-synaptic neuron synchronize. Observe that this type of synchronization is similar (but not identical) to that observed in, for instance, earthquake models [93, 193].

6.7   Conclusions

Cortical avalanches, first observed by Beggs and Plenz [6, 8], were claimed to be genically power-law distributed and, thus, critical. Such a claim led to an outburst of activity in Neuroscience trying to understand the origin and consequences of such a generic scale-invariance. At a theoretical level, Levina, Herrmann, and Geisel [19] proposed a simple model (a variation of the Markram-Tsodyks model for chemical synapses), claimed to reproduce genically scale-invariance. In particular, these authors performed a mean-field calculation leading to the conclusion that, for any value of the control parameter, α, larger than unity, generic critical behavior is observed. They also conducted some computational studies to support their findings.

The LHG model turns out to be very similar to slowly driven models of self-organized criticality such as earthquake and forest-fire models. As in these other models, and in contrast to sandpiles, in the LHG one the dynamics is *non-conserving* (reflecting the leaking/dissipative dynamics of actual synaptic signal

transmission).

It is by now a well-established fact that non-conserving self-organized models are not generically critical but just "hover around" the critical point of an underlying absorbing phase transition, with finite excursions (of tunable amplitude) into the active and the absorbing phases. As they do not converge to the critical point itself, generic scale-invariance cannot be invoked (see [20] and references therein). The term self-organized quasi criticality (SOqC) has been proposed to refer to such a class of systems, emphasizing the differences with conserving SOC models.

Given the contradiction between this general result and the claim in [19], in this chapter we have scrutinized the LHG model, both numerically and analytically, and reached the following conclusions:

- Both in its static and its dynamical form, the model exhibits absorbing and active phases and a non-trivial critical point separating both of them.

- It is only if parameters are fine tuned to such a critical point that true scale-invariance emerges and the distribution of avalanche-sizes is power-law distributed.

- The mean-field calculation in [19], supporting generic criticality, lead indeed to a branching ratio equal to unity in a broad interval of phase space, but this does not imply generic scale-invariance.

- A Langevin equation, including absorbing states, has been derived for the LHG model. Such an equation reduces to the analogous one proposed to describe generically non-conserving self-organized (SOqC) models. Thus, all the general conclusions obtained from such a theory in [20] apply to the LHG model, providing analytical support to the numerical findings above.

It is worth stressing that our results do not subtract merit from the LHG model. Actually, strict criticality might not be required to explain the truncated power-laws reported by Beggs and Plenz; the dynamical LHG model generates partial power-laws compatible with the empirical findings by Beggs and Plenz for a relatively broad parameter (α) interval, as shown in figure 6.11. Moreover, the fact that the model can generate critical, subcritical, and supercritical regimes, depending on parameter values, converts the LHG model into an adequate one to describe the *state-of-the-art in neuronal avalanches*. As mentioned in the Introduction, Pasquale *et al.* have shown in a recent paper [179] that, depending on
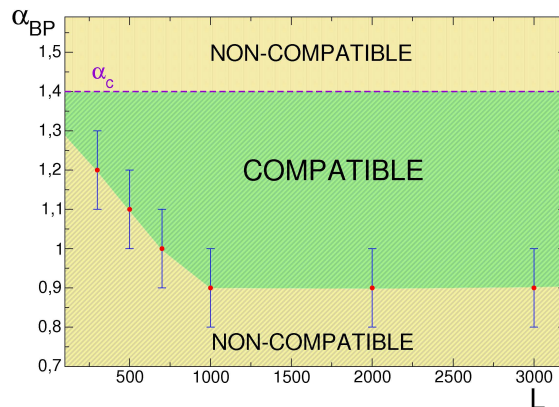
FIGURE 6.11: Range of compatibility between the results of the LHG model, for different values of N, and the empirical results by Beggs and Plenz; for large system sizes ($N > 700$) values of α between 1 and 1.4 give avalanche-size distributions compatible with those observed by Beggs and Plenz [6, 8], even if they are subcritical.

several experimental features, cortical avalanches can indeed be either critical, subcritical, or supercritical.

The main implication of our work can be summarized as follows: if future experimental research conducted on cortical networks were to support that critical avalanches are the norm and not the exception, then, one should look for more elaborate theories, beyond simple self-organization, to explain this. Standard self-organization does not suffice to explain criticality in non-conserving systems. Parameters have to be tuned or "selected" to achieve a close-to-criticality regime. For instance, the claim by Royer and Paré [181] that homeostatic regulation mechanisms keep cortical neural networks with an approximately constant (i.e. *conserved*) global synaptic strength could be at the basis of such a less generic theory beyond simple self-organization. Another inspiring possibility is that natural selection by means of evolutionary and adaptive processes leads to parameter selection, favoring critical or close-to-critical propagation of information in the cortex [180]. A more realistic approach should also include long-term plasticity [194], as well as co-evolutionary mechanisms, shaping the network topology. We shall explore these possibilities in a future work.

Chapter 7

Enhancing neural-network performance via assortativity

The performance of attractor neural networks has been shown to depend crucially on the heterogeneity of the underlying topology. In this chapter we take this analysis a step further by examining the effect of degree-degree correlations – or assortativity – on neural-network behavior. We make use of a method recently put forward for studying correlated networks and dynamics thereon, both analytically and computationally, which is independent of how the topology may have evolved. We show how the robustness to noise is greatly enhanced in assortative (positively correlated) neural networks, especially if it is the hub neurons that store the information.

7.1 Introduction

For a dozen years or so now, the study of complex systems has been heavily influenced by results from network science – which one might regard as the fusion of graph theory with statistical physics [58, 69]. Phenomena as diverse as epidemics [76], cellular function [195], power-grid failures [196] or internet routing [197], among many others [61], depend crucially on the structure of the underlying network of interactions. One of the earliest systems to have been described as a network was the brain, which is made up of a great many neurons connected to each other by synapses [82, 115, 198]. Mathematically, the first neural networks combined the Ising model [62] with the Hebb learning rule [18] to reproduce, very

successfully, the storage and retrieval of information [110, 115, 121]. Neurons were simplified to binary variables (like Ising spins) representing firing or non-firing cells. By considering the trivial fully-connected topology, exact solutions could be reached, which at the time seemed more important than attempting to introduce biological realism. Subsequent work has tended to focus on considering richer dynamics for cells rather than on the way in which these are interconnected [199–201]. However, the topology of the brain – whether at the level of neurons and synapses, cortical areas or functional connections – is obviously far from trivial [4, 23, 24, 57, 74].

The number of neighbors a given node in a network has is called its degree, and much attention is paid to degree distributions since they tend to be highly heterogeneous for most real networks. In fact, they are often approximately scale-free (i.e., described by power laws) [58, 69, 112, 202]. By including this topological feature in a Hopfield-like neural-network model, Torres *et al.* [25] found that degree heterogeneity increases the system's performance at high levels of noise, since the hubs (high degree nodes) are able to retain information at levels well above the usual critical noise. To prove this analytically, the authors considered the *configurational ensemble* of networks (the set of random networks with a given degree distribution but no degree-degree correlations) and showed that Monte Carlo (MC) simulations were in good agreement with mean-field analysis, despite the approximation inherent to the latter technique when the network is not fully connected. A similar approach can also be used to show how heterogeneity may be advantageous for the performance of certain tasks in models with a richer dynamics [164]. It is worth mentioning that this influence of the degree distribution on dynamical behavior is found in many other settings, such as the more general situation of systems of coupled oscillators [203].

Another property of empirical networks that is quite ubiquitous is the existence of correlations between the degrees of nodes and those of their neighbors [204, 205]. If the average degree-degree correlation is positive the network is said to be *assortative*, while it is called *disassortative* if negatively correlated. Most heterogeneous networks are disassortative [58], which seems to be because this is in some sense their equilibrium (maximum entropy) state given the constraints imposed by the degree distribution [26]. However, there are probably often mechanisms at work which drive systems from equilibrium by inducing different correlations, as appears to be the case for most social networks, in which nodes (people) of a kind tend to group together. This feature, known as *assortativity* or *mixing by degree*,

is also relevant for processes taking place on networks. For instance, assortative networks have lower percolation thresholds and are more robust to targeted attack [205], while disassortative ones make for more stable ecosystems and are – at least according to the usual definition – more synchronizable [206].

The approach usually taken when studying correlated networks computationally is to generate a network from the configuration ensemble and then introduce correlations (positive or negative) by some stochastic rewiring process [207]. A drawback of this method, however, is that results may well then depend on the details of this mechanism: there is no guarantee that one is correctly sampling the phase space of networks with given correlations. For analytical work, some kind of hidden variables from which the correlations originate are often considered [208–211] – an assumption which can also be used to generate correlated networks computationally [210]. This can be a very powerful method for solving specific network models. However, it may not be appropriate if one wishes to consider all possible networks with given degree-degree correlations, independently of how these may have arisen. Here we get round this problem by making use of a method recently suggested by Johnson *et al.* [26] whereby the ensemble of all networks with given correlations can be considered theoretically without recurring to hidden variables. Furthermore, we show how this approach can be used computationally to generate random networks that are representative of the ensemble of interest (i.e., they are model-independent). In this way, we study the effect of correlations on a simple neural network model and find that assortativity increases performance in the face of noise – particularly if it is the hubs that are mainly responsible for storing information (and it is worth mentioning that there is experimental evidence suggestive of a main functional role played by hub neurons in the brain [212, 213]). The good agreement between the mean-field analysis and our MC simulations bears witness both to the robustness of the results as regards neural systems, and to the viability of using this method for studying dynamics on correlated networks.

7.2 Preliminary considerations

7.2.1 Model neurons on networks

The attractor neural network model put forward by Hopfield [110] consists of N binary neurons, each with an activity given by the dynamic variable $s_i = \pm 1$. Every time step (MCS), each neuron is updated according to the stochastic transition probability $P(s_i \to \pm 1) = \frac{1}{2}\left[1 \pm \tanh\left(h_i(\vec{S})/T\right)\right]$ (parallel dynamics), where the field $h_i(\vec{S})$ is the combined effect on i of all its neighbors, $h_i(\vec{S}) = \sum_j \hat{w}_{ij}s_j$, and T is a noise parameter we shall call *temperature*, but which represents any kind of random fluctuations in the environment. This is the same as the Ising model for magnetic systems, and the transition rule can be derived from a simple interaction energy such that aligned variables s (spins) contribute less energy than if they were to take opposite values. However, this system can store P given configurations (*memory patterns*) $\xi_i^\nu = \pm 1$ by having the interaction strengths (*synaptic weights*) set according to the Hebb rule [18]: $\hat{w}_{ij} \propto \sum_{\nu=1}^P \xi_i^\nu \xi_j^\nu$. In this way, each pattern becomes an attractor of the dynamics, and the system will evolve towards whichever one is closest to the initial state it is placed in. This mechanism is called *associative memory*, and is nowadays used routinely for tasks such as image identification. What is more, it has been established that something similar to the Hebb rule is implemented in nature via the processes of long-term potentiation and depression at the synapses [214], and this phenomenon is indeed required for learning [120].

To take into account the topology of the network, we shall consider the weights to be of the form $\hat{w}_{ij} = \hat{\omega}_{ij}\hat{a}_{ij}$, where the element $\hat{a}_{ij}$ of the adjacency matrix represents the number of directed edges (usually interpreted as synapses in a neural network) from node j to node i, while $\hat{\omega}$ stores the patterns, as before:

$$\hat{\omega}_{ij} = \frac{1}{\langle k \rangle} \sum_{\nu=1}^P \xi_i^\nu \xi_j^\nu.$$

For the sake of coherence with previous work, we shall assume $\hat{a}$ to be symmetric (i.e., the network is undirected), so each node is characterized by a single degree $k_i = \sum_j \hat{a}_{ij}$. However, all results are easily extended to directed networks – in which nodes have both an *in* degree, $k_i^{\text{in}} = \sum_j \hat{a}_{ij}$, and an *out* degree, $k_i^{\text{out}} = \sum_j \hat{a}_{ji}$ – by bearing in mind it is only a neuron's pre-synaptic neighbors that

influence its behavior. The mean degree of the network is $\langle k \rangle$, where the angles stand for an average over nodes: $\langle \cdot \rangle \equiv N^{-1} \sum_i (\cdot)$ [1].

7.2.2   Network ensembles

When one wishes to consider a set of networks which are randomly wired while respecting certain constraints – that is, an *ensemble* – it is usually useful to define the expected value of the adjacency matrix, $E(\hat{a}) \equiv \hat{\epsilon}$ [2]. The element $\hat{\epsilon}_{ij}$ of this matrix is the mean value of $\hat{a}_{ij}$ obtained by averaging over the ensemble. For instance, in the Erdős-Rényi (ER) ensemble all elements (outside the diagonal) take the value $\hat{\epsilon}_{ij}^{ER} = \langle k \rangle / N$, which is the probability that a given pair of nodes be connected by an edge. For studying networks with a given degree sequence, $(k_1, ... k_N)$, it is common to assume the *configuration ensemble*, defined as

$$\epsilon_{ij}^{conf} = \frac{k_i k_j}{\langle k \rangle N}$$

This expression can usually be applied also when the constraint is a given degree distribution, $p(k)$, by integrating over $p(k_i)$ and $p(k_j)$ where appropriate. One way of deriving $\hat{\epsilon}^{conf}$ is to assume one has k_i dangling half-edges at each node i; we then randomly choose pairs of half-edges and join them together until the network is wired up. Each time we do this, the probability that we join i to j is $k_i k_j / (\langle k \rangle N)^2$, and we must perform the operation $\langle k \rangle N$ times. Bianconi showed that this is also the solution for Barabási-Albert evolved networks [215]. However, we should bear in mind that this result is only strictly valid for networks constructed in certain particular ways, such as in these examples. It is often implicitly assumed that were we to average over all random networks with a given degree distribution, the mean adjacency matrix obtained would be $\hat{\epsilon}^{conf}$. As we shall see, however, this is not necessarily the case [26].

---

[1]In directed networks the mean *in* degree and the mean *out* degree necessarily coincide, whatever the forms of the *in* and *out* distributions.

[2]As in statistical physics, one can consider the *microcanonical* ensemble, in which each element (network) satisfies the constraints exactly, or the *canonical* ensemble, where the constraints are satisfied on average [215]. Throughout this work, we shall refer to canonical ensembles.
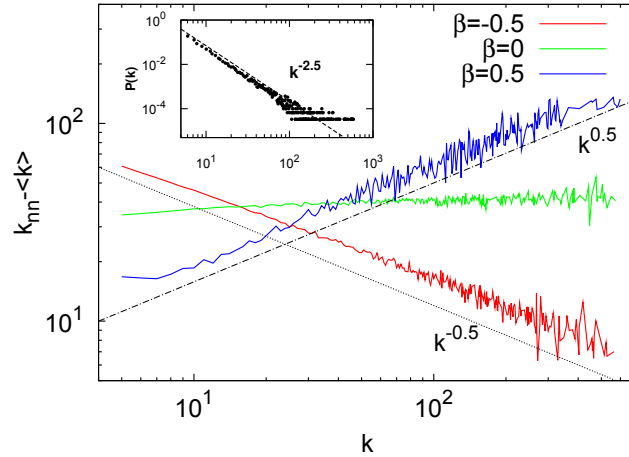
FIGURE 7.1: Mean-nearest-neighbor functions $\overline{k}_{nn}(k)$ for scale-free networks with $\beta = -0.5$ (disassortative), 0.0 (neutral), and 0.5 assortative, generated according to the algorithm described in section 7.3.2. Inset: degree distribution (the same in all three cases). Other parameters are $\gamma = 2.5$, $\langle k \rangle = 12.5$, $N = 10^4$.

7.2.3 Correlated networks

In the configuration ensemble, the expected value of the mean degree of the neighbors of a given node is $\overline{k}_{nn,i} = k_i^{-1} \sum_j \hat{\epsilon}_{ij}^{conf} k_j = \langle k^2 \rangle / \langle k \rangle$, which is independent of k_i. However, as mentioned above, real networks often display degree-degree correlations, with the result that $\overline{k}_{nn,i} = \overline{k}_{nn}(k_i)$. If $\overline{k}_{nn}(k)$ increases with k, the network is said to be assortative – whereas it is disassortative if it decreases with k (see figure 7.1). This is from the more general nomenclature (borrowed form sociology) in which sets are assortative if elements of a kind group together, or assort. In the case of degree-degree correlated networks, positive assortativity means that edges are more than randomly likely to occur between nodes of a similar degree. A popular measure of this phenomenon is Pearson's coefficient applied to the edges [58, 69, 205]: $r = ([k_l k_l'] - [k_l]^2)/([k_l^2] - [k_l]^2)$, where k_l and k_l' are the degrees of each of the two nodes belonging to edge l, and $[\cdot] \equiv (\langle k \rangle N)^{-1} \sum_l (\cdot)$ is an average over edges.

The ensemble of all networks with a given degree sequence $(k_1, ... k_N)$ contains a subset for all members of which $\overline{k}_{nn}(k)$ is constant (the configuration ensemble), but also subsets displaying other functions $\overline{k}_{nn}(k)$. We can identify each one of these subsets (regions of phase space) with an expected adjacency matrix $\hat{\epsilon}$ which simultaneously satisfies the following conditions: **i)** $\sum_j k_j \hat{\epsilon}_{ij} = k_i \overline{k}_{nn}(k_i)$, $\forall i$ (by definition of $\overline{k}_{nn}(k)$), and **ii)** $\sum_j \hat{\epsilon}_{ij} = k_i$, $\forall i$ (for consistency). An ansatz which

fulfills these requirements is any matrix of the form

$$\hat{\epsilon}_{ij} = \frac{k_i k_j}{\langle k \rangle N} + \int d\nu \frac{f(\nu)}{N} \left[\frac{(k_i k_j)^\nu}{\langle k^\nu \rangle} - k_i^\nu - k_j^\nu + \langle k^\nu \rangle \right], \tag{7.1}$$

where $\nu \in \mathbb{R}$ and the function $f(\nu)$ is in general arbitrary [26]. (If the network were directed, then $k_i = k_i^{\text{in}}$ and $k_j = k_j^{\text{out}}$ in this expression.) This ansatz yields

$$\overline{k}_{nn}(k) = \frac{\langle k^2 \rangle}{\langle k \rangle} + \int d\nu f(\nu) \sigma_{\nu+1} \left[\frac{k^{\nu-1}}{\langle k^\nu \rangle} - \frac{1}{k} \right] \tag{7.2}$$

(the first term being the result for the configuration ensemble), where $\sigma_{b+1} \equiv \langle k^{b+1} \rangle - \langle k \rangle \langle k^b \rangle$. To prove the uniqueness of a matrix $\hat{\epsilon}$ obtained in this way (i.e., that it is the only one compatible with a given $\overline{k}_{nn}(k)$) assume that there exists another valid matrix $\hat{\epsilon}' \neq \hat{\epsilon}$. Writing $\hat{\epsilon}'_{ij} - \hat{\epsilon}_{ij} \equiv h(k_i, k_j) = h_{ij}$, then Condition **i)** implies that $\sum_j k_j h_{ij} = 0$, $\forall i$, while Condition **ii)** means that $\sum_j h_{ij} = 0$, $\forall i$. It follows that $h_{ij} = 0$, $\forall i, j$. This means that $\hat{\epsilon}$ is not just one possible way of obtaining correlations according to $\overline{k}_{nn}(k)$; rather, there is a two-way mapping between $\hat{\epsilon}$ and $\overline{k}_{nn}(k)$: every network with this particular function $\overline{k}_{nn}(k)$ and no other ones are contained in the ensemble defined by $\hat{\epsilon}$. Thanks to this, if we are able to consider random networks drawn according to this matrix (whether we do this analytically or computationally; see section 7.3.2), we can be confident that we are correctly taking account of the whole ensemble of interest. In other words, whatever the reasons behind the existence of degree-degree correlations in a given network, we can study the effects of these with only information on $p(k)$ and $\overline{k}_{nn}(k)$ by obtaining the associated matrix $\hat{\epsilon}$. This is not to say, of course, that all topological properties are captured in this way: a particular network may have other features – such as higher order correlations, modularity, etc. – the consideration of which would require concentrating on a sub-partition of those with the same $p(k)$ and $\overline{k}_{nn}(k)$. But this is not our purpose here.

In many empirical networks, $\overline{k}_{nn}(k)$ has the form $\overline{k}_{nn}(k) = A + Bk^\beta$, with $A, B > 0$ [69, 204] – the mixing being assortative if β is positive, and disassortative when negative. Such a case is fitted by equation (7.2) if

$$f(\nu) = C \left[\frac{\sigma_2}{\sigma_{\beta+2}} \delta(\nu - \beta - 1) - \delta(\nu - 1) \right], \tag{7.3}$$

with C a positive constant, since this choice yields

$$\overline{k}_{nn}(k) = \frac{\langle k^2 \rangle}{\langle k \rangle} + C\sigma_2 \left[\frac{k^\beta}{\langle k^{\beta+1} \rangle} - \frac{1}{\langle k \rangle} \right]. \tag{7.4}$$

Johnson *et al.* [26] obtained the entropy of ensembles of networks with scale-free degree distributions ($p(k) \sim k^{-\gamma}$) and correlations given by equation (7.4), and found that the most likely configurations (those maximizing the entropy) generally correspond to correlated networks. In particular, the expected mixing, all other things being equal, is usually a certain degree of disassortativity – which explains the predominance of these networks in the real world. They also showed that the maximum entropy is usually obtained for values of C close to one. Here, we shall use this result to justify concentrating on correlated networks with $C = 1$, so that the only parameter we need to take into account is β. It is worth mentioning that Pastor-Satorras *et al.* originally suggested using this exponent as a way of quantifying correlations [204], since this seems to be the most relevant magnitude. Because β does not depend directly on $p(k)$ (as r does), and can be defined for networks of any size (whereas r, in very heterogeneous networks, always goes to zero for large N due to its normalization [216]), we shall henceforth use β as our assortativity parameter.

So, after plugging equation (7.3) into equation (7.1), we find that the ensemble of networks exhibiting correlations given by equation (7.4) (and $C = 1$) is defined by the mean adjacency matrix

$$\begin{aligned}
\hat{\epsilon}_{ij} &= \frac{1}{N}[k_i + k_j - \langle k \rangle] \\
&+ \frac{\sigma_2}{\sigma_{\beta+2}} \frac{1}{N} \left[\frac{(k_i k_j)^{\beta+1}}{\langle k^{\beta+1} \rangle} - k_i^{\beta+1} - k_j^{\beta+1} + \langle k^{\beta+1} \rangle \right].
\end{aligned} \tag{7.5}$$

7.3 Analysis and results

7.3.1 Mean field

Let us consider the single-pattern case ($P = 1$, $\xi_i = \xi_i^1$). Substituting the adjacency matrix $\hat{a}$ for its expected value $\hat{\epsilon}$ (as given by equation (7.5)) in the expression

for the local field at i – which amounts to a mean-field approximation – we have

$$
\begin{aligned}
h_i(\vec{S}) &= \frac{1}{\langle k \rangle} \xi_i \left\{ \left[(k_i - \langle k \rangle) + \frac{\sigma_2}{\sigma_{\beta+2}} (\langle k^{\beta+1} \rangle - k_i^{\beta+1}) \right] \mu_0 \right. \\
&+ \left. \langle k \rangle \mu_1 + \frac{\sigma_2}{\sigma_{\beta+2}} (k_i^{\beta} - \langle k^{\beta+1} \rangle) \mu_{\beta+1} \right\},
\end{aligned}
$$

where we have defined

$$
\mu_\alpha \equiv \frac{\langle k_i^\alpha \xi_i s_i \rangle}{\langle k^\alpha \rangle}
$$

for $\alpha = 0, 1, \beta+1$. These order parameters measure the extent to which the system is able to recall information in spite of noise [164]. For the first order we have $\mu_0 = m \equiv \langle \xi_i s_i \rangle$, the standard overlap measure in neural networks (analogous to magnetization in magnetic systems), which takes account of memory performance. However, μ_1, for instance, weighs the sum with the degree of each node, with the result that it measures information per synapse instead of per neuron. Although the overlap m is often assumed to represent, in some sense, the *mean firing rate* of neurological experiments, it is possible that μ_1 is more closely related to the empirical measure, since the total electric potential in an area of tissue is likely to depend on the number of synapses transmitting action potentials. In any case, a comparison between the two order parameters is a good way of assessing to what extent the performance of neurons depends on their degree – larger-degree model neurons can in general store information at higher temperatures than ones with smaller degree can [25].

Substituting s_i for its expected value according to the transition probability, $s_i \to \tanh(h_i(\vec{S})/T)$, we have, for any α,

$$
\langle k_i^\alpha \xi_i s_i \rangle = \langle k_i^\alpha \xi_i \tanh(h_i(\vec{S})/T) \rangle;
$$

or, equivalently, the following 3-D map of closed coupled equations for the macroscopic overlap observables μ_0, μ_1 and $\mu_{\beta+1}$ – which describes, in this mean-field approximation, the dynamics of the system:

$$
\begin{aligned}
\mu_0(t+1) &= \int p(k) \tanh[F(t)/(\langle k \rangle T)] \mathrm{d}k \\
\mu_1(t+1) &= \frac{1}{\langle k \rangle} \int p(k) k \tanh[F(t)/(\langle k \rangle T)] \mathrm{d}k \qquad (7.6) \\
\mu_{\beta+1}(t+1) &= \frac{1}{\langle k^{\beta+1} \rangle} \int p(k) k^{\beta+1} \tanh[F(t)/(\langle k \rangle T)] \mathrm{d}k,
\end{aligned}
$$

with

$$
\begin{aligned}
F(t) \equiv{}& (k\mu_0(t) + \langle k \rangle \mu_1(t) - \langle k \rangle \mu_0(t)) \\
&+ \frac{\sigma_2}{\sigma_{\beta+2}}[k^{\beta+1}(\mu_{\beta+1}(t) - \mu_0(t)) \\
&+ \langle k^{\beta+1} \rangle (\mu_0(t) - \mu_{\beta+1}(t))].
\end{aligned}
$$

This can be easily computed for any degree distribution $p(k)$. Note that taking $\beta = 0$ (the uncorrelated case) the system collapses to the 2-D map obtained in Ref. [25], while it becomes the typical 1-D case for a homogeneous $p(k)$ – say a fully-connected network [110]. It is in principle possible to do similar mean-field analysis for any number P of patterns, but the map would then be $3P$-dimensional, making the problem substantially more complex.

At a critical temperature T_c, the system will undergo the characteristic second order phase transition from a phase in which it exhibits memory (akin to ferromagnetism) to one in which it does not (paramagnetism). To obtain this critical temperature, we can expand the hyperbolic tangent in equations (7.6) around the trivial solution $(\mu_0, \mu_1, \mu_{\beta+1}) \simeq (0, 0, 0)$ and, keeping only linear terms, write

$$
\begin{aligned}
\mu_0 ={}& \mu_1/T_c, \\
\mu_1 ={}& \frac{1}{\langle k \rangle^2 T_c} \left[\langle k \rangle^2 \mu_1 + \sigma_2 \mu_{\beta+1} \right], \\
\mu_{\beta+1} ={}& \frac{1}{T_c \langle k \rangle \langle k^{\beta+1} \rangle} \Big[\sigma_{\beta+2} \mu_0 \\
&+ \frac{\sigma_2}{\sigma_{\beta+2}} \left(\langle k^{\beta+1} \rangle^2 - \langle k^{2(\beta+1)} \rangle \right) \mu_0 \\
&+ \langle k \rangle \langle k^{\beta+1} \rangle \mu_1 - \frac{\sigma_2}{\sigma_{\beta+2}} \left(\langle k^{\beta+1} \rangle^2 - \langle k^{2(\beta+1)} \rangle \right) \mu_{\beta+1} \Big].
\end{aligned}
$$

Defining

$$
\begin{aligned}
A \equiv{}& \frac{\sigma_2}{\langle k \rangle^2}, \\
B \equiv{}& \frac{\sigma_2}{\sigma_{\beta+2}} \frac{\langle k^{2(\beta+1)} \rangle - \langle k^{\beta+1} \rangle^2}{\langle k \rangle \langle k^{\beta+1} \rangle}, \\
D \equiv{}& \frac{\sigma_{\beta+2}}{\langle k \rangle \langle k^{\beta+1} \rangle},
\end{aligned}
$$

T_c will be the solution to the third order polynomial equation:

$$
T_c^3 - (B+1)T_c^2 + (B - A)T_c + A(B - D) = 0. \tag{7.7}
$$

Note that for neutral (i.e., uncorrelated) networks, $\beta = 0$, and so $A = B = D$. We then have $T_c = \langle k^2 \rangle / \langle k \rangle^2$, as expected [164].

7.3.2 Generating correlated networks

Given a degree distribution $p(k)$, the ensemble of networks compatible with this constraint and with degree-degree correlations according to equation (7.4) (with some exponent β) is defined by the mean adjacency matrix $\hat{\epsilon}$ of equation (7.5) – as described in section 7.2.3 and in Ref. [26]. Therefore, although there will generally be an enormous number of possible networks in this volume of phase space, we can sample them correctly simply by generating them according to $\hat{\epsilon}$. To do this, first we have to assign to each node a degree drawn from $p(k)$. If the elements of $\hat{\epsilon}$ were probabilities, it would suffice then to connect each pair of nodes (i, j) with probability $\hat{\epsilon}_{ij}$ to generate a valid network. Strictly speaking, $\hat{\epsilon}$ is an expected value, which in certain cases can be greater than one. To get round this, we write a probability matrix $\hat{p} = \hat{\epsilon}/a$ with a some value such that all elements of $\hat{p}$ are smaller than one. If we then take random pairs of nodes (i, j) and, with probability $\hat{p}_{ij}$, place an edge between them, repeating the operation until $\frac{1}{2}\langle k \rangle N$ edges have been placed, the expected value of edges joining i and j will be $\hat{\epsilon}_{ij}$. This method is like the *hidden variable* technique [210] in that edges are placed with a predefined probability (which is why the resulting ensemble is canonical). The difference lies in the fact that in the method here described correlations only depend on the degrees of nodes.

We are interested here in neural networks, in which a given pair of nodes can be joined by several synapses, so we shall not impose the restriction of so-called simple networks of allowing only one edge at most per pair. We shall, however, consider networks with a *structural cutoff*: $k_i < \sqrt{\langle k \rangle N}$, $\forall i$ [217]. This ensures that, at least for $\beta \leq 0$, all elements of $\hat{\epsilon}$ are indeed smaller than one.

Because we can expect effects due to degree-degree correlations to be largest when $p(k)$ is very broad, and since most networks in nature and technology seem to exhibit approximately power-law degree distributions [58, 61, 112, 202], we shall here test our general theoretical results against simulations of scale-free networks: $p(k) \sim k^{-\gamma}$. This means that a network (or the region of phase space to which it belongs) is characterized by the set of parameters $\{\langle k \rangle, N, \gamma, \beta\}$.
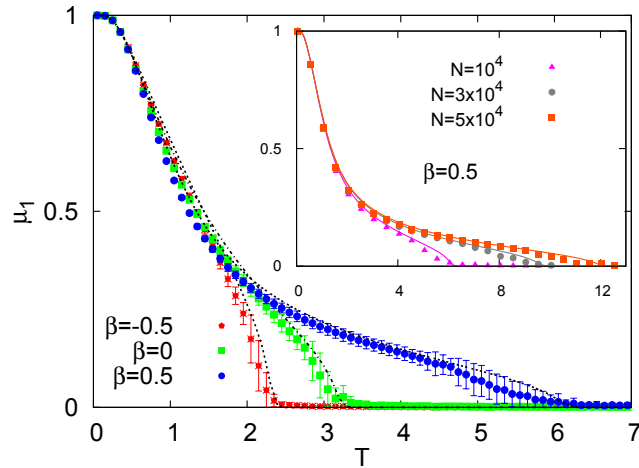
FIGURE 7.2: Stable stationary value of the weighted overlap μ_1 against temperature T for scale-free networks with correlations according to $\bar{k}_{nn} \sim k^{\beta}$, for $\beta = -0.5$ (disassortative), 0.0 (neutral), and 0.5 (assortative). Symbols from MC simulations, with error bars representing standard deviations, and lines from equations (7.6). Other network parameters as in figure 7.1. Inset: μ_1 against T for the assortative case ($\beta = 0.5$) and different system sizes: $N = 10^4$, $3 \cdot 10^4$ and $5 \cdot 10^4$.

7.3.3 Assortativity and dynamics

In figure 7.2 we plot the stationary value of μ_1 against the temperature T, as obtained from simulations and equations (7.6), for disassortative, neutral and assortative networks. The three curves are similar at low temperatures, but as T increases their behavior becomes quite different. The disassortative network is the least robust to noise. However, the assortative one is capable of retaining some information at temperatures considerably higher than the critical value, $T_c = \langle k^2 \rangle / \langle k \rangle$, of neutral networks. A comparison between μ_1 and μ_0 (see figure 7.3) shows that it is the high degree nodes that are mainly responsible for this difference in performance. This can be seen more clearly in figure 7.4, which displays the difference $\mu_1 - \mu_0$ against T for the same networks. It seems that, because in an assortative network a sub-graph of hubs will have more edges than in a disassortative one, it has a higher effective critical temperature. Therefore, even when most of the nodes are acting randomly, the set of nodes of sufficiently high degree nevertheless displays associative memory.

The phase diagram if figure 7.5 shows the critical temperature, T_c, as obtained from equation (7.7). In addition to the effect reported in Ref. [25] whereby the T_c of scale-free networks grows with degree heterogeneity (decreasing γ), it also increases very significantly with positive degree-degree correlations (increasing β).
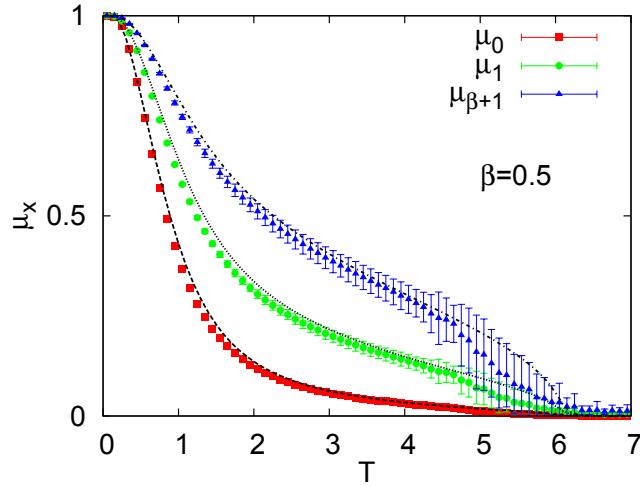
FIGURE 7.3: Stable stationary values of order parameters μ_0, μ_1 and $\mu_{\beta+1}$ against temperature T, for assortative networks according to $\beta = 0.5$. Symbols from MC simulations, with error bars representing standard deviations, and lines from equations (7.6). Other parameters as in figure 7.1.
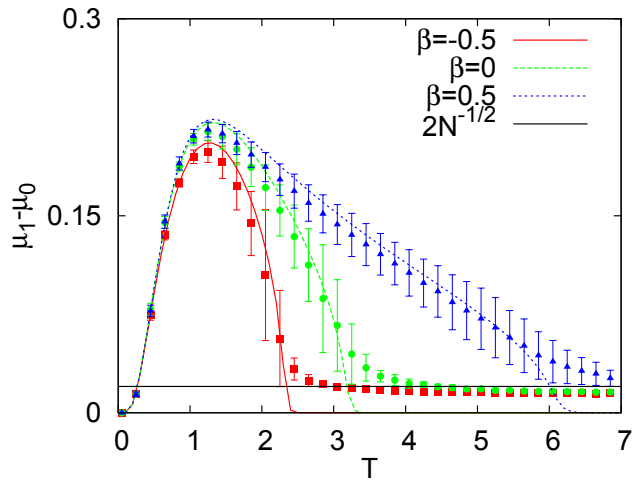
FIGURE 7.4: Difference between the stationary values μ_1 and μ_0 for networks with $\beta = -0.5$ (disassortative), 0.0 (neutral) and 0.5 (assortative), against temperature. Symbols from MC simulations, with error bars representing standard deviations, and lines from equations (7.6). Line shows the expected level of fluctuations due to noise, $\sim N^{-\frac{1}{2}}$. Other parameters as in figure 7.1.

At large values of N, the critical temperature scales as $T_c \sim N^b$, with $b \geq 0$ a constant. However, because the moments of k appearing in the coefficients of equation (7.7) can have different asymptotic behavior depending on the values of γ and β, the scaling exponent b differs from one region to another in the space of these parameters. These are the seven regions shown in figure 7.6, along with the
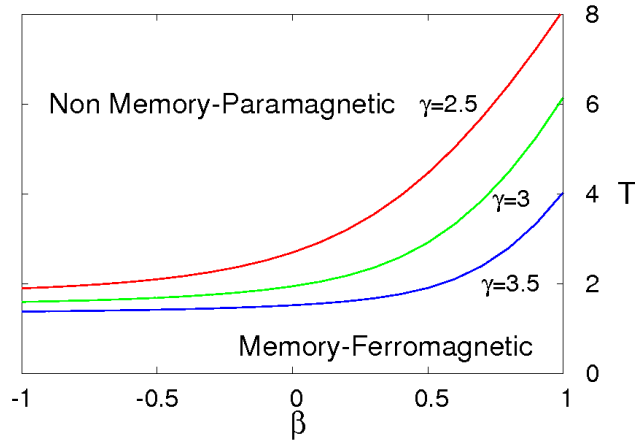
FIGURE 7.5: Phase diagrams for scale-free networks with $\gamma = 2.5$, 3, and 3.5. Lines show the critical temperature T_c marking the second-order transition from a memory (ferromagnetic) phase to a memoryless (paramagnetic) one, against the assortativity β, as given by equation (7.7). Other parameters as in figure 7.1.

scaling behavior exhibited by each one. This can be seen explicitly in figure 7.7, where T_c, as obtained from MC simulations, is plotted against N for cases in each of the regions with $\gamma < 3$. In each case, the scaling is as given by equation (7.7) and shown in figure 7.6. For the four regions with $\gamma < 3$, from lowest to highest assortativity we have scaling exponents which are dependent on: only γ (region I), only β (region II), both γ and β (region III), and, perhaps most interestingly, neither of the two (region IV) – with T_c scaling, in the latter case, as $\sqrt{N}$. As for the more homogeneous $\gamma > 3$ part, regions V and VI have a diverging critical temperature despite the fact that the second moment of $p(k)$ is finite, simply as a result of assortativity.

The case in which more than one pattern are stored ($P > 1$) can be explored numerically. Assuming there are P uncorrelated patterns, we have an order parameter μ_1^ν for each pattern ν. A global measure of the degree to which there is memory can be captured by the parameter ζ, where

$$\zeta^2 \equiv \frac{1}{1 + P/N} \sum_{\nu=1}^{P} (\mu_1^\nu)^2.$$

Notice that the normalization factor is due to the fact that if one pattern is *condensed* – i.e., $|\mu_1| \lesssim 1$ – the others have $|\mu_\nu| \sim 1/\sqrt{N}$, $\nu = 2, ..P$, and so $\zeta \simeq 1$. Figure 7.8 shows how ζ decreases with T in variously correlated networks for $P = 3$
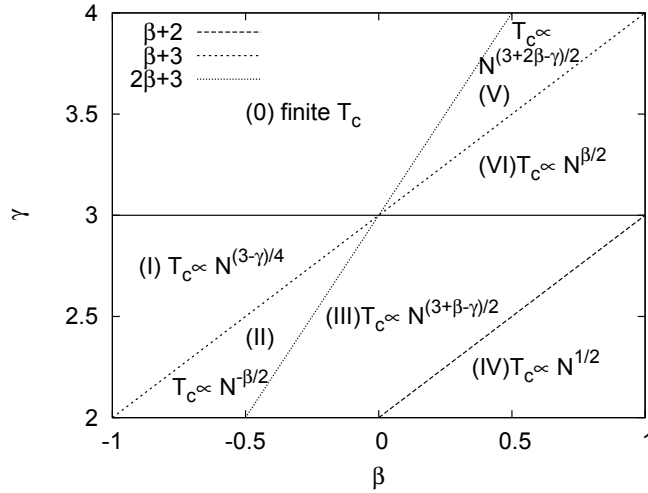
FIGURE 7.6: Parameter space $\beta-\gamma$ partitioned into the regions in which $b(\beta,\gamma)$ has the same functional form – where b is the scaling exponent of the critical temperature: $T_c \sim N^b$. Exponents obtained by taking the large N limit in equation (7.7).
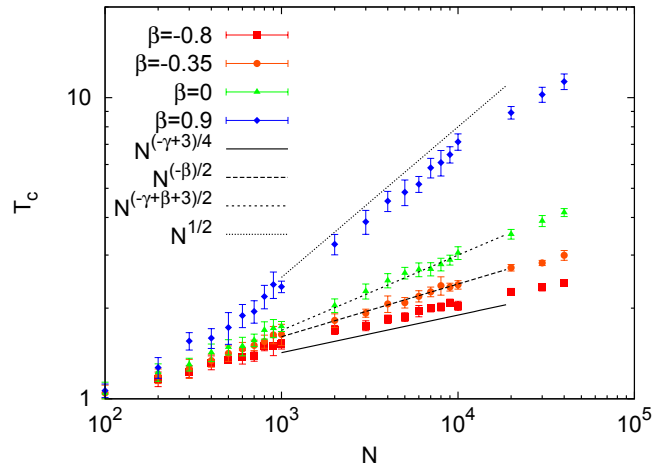
FIGURE 7.7: Examples of how T_c scales with N for networks belonging to regions I, II, III and IV of figure 7.6 ($\beta = -0.8, -0.35, 0.0$ and 0.9, respectively). Symbols from MC simulations, with error bars representing standard deviations, and slopes from equation (7.7). All parameters – except for β and N – are as in figure 7.1.

(left panel) and $P = 10$ patterns (right panel). The behavior is not qualitatively different from that observed for the single-pattern case in the main panel of figure 7.2, suggesting that the influence of assortativity we report is robust as to the number of patterns stored, P.
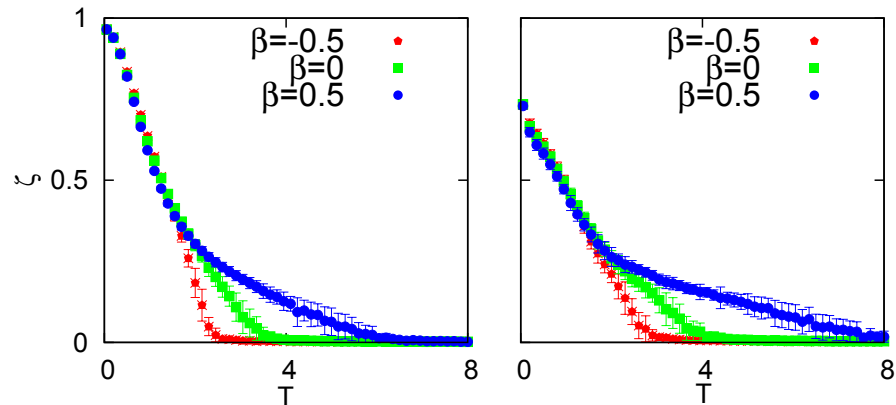
FIGURE 7.8: Global order parameter ζ for assortative ($\beta = 0.5$), neutral ($\beta = 0.0$) and disassortative ($\beta = -0.5$) networks with $P = 3$ (left panel) and $P = 10$ (right panel) stored patterns. Symbols from MC simulations, with errorbars representing standard deviations. All parameters are as in figure 7.1.

7.4 Discussion

We have shown that assortative networks of simple model neurons are able to exhibit associative memory in the presence of levels of noise such that uncorrelated (or disassortative) networks cannot. This may appear to be in contradiction with a recent result obtained using spectral graph analysis – that synchrony of a set of coupled oscillators is highest for disassortative networks [206]. A synchronous state of model oscillators and a memory phase of model neurons are both sets of many simple dynamical elements coupled via a network in such a way that a macroscopically coherent situation is maintained [203]. Obviously both systems require the effective transmission of information among the elements. So why are opposite results as regards the influence of topology reported for each system? The answer is simple: whereas the definition of a synchronous state is that every single element oscillate at the same frequency, it is precisely when most elements are actually behaving randomly that the advantages to assortativity we report become apparent. In fact, it can be seen in figure 7.2 that at low temperatures disassortative networks perform the best, although the effect is small. This is reminiscent of

percolation: at high densities of edges the giant component is larger in disassor-
tative networks, but in assortative ones a non-vanishing fraction of nodes remain
interconnected even at densities below the usual percolation threshold [205]. Be-
cause in the case of targeted attacks it is this threshold which is taken as a measure
of resilience, we say that assortative networks perform the best. The relevance of
partial synchronization and the important role of hubs have already been noted
for systems of (weakly) coupled oscillators [71, 218] – for which, however, assorta-
tivity has not been expected to be of consequence [218]. In general, the optimal
network for good conditions (i.e., complete synchronization, high density of edges,
low levels of noise) is not necessarily the one which performs the best in bad condi-
tions (partial synchronization, low density of edges, high levels of noise). It seems
that optimality – whether in resilience or robustness – should thus be defined for
particular conditions.

We have used the technique suggested in Ref. [26] to study the effect of cor-
relations on networks of model neurons, but many other systems of dynamical
elements should be susceptible to a similar treatment. In fact, Ising spins [215],
Voter Model agents [219], or Boolean nodes [220], for instance, are similar enough
to binary neurons that we should expect similar results for these models. If a
moral can be drawn, it is that persistence of partial synchrony, or coherence of
a subset of highly connected dynamical elements, can sometimes be as relevant
(or more so) as the possibility of every element behaving in the same way. In the
case of real brain cells, experiments suggest that hub neurons play key functional
roles [212, 213]. From this point of view, there may be a selective pressure for
brain networks to become assortative – although, admittedly, this organ engages
in such complex behavior that there must be many more functional constraints
on its structure than just a high robustness to noise. Nevertheless, it would be
interesting to investigate this aspect of biological systems experimentally. For
this, it should be borne in mind that heterogeneous networks have a natural ten-
dency to become disassortative, so it is against the expected value of correlations
discussed in Ref. [26] that empirical data should be contrasted in order to look
for meaningful deviations towards assortativity. Similarly, it may be necessary
to take into account the correlations that could emerge due to the spatial layout
of neurons [23, 78]. In any case, it would be in areas of the cortex specifically
related to memory – such as the temporal (long-term memory) [113, 114] or pre-
frontal (short-term memory) [221, 222] lobes – that this effect might be relevant.
A curious fact that would seem to support our hypothesis is that whereas the vast

majority of non-social networks are disassortative [58], one that appears actually to be strongly assortative is the functional network of the human cortex [4].

Chapter 8

Synchronization phenomena in networks of spiking neurons with a correlated scale-free topology

To go a step further in the understanding of the behaviour of neural populations in networks characterized by non trivial long range degree distributions, we study in this chapter neural networks with a more realistic *spiking* neuron description, by mean of the Integrate and Fire (IF) model (described in section 3.2) in the same class of correlated complex topologies implemented in chapter 7. This allows for the study of the emergence of different type of synchronization dynamical states as a function of the underlying topology and its degree-degree correlations. Our study shows that network global heterogeneity and local degree-degree correlations play a determinant role in the emergence and stability of synchronous states, as well as in the appearance of asynchronous states and mixture states including both synchronous and asynchronous activity within the whole neuron population.

8.1 Introduction

The topology of neural networks has been found recently to be relevant in different computational and storage performance tasks, as well as in their robustness under the effect of noise. Torres *et al.* found in a Hopfield-like neural-network model with a non trivial topology that degree heterogeneity increases the system's performance in the presence of high levels of noise, since the hubs (i.e. the neurons with

high degree) are able to retain information at levels well above the usual critical noise level for the appearance of non-memory states [25]. As described in chapter 7, there are network topologies that could be characterized by finer features, other than the simple degree distribution, that we demonstrated to have a great influence in their emergent behaviour. As we have already introduced in the previous chapter, different empirical networks present correlations between the degrees of a node and those of their neighbours (i.e. the nodes with which it establishes a link) [204, 205]. If the average nodes degree-degree correlation is positive the network is said to be *assortative*, while it is called *disassortative* if negatively correlated. Thus, in chapter 7, we have demonstrated that an assortative Amari-Hopfield neural network enhances associative memory in the presence of high level of noise. Moreover, assortativity seems to be also relevant in different and more complex dynamic processes taking place on networks, see for example [203, 205, 206]. The particular dynamics defined on the nodes of the network is also essential for the role played by assortativity on the behaviour of the system under study, and in some cases it can generate counterintuitive effects. For example, the phenomenology associated to assortative configurations in binary neural networks described in chapter 7 is in contradiction with a recent result obtained using spectral graph analysis, i.e. that synchronizability of a set of coupled oscillators is highest for disassortative networks [206].

Synchronization of distributed brain activity has been proposed as an important mechanism for neural information processing, and the experimentally observed brain activity, characterized by synchronization phenomena over a wide range of spatial and temporal scales, reflects a hierarchical organization of the overall dynamics [224]. Realistic neural network models with richer neuron dynamics have often been modeled in networks with trivial degree distributions, i.e. fully connected or homogeneous (Gaussian or Poisson distributed) [89]. More recent works have investigated the contributions of small world [91] or hierarchically organized [225] network topological features to the dynamic behaviour of excitable neural populations. In this chapter we study a population of neurons, with a leaky Integrate and Fire (IF) dynamics, structured in a scale-free network with non trivial neurons degree-degree correlation, and analyze theoretically and with numerical simulations the different synchronous and asynchronous phases that emerge. The IF mode includes the most simple neuron mechanism of subthreshold membrane potential dynamics, and constitutes the paradigm of the threshold-firing neuron models [85] (see section 3.2 for details). Several works on IF networks have been

focused on the appearance of synchronous states, on the transient dynamics until synchrony is reached [90, 226], or finally on the transition between synchronous and an asynchronous state induced by thermal or quenched noise [227, 228]. In our case the synchronous/asynchronous behaviour of the network depends also on the heterogeneity of the degree-degree correlations. In fact, our analysis shows that heterogeneity in the network topology enhances the appearance of asynchronous activity, involving the whole system or, in some cases, only a subnetwork. Thus disassortative scale-free networks, that display both global and local heterogeneous structures, have a great tendency to desynchronize neuronal activity.

8.2 Definition of the model

8.2.1 Networks of IF neurons

As we have previously described in section 3.1, one of the main features regarding the generation of an action potential in neurons is the threshold mechanism of membrane potential. By virtue of this mechanism, a neuron integrates the signals incoming from the presynaptic inputs by depolarizing its membrane potential until this reaches a threshold value. Then the neuron emits an action potential, which finally generates the output signals in the postsynaptic terminations. Let us consider a network of N excitatory Integrate and Fire neurons where the membrane voltage of each neuron i, namely V_i, follows the dynamics

$$\tau_m \dot{V}_i = -V_i + R(I_i^{ext} + I_i^{net}), \tag{8.1}$$

where R is the membrane resistance, $\tau_m = 20 \ ms$ is the membrane time constant and I_i^{ext} is the external current applied to neuron i and I_i^{net} is the contribution of the other neurons in the network. As a consequence of the incoming inputs, the neuron membrane depolarizes and once it reaches the threshold $\theta = 20 \ mV$, neuron emits an action potential after which the voltage membrane is reset to a resting value $V_r = 10 \ mV$ during a refractory period $\tau_{ref} = 5 \ ms$. Each one of the

inputs current terms usually are defined as follows

$$RI_i^{ext} = \omega + D\sqrt{\tau_m}\xi_i(t)$$

$$RI_i^{net} = \tau_m \sum_{j=1}^{N} \sum_n a_{ij} \, Jg(t - t_j^n). \tag{8.2}$$

Here ω is the mean external current, D is the amplitude of a Gaussian noise $\xi_i(t)$, while the parameter $J = 0.1 \, mV$ is the synaptic coupling strength and a_{ij} is the adjacency matrix (defined in chapter 7) which contains all the information about the topological structure of the network. The function $g(t - t_j^n)$ describes the shape of the depolarization in the postsynaptic neuron i caused by the arrival of an action potential in the presynaptic neuron j at time t_j^n. We consider here $g(t)$ with the form of a narrow pulse

$$g(t - t_j^n) = \begin{cases} 1 & t \in \left[t_j^n, t_j^n + \lambda\right] \\ 0 & t \notin \left[t_j^n, t_j^n + \lambda\right] \end{cases} \tag{8.3}$$

with $\lambda = 1 \, ms$. All the values of the parameters have been set within the physiological range [84].

8.2.2 Network generation

Throughout the analysis that follows, we have considered random networks with sparse connectivity, which is characterized by some probability distribution $p(k)$ to have a given neuron with some connectivity degree k. We assume here that $p(k)$ follows a scale-free distribution, that is $p(k) \sim k^{-\gamma}$, with mean degree $\langle k \rangle$ and standard deviation σ. In addition, we consider non trivial correlations among the degrees of the nearest neighbour neurons, assuming that the neighbours average degree for a neuron with degree k also follows a power law. The number of incoming synapses to a postsynaptic neuron i, i.e. the degree of neuron i, is denoted by k_i. Similarly to the method implemented in section 7.2, we generate such kind of neural networks by sorting *a priori* the degree of each one of the N neurons $(k_1, ...k_N)$ from the distribution $p(k)$, and then considering the following

probability to have a link between neurons i and j:

$$
\begin{aligned}
\hat{\epsilon}_{ij} &= \frac{1}{N}[k_i + k_j - \langle k \rangle] \\
&+ \frac{\sigma_2}{\sigma_{\beta+2}} \frac{1}{N} \left[\frac{(k_i k_j)^{\beta+1}}{\langle k^{\beta+1} \rangle} - k_i^{\beta+1} - k_j^{\beta+1} + \langle k^{\beta+1} \rangle \right].
\end{aligned}
\tag{8.4}
$$

With this choice, the mean degree of the neighbours of a given neuron i results to be a power law function of k_i, i.e.

$$
\overline{k}_{nn,i} \equiv k_i^{-1} \sum_j \hat{\epsilon}_{ij} k_j = \frac{\langle k^2 \rangle}{\langle k \rangle} + \sigma_2 \left[\frac{k^\beta}{\langle k^{\beta+1} \rangle} - \frac{1}{\langle k \rangle} \right] \propto k^\beta.
\tag{8.5}
$$

Neurons degree-degree correlations are positive if $\beta > 0$, and the network is said assortative, while it is disassortative when $\beta < 0$.

8.3   Mean-field analysis

A mean field study of the system can be done if the mean activity in the network is almost constant and persistent during time. In order to do that, we first approximate the adjacency matrix by its mean value, following the *configurational model* also employed in [22, 26]:

$$
a_{ij} \simeq \overline{a_{ij}} = \frac{1}{N}[k_i + k_j - \langle k \rangle] + \frac{\sigma_2}{\sigma_{\beta+2}} \frac{1}{N} \left[\frac{(k_i k_j)^{\beta+1}}{\langle k^{\beta+1} \rangle} - k_i^{\beta+1} - k_j^{\beta+1} + \langle k^{\beta+1} \rangle \right].
$$

Then, it is straightforward to write the recurrent part of the input current in equations (8.1)-(8.2) as

$$
R I_i^{net}(t) = \tau_m J F_i + J \sqrt{\tau_m F_i} \xi_i(t)
\tag{8.6}
$$

where F_i is defined as

$$
\begin{aligned}
F_i &\equiv (k_i \mu_0 + \langle k \rangle (\mu_1 - \mu_0)) \\
&+ \frac{\sigma_2}{\sigma_{\beta+2}} [k_i^{\beta+1}(\mu_{\beta+1} - \mu_0) \\
&+ \langle k^{\beta+1} \rangle (\mu_0 - \mu_{\beta+1})],
\end{aligned}
$$

where μ_α is defined as

$$\mu_\alpha \equiv \frac{\sum_{i=1}^{N} k_i^\alpha \nu_i}{N\langle k^\alpha \rangle}, \tag{8.7}$$

with ν_i being the stationary firing rate of the subpopulation of neurons with degree k_i. For $\alpha = 0$ μ_0 constitutes the mean firing rate per synapse in steady state conditions. In case of a homogeneous network, one has $\mu_0 = \nu_0$ (with ν_0 being the stationary network mean firing rate), whereas in case of having a heterogeneous network, some deviations from this value may appear. If we put equation (8.6) in (8.1), the IF equation becomes a Langevin equation for the membrane voltage, i.e.

$$\tau_m \dot{V}_i = -V_i + \chi_i + D_i \sqrt{\tau_m} \xi_i(t) \tag{8.8}$$

where χ_i is the deterministic part of the total current arriving at neuron i, given by

$$\chi_i = \omega + \tau_m J F_i. \tag{8.9}$$

On the other hand, the fluctuations of the total current arriving at neuron i are

$$D_i = \sqrt{D^2 + \tau_m J^2 F_i}. \tag{8.10}$$

The mean firing rate of the neuron i in stationary conditions can be computed using the first-passage time calculus for a leaky IF neuron model (see [86] for further details), that yields

$$\nu_i = \left[\tau_{ref} + \tau_m \int_{y_r^i}^{y_\theta^i} f(z)dz \right]^{-1}, \tag{8.11}$$

where $y_\theta^i = \frac{\theta - \chi_i}{D_i}$, $y_r^i = \frac{V_r - \chi_i}{D_i}$ and $f(z) = \sqrt{\pi} \exp(z^2)(1 + \mathrm{erf}(z))$. In order to obtain the stationary mean firing rate per synapse of the network, we have to average over all the stationary firing rates. However, assuming that the variability in the firing rates is caused by the heterogeneity of the connectivity degree, which follows a distribution $p(k)$, a reasonable hypothesis is to consider $\nu_i = \nu_i(k_i)$. Then, in the limit $N \to \infty$ one can replace the sum in (8.7) by an integral over $p(k)$. Now,

using (8.11) one finally obtains:

$$
\mu_0 = \int_{k_{min}}^{k_{max}} p(k)dk \left[\tau_{ref} + \tau_m \int_{y_r(k)}^{y_\theta(k)} f(z)dz \right]^{-1}
$$

$$
\mu_1 = \frac{1}{\langle k \rangle} \int_{k_{min}}^{k_{max}} kp(k)dk \left[\tau_{ref} + \tau_m \int_{y_r(k)}^{y_\theta(k)} f(z)dz \right]^{-1} \tag{8.12}
$$

$$
\mu_{\beta+1} = \frac{1}{\langle k^{\beta+1} \rangle} \int_{k_{min}}^{k_{max}} k^{\beta+1} p(k)dk \left[\tau_{ref} + \tau_m \int_{y_r(k)}^{y_\theta(k)} f(z)dz \right]^{-1},
$$

where

$$
y_\theta(k) = \frac{\theta - \chi - \tau_m J F(k)}{\sqrt{D^2 + \tau_m J^2 F(k)}}, \quad y_r(k) = \frac{V_r - \chi - \tau_m J F(k)}{\sqrt{D^2 + \tau_m J^2 F(k)}}. \tag{8.13}
$$

We have numerically implemented the self consistent system of equations (8.12) with an iterative method. At each step we randomly sort only one subpopulation of neurons with degree $\hat{k}$, and then calculate their correspondent new firing rate $\nu(\hat{k})_{new}$ with the use of equation (8.11). Finally replacing $\nu(\hat{k})_{new}$ in the integrals of right sides of equations (8.12), we obtain the new values of μ_0, μ_1 and $\mu_{\beta+1}$. The iteration is repeated until μ_0, μ_1 and $\mu_{\beta+1}$ reach a steady state.

8.4 Results

8.4.1 Global synchronization dynamics

Extensive numerical simulations and the mean field results have allowed us to distinguish three different dynamical behaviours in the system: the silent phase, the synchronous phase and the asynchronous phase. In the silent phase the external current is not sufficient to produce any activity in the network. In the synchronous phase all neurons fire at the same frequency. Finally in the asynchronous phase each neuron fires with a frequency $\nu(k)$ dependent on their degree k. For some topological constraints and parameter conditions, is also possible to obtain a mixture phase, characterized by synchronous firing for neurons with a degree $k \in [k_-, k_+]$ and asynchronous firing for neurons with a degree out of this interval. The stability of the mixture phase, as well as the range of synchrony, depends on the level of network assortativity. A first quantitative description of these phases could be done with the analysis of time series of the instantaneous

mean firing rate $m_0(t)$, defined as:

$$m_0(t) \equiv \frac{\sum_n \sum_{i=1}^N \delta(t - t_i^n)}{N}.$$

In the synchronous phase all neurons fire in phase at the same frequency, as depicted in the top panel of figure 8.1. In the mixture phase, see middle panel of figure 8.1, only a subpopulation of neurons with a degree included in a compact range, i.e. $k \in [k_-, k_+]$, fires synchronously with the same frequency, while all other neurons in the system fire asynchronously with a frequency which depends on its degree as it is predicted by the mean-field equations (8.11)-(8.12) (see black solid lines in right panels in figure 8.1). Finally in the asynchronous phase (bottom panels of figure 8.1) all neurons in the whole range of k have a degree dependent frequency. In this case, the frequency distribution of the whole system agrees optimally with the one obtained within the theoretical mean-field approach. On the other hand, the time average of $m_0(t)$ (corresponding in the stationary state to the mean firing rate μ_0 defined in equation (8.7)), depicted in the diagrams of figure 8.2 as a function of the external current parameters (ω, D), assumes high values in the asynchronous phase, due to the little but persistent activity of the network. In the synchronous phase however, the network is silent for the most of the time, except when all neurons fire abruptly in a narrow time window with a fixed frequency. Then μ_0 have a low value in this phase and the standard deviation of $m_0(t)$, i.e $\sigma(m_0) \equiv \sqrt{\langle m_0(t)^2 \rangle_t - \langle m_0(t) \rangle_t^2}$ (shown in the diagrams of figure 8.3), has higher values than in the asynchronous phase. Assortative topologies makes the synchronous phase more robust under the desynchronization induced by high values of the mean external driving ω and the external noise D, as one can deduce by direct comparison of the diagrams of figures 8.2-8.3 for assortative and disassortative configurations. This conclusion can be easily understood by looking on the behaviour of excitatory IF networks with homogeneous topologies (e.g. uniformly, Gaussian or Poisson distributed), where the synchronous state is extremely robust [226]. In fact, among the networks with heterogeneous degree distributions, like the scale-free networks, assortative configurations result to be locally homogeneous, and can be considered as the union of different and *almost homogeneous* subnetworks (with different mean degrees). Thus for each k we can define an almost homogeneous subnetwork constituted by all neurons with degree k and their nearest neighbours, which have degree $\hat{k} \sim k_{nn}(k) \sim k$. Each one of these subnetworks has a high tendency to synchronize and moreover
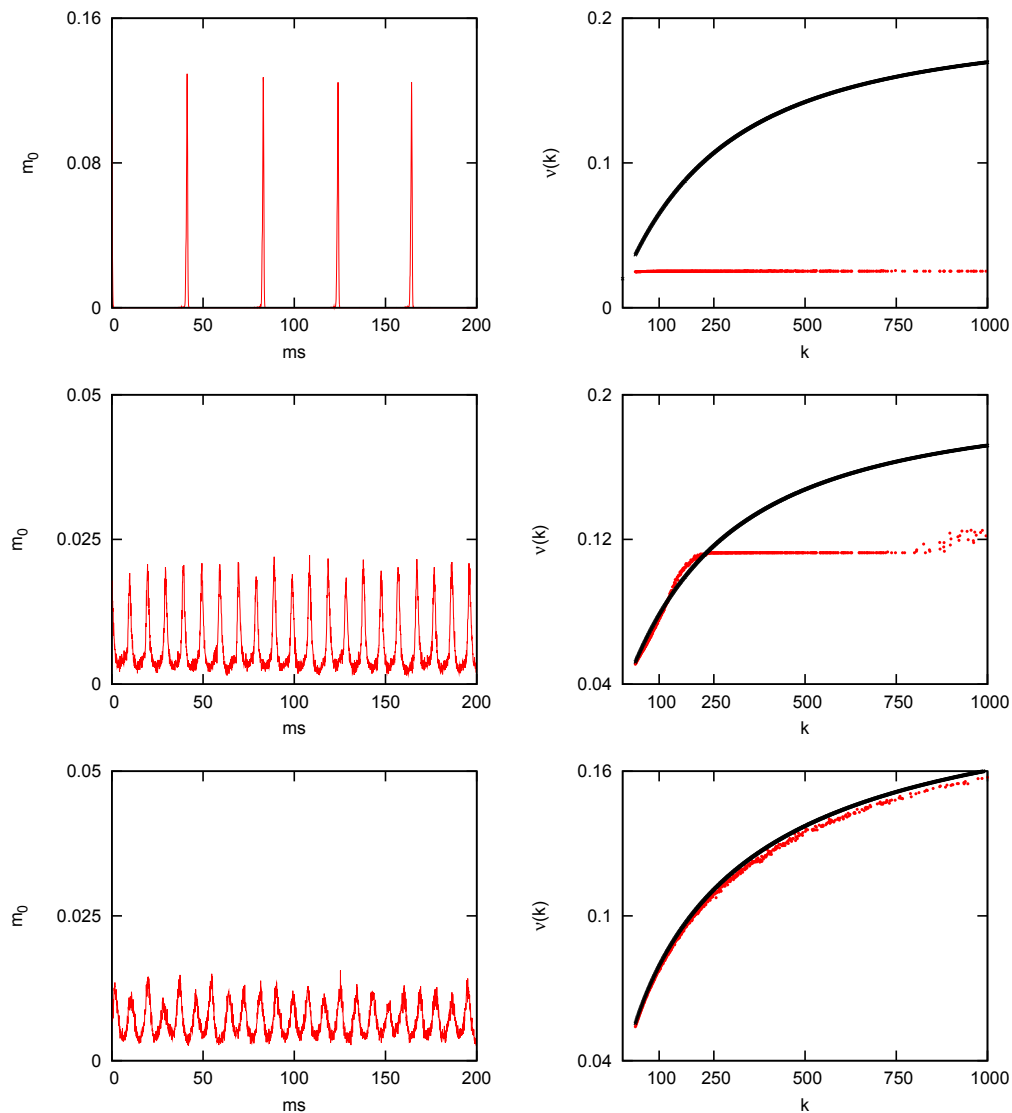
FIGURE 8.1: Instantaneous mean firing rate $m_0(t)$ (left panels) and the mean firing rate *per degree* distribution $\nu_k(t)$ (right panels), for a network of $N = 10^4$ IF neurons with a scale-free degree distribution (with exponent $\gamma = -2.5$) and mean neighbours degree $\overline{k}_{nn}(k) \propto k^\beta$. Top: Synchronous phase in an assortative configuration ($\beta = 0.5$), with $\omega = 20\ mV$ and $D = 0,89\ mV$. Middle: mixture phase for the same assortative case, with $\omega = 24\ mV$ and $D = 0,89\ mV$. Bottom: asynchronous regime in a disassortative configuration ($\beta = -0.5$), with $\omega = 24\ mV$ and $D = 0,89\ mV$.

only subnetworks with similar mean degree have some neuron in common. The result is the emergence of a global synchronous state, where in any subnetwork neurons fire with the same frequency. On the contrary, disassortative networks are extremely heterogeneous both globally and locally, except in a subnetwork of neurons with degree $k \sim \langle k \rangle$ (i.e. around the crossing point between curves $k_{nn}(k)$

and $\langle k \rangle$), and therefore induce more likely asynchronous phases [228]. For any
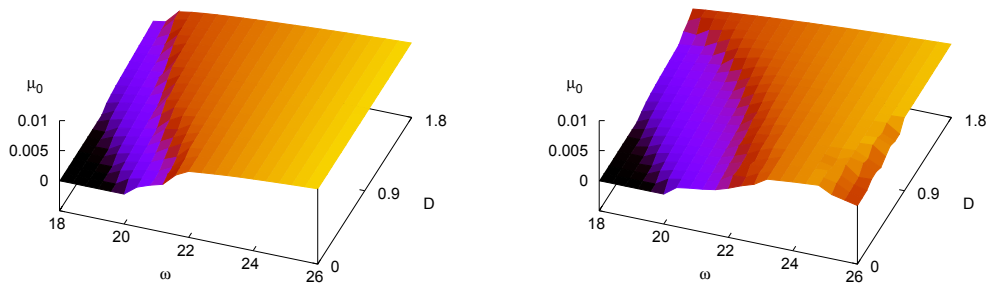
FIGURE 8.2: Mean firing rate μ_0 as a function of ω and D, for a scale-free IF network with $\beta = -0.5$ (disassortative, left) and 0.5 (assortative, right), generated according to the algorithm described in Sec. 7.3.2. Other parameters are $\gamma = 2.5$, $\langle k \rangle = 100$, $N = 10^4$.
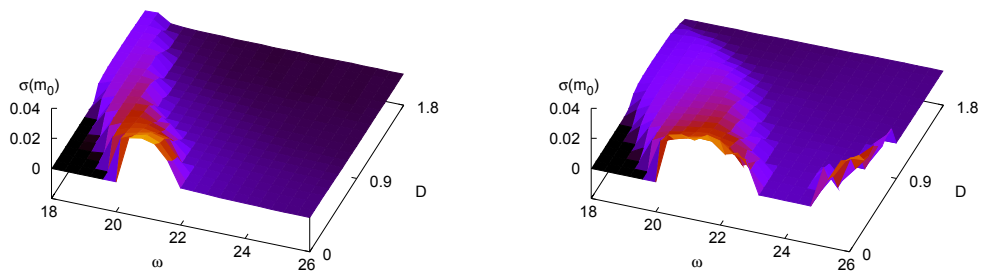
FIGURE 8.3: Variance of mean firing rate as a function of ω and D, for a scale-free IF network with $\beta = -0.5$ (disassortative, left) and 0.5 (assortative, right), for the same networks of figure 8.2.

assortativity level of the network topology, i.e. for any β, the transition between silent and synchronous phases results to be of second order, while the one between synchronous and asynchronous phases (i.e. the proper asynchronous phase or the mixture phase) is a discontinuous, first order, transition, see figure 8.4. In the extreme case of an assortative network with low level of external noise D, the synchronous/asynchronous coexistence region could be extremely broad, as depicted in figure 8.4 (bottom-left panel). On the other hand the mean field approximation, developed with the assumption of a stationary regime, fits well only with the asynchronous regime.
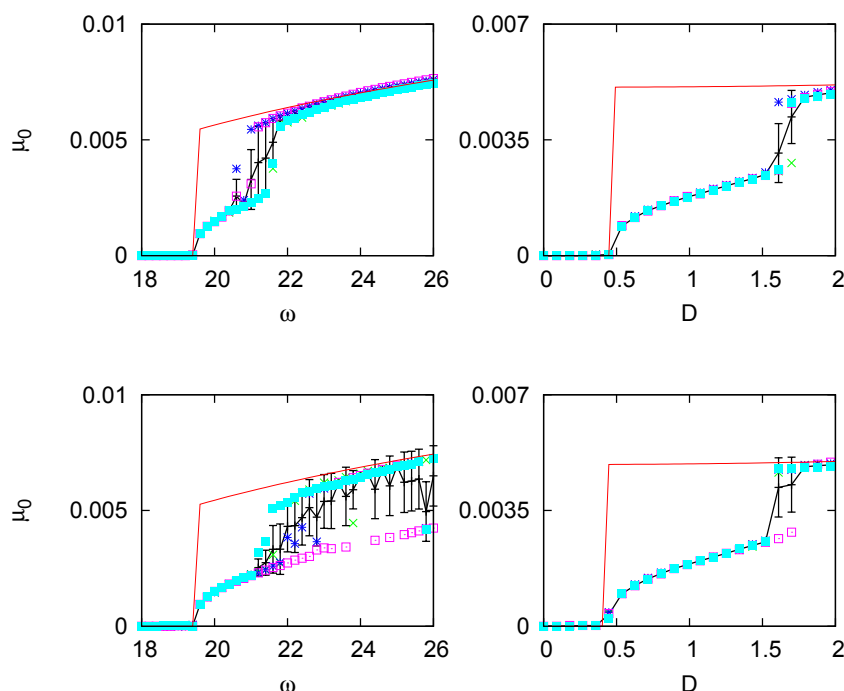
FIGURE 8.4: Mean firing rate μ_0 for a scale-free IF network with $\beta = -0.5$ (disassortative, upper panels) and 0.5 (assortative, bottom panels), with fixed $D = 0.179$ (left panels) and $\omega = 18.8$ (right panels). Symbols correspond to different network realizations, black curve with their average, and red curve with the mean field approximation resulting from equations 8.12. Transitions from silent phase to synchronous phase are of second order, while from synchronous to asynchronous phase there is a discontinuous first order transition.

8.4.2 Emergence of mixture phase and robustness of synchronization in central cluster

It is important to remark that, during the transition to the asynchronous phase, once the desynchronization affects the large majority of the nodes, let's say all the neurons until a degree $k \sim \langle k \rangle$, is not possible to distinguish between mixture and asynchronous phases from the values of m_0 and $\sigma(m_0)$ alone (compare, for instance, middle and bottom panels of figure 8.1). Nevertheless the analysis of frequencies $\nu(k)$ allows to analyze the mixture states and their corresponding transitions to a completely asynchronous state. The mixture state of assortative networks present synchronous activity only in neurons that have a degree in an interval $k \in [k_-, k_+]$. Such group of synchronous neurons is larger and more robust than in the case of dissasortative networks, as it is depicted in figure 8.5. Thus assortative networks keep synchronized the global neuron activity (at a low frequency) for a broad
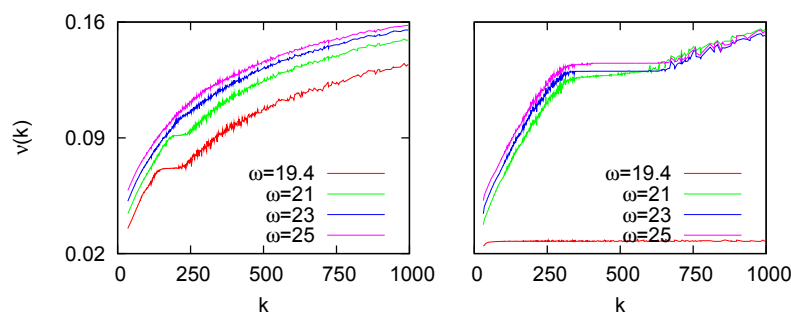
FIGURE 8.5: Frequencies vs neurons degree $\nu(k)$, with $D = 1.342$, for networks with $\beta = -0.5$ (disassortative, left panel) and $\beta = 0.5$ (assortative, right panel). Network activity is asynchronous in all cases, except for the red curve of right panel, corresponding to a synchronous phase.

region of parameters and, even when the system is in the asynchronous phase, it still has a considerable number of synchronized neurons (at a high frequency). On the contrary once a disassortative network enters in the asynchronous phase, almost all neurons have an asynchronous activity, except the ones with a degree $k \sim \langle k \rangle$ in a narrow region of parameters. In any case during the mixture state desynchronization starts from the neurons with degree at the lower and upper limit of the degree distribution. In fact, neurons with degree $k \sim \langle k \rangle$ constitute a central cluster with a robust synchronized activity because for any level of assortativity they form a local, almost homogeneous, subnetwork.

In order to go a step further in a detailed description of local synchronization, we have analyzed the time series of the instantaneous mean firing rate *per degree* distribution, defined as the density of neurons with degree k firing at time t, i.e.

$$\nu_p(k, t) \equiv \frac{\sum_n \sum_{i:k_i=k} \delta(t - t_i^n)}{Np(k)}. \tag{8.14}$$

In the top panel of figure 8.6, it is depicted a typical synchronous phase, where neurons of any k fire with the same frequency and phase, while in the partial asynchronous phase (shown in the middle panel), neurons with $k < \langle k \rangle$ fire with different frequencies and not in phase (as it is possible to deduce from the low level of $\nu_p(k,t)$), with a persistent background activity. Surprisingly, when disassortative networks are in a completely asynchronous phase (see bottom panel of figure 8.1), one can still observe the central cluster with an almost synchronous activity, as depicted in the bottom panel of 8.6, although here neurons with different degrees fire with different mean frequencies. In this case, as expected, for any

k degree subpopulations out of the central cluster, neurons fire out in phase. As commented in section 8.4.1, the emergence of a stable synchronous central cluster is probably due to the heterogeneous subnetwork composed by neurons with degree $k \sim \langle k \rangle$.
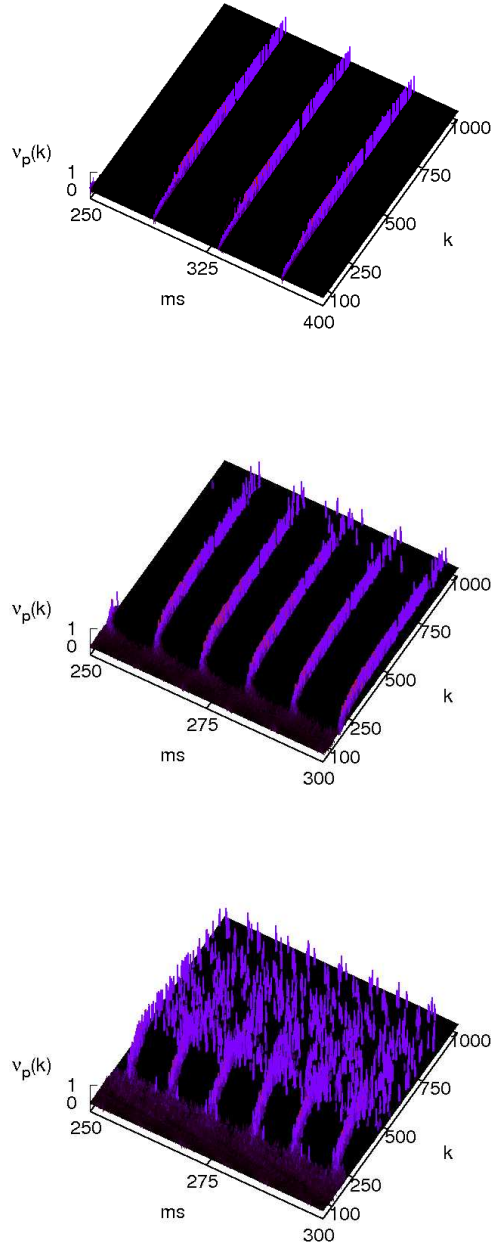
FIGURE 8.6: Time series of mean firing rate *per degree* distribution $\nu_p(k, t)$ for the same networks described in figure 8.1 (top panel: $\beta = 0.5$, $\omega = 20\ mV$ and $D = 0,89\ mV$; middle panel: $\beta = 0.5$, $\omega = 24\ mV$ and $D = 0,89\ mV$; bottom panel: $\beta = -0.5$, $\omega = 24\ mV$ and $D = 0,89\ mV$).

8.5 Discussion

In the last decade several works have fully characterized the different synchronous and asynchronous phases appearing in networks of IF spiking neurons with homogeneous topologies [89], as for instance, the random Erdös-Rény topology [77], introducing both excitatory and inhibitory synapses and a transmission delay of spikes. Other works have shown that in the most simple case of IF neuron networks with only excitatory synapses and a homogeneous topology, synchronization is the only active phase observed [91, 226]. In our model of IF excitatory neurons, however, we have observed that the heterogeneity of the topology also induces the emergence of a completely asynchronous phase, with a distribution of typical frequencies, which depends on the degree of the neurons in the network, as well as a mixture phase, where there is a subpopulation of neurons that fires synchronously. In addition, the level of assortativity, that modulates the local neuron degree-degree correlation, influences the robustness of the different phases under variation of external stimulation parameters. Global and partial synchronization are enhanced by networks with assortative configurations, in which a certain level of homogeneity is guaranteed, at least locally. Between synchronous and asynchronous phases there is a discontinuous first order phase transition, particularly prominent in the assortative case at low level of external noise, where there is a broad region of coexistence between the synchronous and mixture phases. This broad region of coexistence can have important computational consequences because it allows for bistability of two dynamical behaviours with very different frequencies (the low frequency of the synchronous phase and the high frequency of the mixture phase), and the possibility to switch among them under an appropriate external stimulation. Moreover, important consequences concerning the functionality or the emergent activity of different neural media could be derived from our study, once the correlations among neurons in different parts of the brain or other neural systems will be revealed definitively in experimental works.

Chapter 9

Self affinity and dynamic scaling in tumour growth

The state of the art concerning the knowledge of tumour growth has revealed certain of common traits in malignant tumour dynamics. Tumour cells are known to escape from the complex set of biochemical checks that regulate the normal cell cycle, evading in particular programmed cell death or apoptosis, by accumulating genetic mutations. The multiple genetic changes which result in cancer may take many years to accumulate. During this time, the biological behavior of the pre-malignant cells slowly change from the properties of normal cells to cancer-like properties. Pre-malignant tissue can have a distinctive appearance under the microscope. Among the distinguishing traits are an increased number of dividing cells, variation in nuclear size and shape, variation in cell size and shape, loss of specialized cell features, and loss of normal tissue organization. Dysplasia is an abnormal type of excessive cell proliferation characterized by loss of normal tissue arrangement and cell structure in pre-malignant cells. These early neoplastic changes must be distinguished from hyperplasia, a reversible increase in cell division caused by an external stimulus, such as a hormonal imbalance or chronic irritation. The most severe cases of dysplasia are referred to as "carcinoma in situ", referring to an uncontrolled growth of cells that remains in the original location and has not shown invasion into other tissues. Nevertheless, carcinoma in situ may develop into an invasive malignancy. In malignant tumours cells acquire the ability to penetrate the walls of lymphatic and/or blood vessels, after which they are able to circulate through the bloodstream to other sites and tissues in the body, forming a new tumour. The newly formed "daughter"

tumours are called a local metastasis. An important feature stressed by clinical analysis is the relation between malignancy and morphology. In fact clinicians use to forecast tumour evolution, by the observation of tumour contours shape. On the other hand, malignant tumours, after reaching a few cubic millimeters in size develop an irregular microscopic structure [14]. At the beginning of 60's Eden formulate one of the first discrete automata model, in attempting to describe solid tumor growth [229], while recently normal and tumor cell patterns *in vivo* and *in vitro* were characterized by their fractal dimensions and cluster size distribution functions [230, 231], reinforcing the great current interest in the search for basic principles of growth in living organisms, which are the most complex and challenging self-organized systems. For tumour growth, one of the most aggressive phenomena in biology, numerous mathematical models have recently been investigated in order to describe features of tumour development, like front velocity, necrotic core and proliferative rim dynamics, interactions with the extracellular medium and vasculogenesis, with and without the exposure to chemicals and radiation. A central problem in the mathematical modelling of biological processes is the evaluation of its biological relevance. In particular, for the problem of tumour development numerous models have been proposed but the methods to check their consistency with experiments or medical observations are sometimes ambiguous or qualitative. In each case the goal consists in create models that fit with the experimental quantities or functions commonly used by biologist and medical doctors, such as tumour growth speed, spatiotemporal pattern formation, tumour cell population evolution. Mathematicians use to adapt their models to the experiments. An essential question is which of the existing model assumptions are justified for simulating tumour growth, see [232] and chapter 11. From the other hand a complementary approach one can consider, in order to implement mathematical models able to made quantitative predictions on tumour evolution, establishes its starting point on the experimental observations performed by mean of measures originally developed in some mathematical theoretical frameworks. In others words while in the first approach mathematicians create models in order to fit the relevant standard parameters or functions used by biologists in experiments, in the second one they first measure, on biological samples, observables or functions included is a robust and consistent theoretical framework, and then try to trace back tumour dynamics to an existent mathematical model, sharing the same observables behaviour. Here we deal with experiments driven by maths tools, while before one has maths models driven by experiments. One of the advantage

of this approach consists in improve quantitatively the information that can be extracted from experiments, and thus the respective conclusions, with new innovative tools coming from the mathematical disciplines, theoretically more rigorous and stable. Moreover, in moving the problem from experimental observations to a well established model, the efforts in order to better understand tumour growth will be focused on finding a relation between the theoretical model and more realistic and biologically plausible ones, eventually connecting causally short scale (biomolecular, genetic) and large scale (cellular, tissue) mechanisms by mean of multiscale modelling. The first step of the experiments driven by maths tools approach has been performed by Br et al. [15] with some experimental works on *in vivo* cell colonies lines and *in vitro* tumour samples, taking advantage of dynamic scaling theory, originally used to study the problem of thin films surface growth by atomic random deposition, see section 2.5 and [27], in order to characterize the rough surface of solid avascular tumour mass. They observed that the shape of the 1D cutted sections of solid tumour surfaces, i.e. their front of expansion, is a self affine object, it scales as $h(x,t) = \lambda^{-\alpha} h(\lambda x, t)$ with $\alpha > 0$ (with $h(x,t)$ height function, defined in section 2.5), and the scale transformation is anisotropic. This way, the roughness exponent α reveals a morphological characteristic of the interface. One of the statistical observables used in dynamic scaling theory is the mean of the interface width, characterizing the roughness of the interface, given by:

$$W(L,t) = \left\langle \sqrt{\langle h^2 \rangle_L - \langle h \rangle_L^2} \right\rangle_r ,$$

where $< \cdot >_L$ is the mean value over different the system of total size L, and $< \cdot >_r$ over different replicas r (i.e. system realizations). Usually $W(L,t)$ follows the Family-Vicsek *ansatz* behaviour

$$W(L,t) \propto t^\beta f\left(\frac{L}{\xi}\right) \qquad f(u) = \begin{cases} u^\alpha \propto t^{-\beta} & u \ll 1 \quad (L \ll \xi) \\ const & u \gg 1 \quad (L \gg \xi) \end{cases}$$

The values of exponents α and β give indications of the essential surface spatiotemporal dynamic mechanism. The most of individual discrete models implemented to describe surface growth, in which deposition and relaxation rules are explicitly applied to each single atom, are equivalent to a general Langevin stochastic PDE description. Br et al claimed that all avascular solid tumours share the same fractal surface dynamics. In particular, these exponents are typical of the MBE/MH (Molecular Beam Epitaxy/Mullins Herring) surface dynamics, characterized by

cells generated (or deposited) randomly on the surface and then relaxing towards the highest surface curvature region:

$$\frac{\partial h(x,t)}{\partial t} = -K\nabla^4 h(x,t) + F + \eta(x,t). \tag{9.1}$$

Equation (9.1) describe proliferative and diffusive processes exclusively limited to the surface, thus MBE characterization supports the following conclusions on solid tumour growth dynamics:

- Cell diffusion at the colony or tumor borders

- Cell proliferation mainly restricted to the colony or tumour border, i.e., growth is greatly inhibited inside the colony or tumour

- A linear growth for both colonies and tumours, by virtue of the constant growth rate F in equation (9.1)

It is important to underline that, from these observations, MBE/MH equation seems to characterize the essential dynamics of all solid avascular tumours. This universal behaviour could be extremely determinant in planning therapeutic strategies based on tumour mechanic properties, e.g. generating some targeted attack from the extracellular matrix (ECM), in which tumour expands, in order to obstacle the natural cellular dynamics on the front. One attempt in this direction has been made by Br et al. In treating mice with implanted tumours with GM-CSF, a maturation factor for neutrophils. Neutrophils are non specific cells of the immune system, very resistant to high Ph values (acid environment), thus they are able to get very close to the deep valleys of tumour front, developed by MBE dynamics. In these experiments front dynamics universality seems to change in response to the interaction with immune system population cells, modeled in a Langevin approach as a quenched noise [16]. They observed a transition from the MH/MBE universality class to quenched universality, i.e. QEW universality, described by:

$$\frac{\partial h(x,t)}{\partial t} = D\nabla^2 h(x,t) + F + \hat{\eta}(x,h(x,t))$$

Quenched noise $\eta(x,h(x,t))$ determines a new class of Langevin equations, different from the one of equation (9.1), considered in section 2.5. In fact, it is independent from time, and is characterized essentially by its first two moments

$$\langle \hat{\eta}(x,t) \rangle = 0 \quad \langle \hat{\eta}(x,t)\hat{\eta}(x',t') \rangle = 2f_q(x-x'), \tag{9.2}$$

where $f_q(x)$ is a function of distance, rapidly decreasing to 0. This class of equations have been extensively used to model fluid expansion process in an external, disordered medium. Quenched noise takes in consideration the impurities of external medium, in our case it account for the pinning effect generated by neutrophils. QEW equation is characterized by a phase transition, at a critical driving force F_c, between a frozen front ($F < Fc$) and a growing front ($F > Fc$) phase [233]. Br et al. reported in these same experiments this phenomenology, in which pinned surface dynamics block the increasing of the front, thus stopping tumour growth. Fractal scaling could be definitively an efficient tool to evaluate tumour models, and to link their mathematical assumptions with real biological properties.

Chapter 10

Fractal analysis and tumour growth

Tumour growth can be described in terms of mathematical models from different points of view due to its multiscale nature. Dynamic scaling is an heuristic discipline that exploits the geometrical features of growing fronts using different concepts from the theory of stochastic processes and fractal geometry. This chapter is concerned with some problems that arise in the study of tumour-host interfaces. The behaviour of their fluctuations lead to some stochastic evolution equations, which are studied here in the radial symmetry case. Some questions concerning the dynamic scaling of these models and their comparison with experimental results are addressed.

10.1   Introduction

Tumour growth has become a paradigmatic example of multidisciplinar research, where biology and mathematics have met each other to deal with a multiscale problem. The search for a few general laws involving measurable macroscopic quantities is the *leit-motive* of an ever-increasing number of modelization attempts. This special issue puts together a number of examples concerning the mathematical description of cancer. Although this is a difficult task, there is also confidence about the benefits that could be obtained from this research line [234–237].

One of the modelization tools that has recently been applied to describe tumour growth is the so-called *dynamic scaling* of interfaces [27]. Following the

work by Brú et al [15, 16, 28], there is a strong experimental evidence that the fluctuations of these interfaces show a non-trivial spatiotemporal behaviour, which shows the fingerprints of self-affinity. In fact, the interface fluctuations seem to evolve according to some power laws with robust exponents. These findings are the starting point of some continuous models in terms of stochastic partial differential equations (SPDE), that in some appropiate sense share the same statistical properties than the experimental interfaces.

In this chapter we first review the state of the art of dynamic scaling and then address some questions concerning its use in the description of interfaces as those appearing in tumour growth. Dynamic scaling was first developed to describe the roughening of initially flat interfaces due to external noise. Thus, the archetypal example is provided by a SPDE of a function $h(\mathbf{x}, t)$ in the real interval $[0, L]^n$, where L is the system size (fixed), and the initial condition is $h(\mathbf{x}, 0) = 0$. Most of the analytical results and proposed models in the literature have been performed in such a situation, where one looks for a scaling function which encompasses the power-law behaviour of the interface fluctuations. It is an open problem to ascertain if these scaling functions are relevant in a different setting, as that corresponding to radially growing or multivalued interfaces, that are usually found in experiments and real systems. In the latter situation, there is some agreement that if the number or size of the overhangs is residual with respect to the system size, the currently scaling functions still reflect the actual dynamical properties [238].

A key question in our approach concerns the analysis of the fluctuations of radially growing fronts in terms of dynamic scaling techniques. More precisely, a fundamental problem consists in determining if the models exhibiting radial simmetry belong to the currently known universality classes, or else make part of some new ones. A similar remark applies to the case of one-dimensional moving interfaces. This is particularly relevant in the case of experimental models, where the scaling techniques commonly used are one-dimensional. These questions are discussed throughout this chapter which is organized as follows. After a brief account of dynamic scaling and remark on some of its current limitations, we introduce some continuous models in radial symmetry that are expected to belong to well-known universality classes and describe their scaling behaviour. Then we describe some one-dimensional (in space) examples where we distinguish between dilatational and agreggation dynamics for moving interfaces and find very different scaling behaviors for them, a fact that calls for further analysis of experimental

interfaces.

10.2 A bird's eye view of Dynamic Scaling:

The spontaneous generation of fractal interfaces or fronts has been observed in many natural processes [27, 79], and fractal geometry is a mathematical tool that allows us to compute some of their morphological properties. A basic hypothesis is that these objects exhibit self-similarity, that is, their statistical properties do not change under isotropic scale variations. The lack of any characteristic length is a common property of fractal objects. Dynamic scaling deals with fronts that roughen in time but remain graphs (i.e. can be described by means of continuous functions) showing self-affinity. In this case, the interface scales as $h(\vec{r}, t) \sim b^{-\alpha} h(b\vec{r}, t)$ with $\alpha > 0$ and the scale transformation is anisotropic. This way, the *roughness exponent* α reveals a morphological characteristic of the interface. To account for that roughening and self-affine properties, a number of discrete and continuous growth models have been proposed. In the continuum setting and under the assumption of linear symmetry (that is, one space dimension), they are usually written in terms of Langevin-like equations:

$$\frac{\partial h(\vec{r}, t)}{\partial t} = F + G(h(\vec{r}, t)) + \eta(\vec{r}, t) \quad , \tag{10.1}$$

where $h(\vec{r}, t)$ stands for the growing front, G is a generic function of $\vec{r}$, t, h and its derivatives, F is the driving force and $\eta(\vec{r}, t)$ is the noise term which accounts for the roughening of the front. Then, the growing process proceeds along the following rules: mass is created over the surface $h(\vec{r}, t)$ with a mean rate F and $\eta(\vec{r}, t)$ accounts for deviations from the local mean rate (for instance, deviations from the cell duplication mean time). The noise is due to the averaging of microscopic degrees of freedom (i.e. noisy environment, microscopic biochemical processes...). The functional G represents the processes by which the surface relaxes (i.e. surface diffusion, surface tension) and plays the main role in determining both the short-time and steady state properties of the growing interface. One usually finds that an initially flat front roughens in time, attaining in the long-time limit a steady state in which some observables show non-trivial spatial scaling. Henceforth the interface is studied as an stochastic process, and the evolution of its fluctuations is the main point at issue. Because of the interface self-affinity, fluctuations display

power law behaviours. To begin with, let us consider for simplicity the case of a (1+1) dimensional interface $h(x, t)$. It can be characterized by means of the *interface width*:

$$W(L, t) = < [h(x, t) - \bar{h}(t))^2]_L >^{1/2} \quad , \tag{10.2}$$

where $\bar{h}$ is the mean height of the interface and fluctuations around $\bar{h}$ are averaged over the whole system of size L and over n realizations of the experiment or model as denoted by $<>$. Moreover, the *height-height correlation function* $C(l, t)$ given by:

$$C(l, t) = < [(h(x, t) - h(x + l, t))^2]_L > \quad , \tag{10.3}$$

can be used to study the small-scale fluctuations of size l. Finally, the *power spectrum density*:

$$S(k, t) = < \hat{h}(k, t)\hat{h}(-k, t) > \quad , \tag{10.4}$$

where

$$\hat{h}(k, t) = L^{-1/2} \sum_x [h(x, t) - \bar{h}(t)] \exp(ikx) \quad , \tag{10.5}$$

describes the scaling behavior of the Fourier modes of the interface and obeys the following relationships [239]:

$$C(l, t) \sim \int_{2\pi/L}^{\pi/a} \frac{dk}{2\pi} [1 - \cos(kl)] S(k, t) \quad ,$$

$$W^2(L, t) = \int \frac{dk}{2\pi} S(k, t) \quad . \tag{10.6}$$

These quantities are instrumental to describe the scaling behavior of the fluctuations of a rough interface around its mean position. A typical behavior of the interface width $W(L, t)$ can be summarized as follows. For short times, the width increases as a function of time, $W(L, t) \sim t^\beta$, where β is called the *growth exponent*. This power-law behavior is followed by a saturation regime where $W(L, t) = W_{sat}$. The crossover occurs at a time t_c, when the lateral correlation length reaches the system size. Both the saturation width and crossover time depend on the system size, and one usually has that $W_{sat}(L) \sim L^\alpha$ and $t_c \sim L^z$, where α is the *roughness exponent* and z is the so-called *dynamic exponent*. One readily sees that $z = \alpha/\beta$ in order to match the $t \to t_c^\pm$ limits. These empirical laws can be summarized in

a scaling ansatz for the interface width:

$$W(L,t) = L^\alpha f(L/\zeta(t)) \quad , \qquad f(u) \sim \begin{cases} u^\alpha & \text{if} \quad u \gg 1 \quad , \\ \\ \text{const} & \text{if} \quad u \ll 1 \quad , \end{cases} \qquad (10.7)$$

where $\zeta(t) \sim t^{1/z}$ stands for the correlation length parallel to the interface. The function $f(u)$ is the so-called *scaling function* which captures the aforementioned behavior (see figure 10.1). If a particular model or experimental system is assumed to obey this ansatz, a set of graphs $W(L,t)/t^{\alpha/z}$ versus $L/t^{1/z}$ for several values of L must collapse into a single curve corresponding to the $f(u)$ behavior above. But the whole scaling picture turns out to be less clear when the local scales are
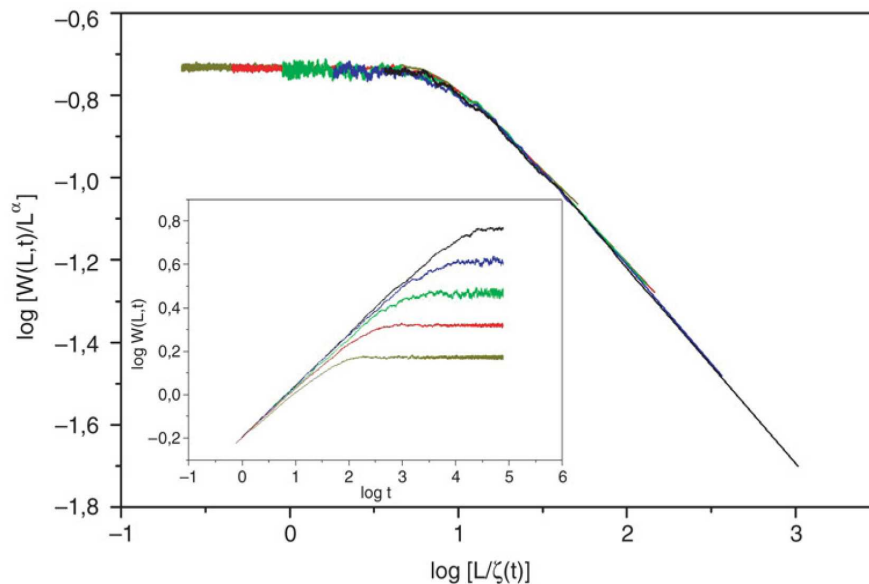
FIGURE 10.1: Example of data collapse of the interface width according to equation (7) for simulations of size 64, 128, 256, 512, 1024 using $\alpha = 1/2$, $z = 2$. Inset: The original log-log plot of $W(L,t)$ versus time.

involved. A variety of short-time behaviors have been observed [28, 240–242] and, as a consequence, $C(l,t)$ may show an anomalous scaling that can be accounted for by means of more refined ansatzs. Arguably, the more generic scaling behavior proposed to date has been introduced in [241] in terms of the power spectrum

density:

$$S(k,t) = k^{-(2\alpha+1)}s(kt^{1/z}) \quad,$$

$$s(u) \sim \begin{cases} u^{2(\alpha-\alpha_s)} & if \quad u \gg 1 \quad, \\[2ex] u^{2\alpha+1} & if \quad u \ll 1 \quad, \end{cases} \tag{10.8}$$

where $s(u)$ is a new scaling function and α_s is the *spectral roughness exponent*. The scaling of the correlation function $C(l,t)$ can be computed using (10.6):

$$\sqrt{C(l,t)} = t^\beta g(l/\zeta(t)) \quad, \tag{10.9}$$

but now several cases arise concerning the choice of α_s. Whether the spectral roughness exponent is lower or greater than 1, the scaling function is:

$$g_{\alpha_s<1}(u) \sim \begin{cases} u_s^\alpha & if \quad u \ll 1 \quad, \\ \mathrm{const} & if \quad u \gg 1 \quad, \end{cases} \tag{10.10}$$

or

$$g_{\alpha_s>1}(u) \sim \begin{cases} u & if \quad u \ll 1 \quad, \\ \mathrm{const} & if \quad u \gg 1 \quad. \end{cases} \tag{10.11}$$

Thus, there are two main categories of scaling behavior. If $\alpha_s < 1$, this exponent describes the scaling of small-length scales, and is called the local roughness exponent α_{loc}. On the contrary, when $\alpha_s > 1$ the small-length scales show a trivial scaling with $\alpha_{loc} = 1$. This generic picture includes most of the scaling behaviors found so far in models and experiments. For example, tumour growth has been experimentally shown to obey an infrequent superrough dynamics [15, 28], characterized by $\alpha_{loc} = 1$ and $\alpha = \alpha_s > 1$. Using the corresponding scaling function (11), one can see that the short time behavior is $\sqrt{C(l,t)} \sim lt^{\beta^\star}$ (instead of the standard behavior $\sqrt{C(l,t)} \sim l$), where $\beta^\star$ is called the *anomalous growth exponent*, $\beta^\star = (\alpha - \alpha_{loc})/z$. Therefore anomalous fluctuations at small scales are particularly relevant in this case. We refer the reader to [241] for a complete description of the scaling behaviours that follow from (10.8).

The aim of dynamic scaling is to perform a classification of growth processes into a few universality classes, to develop general tools to ascertain their asymptotic behaviour. Every set of critical exponents is intended to define a universality class, where some dynamical features are shared by all the processes belonging to that class. When implementing such approach, a number of open problems

arise that are poorly understood , particularly in size-changing domains as those corresponding to tumour growth. For instance, the steady state scaling properties after saturation are often required to determine the actual universality class the process belongs to. But if one has to deal with a non-fixed size interface, the steady state could be out of reach. Moreover, the scaling functions obtained for fixed domains need not represent such a system. In particular, this is the case for radially growing interfaces, where less is known about the universality properties of the simplest models, and there are few analytical results available.

A physical system we are particularly interested in is solid tumour growth. Cell colony growth and tumour-host interfaces have been studied experimentally using dynamic scaling. In [15, 28], it was found that the fluctuations of these interfaces scale as those of the MBE universality class in $(1 + 1)$ dimensions:

$$\frac{\partial h}{\partial t} = -K\frac{\partial^4 h}{\partial x^4} + F + \eta(x,t) \quad , \tag{10.12}$$

where $h(x,t)$ represents the cell colony or tumour-host profile. The fourth order derivative accounts for a local potential that is proportional to the curvature of the interface ([243, 244]). This term describes a surface diffusion current at the interface that transports mass from high curvature to low curvature locations. Considering the fact that almost all proliferating cells are located at an outer rim of the colony, this surface diffusion accounts for the movement of newly produced cells along the tumour border. Cells diffuse until they come to rest in, and gradually fill, the available concavities of the tumour front. Actually, experimental interfaces often grow in radial symmetry (at least in early stages), but the relationship between scaling functions in one-dimensional and radial growth is not known as yet. We address this issue in the following Section. As a starting point, in this paper we study the scaling behaviour of two models in radial symmetry that are expected to belong to the EW and KPZ universality classes. Different dynamical behaviours showing anomalous fluctuations (as for instance the MBE case illustrated by (12)) will be discussed elsewhere.

10.3 Scaling analysis of continuum models in radial symmetry.

Bearing in mind our previous remarks, in this section we examine some general questions about the scaling properties of stochastic equations in radial symmetry, in an attempt to clarify some issues concerning the proper handling of radial interfaces. To begin with, consider a general growth equation for a surface in a $(D+1)$-dimensional space (cf. [245]):

$$\partial_t \vec{r}(\underline{s}, t) = \hat{n}(\underline{s}, t) G(\vec{r}(\underline{s}, t)) + \vec{F}(\underline{s}, t) \quad , \tag{10.13}$$

where the vector $\vec{r}(\underline{s}, t)$ runs over the surface as $\underline{s}$ varies in the parameter space. The outer normal vector to the surface is denoted by $\hat{n}$, and G is a functional containing a deterministic growth mechanism that causes growth along the normal. Finally, a random ad-hoc force $\vec{F}$ is introduced . From this general model, one can obtain different equations according to the physics of the problem (which specifies the form of G and $\vec{F}$) as long as reparametrization invariance is satisfied. This requires that only terms that are independent of the particular choice of $\underline{s}$ should appear in the equation. For instance, one can consider the well-known one-dimensional KPZ equation:

$$\frac{\partial h}{\partial t} = \nu \nabla^2 h + \lambda (\nabla h)^2 + \eta(\vec{r}, t) \quad , \tag{10.14}$$

which contains a surface diffusion term that minimizes the surface tension energy ($A = \nu \int_0^1 \sqrt{g} ds$, where g is the determinant of the metric tensor, $g = |d\vec{r}/ds|^2$), a term of preferential growth normal to the interface with a rate λ, and a noise term (for a recent work that considers the curvature term of the MBE equation, see [246]). According to these rules, the radial version of (14) has been obtained from (13) in [247]:

$$\frac{\partial \vec{r}}{\partial t} = \nu \frac{1}{\sqrt{g}} \frac{\partial}{\partial s} \left(\frac{1}{\sqrt{g}} \frac{\partial \vec{r}}{\partial s} \right) + \lambda \hat{n} + \eta \quad , \tag{10.15}$$

where the noise term has the form:

$$< \eta^\alpha(s, t) \eta^\beta(s', t') > = 2D \delta^{\alpha\beta} \frac{\delta(s - s')}{\sqrt{g(s)}} \delta(t - t') \quad , \tag{10.16}$$

This precise choice for the noise ensures that the previous equation is independent of the parametrization selected. If we use polar coordinates ($x(s,t) = \rho(s,t)\cos\theta(s,t), y(s,t) = \rho(s,t)\sin\theta(s,t)$), then $g = \rho_s^2 + \rho^2\theta_s^2$, and assuming that $\rho(s,t) = \rho(\theta,t)$ (a single-valued interface), we obtain:

$$
\frac{\partial\rho}{\partial t} = \nu\frac{1}{\sqrt{\rho_\theta^2 + \rho^2}}\frac{\partial}{\partial\theta}\left(\frac{\rho_\theta}{\sqrt{\rho_\theta^2 + \rho^2}}\right) - \frac{\nu}{\rho}\left(1 + \frac{\rho_\theta^2(\rho_\theta^2 - \rho\rho_{\theta\theta})}{(\rho_\theta^2 + \rho^2)^2}\right) +
$$
$$
+ \frac{v}{\rho}\sqrt{\rho_\theta^2 + \rho^2} + \frac{(\rho_\theta^2 + \rho^2)^{1/4}}{\rho}\eta(\theta,t) \quad ,
$$

(10.17)

where $\rho_\theta = \partial\rho/\partial\theta$ and the noise has the following correlations:

$$
< \eta(s,t)\eta(s',t') > = 2D\delta(\theta - \theta')\delta(t - t') \quad .
$$

(10.18)

A further assumption is to consider the large–radius limit $\rho_\theta/\rho \ll 1$, to obtain a simplified version of the KPZ equation in radial symmetry:

$$
\frac{\partial\rho}{\partial t} = \frac{\nu}{\rho^2}\frac{\partial^2\rho}{\partial\theta^2} - \frac{\nu}{\rho} + v\left(1 + \frac{1}{2\rho^2}\left(\frac{\partial\rho}{\partial\theta}\right)^2\right) + \frac{1}{\sqrt{\rho}}\eta(\theta,t) \quad .
$$

(10.19)

This is the equation we are going to consider next.

10.3.1   EW universality

In the case where the surface tension term dominates, the stochastic growth equation would be the radial counterpart of the Edwards-Wilkinson equation:

$$
\frac{\partial\rho}{\partial t} = \frac{\nu}{\rho^2}\frac{\partial^2\rho}{\partial\theta^2} - \frac{\nu}{\rho} + v + \frac{1}{\sqrt{\rho}}\eta(\theta,t) \quad ,
$$

(10.20)

where a constant velocity term v is maintained. The main difference with respect to the one-dimensional case is that the equation is nonlinear. Moreover, let us consider that the interface is self-affine, so that if we scale an arc-length element as $l \to bl$, the interface scales as $\rho \to b^\alpha\rho$. This implies that the angle variable scales as $\theta \to b^{1-\alpha}\theta$. Finally, the dynamic exponent governs the time scaling, $t \to b^z t$. The previous equation is invariant under this transformation if the critical exponents are those of the EW universality class ($z = 2$, $\alpha = 1/2$) but only when the nonlinear term ν/ρ is disregarded. When this last isotropic shrinking

term is kept, the equation is not invariant under the $\rho \rightarrow -\rho$ inversion, and an interface of initial radius ρ_0 can either grow or collapse. This fact breaks down the traslational invariance that is an exact symmetry in the linear case, and does not allow to study the dynamics in a co-moving frame reference $h \rightarrow h + vt$. However the actual significance of the non-linear term on the scaling properties could be marginal, by virtue of the v constant term in the large-radius limit. So, we want to study if, above a critical radius, the previous equation belongs to the EW universality class. The critical radius can be easily obtained. To this end, we make use of the following expansions:

$$\rho(\theta, t) = \sum_{n=-\infty}^{+\infty} \rho_n(t) e^{in\theta} \quad , \qquad \eta(\theta, t) = \sum_{n=-\infty}^{+\infty} \eta_n(t) e^{in\theta} \quad , \tag{10.21}$$

with $< \eta_n(t)\eta_n(t') > = \frac{D}{\pi}\delta(t - t')$. By substituting in equation (10.20) and using the center of mass as the origin of the radial variable, one can readily obtain for radially symmetric solutions:

$$\rho_0(t) = -\frac{\nu}{\rho_0} + v + \frac{\eta_0}{\sqrt{\rho_0}} \quad . \tag{10.22}$$

Therefore, the deterministic zeroth-order estimate for the critical radius is $\rho_c =$
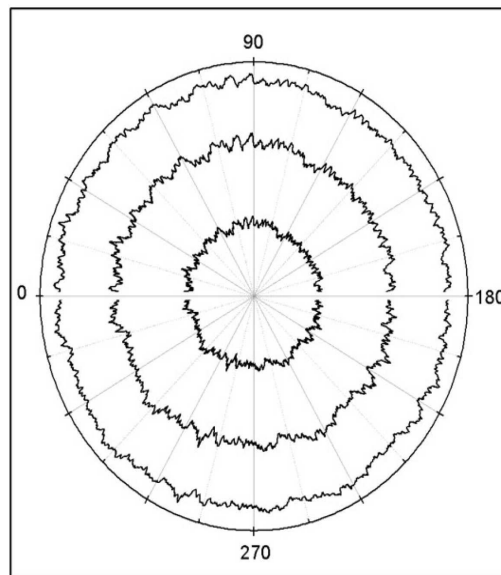
FIGURE 10.2: Numerical solution of the radial EW equation.

ν/v. We have performed the numerical integration of equation (10.20) for an initial radius greater than ρ_c (see figure 10.2). figure 10.3 shows the behaviour

of $W(L,t)$ versus time. As shown therein, a power-like growth t^β with $\beta \sim 1/4$ is sustained for long times of evolution. Thus, the growth exponent is similar to that of the one-dimensional EW universality class. Moreover, this result does not depend upon the particular value of the velocity v, whenever the condition $\rho(t=0) \gg \rho_c$ is satisfied, as can be seen in the inset of figure 10.3. An intriguing fact is that the fluctuations do not saturate for long times, as it happens in the one-dimensional case for not too long evolutions (see Figure 1). This novel feature may be related with the non-fixed size of radial interfaces. We have noticed above that the saturated state is reached when the correlation length is equal to the system size, and this might not happen for a growing size interface. As a matter of fact, taking into account that the lateral correlation length scales as $l_c \sim t^{1/z}$, saturation will take place whenever the system size grows slower than $t^{1/z}$ (for an example of this case see [238]). In the current example, it can be seen (data not shown) that $L(t) \sim t > t^{1/2}$, and saturation is out of reach. Therefore $W(L,t)$ does not encodes
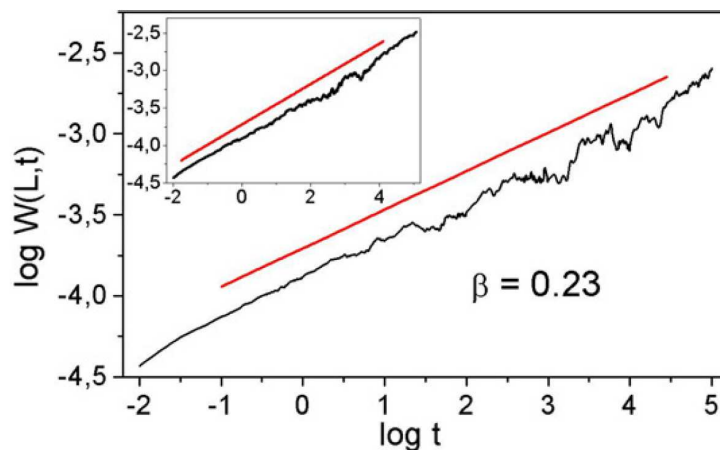
FIGURE 10.3: Time evolution of $W(L,t)$ for the radial EW equation. The parameters are: $\rho(t=0) = 10$, $\nu = 0.01$, $D = 1$, $v = 0.003$. Inset: The same for $v = 0.1$. A best fit yield a slope of 0.23 ± 0.03, the value of β for the EW universality class.

the whole scaling properties of equation (10.20), and we need to proceed further in order to obtain the complete set of critical exponents. To that end, we would like to make use of either the correlation function $C(l,t)$ or the power spectrum density $S(k,t)$. A graph of the former for several times is shown in figure 10.4. These data are obtained by computing $C(l,t)$ as a function of the arc-length variable l, while the discretization is performed with $d\theta$ fixed. Then the element of arc-length grows with time as $dl \sim \bar{\rho}(t)d\theta$, as so does the arc-length of the full interface. This fact

can be readily seen in figure 10.4 by keeping track of the minimum and maximum abscissa for different times. Notice that at first sight the correlation functions look similar to those of a one-dimensional equation. In fact, the smaller scales below the correlation length follow a power-law $C(l, t) \sim l^\alpha$, with $\alpha \sim 0.5$ (the value of the EW universality class, as predicted by the invariance of equation (10.20) without the nonlinear term). In view of the previous remark we may wonder which
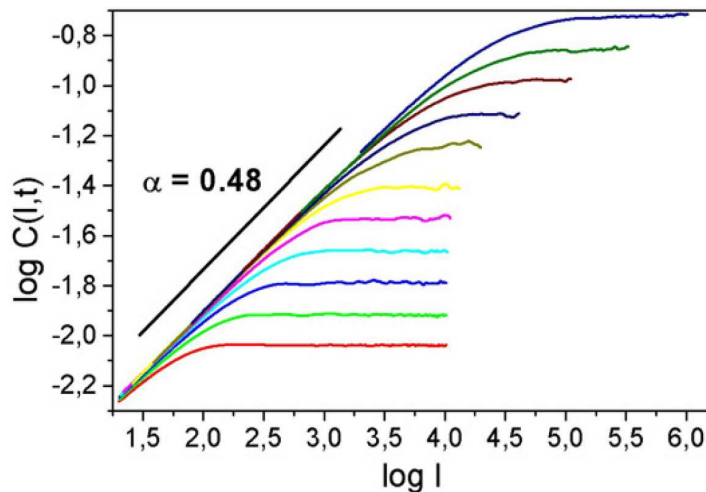
FIGURE 10.4: Correlation function for the radial EW equation for several times. A best fit yield a slope of 0.48 ± 0.03, the value of α for the EW universality class.

scaling function would correspond to the behaviour of $C(l, t)$ just described. We have mentioned above that there is a lack of analytical results for this kind of systems, although some heuristic proposals have recently been discussed (see next section). However, when the interface is parametrized according to the arc-length variable, the currently known scaling functions are very often employed. Then, if we make use of the same scaling function than that of the one-dimensional EW equation (see the previous section), we obtain a good data collapse (figure 10.5) using the theoretical values $z = 2$ and $\alpha = 1/2$.

10.3.2 KPZ universality

The celebrated nonlinear KPZ equation (14) [248] has been proposed to describe the scaling properties of a number of systems far from equilibrium. This equation accounts for lateral growth through the term $(\partial_x h)^2$ (see equation 14) that
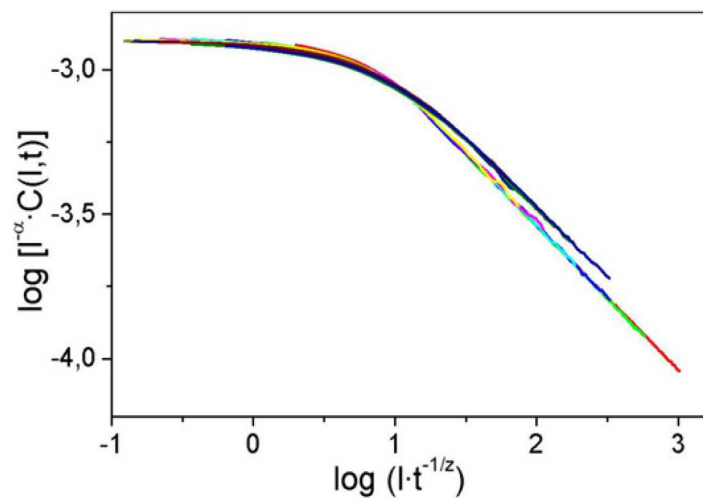
FIGURE 10.5: Data collapse of $C(l,t)$ in figure 10.4 according to equations 9–10.

dominates the scaling behavior of the steady state. This nonlinearity prevents us from obtaining the critical exponents by power counting argument as for the EW equation. However, in dimension $d = 1$, there are two properties that can be used to circumvent a more difficult computation. In fact, the KPZ equation can be mapped into the Burgers equation for $\mathbf{v}$ by changing variables as $\mathbf{v} = -\nabla h$. Thus, they share the same Galilean's invariance that leads to the relationship $\alpha + z = 2$. Moreover, an application of the fluctuation-dissipation theorem tell us that the local slopes ∇h are distributed according to a gaussian distribution, and therefore the interface can be generated as a Brownian motion. In this way, we obtain $\alpha = 1/2$ and, as a consequence, $z = 3/2$. Whether the same arguments can be applied for equation (19) in other cases is unknown. As a matter of fact, the invariant form of the Langevin equation in the case of a growth term derived from a potential is [245]:

$$\frac{\partial \vec{r}(\underline{s}, t)}{\partial t} = -\sqrt{g} \quad \Gamma \frac{\delta H}{\delta \vec{r}(\underline{s}, t)} + \eta(\underline{s}, t) \quad . \tag{10.23}$$

A classical argument shows that the associated Fokker-Planck equation has a stationary solution of the form [249]:

$$P[\vec{r}(\underline{s}), t \to \infty] \sim \exp\left[-\frac{H(\vec{r}(\underline{s}))}{T}\right] \tag{10.24}$$

for the configurational probability $P[\vec{r}(\underline{s}), t]$. In the case of the KPZ equation, we have:

$$H(\vec{r}(\underline{s}) = H_{KPZ} = \int d\underline{s}(D\sqrt{g} - vh) \qquad (10.25)$$

which is unbounded as $h \to \infty$. Thus, the KPZ equation does not have the previous equilibrium distribution $P[\vec{r}(\underline{s}), t \to \infty]$. Anyway, it is not clear if (as it happens in linear symmetry), a different choice can be done for the stationary solution leading to the exact values of the critical exponents. The standard approach consists instead in making use of renormalization group techniques to derive the scaling behaviour of this equation [27]. Following the same scheme as for the EW
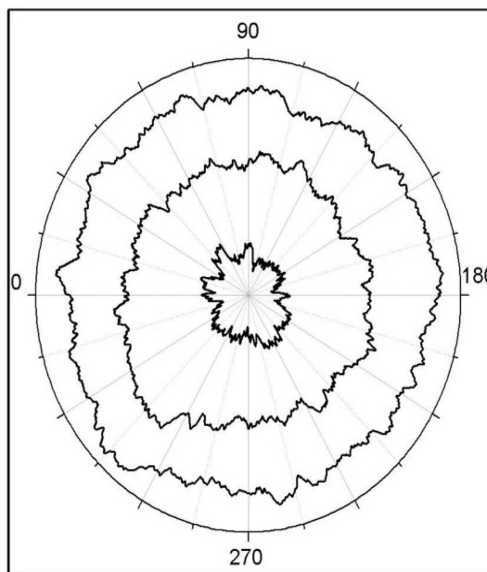
FIGURE 10.6: Numerical solution of the radial KPZ equation at different times.

equation, we have performed the numerical integration of equation (19). The critical radius remains the same in this case, because the nonlinear term does not contribute to the zeroth-order radially symmetric solution in the linear stability analysis. Figure 10.6 shows some simulations of expanding interfaces. The next figure 10.7, describes the time evolution of the fluctuations $W(L, t)$. It can be readily seen that, after a transient regime dominated by the EW term, the interface width grows as $W(L, t) \sim t^\beta$ with $\beta \sim 1/3$, close to the theoretical value of the KPZ universality class. We remark on pass that the presence of transient regimes is usually found whenever several terms appear in the growth functional, and the interplay between these terms (depending on the model and the value of the parameters) determines the crossover times. Again, due to the fact that the system size is not constant, we need to look at the correlations or power spectrum
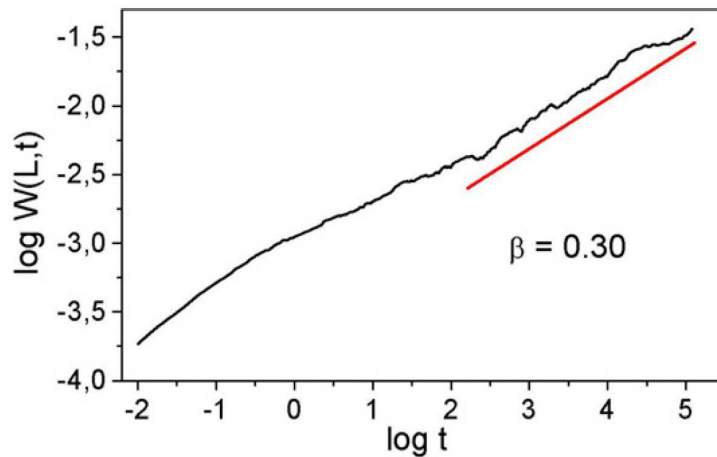
FIGURE 10.7: Time evolution of $W(L,t)$ for the radial KPZ equation. The parameters are: $\rho(t=0) = 10$, $\nu = 0.001$, $D = 1$, $v = 0.01$. The straight line is a best fit with slope 0.30 ± 0.03, close to the value of β for the KPZ universality class.

density to obtain the remaining critical exponents. For instance, the behavior of the correlations (data not shown) is again well described by the Family-Vicsek scaling function, and we obtain $\alpha = 1/2$, so that $z = 3/2$. It thus seems reasonable to think that in the large radius approximation, the KPZ equation in radial symmetry belongs to the expected universality class.

10.4 Aggregation vs. dilatation: a model problem.

In this section we want to focus in one-dimensional, size changing domains, paying attention to the particular growth properties of the system that one wants to study. As a starting point, we introduce two main categories of systems. Some systems grow by aggregation or generation of new particles over the surface (for instance, in the case of a cell colony). In this situation, there exists a natural lower cut-off, namely, the typical size of the particles σ. But in a coarse-grained description, the same system can be envisaged as a continuum, and the growing size L is accounted for a dilatational term. Actually, these two categories correspond to the limits $L/\sigma \to 1$ and $L/\sigma \to \infty$, respectively. The main idea under this classification is that, in practice, one always has to deal with a discrete function for the interface position, and therefore the discretization should be consistent with one of the

aforementioned limits. In fact, just from an analytical point of view, one has to take care of these limits to obtain the scaling proposal. For instance, the generic dynamic scaling introduced in Section 2 was obtained after a careful examination of the limits $a \to 0$, $L \to \infty$ and $\zeta/L \to \infty$ (where a is the lower cut-off and ζ stands for the correlation length) which do not commute [241]. In fact, the ambiguity of the scaling analysis in the case $L = L(t)$ comes from the fact that the $\zeta/L \to \infty$ limit could be unreachable. Because of the lack of analytical results, some authors have introduced heuristic scaling functions to address this problem. In [250], a generalization of the generic dynamic scaling was performed by changing variables as $L \to f(t)L$, $l \to f(t)l$, $k \to k/f(t)$ (k being the Fourier variable) where $f(t)$ stands for a dilatational factor that is intended to rescale the system before the critical exponents are involved. The strong hypothesis underlying this proposal is that $f(t)$ affects equally all length scales. It is then clear that a successful application of this ansatz will depend upon the selected limit, and its validity in systems with a well-known dynamics has not been checked as yet.

We have studied a couple of simple problems in one space dimension that could illustrate these ideas. The first one is a discrete model belonging to the EW universality class, where the discretization length a is constant throughout the evolution. We begin with a system of size L and new particles are created over the surface according to a prescribed rule. Since the system evolves according to the EW dynamics, the correlation length grows as $l_c \sim t^{1/2}$. Thus, we choose a dilatational factor of the form $f(t) \sim t^\gamma$, and we study the cases $\gamma < 1/2$, $\gamma > 1/2$. The aggregation rule is as follows: according to $f(t)$, a random position x_r is chosen at the interface at consecutive times. We choose at random a nearest neighbour of x_r, denoted by x_r^0. A new interface position is created between the two points to locate the newly created particle y, and $h(y) = 1/2(h(x_r) + h(x_r^0))$. Henceforth, the interface evolves according to the EW equation in $(1+1)$ dimensions. This model problem behaves in a standard way, and remains inside the EW universality class. In the following plots we show the behaviour of the fluctuations and the power spectrum density. From the value of β in figure 10.8, and the critical exponents that collapse the power spectrum data in figure 10.9, it follows that a EW-like dynamics is achieved independently of the particular value of γ. It is worth to mention that this is not a trivial fact, due to the anomalous fluctuations induced by the aggregation rule. In fact, the source of anomalous scaling behaviours has to do with the evolution of the local slopes that grow as $< |\nabla h| > \sim t^{\beta^*}$, where β^* is the anomalous growth exponent. Our aggregation rule does not preserves the

value of the local slopes, but the results obtained seem to confirm the weakness of this effect.
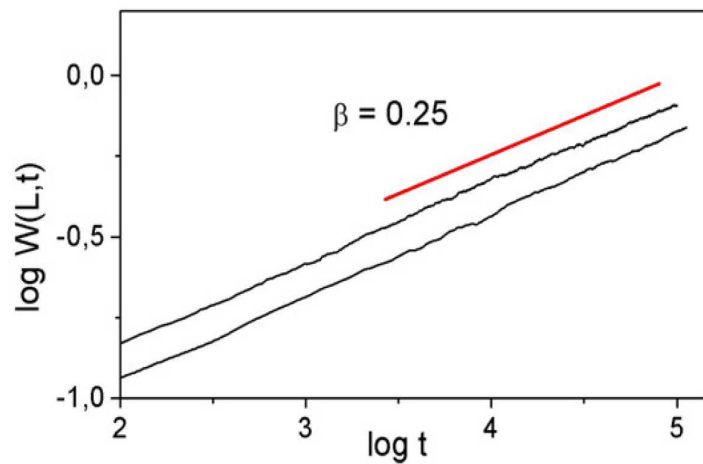
FIGURE 10.8: Time evolution of $W(L,t)$ for the aggregation model for $\gamma = 0.4$ (lower curve) and $\gamma = 0.6$. The red line has a slope of 0.25, the value of β for the EW universality class.
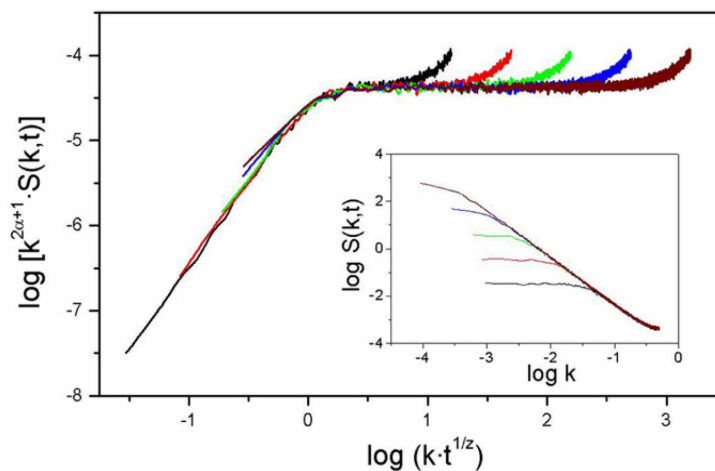
FIGURE 10.9: Data collapse for the density of the power spectrum of the aggregation model using $\alpha = 0.5$, $z = 2$. Inset: Original data.

In what follows, we want to reproduce graphically some of the arguments that were just outlined concerning the accessibility of the steady state. In these simulations we have computed the evolution of the lateral correlation length. Using the correlation function, this can be done by matching the l^α regime and the saturated region. In figure 10.10 the correlation function is represented along with the power-law fit of the computed $\zeta(t)$ and the system size $L(t)$. It can be seen

that for $\gamma = 0.4 < 1/z$, the correlation length will eventually equal the system size and the scaling properties of the steady state will be obtained. Not surprisingly, if $\gamma = 0.6 > 1/z$, the steady state is not reached. The second model problem that
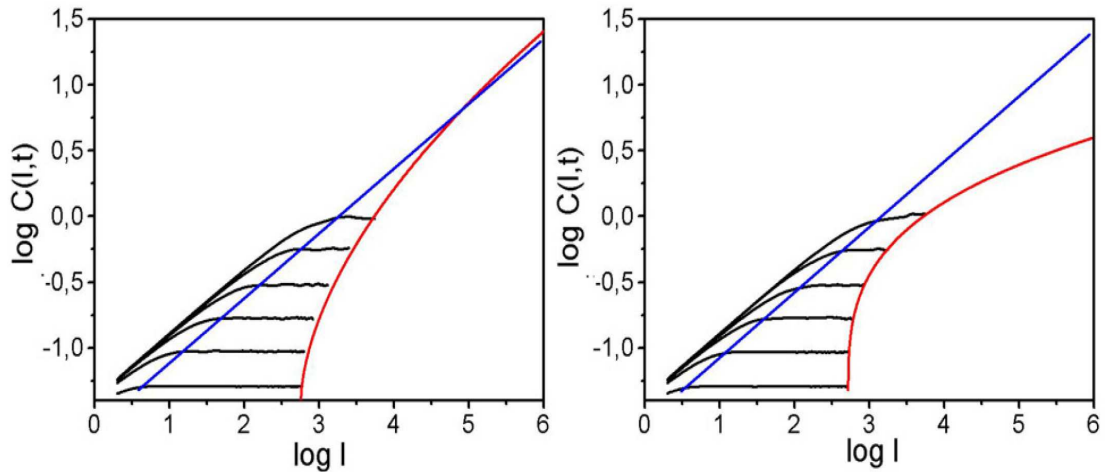
FIGURE 10.10: Comparison of the evolution of the correlation length (blue) and the system size (red) for $\gamma = 0.4$ (left) and $\gamma = 0.6$ (right).

has been analyzed concerns the properties of a pure dilatational dynamics. To do this, we have performed numerical integrations of the EW equation in linear symmetry with a non-constant discretization length $dx' \to f(t)dx$. Again, we impose the particular form of $f(t)$ similarly to the previous model problem. But in this case, the growth rule equally enlarges all length scales greater than dx. In this manner, this model problem is intended to be the large radius limit of a radially growing interface. We do not discuss the behaviour of the correlation length and the approach to the steady state, referring the reader to the previous aggregation problem because the same ideas apply here. On the contrary, there is now a number of novel features that have not appeared before, closely related with the particular character of this model. To begin with, one can figure out what happens when the discretization length begins to grow. As the distance between neighbour points increases, the intensity of the diffusion term is weakened while the intensity of the noise remains constant. Therefore, there is a continuous source of fluctuations at the smallest length scales that are not triggered by diffusion and an anomalous behaviour is expected. Eventually, the noise dominates the process, and a pure Poissonian growth will be observed with $\beta = 1/2$, while the crossover time should depend upon the dilatational velocity. This hypothesis can be checked on in figure 10.11 below. An intriguing feature of this model is the different behaviours of $C(l, t)$ and $S(k, t)$. Figure 10.12 shows the evolution
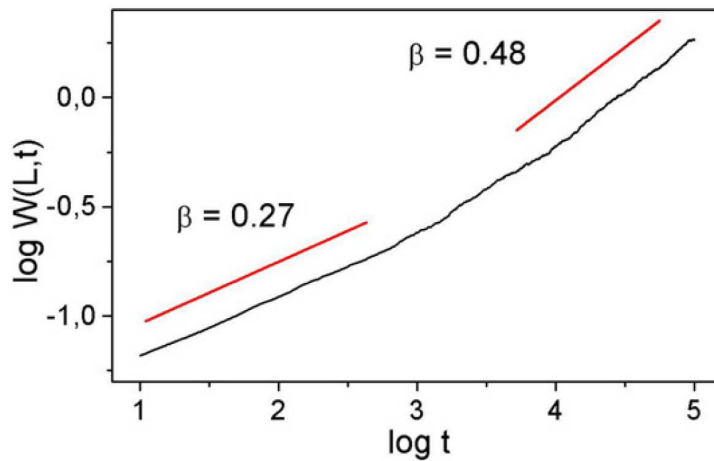
FIGURE 10.11: Time evolution of $W(L,t)$ for the dilatational model for $\gamma = 0.6$. The straight lines have a slope of 0.27 ± 0.01, the value of β for the EW universality class, and 0.48 ± 0.01 corresponding to noise dominance.

of the power spectrum density in time, with the corresponding displacement of the Fourier modes k due to dilatation. Surprisingly, $S(k,t)$ does not show any anomalous behaviour and a good data collapse is obtained using the EW critical exponents and the Family-Vicsek scaling hypothesis. On the contrary, anomalous
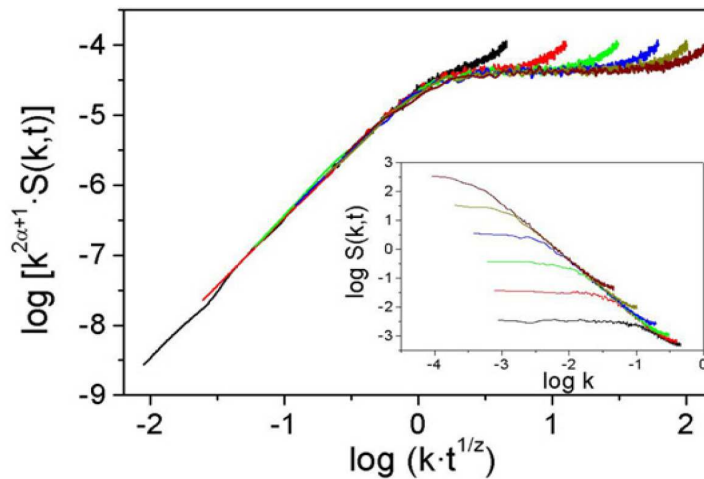
FIGURE 10.12: Data collapse for the density of the power spectrum of the dilatational model using $\alpha = 0.5$, $z = 2$. Inset: Original data.

fluctuations are displayed by the correlation function, as can be noticed from the small-l behaviour in figure 10.13. It is apparent that we need a different scaling function to take into account these anomalous fluctuations. In fact, inspecting the $C(l,t)$ behaviour one can observe that the saturation value does not follows

the usual power-law regime, and a progressive shift develops. This may be due to the additional correlations induced by the noise dominance. On the other hand, we have computed (data not shown) the correlation length, and show it obeys a standard power law. This suggests trying a collapse using the scaling hypothesis:

$$C(l,t) \sim (lf(t))^{\alpha_{loc}} G\left(\frac{\zeta}{l}\right) \quad , \qquad (10.26)$$

where $G(u)$ is again the scaling function corresponding to the Family-Vicsek ansatz. The obtained data collapse can be seen in Figure (13). The scaling be-
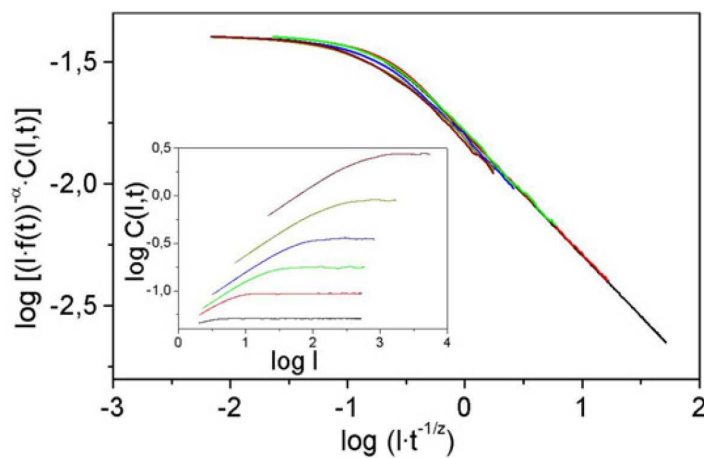
FIGURE 10.13: Data collapse for the correlation function of the dilatational model using $\alpha = 0.5$, $z = 2$ and the scaling function in the text. Inset: Original data.

haviour of this last model problem resembles that of a superrough dynamics, where the anomalous fluctuations are not shown by power spectrum density. In any case, the unusual features of this example are mentioned here to remark the ambiguous status of dynamic scaling techniques concerning the study of growing-size systems both in mathematical models and real systems.

10.5 Discussion

The stochastic approach to the modelling of growth processes intends to provide some insight about the macroscopic features of developing patterns. Roughly speaking, it can be considered as a first step to describe the different mechanisms

that enter into the dynamics, where the microscopic degrees of freedom are gathered as a random event. This is actually the main idea behind dynamic scaling and the main reason of its wide-ranging scope: to capture the core properties before coming into details. We have recalled some of the various ideas that are used in this technique, which have their origins in the theory of stochastic processes, non-equilibrium thermodynamics and critical phenomena, and fractal geometry.

With tumour growth in mind, there is a number of practical problems that have to be overcome in order to analyze cell colony interfaces and to eventually achieve, a complete analytical description of interface growth. At first, the main issue to be handled is the analysis of fluctuations in radially propagating fronts. We have shown that using the customary parametrization of the interface in terms of the arc-length variable we are able to obtain the whole set of critical exponents in this case, at least on the large-radius approximation of one of simpler growth equations. The highly non-linear character of the general model prevents us from doing an heuristic approach in this case, and a complete numerical study of the fluctuations as well as a rigorous derivation of the steady-state properties (i.e., by means of renormalization arguments) has not been achieved as yet. In this respect, an intriguing question is how to handle the limit $\zeta(t)/L \to \infty$ when $L(t)$ is a increasing function. We have shown numerically an otherwise natural result: the steady state is not attained whenever $L(t)$ grows faster than the correlation length. Although in this case most of the scaling concepts are still valid, the formal derivation of new scaling functions is tricky. A reasonable working plan would be to study a broad number of systems in order to gain some knowledge about the different scaling regimes to be expected, and then to gather them in a new scaling proposal. After that, some analytical computations will be needed in order to obtain the whole scaling picture, in the same manner that was done in [241]. Similar arguments can be applied to other limits indeed. Self-affinity is a morphological feature that appears in many growth processes when observed at certain length scales. Beyond these limits, there are lower and higher cut-offs that have to be done in the systems under consideration. The discrete nature of our measuring tools, both numerical and experimental, has to be taken into account when we compute the evolution of fluctuations because other important limits may become relevant. Whenever the discretization length dl and the typical particle size σ (the lower cut-off of self-affinity) are such that $\sigma/dl \ll 1$, the system can be regarded as continuous and we can make use of the scaling arguments at hand. The recognition of the relevance of this issue is far-reaching in practice,

since a wrong parametrization of the interface can lead to incorrect results (see [238]). Furthermore, albeit the continuum description of radial growth includes a dilatational driving force, we need to understand the real influence of such a term in the dynamical properties of the fluctuations. Our numerical results show the emergence of anomalous fluctuations due to noise dominance, and only a rigorous analysis of future scaling ansatzs could clarify this issue.

Chapter 11

Analysis of Lattice-Gas Cellular Automaton Models for Tumour Growth by Means of Fractal Scaling

Mathematical modeling of tumor development has become a real hype within the last decade. The abundance of mathematical models has created a great need for the validation of their biological relevance. Recently, in order to characterize the tumor growth dynamics, Brú et al. have determined some statistical properties of both *in vitro* and *in vivo* solid tumor-surfaces by using fractal scaling analysis. Surprisingly, for all tumor surfaces, the statistical observables converged to a unique set of critical exponents which indicates some common features of tumor growth dynamics (linear growth rate, growth activity limited to the outer rim of the tumor mass and diffusion of newborn tumor cells on the surface from lower to higher curvature regions, typical of Molecular Beam Epitaxy (MBE) Universality). Here, we develop and analyze a lattice-gas cellular automaton (LGCA) model of solid tumor growth. Random walk dynamics are assumed for tumor cell migration and a density-dependent birth process describes the cell mitotic dynamics. Fractal scaling analysis shows that for any parameter variation the model interface dynamics follow Edward-Wilkinson (EW) Universality. Interestingly, the observation of the linear growth rate of the tumor radius and the location of proliferative activity characterizing *in vitro* and *in vivo* solid tumors are recovered by the model.

11.1 Introduction

At the beginning of 60's Eden formulate one of the first discrete automata model, in attempting to describe solid tumor growth [229]. Recently, there is a boom of new mathematical models describing various aspects of tumor growth and development. Different mathematical models have been developed in order to describe features of tumor development, like front velocity, necrotic core and proliferative rim dynamics, interactions with the extracellular medium and vasculogenesis, with and without the exposure to chemicals and radiation [251–253]. A central problem in the mathematical modeling of biological processes is the evaluation of its biological relevance. In particular, for the problem of tumor development numerous models have been proposed but the methods to check their consistency with experiments or medical observations are sometimes ambiguous or qualitative. Researchers have tried to compare different characteristics of their models such as growth speed, spatiotemporal pattern formation, tumor cell population evolution with *in vivo* or *in vitro* observations. An essential question is which of the existing model assumptions are justified for simulating tumor growth. Brú et al. have claimed, on the evidence of their experimental investigation of in vivo and in vitro tumor samples, that all avascular solid tumors share the same fractal surface dynamics [15, 28, 30]. In particular, these exponents are typical of the MBE/MH (Molecular Surface Dynamic/Mullins Herring) surface dynamics [29], characterized by particles/cells generated (or deposited) randomly on the surface and then relaxing towards the highest surface curvature region. This characterization supports the following conclusions on solid tumor growth dynamic: linear growth rate, cell replication activity limited to the outer rim of the tumor mass and displacement of newborn tumor cells on the surface preferable in lower curvature regions. Fractal scaling could be definitively an efficient tool to evaluate tumor models, and to link their mathematical assumptions with real biological properties. In the present study, we analyze a discrete model with diffusive-kinetic dynamics, i.e. cells perform random walks and undergo birth/death processes. These are two classical assumptions and a lot of continuous [254–256] and discrete [257] tumor growth models are based on them. Hatzikirou et al. have developed a tumor growth lattice-gas cellular automaton (LGCA) model [31, 32], which incorporates these diffusion-kinetic assumptions. In this paper, we analyze the growing front in model simulations by using fractal scaling analysis. The main goal is to calculate numerically the statistical observables that allow for the extraction of the critical

scaling exponents and to relate them with the proper universality class. We investigate the exponents' dependence on different lattices (square and hexagonal), and on relevant model parameters. Numerical analysis indicates that diffusive dynamics induces the tumor surface developing according to Edward-Wilkinson (EW) Universality, which is not consistent with real in vitro and in vivo tumors. To obtain the correct MBE/MH Universality [258] it is necessary to introduce adhesive cell-cell interactions. The paper is organized in the following way: first, we introduce briefly the model, describing its main assumptions and formalizing the mathematical notation. Then we give a basic description of fractal scaling analysis. In the following, we present numerical results about surface critical exponents' extraction, and investigate the compatibility of our model with some appropriate universality class. Finally, some suggestions for future tumor modeling approaches are given.

11.2 The Model

We consider a lattice-gas cellular automaton [41] defined on a two-dimensional regular lattice $\mathcal{L} = L_x \times L_y \in \mathbb{Z}^2$, where L_x, L_y are the lattice dimensions. Let b denote the coordination number of the lattice, that is $b = 4$ for a square lattice and $b = 6$ for a hexagonal lattice, respectively. Cells move on the lattice with discrete velocities, i.e. they hop at each time step from a given node to a neighboring one, as determined by the cell velocity. The set of velocities for the square lattice is represented by the two-dimensional channel velocity vectors $\mathbf{c_1} = \begin{pmatrix} 1 \\ 0 \end{pmatrix}$, $\mathbf{c_2} = \begin{pmatrix} 0 \\ 1 \end{pmatrix}$, $\mathbf{c_3} = \begin{pmatrix} -1 \\ 0 \end{pmatrix}$, $\mathbf{c_4} = \begin{pmatrix} 0 \\ -1 \end{pmatrix}$, $\mathbf{c_5} = \begin{pmatrix} 0 \\ 0 \end{pmatrix}$, while for the hexagonal lattice it is $\mathbf{c_1} = \begin{pmatrix} 1/2 \\ \sqrt{3}/2 \end{pmatrix}$, $\mathbf{c_2} = \begin{pmatrix} 1 \\ 0 \end{pmatrix}$, $\mathbf{c_3} = \begin{pmatrix} 1/2 \\ -\sqrt{3}/2 \end{pmatrix}$, $\mathbf{c_4} = \begin{pmatrix} -1/2 \\ -\sqrt{3}/2 \end{pmatrix}$, $\mathbf{c_6} = \begin{pmatrix} -1 \\ 0 \end{pmatrix}$, $\mathbf{c_7} = \begin{pmatrix} -1/2 \\ \sqrt{3}/2 \end{pmatrix}$, $\mathbf{c_8} = \begin{pmatrix} 0 \\ 0 \end{pmatrix}$. In each of these channels, we impose an exclusion principle, i.e. we allow at most one cell per channel. We denote by $\tilde{b} = b + b_0$ the total number of channels per node which can be occupied simultaneously, where b_0 is the number of channels with zero velocity (rest channels). We represent the channel occupancy by a Boolean random variable called *occupation number* $\eta_i(\mathbf{r}, t) \in \{0, 1\}$, where $i = 1, ..., \tilde{b}$, $\mathbf{r} = (r_x, r_y) \in \mathbb{Z}^2$ the spatial variable and $t \in \mathbb{N}$
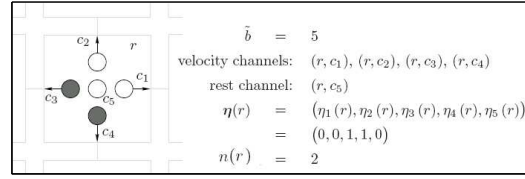
FIGURE 11.1: Example of node configuration in a lattice-gas cellular automaton: channels of node r in a two-dimensional square lattice ($b = 4$) with one rest channel ($b_0 = 1$). Gray dots denote the presence of a cell in the respective channel.

the time variable (see figure 11.1). The $\tilde{b}$-dimensional vector

$$\boldsymbol{\eta}(\mathbf{r}, t) := (\eta_1(\mathbf{r}, t), ..., \eta_{\tilde{b}}(\mathbf{r}, t)) \in S$$

is called *node configuration* and $S = \{0, 1\}^{\tilde{b}}$ the automaton *state space*. We define a *total node density* as the sum of node densities:

$$n(\mathbf{r}, t) := \sum_{i=1}^{\tilde{b}} \eta_i(\mathbf{r}, t)$$

The *global configuration* is given by

$$\boldsymbol{\eta}(t) := (\boldsymbol{\eta}(\mathbf{r}, t))_{\mathbf{r} \in \mathcal{L}}$$

11.2.1 LGCA dynamics

In our automaton model, cell dynamics are defined by rules. Automaton dynamics arise from the repetition of three rules (operators): Propagation (P), reorientation (O) and growth (R). In particular, the combination of reorientation and propagation operators describe [32] cell motion while the growth operator controls the change of the local number of cells on a node. In the following, we describe these operators in detail.

11.2.1.1 Propagation (P)

The propagation step is deterministic and it is governed by an operator P. By the application of P all cells are transported simultaneously to nodes in the direction of their velocity, i.e. a cell residing in channel $(\mathbf{r}, \mathbf{c}_i)$ at time k is moved to a
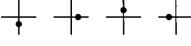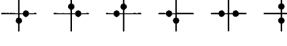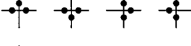
FIGURE 11.2: Reorientation rule of random motion. The first column corresponds to the number of cells on a node $n(\mathbf{r}, k)$ at a time km, with capacity $\tilde{b} = 4$. The right column indicates all the possible cell configurations on node and the transition probability of obtaining a certain configuration (11.1).

neighboring channel $(\mathbf{r}+m\mathbf{c}_i, \mathbf{c}_i)$ during one time step (see figure 11.1). Here $m \in \mathbb{N}$ determines the speed and $m\mathbf{c}_i$ is the translocation of the cell. Cells residing on rest channels do not move since they have zero velocity. We note that this operator is mass and momentum conserving.

11.2.1.2 Reorientation(O)

The reorientation operator is responsible for the redistribution of cells among the velocity channels of a node, providing a new node velocity distribution. Here, we assume that cells perform random walks. A possible choice for the corresponding transition probabilities is

$$P(\boldsymbol{\eta} \to \boldsymbol{\eta}^{\mathrm{O}})(\mathbf{r}, t) = \frac{1}{Z}\delta\big(n(\mathbf{r}, t), n^{\mathrm{O}}(\mathbf{r}, t)\big), \tag{11.1}$$

where $Z = \sum_{\boldsymbol{\eta}^{\mathrm{O}}(\mathbf{r},t)} \delta\big(n(\mathbf{r}, k), n^{\mathrm{O}}(\mathbf{r}, k)\big)$ is a the normalization factor. The Kronecker δ guarantees the mass conservation of this operator. Simply, we choose one configuration at random among those with the same number of particles as the initial one (see figure 11.2). The particular choice for the reorientation operator is one out of various possible ways to describe random motion by means of LGCA models [41]. This choice greatly simplifies the possible analytical derivation of the equations describing the meso- and macroscopic evolution of the automaton [31, 32].

11.2.1.3   Cell Kinetics (R)

In our model we take into account only mitotic processes (and neglect cell death). We assume that tumor cells can divide only if they have just a few competitors on the node, i.e. the cancer node density $n_C(r, t)$ should be lower than a threshold θ_M. The probability of mitosis r_M is a function of tumor node density:

$$n^R(\mathbf{r}, t) := \begin{cases} n(\mathbf{r}, t) + 1, \text{w.p. } r_M \text{ if } n(\mathbf{r}, t) \leq \theta_M \\ n(\mathbf{r}, t), \text{else} \end{cases} \qquad (11.2)$$

where w.p. denotes "with probability". In practice at time t one adds a cell in the node with coordinates $\mathbf{r}$ in a randomly chosen channel, accomplishing its occupation number, with probability r_M. In a more complete formulation an additional population of necrotic cells (dead cells) model is considered [31]. These interact with tumor cells when the total node density exceeds θ_N, assuming that the nutrient consumption is critical and inducing tumor cell necrosis. Generally, the precise definition of these interactions is a difficult and ambitious task. For *in vivo* tumors the complexity of the interacting phenomena cannot be captured easily by computational models. However, necrotic-tumor population interactions are not relevant in analyzing tumor front fluctuation dynamics since necrosis typically occurs some distance away from the tumor front and in our work it has been disregarded.

11.3   Basics of Fractal Scaling Analysis

Physical systems such as surfaces growing on a substrate by a particles deposition-relaxation process often have a fractal self-affine nature; such systems have been mathematically described both by using continuous Langevin equations and discrete models [27]. The main information that can be extracted from these systems is the spatiotemporal evolution of some statistical observables, such as the dispersion of the surface height around the mean value calculated on the whole surface. These statistical observables typically have a power-law dependence in space and time. The dominant dynamic process may be characterized by measuring the value of the power-laws' exponents, also called scaling critical exponents (for details see [241]). Taking into consideration the fractal scaling analysis of the experimental results found by Brú et al. [15, 28], here we describe a way to define a surface

for the propagating front of a 2D tumor growth LGCA model, and the respective method of scaling exponents measurements, trying to establish relations between the local microscopic rules (birth death process, re-orientation process) and the surface behavior dynamics (defined by the critical exponents).

A self-affine surface is represented by a height function $h(\vec{r}, t)$[1], that is the height coordinate r_y of the surface for the substrate point described by coordinates $\vec{r}$ at time t, having the scaling properties:

$$h(\lambda \vec{r}, \omega t) = \lambda^\alpha \omega^\beta h(\vec{r}, t) \tag{11.3}$$

where α, β and $z = \frac{\alpha}{\beta}$ are the scaling exponent; this last governs the characteristic surface correlation length dynamic $\xi \propto t^{\frac{1}{z}}$. β is called the *growth exponent*, while α is the *roughness exponent* and z is the so-called *dynamic exponent*. This scaling exponent can be measured by the local surface width $W(l, t)$ and the correlation function $C(l, t)$ defined as:

$$W(l, t) = \left\langle \left\langle \sqrt{\langle h^2 \rangle_l - \langle h \rangle_l^2} \right\rangle_L \right\rangle_r \quad C(l, t) = \sqrt{\left\langle \left\langle (h(\vec{r}) - h(\vec{r} + \vec{l}))^2 \right\rangle_L \right\rangle_r}, \tag{11.4}$$

where $\langle \cdot \rangle_l$ is the mean value over a window of size l, $\langle \cdot \rangle_L$ over different windows of the system of total size L^2, and $\langle \cdot \rangle_r$ over different replicas r (i.e. system realizations), see figure 11.3. These two quantities follow similar power laws in t and l:

$$C(l, t) \approx W(l, t) \propto t^\beta f\left(\frac{l}{\xi}\right), \tag{11.5}$$

where $f\left(\frac{l}{\xi}\right)$ is the scaling function, dependent only on the value of the correlations size respect to the system size

$$f(u) = \begin{cases} u^{\alpha_{loc}} & u \ll 1 \\ const & u \gg 1 \end{cases} \tag{11.6}$$

The exponent α_{loc} is called the *local roughness exponent*. There are two main categories of scaling behavior. If $\alpha < 1$, this exponent describes both the scaling of large and small-length scales, and $\alpha = \alpha_{loc}$. For this case $C(l, t)$ and $W(l, t)$ increase until a time t_{thr}, when the characteristic correlation length $\xi \gg l$, and they

---

[1] Alternatively, it is defined as the furthermost occupied node in L_y direction, for each $r_x \in L_x$

[2] More rigorous definitions could be given by: $\langle f \rangle_{l,x} = \int_x^{x+l} f(x') \left(\frac{1}{l}\right) dx'$ and $\left\langle \langle f \rangle_{l,x} \right\rangle_L = \int_0^L \langle f \rangle_{l,x} \left(\frac{1}{L}\right) dx$.

reach a threshold value $W_{thr} \approx C_{thr} \propto l$, as one can observe for example in figure 11.5. On the contrary, when $\alpha > 1$ the small-length scales show a trivial scaling with $\alpha_{loc} = 1$. This generic picture includes most of the scaling behaviors found so far in models and experiments. tumor growth has been experimentally shown to obey an infrequent superrough dynamics [15, 28], characterized by $\alpha_{loc} = 1$ and $\alpha > 1$. Using the corresponding scaling function of equation (11.5), one can see that the long time behavior is $C(l,t) \sim l^{\alpha_{loc}}t^{\beta^\star}$ (instead of the standard behavior $C(l,t) \sim l^\alpha$), where $\beta^\star$ is called the *anomalous growth exponent*, $\beta^\star = (\alpha - \alpha_{loc})/z$. Therefore anomalous fluctuations at small scales are particularly relevant in this case. An useful observable measuring α is the Power Spectrum of $h(\vec{r}, t)$, namely the spatial Fourier Transform

$$S(\vec{k}, t) = \left\langle \hat{h}(\vec{k}, t), \hat{h}(-\vec{k}, t) \right\rangle_r = k^{-(2\alpha+1)}s(k\xi) \tag{11.7}$$

where the scaling function has the form

$$s(u) = \begin{cases} u^{2\alpha+1} & u \ll 1 \\ const & u \gg 1 \end{cases} \tag{11.8}$$

The most general stochastic Langevin equation describing the dynamic of interface growth function $h(\vec{r}, t)$ is

$$\frac{\partial h}{\partial t} = G(\vec{r}, h, t) + F(\vec{r}, t) \tag{11.9}$$

where $F(\vec{r}, t)$ term is responsible for the addition/deposition, in our case "reproduction", of new particles on the surface and $G(\vec{r}, h, t)$ dictates their movements and interactions on it. Typically, $F(\vec{r}, t)$ is composed of a constant growth rate f plus a white noise $\zeta(\vec{r}, t)$, having its first two moments:

$$\langle \zeta(\vec{r}, t) \rangle = 0 \quad \langle \zeta(\vec{r}, t)\zeta(\vec{r}, t') \rangle = 2A\delta^d(\vec{r} - \vec{r})\delta(t - t'); \tag{11.10}$$

on the other hand $G(\vec{r}, h, t)$ is a function of time t, spatial coordinates $\vec{r}$ and surface profile h and it is generally represented by a differential operator. In some simple cases by means of heuristic scaling arguments, deriving spectral properties or applying renormalization group theory, is possible to derive the theoretical values of the scaling exponents, that depends in general on the geometrical dimension of the surface d. In table 11.1 are defined the universality classes discussed in our work in terms of their set of critical exponents.

	$G(\vec{r}, h, t)$	α	β	z
EW	$D\nabla^2 h$	$\frac{2-d}{2}$	$\frac{2-d}{4}$	2
MBE/MH	$-K\nabla^4 h$	$\frac{4-d}{2}$	$\frac{4-d}{8}$	4

TABLE 11.1: Edward Wilkinson (EW) and Molecular Beam Epitaxy/Mullins Herring (MBE/MH) universality classes, defined in terms of their set of critical exponents α, β and z. The value of critical exponents depends on the geometrical dimension d of the surface.

While Edward Wilkinson (EW) dynamic has a diffusive interaction term, typical of particles random motion. The fourth order term corresponds to the Molecular Beam Epitaxy/Mullins Herring (MBE/MH) Universality, whose scaling exponents are compatibles with the ones measured by Brú et al., results from particles moving from lower to higher curvature regions, trying to minimize surface curvature.

11.4 Numerical Analysis and Results

We have implemented the model described in section 11.2 on a 2D lattice ($b = 4$ velocity channels) and hexagonal lattice ($b = 6$ velocity channels) lattice $\mathcal{L} = L_x \times L_y$, with $|L_x| = |L_y| = \{1024, 2048\}$ [3], lateral periodic boundary conditions and reflecting boundary at L_x (e.g. a particle in a velocity channel pointing towards the boundary, is placed - reflected - in the opposite velocity channel). The initial conditions are defined as $n\big((r_x, 1), 0\big) = 1, \forall r_x \in L_x$. We consider principally the case in which mitotic threshold is half of the maximum node density, i.e. $\theta_M = \tilde{b}/2$, and the number of rest channels $b_0 = 4$.

Height function $h(x, t)$ at x is defined as the y coordinate of the lattice site with the last nonzero cell density at time t, measuring the density of the $x - th$ column starting from $r_y = 1$, see figure 11.4. Alternative definitions of height function have been considered for lattice gas or percolation front [238, 259], producing multivalued surfaces with overhangs. Our definition can be considered as one of the most simplest in order to perform dynamic scaling, and has a good consistency at least in the case of compact tumors observed at short scale, in linear approximation. In the case of more jagged profiles and non linear geometries, more sophisticated definition of height function have to be considered to obtain a consistent scaling,

---

[3]The notation $|\cdot|$ denotes the cardinality of a given set, i.e. $|L_x| = 1024$ when $L_x = [1, 1024]$

able to identify correctly the universality class [28].

In all cases studied, the front velocity, which is defined as the slope of the mean height $\langle h(t) \rangle_x$, was found to be constant (see [31]). We note that the height function $h(x,t)$ provides the actual position of the front, as in figure 11.4 up-right. The cell proliferation activity is concentrated to a narrow region near to the front (see the two lower graphs of figure 11.4). The location of the proliferation events is in good agreement with the observations of in vivo and in vitro tumors [15]. The surface height function $h(x,t)$ exhibits non trivial spatiotemporal scaling exponents when varying the mitotic rate r_M in a broad range (up to 3 orders of magnitude). The scaling exponent $\beta = \frac{\alpha}{z}$ is evaluated by direct calculation of $W(L,t)$ time slope, while α and z by the data collapse of a set of functions $W(l,t_s)$ (or $C(l,t_s)$) taken at different times t_s (see equation (11.5)). The fractal scaling analysis shows that the exponents fit well with EW universality, as it is shown in figures 11.5-11.7. Variation in mitotic threshold θ_M and in the number of rest channels b_0 does not seem to affect universality, as one can see in figure 11.6. Some differences are observed due to the lattice topology. In particular, on the hexagonal lattice the global width $W(L,t)$, after an initial transient, grows with an exponent typical of the EW regime for a broad range of mitotic rates $r_M \in (0.01, 0.5)$. The stationary regime is observed in our simulations even in the case of small system size, i.e. $L_x = 1024$. However, in the square lattice it is more difficult to observe the final growth - stationary - regime, due to a very long transient that follows KPZ dynamics, with $\beta = \frac{1}{3}$, as a result of the square lattice induced symmetry (data not shown), particularly persistent for high r_M. The surface correlation functions $C(l,t)$ exhibit also an EW-compatible regime. Moreover, the spatial correlations collapse in a suitable way using both the EW universality spatial α and temporal β exponents, at least for long spatial distances l. The spatial correlations are mainly developing due to the proliferation events, since the random walk dynamics induce only uncorrelated spatial structures. Thus, we can state that the low mitotic probabilities r_M, in combination with a short domain size, are responsible for the lack of a sufficiently large number of proliferative events for the building up of significant spatial correlations. From the other hand with high r_M fluctuations in surface roughness reaches saturation rapidly, thus also in this case finite system size play a main role in the observation of EW regime in temporal scaling of global width $W(L,t)$. Thus in the limit of low mitotic probability and large system size, surface front grows following a power law with a typical EW exponent for many decades.

11.5 Conclusions and Perspectives

In this study, motivated by the work of Brú et al., we used fractal scaling analysis to evaluate the suitability of some common assumptions in tumor growth modeling. In particular, we tested the hypothesis that avascular tumor dynamics may emerge from the combination of random cell motion coupled with a stochastic birth process. The corresponding model is motivated by a recently developed LGCA model [31, 32], which can effectively describe the avascular growth phase. The key idea is to check if the resulting spatiotemporal dynamics of the front, described in terms of fractal scaling exponents, match with the ones found by Brú et al.

We have considered our model in 2D with appropriate periodic cylindrical boundary conditions, that allow for the development of a well defined 1D front, described by a corresponding height function $h(x, t)$. Then we have measured the self affine properties of increasing tumor border in our simulations by means of fractal scaling analysis. Our study provides numerical evidence that our virtual tumor surfaces are compatible with the EW universality, which describes, in the context of surface growth by random particle deposition, a relaxation process that moves the particle towards the local height gradient minimum. It is worth pointing out that the spatially homogeneous migration/proliferation dynamic rules produce non-trivial front structures, usually obtained by one-dimensional models involving only surface particle interactions.

This model is a very simplified view of tumor growth. Actually microenvironment, by means of diffusive signals (nutrients, growth factors etc.), ECM components or other stroma interactions, plays a significant role in tumor development. The major difference between 2D and 3D embedded geometry is the penetration length of diffusible signals in the tumor bulk. This fact can lead to important phenomena such as diffusion barriers, which is one of the major reasons for chemotherapeutic treatment failure, since chemotherapy efficiency is based on the penetration of the diffusible agents. Another point we want to stress out concerns the actual experimental setup limitations of Brú et al. in the measure of critical exponents. In fact critical properties are extracted in *in vivo* samples from 2D cut sections of a 3D tumour mass, while in *in vitro* case the original systems grow just on a plane on the Petri dish. Then one of the main criticisms to their work is related to the finding, in both cases, of 1D MBE universality scaling exponents, measured on a linear front, where a real tumor growth in a three dimensional space, with a 2D spherical surface front. This is still an interesting open question, out the purpose

of this work, so we limited our analysis to 2D planar systems, mimicking better *in vitro* experiments, at least at short scales, where an arc segment can be approximated with a straight line. There are few studies on self affine surface growth that consider cut section or geometries different from the euclidean [30, 246], and more solid numerical and theoretical works are needed in these topics, in order tackle with more realistic tumor models, replicating at the best both spherical growth dynamic and experimental techniques.

Implementing our model within a hexagonal lattice geometry has some advantages with respect to a square lattice, such as higher order directional isotropy. This effect is expressed in the front dynamics on hexagonal lattices as a shorter temporal dynamic transient, a prominent asymptotic growth dynamics under both size and mitotic rate modulations, and the shorter equilibration of the relevant surface statistical observables. On the contrary, front dynamic on square lattice are characterized by a long r_M-dependent KPZ transient.

Our model predicts two of the solid tumor dynamic features claimed by Brú et al, i.e. proliferation concentrated at the outer rim of the tumor bulk and a linear front velocity. However, the universality class of the surface front dynamics found here is not the MBE/HM found by Brú et al. [15, 28]. Microscopically, the traditional view on MBE dynamics imposes a particle relaxation process which directs particles to the minimum of the surface curvature. The latter suggests us to implement a different reorientation rule, for example dependent on a function of local cell density gradients, in order to find the universality characterizing real tumors. Please note, that MBE dynamics describe a non-local mechanism of motion, in contrast to EW, whereas the curvature "information" is non-local, i.e. refer to an extended neighborhood. In a following study, we will introduce a mechanism that provides the desired universality for the surface dynamics. Finally, another very intriguing and important step is the derivation of a coarse-grained partial differential equations for density $\rho(\vec{r}, t)$ in d dimensions, obtained from the microscopic model, by use of standard mean-field techniques [31, 32, 260], and the calculation of the corresponding Langevin equation describing the $(d-1)$-dimensional surface front dynamics for $h(x, t)$.
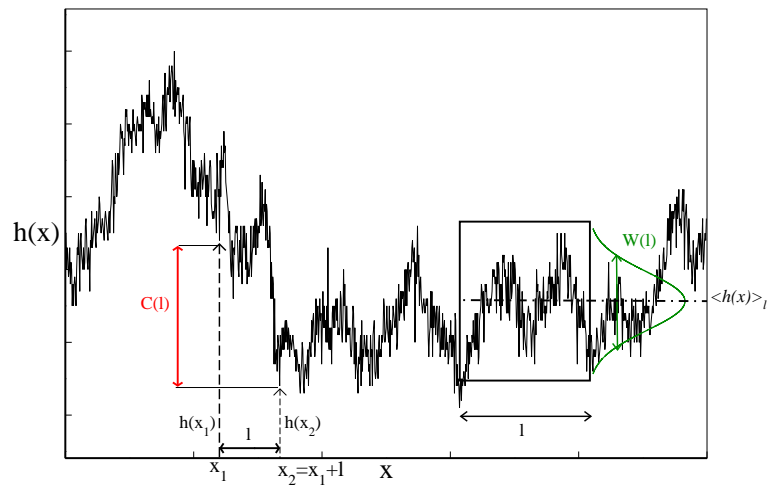
FIGURE 11.3: The correlation function $C^2(l,t) = \langle(h(x_1,t) - h(x_2 = x_1 + l,t))^2\rangle$ is defined as the mean square height difference among all pairs of surface points $(x, y = h(x,t))$ placed at a distance d from x. The local surface width $W(l,t)$ is the mean of the local variances of $h(x)$, calculated around a mean height $\langle h(x)\rangle_l$ over a domain of fixed size l.
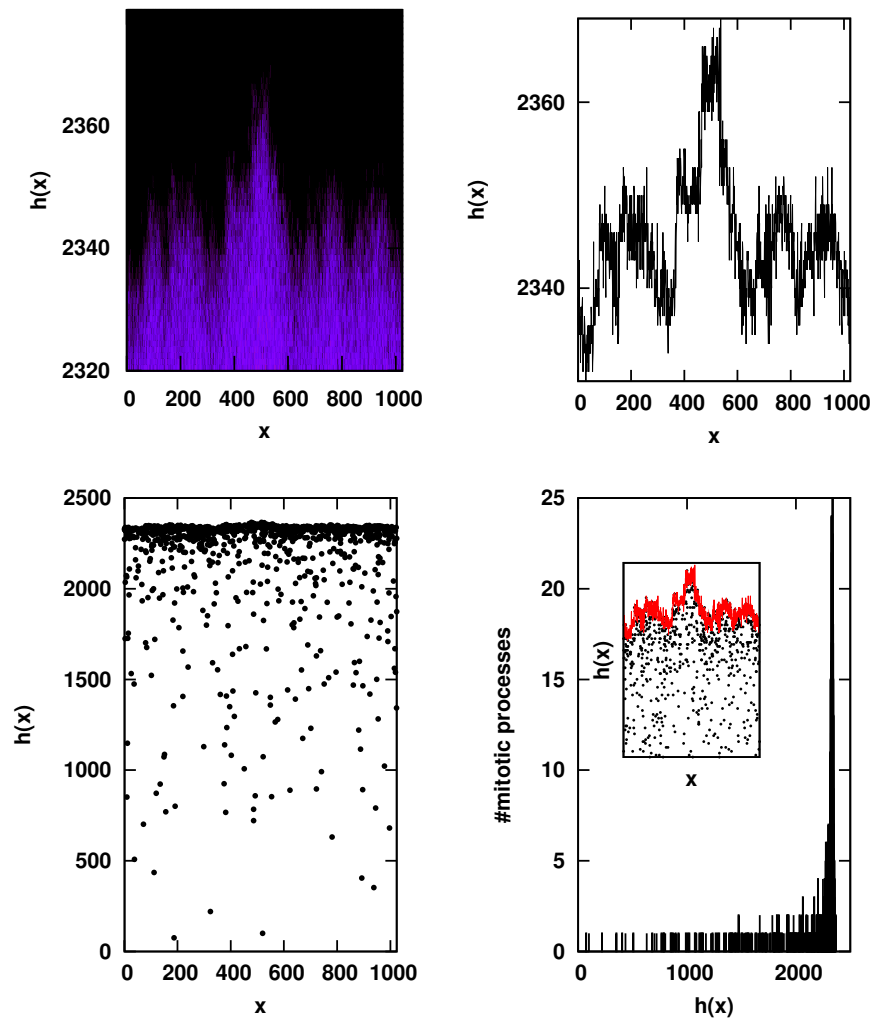
FIGURE 11.4: Top: Front cell density profile (left) and height function $h(x, t)$ (right) for the LGCA model (parameters $\theta_M = 5$, $r_M = 0.1$) on a hexagonal lattice (number of rest channels $b_0 = 4$) with x size $L = 1024$. Bottom: Mitotic events at a given time step (left and right inset) and their frequency distribution vs the height level $y = h(x)$. Mitotic activity is highly concentrated on a thin front layer, consistent with the hypothesis of Brú about linear growth concentrated on the outer rim of the tumor mass
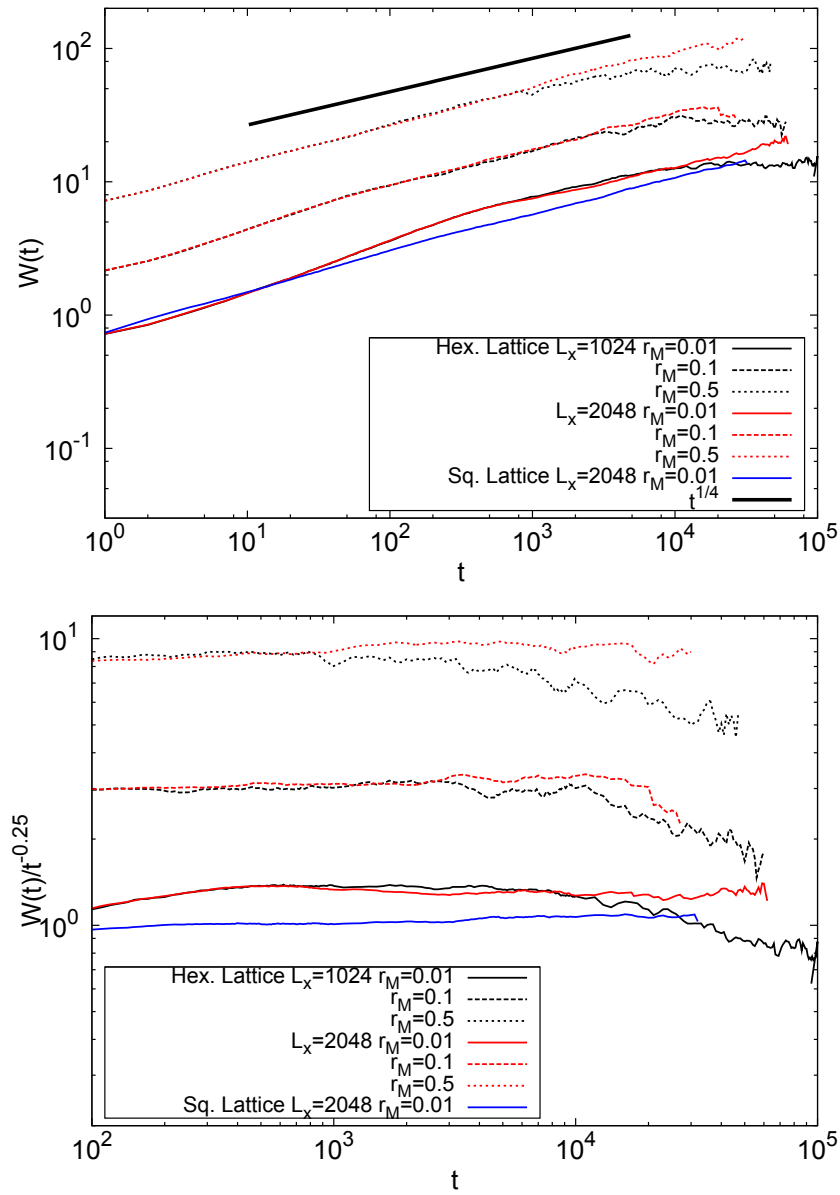
FIGURE 11.5: Global surface width $W(L, t)$ (top) and its scaling with the EW universality β exponent (bottom), for different lattice geometries, system sizes and mitotic rates r_M. Mitotic threshold is set to $\theta_M = \tilde{b}/2$. For all cases global width growth is compatible with the typical EW universality scaling Ansatz $W(L, t) \propto t^\beta$ with $\beta = \frac{1}{4}$. It is possible moreover to observe for size $L = 1024$ the transition between growth regime and threshold regime, as predicted by scaling Ansatz in equations (11.5)-(11.6), when characteristic correlation length reach the system size. Each curve has been averaged over 50 different realizations (10 realizations for $b_0 = 1$). Curves corresponding to different r_M are shifted in y direction for a better visualization.
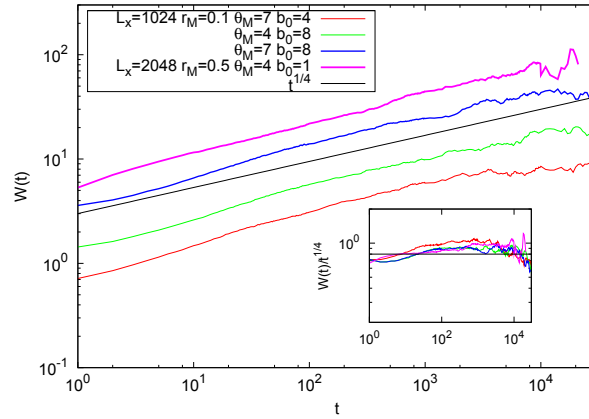
FIGURE 11.6: Global surface width $W(L,t)$ and its scaling with the EW universality β exponent (inset), for systems in exhagonal lattice, with different mitotic thresholds θ_M and mitotic rates r_M. Global width growth is compatible with the typical EW universality scaling Ansatz $W(L,t) \propto t^\beta$ with $\beta = \frac{1}{4}$. Each curve has been averaged over 10 realizations. Curves are shifted in y direction for a better visualization.
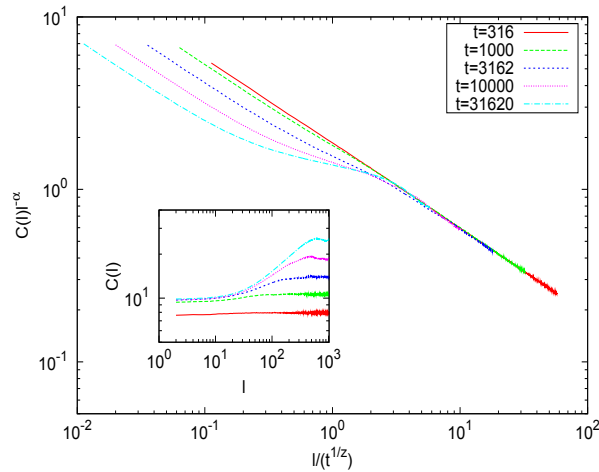
FIGURE 11.7: Collapse of surface correlation functions $C(l,t)$ (Inset: original unscaled functions) calculated at different logarithmic times, for a system on hexagonal lattice, with $L = 2048$, $b_0 = 4$, using EW universality exponents. Data collapse indicate the compatibility of the surface dynamics with an EW universality scaling Ansatz $C(l,t) \propto l^\alpha f(l/t^{1/z})$, described in section 11.3, at least for $l > 50$. Each curve has been averaged over 30 different realizations.

Conclusions

In this thesis we have studied critical phenomena appearing in different biological motivated systems. In particular, our work has been focused on some fundamental aspects concerning the dynamics of neural networks and the growth of solid tumours, which can be considered as prominent examples of complex systems. These are systems composed of many elements, cells in this case, with simple and short-range interactions, mediated by the synapses in the case of neural networks, or by contact enhanced signals and exchange of chemical messengers in the case of cancer cells.

As described in chapter 2, when a complex system is in a critical state (e.g. near a second order phase transition, or near a self organized critical state), its dynamics is determined by non trivial spatiotemporal correlations in its correspondent emergent collective behaviour. In order to study these collective properties, systems have to be considered as a whole, and not merely as the sum of all its elements, and it is useful to study their dynamics within a probabilistic approach. Thus, the framework used to implement the models and the mathematical tools of analysis here considered are part of equilibrium and non-equilibrium statistical mechanics.

Different experimental works have shown a broad range of phenomena in neural systems depicting criticality, which is associated to the observation of correlations power law distributed, as described in chapter 4. The efforts to find and describe critical states in neural systems has generated a great interest in the scientific community due to their functional relevance. In fact, it is known from the study of criticality in classic physical systems, e.g. in the Ising model, that long range correlations increase the sensitivity of the system to small perturbations or stimuli [5]. On the other hand, concerning some biological systems, critical states allow for an optimization of their functional properties. For example, a neural system in

the critical state optimizes transmission and storage of information, computational capabilities, large network stability and sensitivity to sensory stimuli, to name a few [10, 132]. Another class of biological systems in which emergent properties related with criticality have been observed are solid tumours, described in chapter 10. During solid tumour growth, the critical behaviour of the front of expansion, that evolves as a self affine surface, leads to an increasing surface/volume ratio, allowing for the optimization of oxygen and nutrients intake and furthermore for an effective invasion strategy, by mean of extracellular matrix degradation.

By virtue of the emergence of these important properties in critical systems, the motivation of the research work done in this thesis has been to investigate the most relevant mechanisms responsible for the appearance of critical states in different neural systems and in tumour growth processes. To reach this main objective we have developed original biologically inspired mathematical models, in general constituted by many elements, that we have studied using both numerical simulations and some analytical approaches as mean-field techniques.

In chapter 5 we have implemented a non-equilibrium version of the standard Hopfield ANN model introducing fast synaptic fluctuations, whose steady-state distribution depends on the current activity of the network in such a way that it models synaptic plasticity dynamics [106]. In addition we have considered an hybrid synchronous-asynchronous neuron updating [125], i.e. the so called partial updating (i.e. a sort of half way between sequential and parallel updating, usually considered), which introduces the possibility of simulate a network with silent neurons [155] or with partially synchronized states. Previously it has been shown that one may capture some of the experimentally observed shaky mechanisms and instabilities in the attractors of neural systems [46, 145, 146] by taking into account these two features [150]. The main properties of this model are:

- The appearance of non equilibrium phases, which are characterized by chaotic fluctuations of the network state among different patterns of activity, related with the previously stored memories, or among different oscillatory memory states, defined as pattern-antipattern oscillations.

- The emergence of a continuous second order phase transition between the memory retrieval phase and the chaotic phase. The onset of criticality in the dynamics of the network is depicted at this transition by the appearance of power-law distributed temporal correlations in synaptic currents or local

fields time series. Such criticality at the edge of chaos resulted to be relevant in order to optimize the sensitivity of the network to external stimuli, improving dynamic memory retrieval tasks.

Our systematic study adds up some elements to understand the role of fast synaptic fluctuations in the appearance of criticality in neural states at the edge of chaos, experimentally observed and sometimes associated to a dynamics that explores different memories [4, 8, 46] and in the emergence of strange attractors in neural dynamics recently reported in some experimental works [145, 146].

In order to study more in depth the role of activity dependent synaptic processes (occurring at short time scales) on the emergence and the stability of neural critical states, we have considered in chapter 6 a more realistic neuron and synapses description, and implemented the Levina, Herrmann and Geisel model [19] (LHG), that includes the Tsodyks-Markram model for synaptic depression, a mechanism of great importance for synaptic plasticity [175], and an Integrate and Fire (IF) dynamics for neuron excitability. This model allows to describe neural avalanches similar to those observed in experiments on cortical neural tissues [6, 8]. Under a mathematical point of view, this model is essentially equivalent to the well-known sandpile model, with grain height representing on the LHG model membrane graded potential and, instead of a grain toppling mechanism, energy is dissipated to neighbour sites through synapses modeled with the Tsodyks-Markram model.

LHG model has been claimed by their authors to reproduce generically scale-invariance, in the form of SOC neural avalanches of activity. However in the LHG model the dynamics is *non-conserved*, reflecting the leaking/dissipative mechanisms of actual synaptic transmission, and generic scale-invariance cannot be invoked. The term self-organized quasi criticality (SOqC) has been proposed to refer to such a class of systems, emphasizing the differences with conserving SOC models [20]. In order to investigate the SOC or SOqC features of the LHG model, we have scrutinized it, both numerically and analytically, and obtained the following results [21]:

- The LHG model exhibits absorbing and active phases and a non-trivial critical point separating both phases. Thus, only when the control parameters of the model are fine tuned to such a critical point, true scale-invariance emerges and the distribution of avalanche-sizes is power-law distributed.

- The mean-field calculation in [19], supporting generic criticality, leads indeed to a branching ratio equal to unity in a broad interval of phase space. In addition a Langevin equation, analogous to the one proposed to describe generically non-conserving self-organized (SOqC) models in [20], has been derived for the LHG model.

As a general conclusion our study suggests that synaptic plasticity mechanisms are not sufficient to guarantee the appearance of self organized criticality in neural activity, as argued in [19, 136] with respect to recent experiments on neural avalanches of activity [6, 8]. Anyway, even in absence of proper SOC, the dynamical LHG model generates partial power-laws compatible with the empirical findings for a relatively broad interval of the relevant parameters which ensures the stability of such *quasi* critical states. If future experimental research conducted on cortical networks will support the robustness of critical avalanches, we suggest to investigate for more elaborate theories, beyond simple self-organization, to explain this. For instance one can consider the interplay of homeostatic regulation mechanisms [181] for synaptic strength, or an evolutionary/adaptive processes leading to critical (or close-to-critical) propagation of information[180].

On the other hand, the topology of the brain has been observed to have an highly non trivial structure, with evidences that different regions of brain cortex are structured in a scale free topology, at least functionally [4]. Scale free connectivity distribution encompasses a huge variety of networks that differ in fine and microscopic structures, as for example in the correlation between the degrees of nearest neighbors nodes. Degree-degree correlations both positive, also called assortative, and negative, i.e. disassortative, have been found in many empirical networks, among others, neural networks [4, 58]. With this in mind, in chapter 7 we have studied a simple model of an Amari-Hopfield neural network in a scale free topology, i.e. with a power law degree distribution, focusing on the non trivial node-node correlations, and its relevance on memory storage and retrieval [22]. The main results of our analysis were:

- The memory retrieval performance increases is enhanced in assortative networks against a general stochastic noise, in particular due to the hubs which are the main responsible for the storage of information.

- At low temperature, however, disassortative networks perform the best, i.e. their overlap is higher than assortative ones, although the effect measured is small.

As a general conclusion, we claim that the optimal network for good conditions (i.e., complete synchronization, high density of edges, low levels of noise) is not necessarily the one which performs the best in bad conditions (partial synchronization, low density of edges, high levels of noise). It seems that optimality should thus be defined for particular environmental variables and tasks that the network has to deal with. Persistence of partial synchrony, or coherence of a subset of highly connected dynamical elements, can sometimes be as relevant as the possibility of every element behaving in the same way, in a perfectly synchronized state. In real neuronal networks, experiments suggest that hub (high degree nodes) neurons play key functional roles [212, 213]. From this point of view, there may be a selective pressure for brain networks to become assortative, in particular in areas of the cortex specifically related to memory [113, 114] or prefrontal [221, 222] lobes, where this effect might be relevant.

In order to go a step further in the study of collective behaviours of actual neural system whith complex topologies, in chapter 8 we have studied in the same class of scale-free assortative topologies considered in chapter 7, the dynamics of a population of spiking neurons, with a more realistic description of neuron membrane dynamics, using the Integrate and Fire (IF) model (see section 3.2 for details). Our study have shown that these networks depict different dynamical phases depending on the particular features of the degre-degree correlations, including synchronous and asynchronous spiking activity, and mixture phases with different populations of neurons with different synchronization behaviour. The main results of our analysis were:

- Heterogeneous scale-free topologies allow for the appearance of asynchronous phases and a crossover regime where a mixture of synchronous and asynchronous activity appears. On the contrary excitatory networks with a homogeneous topology, often considered in other works, tend always to rapidly synchronize all neurons in the network [91, 226].

- Both global and partial synchronization are enhanced by networks with assortative configurations, in which a certain level of homogeneity is guaranteed, at least locally.

- Between synchronous and mixture phase there is a discontinuous first order transition. In particular assortative networks have a broad region of phase coexistence, which can be considered in order to allow the network to switch between two frequencies (the low frequency of synchronous phase and the high frequency of the synchronous part of the mixed phase) under an appropriate external stimulation.

In the second part of this thesis, starting on chapter 10, we considered some modeling problems related to the dynamic scaling analysis for the solid tumours fronts of invasion, studied and characterized as critical self affine objects. In particular we concern for the analysis of the fluctuations in radially growing fronts and in interfaces with non constant substrate size, in terms of dynamic scaling techniques [30]. Our main goal stays in determining if the models exhibiting non planar geometries belong to the currently known universality classes, or else make part of some new ones. The main results of our analysis were:

- EW and KPZ equations, implemented in radial symmetry, result to still belong to the respective well-known one dimensional universality classes, at least in the limit of large radius and short evolution time, prescribed by the Family-Vicsek *Ansatz*.

- In one dimensional continuous Langevin models with non constant substrate (i.e. the substrate size increase exponentially) there are importante differences between the growth for dilatation (in which the spatial discretization dx stretches), and the growth for aggregation (in which discretization points increase at fixed dt) case. Concerning the growth for aggregation, the usual Family-Vicsek scaling *Ansatz* still holds. On the other hand systems with growth for dilatation behave with a new scaling behaviour, where the scaling of the correlation function depends from the substrate growth rate, and in the asymptotic limit, the interface is completely uncorrelated.

These results call for a more precise and rigorous study of the limit for a continuous description of microscopically discrete systems, like cells forming solid tumours, and a further analysis of experimental interfaces. Self-affinity is a morphological feature that appears in many growth processes when observed at certain length scales. Beyond these limits, there are lower and higher cut-offs that have to be done in the systems under consideration. The discrete nature of our measuring

tools, both numerical and experimental, has to be taken into account when we compute the evolution of fluctuations because other important limits may become relevant. Furthermore, albeit the continuum description of radial growth includes a dilatational driving force, we need to understand the real influence of such a term in the dynamical properties of the fluctuations.

In chapter 11, motivated by the work of Brú *et al.*, we used the fractal scaling analysis to evaluate the suitability of some common assumptions in tumor growth modeling, i.e. the combination of random cell motion and a stochastic birth process. The model we have considered is based on a Lattice Gas Cellular Automata (LGCA) [31, 32], which can effectively describe tumour growth, implemented in 2D with a well defined 1D front of invasion. The key idea is to check if the resulting spatiotemporal dynamics of the front, described in terms of fractal scaling exponents, match with the ones found by experimentally by Brú *et al.* [15]. The main results of our analysis were:

- The velocity of the front advance was found to be constant, and the cell proliferation activity is concentrated to a narrow region near to the front.

- The front of invasion exhibits non trivial spatiotemporal correlations, and thus could be actually considered a self affine curve, with characteristic scaling exponents. The measured dynamic exponents fit well with EW universality, and this results seems to be robust under variations in mitotic density threshold, in mitotic rate and in the maximum density per node.

Our model resemble two of the solid tumour dynamic features claimed by Brú *et al.*, i.e. proliferation concentrated at the outer rim of the tumor bulk and a linear front velocity. However the universality class of the front dynamics found here is not the MBE/HM found in their experiments [15, 28]. MBE dynamics, in contrast to EW, describes a cells motion on the front dependent on non-local "information", i.e. that refers to an extended neighborhood. These considerations suggest us to implement a different cell motion rule, for example dependent on the local cell density gradients, in order to find the universality characterizing actual tumors.

Publications derived from the thesis

Journals and book chapters

1. *Analysis of Lattice Gas Models of Tumor Growth by Means of Fractal Scaling*, S. de Franciscis, H. Hatzikirou and A. Deutsch, *Acta Physica Polonica B*, 4 (2), 167–182 (2011)

2. *Enhancing neural-network performance via assortativity*, S. de Franciscis, S. Johnson, and J.J. Torres, *Physical Review E*, 83 (3), 036114 (2011)

3. *Unstable Dynamics, Nonequilibrium Phases and Criticality in Networked Excitable Media*, S. de Franciscis, J.J. Torres and J. Marro, *Physical Review E*, 82 (4), 041105 (2010)

4. *Excitable Networks: Non-Equilibrium Criticality and Optimum Topology*, J.J. Torres, S. de Franciscis, S. Johnson and J. Marro, *International Journal of Bifurcation and Chaos*, 20 (3), 1–7 (2010)

5. *Self-organization without Conservation: are Cortical Networks Critical?*, J.A. Bonachela, S. de Franciscis, J.J. Torres and M.A. Muñoz, *Journal of Statistical Mechanics*, P02015 (2010)

6. *Nonequilibrium behavior in neural networks: criticality and optimal performance*, J.J. Torres, S. Johnson, J.J. Mejas, S. de Franciscis and J. Marro, *Advances in Cognitive Neurodynamics (II)*, Wang, Rubin; Gu, Fanji, 597–603, Springer, ISBN: 978-90-481-9694-4 (2011), Proceedings of Second International Conference on Cognitive Neurodynamics (ICCN2009), Hangzhou (China) 15-19 November 2009.

7. *Chaos in Heterogeneous Networks with Temporally Inert Nodes*, J.J. Torres, J. Marro and S. de Franciscis, *International Journal of Bifurcation and Chaos*, 19 (2), 677–686 (2009)

8. *Excitable Networks: Non-Equilibrium Criticality and Optimum Topology*, J.J. Torres, S. de Franciscis, S. Johnson and J. Marro, *Modelling and Computation on Complex Networks and Related Topics*, Criado, Gonzalez-Vias, Mancini and Romance Edts. (2008), Proceedings of the conference "Net-Works 2008"

9. *Complex networks with time-dependent connections and silent nodes*, J. Marro, J.J. Torres, J.M. Cortes and S. de Franciscis, *New Trends and Tools in Complex Networks*, Criado, Pello and Romance Edts. (2007), Proceedings of the conference "Net-Works 2007"

10. *Fractal analysis and tumor growth*, A. Brú, D. Casero, S. de Franciscis and M.A. Herrero, *Mathematical and Computer Modelling*, 47 (5–6) (2008)

Resumen en Castellano

El estudio del sistema nervioso se ha incrementado significativamente durante la segunda mitad del siglo pasado, principalmente debido a los avances en biología molecular y en electrofisiología, y al desarrollo de la neurociencia computacional. Se ha hecho posible comprender y simular en detalle un gran número de procesos biofísicos complejos, cómo por ejemplo los mecanismos intracelulares de la neurona. Sin embargo, aún se conoce poco sobre cómo se generan fenómenos cognitivos y comportamientos complejos en redes constituidas por un gran número de neuronas conectadas entre sí por las sinapsis.

Entender el funcionamiento del cerebro es uno de los problemas más desafiantes que puedan atraer a un físico. El cerebro, considerado como un sistema compuesto de una gran cantidad de elementos (es decir, las neuronas y las sinapsis), y regulado por distintos mecanismos dinámicos no lineales, tanto a nivel celular como de red, muestra fenómenos de dinámica colectiva que en muchos aspectos se parecen a algunos de los típicos problemas de la física estadística. Uno de los comportamientos colectivos más interesantes observados recientemente en los sistemas neuronales consiste en la aparición de fenómenos críticos. Los estados críticos se caracterizan por la aparición de correlaciones espacio-temporales de largo alcance, que se manifiestan a través de distribuciones de ley de potencia, también llamadas *libres de escala* (*scale-free*), para algunas magnitudes de interés. Este comportamiento crítico ha sido observado experimentalmente, tanto a escala de todo el cerebro (donde por ejemplo, se caracteriza por la existencia de correlaciones de largo alcance y por la divergencia de la longitud de correlación) [9], como en escalas relativamente pequeña (donde los circuitos corticales presentan avalanchas neuronales, es decir cascadas de actividad que presentan distribuciones estadísticas con leyes de potencia inversa, así como correlaciones de largo alcance) [6].

Tal como se describe en el capítulo 2, cuando un sistema complejo se encuentra en un estado crítico (por ejemplo, cerca de una transición de fase de segundo orden, o en un estado crítico auto organizado), su dinámica está determinada por las correlaciones espacio-temporales no triviales en su comportamiento colectivo emergente. Para el estudio de sus propiedades colectivas, los sistemas tienen que ser considerados en su conjunto, y no sólo como la suma de todos sus elementos, con un enfoque probabilístico. Por lo tanto, el marco teórico utilizado para implementar los modelos y las herramientas matemáticas de análisis aquí considerados es el de la mecánica estadística tanto de equilibrio y como de no equilibrio.

Los estados críticos han generado una gran expectación en neurociencia y en neurociencia computacional debido a las interesantes propiedades funcionales que implican. A pequeña escala, la aparición de avalanchas neuronales críticas se ha asociado con la optimización de diferentes propiedades de la red neuronal, como por ejemplo la transmisión y almacenamiento de información, las capacidades computacionales, la estabilidad misma de la red y la sensibilidad frente a estímulos sensoriales [10]. Por otro lado, a gran escala, patrones críticos de actividad (espacio-temporal) que caracterizan la dinámica colectiva de un gran número de neuronas que interactúan a lo largo de toda la corteza cerebral, favorecen algunas funciones superiores del cerebro (como la percepción, el aprendizaje y el movimiento dirigido) y su continua adaptación en un entorno variable [11, 12], o bién en otros casos pueden representar la huella de algunas enfermedades neurológicas como la epilepsia [13].

Los problemas a resolver más relevantes con respecto a los estados críticos neuronales son aquellos relacionados con los mecanismos dinámicos de las neuronas y las estructuras de las proprias redes neuronales (es decir, las topologías que definen las conexiones entre neuronas) que son responsables de su aprición y de su estabilidad. Por otra parte, las relaciones entre estos elementos y las propiedades funcionales óptimas de las redes críticas aún no están completamente comprendidas.

Diferentes trabajos experimentales en medios neuronales que han puesto de manifiesto fenómenos críticos se describen en el capítulo 4, mientras que en el capítulo 3 se presentan algunos fundamentos de la biología del tejido neuronal y se introducen algunos modelos matemáticos utilizados para estudiar su comportamiento. Estos principios constituyen el punto de partida de los modelos teóricos desarrollados y estudiados en esta tesis.

Por otra parte, otros fenómenos críticos interesantes en sistemas biológicos son

aquellos relacionados con el crecimiento de tumores sólidos, objeto en tiempos recientes de un intenso debate. También en este caso se tiene un sistema formado por un gran número de unidades, es decir, las células, que presentan interacciones complejas no-lineales entre ellas. Algunos experimentos han demostrado que los tumores se desarrollan como objetos auto-afines [14], con correlaciones espacio-temporales típicas distribuidas mediante leyes de potencia [15]. La medida de los exponentes críticos asociados (es decir, los exponentes de las leyes de potencia de las funciones de correlación) son muy importantes para entender los procesos dinámicos fundamentales involucrados en la invasión tumoral. Por otra parte es importante encontrar la relación que existe entre los valores de los exponentes y los mecanismos de proliferación de las células tumorales, con el fin de desarrollar herramientas terapéuticas [16].

El objetivo de esta tesis es investigar, utilizando diferentes métodos matemáticos y de simulación numérica, los mecanismos responsables para la aparición de estados críticos en diferentes sistemas neuronales, así como sus propiedades óptimas funcionales emergentes. En segundo lugar, con el propósito de ampliar el estudio de la criticalidad a otras clases de sistemas biologícos, se investiga, en el mismo marco, las relaciones entre la caracterización crítica del crecimiento tumoral y su dinámica fundamental de invasión.

Los principales objetivos de esta tesis son los siguientes:

- Explorar el papel que la actividad sináptica juega en la dinámica de las redes neuronales y su influencia en la aparición de fenómenos críticos [125], así como en su robustez y estabilidad [21], y finalmente en la optimización de las propiedades funcionales de las mismas redes neuronales en tales estados críticos (véanse los capítulos 5-6).

- Buscar las relaciones entre la redes con topologías no triviales, i.e. *libre de escala* [26, 60] (tanto en la distribución de enlaces como en las correlaciones entre número de enlaces de los nodos primeros vecinos) y el rendimiento optimo de algunos modelos de redes neuronales [89, 154] (por ejemplo, durante el proceso de recuperación de patrones estáticos y dinámicos de actividad neuronal) (véanse los capítulos 7-8).

- Mejorar las técnicas de análisis de *scaling* dinámico en la caracterización de los procesos dinámicos fundamentales de invasión de los tumores sólidos [30, 234], estudiando los frentes de invasión de estos últimos como superficies auto-afines [27], y estudiar la relación entre los mecanismos de proliferación celular del tumor y el comportamiento de las fluctuaciones en la superficie del tumor (véanse los capítulos 10-11).

Bibliography

[1] A. Eke, P. Herman, L. Kocsis, and L. R. Kozak. Fractal characterization of complexity in temporal physiological signals. *Physiological Measurement*, 23 (1):R1, 2002.

[2] S. Das Sarma, C. J. Lanczycki, R. Kotlyar, and S. V. Ghaisas. Scale invariance and dynamical correlations in growth models of molecular beam epitaxy. *Phys. Rev. E*, 53(1):359–388, Jan 1996.

[3] A. L. Hodgkin and A. F. Huxley. Action potentials recorded from inside a nerve fibre. *Nature*, 144:710–711, 1939.

[4] V. M. Eguíluz, D. R. Chialvo, G. A. Cecchi, M. Baliki, and A. V. Apkarian. Scale-free brain functional networks. *Phys. Rev. Lett.*, 94(1):018102, Jan 2005.

[5] D. Fraiman, P. Balenzuela, J. Jennifer, and D. R. Chialvo. Ising-like dynamics in large-scale functional brain networks. *Phys. Rev. E*, 79(6):061922, Jun 2009.

[6] J. M. Beggs and D. Plenz. Neuronal avalanches in neocortical circuits. *J. Neurosci.*, 23(35):11167–11177, 2003.

[7] S. Fujisawa, N. Matsuki, and Y. Ikegaya. Single neurons can induce phase transitions of cortical recurrent networks with multiple internal states. *Cerebral Cortex*, 16(5):639–654, 2006.

[8] J. M. Beggs and D. Plenz. Neuronal avalanches are diverse and precise activity patterns that are stable for many hours in cortical slice cultures. *J. Neurosci.*, 24(22):5216–5229, 2004.

[9] D. R. Chialvo, P. Balenzuela, and D. Fraiman. The brain: What is critical about it? *AIP Conference Proceedings*, 1028(1):28–45, 2008.

[10] J. M. Beggs. The criticality hypothesis: How local cortical networks might optimize information processing. *Phil. Trans. R. Soc. A*, 366(1864):329–343, 2008.

[11] D. R. Chialvo. Are our senses critical? *Nature Physics*, 2:301–302, 2006.

[12] D. R. Chialvo. Emergent complex neural dynamics. *Nature Physics*, 6: 744–750, 2010.

[13] I. Osorio, M. G. Frei, D. Sornette, J. Milton, and Y.-C. Lai. Epileptic seizures: Quakes of the brain? *Phys. Rev. E*, 82(2):021919, Aug 2010.

[14] S. C. Ferreira, M. L. Martins, and M. J. Vilela. Reaction-diffusion model for the growth of avascular tumor. *Phys. Rev. E*, 65(2):021907, Jan 2002.

[15] A. Brú, S. Albertos, J. L. Subiza, J. L. García-Asenjo, and I. Brú. The universal dynamics of tumor growth. *Biophysical Journal*, 85(5):2948–2961, 2003.

[16] A. Brú, S. Albertos, J. A. López García-Asenjo, and I. Brú. Pinning of tumoral growth by enhancement of the immune response. *Phys. Rev. Lett.*, 92(23):238101, Jun 2004.

[17] J. Marro, J. J. Torres, J. M. Cortes, and S. de Franciscis. Complex networks with time-dependent connections and silent nodes. *Proceedings of the Workshop Net-Works 2007, Aranjuez, 10-11 September 2007*, pages 1–16, Sep 2007.

[18] D. O. Hebb. *The Organization of Behavior: A Neuropsychological Theory.* Wiley, 1949.

[19] A. Levina, J. M. Herrmann, and T. Geisel. Dynamical synapses causing self-organized criticality in neural networks. *Nature Physics*, 3(12):857–860, 2007.

[20] J. A. Bonachela and M. A. Muñoz. Self-organization without conservation: true or just apparent scale-invariance? *J. Stat. Mech.*, page P09009, Sep 2009.

[21] J. A. Bonachela, S. de Franciscis, J. J. Torres, and M. A. Muñoz. Self-organization without conservation: are neuronal avalanches generically critical? *J. Stat. Mech.*, page P02015, Feb 2010.

[22] S. de Franciscis, S. Johnson, and J. J. Torres. Enhancing neural-network performance via assortativity. *Phys. Rev. E*, 83(3):036114, Apr 2011.

[23] O. Sporns, D. R. Chialvo, M. Kaiser, and C. C. Hilgetag. Organization, development and function of complex brain networks. *Trends in Cognitive Sciences*, 8(9):418–425, 2004.

[24] A. Arenas, A. Fernández, and S. Gómez. A complex network approach to the determination of functional groups in the neural system of c. elegans. *Lect. Notes Comp. Sci.*, 5151:9–18, 2008.

[25] J. J. Torres, M. A. Muñoz, J. Marro, and P. L. Garrido. Influence of topology on the performance of a neural network. *Neurocomputing*, 58-60:229–234, 2004.

[26] J. J. Torres, S. Johnson, J. Marro, and M. A. Muñoz. Entropic origin of disassortativity in complex networks. *Physical Review Letters*, 104:108702, 2010.

[27] A. Barabási and H. E. Stanley. *Fractal Concepts in Surface Growth*. Cambridge University Press, 1995.

[28] A. Brú, J. M. Pastor, I. Fernaud, I. Brú, S. Melle, and C. Berenguer. Super-rough dynamics on tumor growth. *Phys. Rev. Lett.*, 81(18):4008–4011, Nov 1998.

[29] Z.-W. Lai and S. Das Sarma. Kinetic growth with surface relaxation: Continuum versus atomistic models. *Phys. Rev. Lett.*, 66(18):2348–2351, May 1991.

[30] A. Brú, D. Casero, S. de Franciscis, and M. A. Herrero. Fractal analysis and tumour growth. *Mathematical and Computer Modelling*, 47(5-6):546–559, 2008.

[31] H. Hatzikirou, L. Brusch, C. Schaller, M. Simon, and A. Deutsch. Prediction of traveling front behavior in a lattice-gas cellular automaton model for tumor invasion. *Computers Mathematics with Applications*, 59(7):2326–2339, 2010.

[32] H. Hatzikirou and A. Deutsch. Cellular automata as microscopic models of cell migration in heterogeneous environments. *Current Topics in Developmental Biology*, 81(07):401–434, 2008.

[33] M. I. Rabinovich, J. J. Torres, P. Varona, R. Huerta, and P. Weidman. Origin of coherent structures in a discrete chaotic medium. *Phys. Rev. E*, 60(2):R1130–R1133, Aug 1999.

[34] S. Amari. Dynamics of pattern formation in lateral inhibition type neural fields. *Biological Cybernetics*, 27:77–87, 1977.

[35] U. Börner, A. Deutsch, and M. Bär. A generalized discrete model linking rippling pattern formation and individual cell reversal statistics in colonies of myxobacteria. *Physical Biology*, 3(2):138, 2006.

[36] E. Ben-Jacob, O. Schochet, A. Tenenbaum, I. Cohen, A. Czirók, and T. Vicsek. Generic modelling of cooperative growth patterns in bacterial colonies. *Nature*, 368:46–49, Mar 1994.

[37] H. Meinhardt and M. Klingler. A model for pattern formation on the shells of molluscs. *J. theor. Biol*, 126:63–69, 1987.

[38] N. Brunel and V. Hakim. Fast global oscillations in networks of integrate-and-fire neurons with low firing rates. *Neural Computation*, 11(7):1621–1671, 1999.

[39] A. M. Turing. The chemical basis of morphogenesis. *Phil. Trans. R. Soc. Lond. B*, 237(641):37–72, Aug 1952.

[40] J.D. Murray. *Mathematical Biology: Vol. I An Introduction and Vol. II Spatial Models and Biomedical Applications*. Springer-Verlag, 3rd ed., 2003.

[41] A. Deutsch and S. Dormann. *Cellular Automaton Modeling of Biological Pattern Formation*. Boston, MA: Birkhäuser, 2005.

[42] H. Meinhardt. *Models of biological pattern formation*. Academic Press, London, 1982.

[43] H. E. Stanley, S. V. Buldyrev, A. L. Goldberger, J. M. Hausdorff, S. Havlin, J. Mietus, C.-K. Peng, F. Sciortino, and M. Simons. Fractal landscapes in biological systems: long-range correlations in dna and interbeat heart intervals. *Physica A*, 191(1–4):1–12, Dec 1992.

[44] T. R. Nelson, B. J. West, and A. L. Goldberger. The fractal lung: Universal and species-related scaling patterns. *Cellular and Molecular Life Sciences*, 46:251–254, 1990.

[45] N. G. van Kampen. *Stochastic processes in physics and chemistry.* North-Holland, 1990.

[46] T. Petermann, T. A. Thiagarajan, M. Lebedev, M. Nicolelis, D. R. Chialvo, and D. Plenz. Spontaneous cortical activity in awake monkeys composed of neuronal avalanches. *Proc. Nat. Acad. Sci.*, 106(37):15921–15926, Sep 2009.

[47] V. Priesemann, M.H. J. Munk, and M. Wibral. Subsampling effects in neuronal avalanche distributions recorded in vivo. *BMC Neuroscience*, 10(40), Apr 2009.

[48] J. Bonachela, C. Nadell, J. Xavier, and S. Levin. Universality in bacterial colonies. *Journal of Statistical Physics*, pages 1–13, 2011.

[49] D. Chandler. *Introduction to Modern Statistical Mechanics.* Oxford University Press, 1987.

[50] L. Peliti. *Appunti di Meccanica Statistica.* Bollati Boringhieri, Torino, 2003.

[51] Lars Onsager. Crystal statistics. i. a two-dimensional model with an order-disorder transition. *Phys. Rev.*, 65(3-4):117–149, Feb 1944.

[52] T. D. Schultz, D. C. Mattis, and E. H. Lieb. Two-dimensional ising model as a soluble problem of many fermions. *Rev. Mod. Phys.*, 36(3):856–871, Jul 1964.

[53] G. Grinstein and C. Jayaprakash. Simple models of self-organized criticality. *Computers in Physics*, 9(2):164–169, Mar 1995.

[54] M. E. J. Newman. Power laws, pareto distributions and zipfs law. *Contemporary Physics*, 46(5):323–351, Sep-Oct 2005.

[55] J. Marro and R. Dickman. *Nonequilibrium Phase Transition in Lattice Models.* Cambridge University Press, 1999.

[56] P. Bak, C. Tang, and K. Wiesenfeld. Self-organized criticality: An explanation of the 1/f noise. *Phys. Rev. Lett.*, 59(4):381–384, Jul 1987.

[57] L. A. N. Amaral, A. Scala, M. Barthélémy, and H. E. Stanley. Classes of small-world networks. *Proc. Natl. Acad. Sci.*, 97(21):11149–11152, Oct 2000.

[58] M. E. J. Newman. The structure and function of complex networks. *SIAM Review*, 45(2):167–256, 2003.

[59] P. Meakin and B. Jamtveit. Geological pattern formation by growth and dissolution in aqueous systems. *Proc. R. Soc. A*, 466:659–694, 1999.

[60] A. Barabási and R. Albert. Emergence of scaling in random networks. *Science*, 286:509–514, Oct 1999.

[61] A. Arenas, A. Díaz-Guilera, J. Kurths, Y. Moreno, and C. Zhou. Synchronization in complex networks. *Phys. Rep.*, 469:93–153, 2008.

[62] S. G. Brush. History of the lenz-ising model. *Rev. Mod. Phys.*, 39(4):883–893, Oct 1967.

[63] D. J. Amit. *Field Theory, the Renormalization Group, and Critical Phenomena*. World Scientific, 2nd Ed., 1984.

[64] H. E. Stanley. Scaling, universality, and renormalization: Three pillars of modern critical phenomena. *Rev. Mod. Phys.*, 71(2):S358–S366, Mar 1999.

[65] P. Bak, C. Tang, and K. Wiesenfeld. Self-organized criticality. *Phys. Rev. A*, 38(1):364–374, Jul 1988.

[66] R. Dickman, M. A. Muñoz, A. Vespignani, and S. Zapperi. Paths to self-organized criticality. *Brazilian Journal of Physics*, 30:27–41, 03 2000.

[67] P. Bak and K. Sneppen. Punctuated equilibrium and criticality in a simple model of evolution. *Phys. Rev. Lett.*, 71(24):4083–4086, Dec 1993.

[68] Juan Antonio Bonachela Fajardo. *Universality in Self-Organized Criticality*. PhD Thesis, Departamento de Electromagnetismo y Física de la Materia and Institute Carlos I for Theoretical and Computational Physics, University of Granada, Spain, 2008.

[69] S. Boccaletti, V. Latora, Y. Moreno, M. Chavez, and D.-U. Hwang. Complex networks: Structure and dynamics. *Physics Reports*, 424(4–5):175–308, 2006.

[70] R. Segev, Y. Shapira, M. Benveniste, and E. Ben-Jacob. Observations and modeling of synchronized bursting in two-dimensional neural networks. *Phys. Rev. E*, 64(1):011920, Jun 2001.

[71] J. Gómez-Gardeñes, Y. Moreno, and A. Arenas. Paths to synchronization on complex networks. *Phys. Rev. Lett.*, 98:034101, 2007.

[72] D. Eytan and S. Marom. Dynamics and effective topology underlying synchronization in networks of cortical neurons. *Journal of Neuroscience*, 26 (33):8465 – 8476, 2006.

[73] B. Mitra, N. Ganguly, S. Ghose, and F. Peruani. Generalized theory for node disruption in finite-size complex networks. *Phys. Rev. E*, 78(2):026115, Aug 2008. doi: 10.1103/PhysRevE.78.026115.

[74] S. Johnson, J. Marro, and J. J. Torres. Evolving networks and the development of neural systems. *J. Stat. Mech.*, page P03003, Mar 2010.

[75] A. Barabási and R. Albert. Topology of evolving networks: Local events and universality. *Phys. Rev. Lett.*, 85(24):5234–5237, Dec 2000.

[76] D. J. Watts and S. H. Strogatz. Collective dynamics of 'small-world' networks. *Nature*, 393:440–442, Jun 1998.

[77] P. Erdös and A. Rényi. The evolution of random graphs. *Magyar Tud. Akad. Mat. Kutató Int. Közl*, 5:17–61, 1960.

[78] S. Johnson, J. Marro, and J. J. Torres. Cluster Reverberation: A mechanism for robust short-term memory without synaptic learning. *arXiv:1007.3122*, 2011.

[79] P. Meakin. *Fractals, scaling and growth far from equilibrium.* Cambridge University Press, 1998.

[80] T. Vicsek. *Fractal Growth Phenomena.* Wold Scientific, 1992.

[81] Dee Unglaub Silverthorn. *Human Physiology: An Integrated Approach.* Benjamin Cummings, 4th Ed., 2008.

[82] J. J. Torres and P. Varona. *Modeling Biological Neural Network, chapter in book Handbook of Natural Computing.* Springer, G. Rozenberg, T. H. W. Bäck, J. N. Kok (Eds.), 2010.

[83] R. Bertram, A. Sherman, and E. F. Stanley. Single-domain/bound calcium hypothesis of transmitter release and facilitation. *Journal of Neurophysiology*, 75(5):1919–1931, 1996.

[84] E. R. Kandel, J. H. Schwartz, and T. M. Jessell. *Principles of neural science, 4th ed.* McGraw-Hill, New York, 2000.

[85] N. Brunel and M. C. van Rossum. Lapicque's 1907 paper: from frogs to integrate-and-fire. *Biol. Cybern.*, 97:337–339, 2007.

[86] H. C. Tuckwell. *Introduction to theoretical neurobiology. Volume 2: nonlinear and stochastic theories.* Cambridge, 1989.

[87] J. F. Mejías and J. J. Torres. The role of synaptic facilitation in spike coincidence detection. *Journal of Computational Neuroscience*, 24:222–234, 2008.

[88] E. M. Izhikevich. Which model to use for cortical spiking neurons? *IEEE Trans. Neural Networks*, 15(5):1063–1070, 2004.

[89] N. Brunel. Dynamics of sparsely connected networks of excitatory and inhibitory spiking neurons. *J. Comp. Neurosci.*, 8:183–208, 2000.

[90] X. Guardiola, A. Díaz-Guilera, M. Llas, and C. J. Pérez. Synchronization, diversity, and topology of networks of integrate and fire oscillators. *Phys. Rev. E*, 62(4):5565–5570, Oct 2000.

[91] Alex Roxin, Hermann Riecke, and Sara A. Solla. Self-sustained activity in a small-world network of excitable neurons. *Phys. Rev. Lett.*, 92(19):198101, May 2004.

[92] L. da Fontoura Costa. Activation confinement inside complex networks communities. *arXiv:0802.1272v1*, 2008.

[93] Á. Corral, C. J. Pérez, A. Díaz-Guilera, and A. Arenas. Self-organized criticality and synchronization in a lattice model of integrate-and-fire oscillators. *Phys. Rev. Lett.*, 74(1):118–121, Jan 1995.

[94] D. Millman, S. Mihalas, A. Kirkwood, and E. Niebur. Self-organized criticality occurs in non-conservative neuronal networks during /'up/' states. *Nature Physics*, 6(10):801–805, 2010.

[95] M. V. Tsodyks and H. Markram. The neural code between neocortical pyramidal neurons depends on neurotransmitter release probability. *Proc. Natl. Acad. Sci. USA*, 94:719–723, 1997.

[96] H. Kamiya and R. S. Zucker. Residual ca2+ and short-term synaptic plasticity. *Nature*, 371(6498):603–606, 1994.

[97] L. F. Abbott and W. G. Regehr. Synaptic computation. *Nature*, 431:796–803, Oct 2004.

[98] C. I. Buia and P. H. E. Tiesinga. Rapid temporal modulation of synchrony in cortical interneuron networks with synaptic plasticity. *Neurocomputing*, 65-66:809–815, 2005.

[99] D. Holcman and M. Tsodyks. The emergence of up and down states in cortical networks. *PLoS Comput Biol*, 2(3):e23, 03 2006.

[100] Jorge F. Mejías Palomino. *Short-Term Synaptic Plasticity: Computational Implications in the Emergent Behavior of Neural Systems*. PhD Thesis, Departamento de Electromagnetismo y Física de la Materia and Institute Carlos I for Theoretical and Computational Physics, University of Granada, Spain, 2009.

[101] L. Pantic, J. J. Torres, H. J. Kappen, and S. C. A. M. Gielen. Associative memory with dynamic synapses. *Neural Comput.*, 14:2903–2923, 2002.

[102] J. M. Cortes, J. J. Torres, J. Marro, P. L. Garrido, and H. J. Kappen. Effect of fast presynaptic noise in attractor neural networks. *Journal of Neural Computation*, 18(3):614–633, 2006.

[103] V. Matveev and X. J. Wang. Differential short-term synaptic plasticity and transmission of complex spike trains: to depress or to facilitate? *Cerebral Cortex*, 10:1143–1153, 2000.

[104] A. Destexhe and E. Marder. Plasticity in single neuron and circuit computations. *Nature*, 431:789–795, 2004.

[105] J. F. Mejías and J. J. Torres. The role of synaptic facilitation in spike coincidence detection. *J. Comput. Neurosci.*, 24(2):222–234, 2008.

[106] M. V. Tsodyks, K. Pawelzik, and H. Markram. Neural networks with dynamic synapses. *Neural Comput.*, 10:821–835, 1998.

[107] L. F. Abbott, J. A. Valera, K. Sen, and S. B. Nelson. Synaptic depression and cortical gain control. *Science*, 275(5297):220–224, 1997.

[108] D. P. Pelvig, H. Pakkenberg, A. K. Stark, and B. Pakkenberg. Neocortical glial cell numbers in human brains. *Neurobiology of Aging*, 29(11):1754–1762, 2008.

[109] L. Alonso-Nanclares, J. Gonzalez-Soriano, J. R. Rodriguez, and J. DeFelipe. Gender differences in human cortical synaptic density. *Proc. Natl. Acad. Sci.*, 38(105):14615–14619, Sep 2004.

[110] J. J. Hopfield. Neural networks and physical systems with emergent collective computational abilities. *Proc. Natl. Acad. Sci. USA*, 79:2554–2558, 1982.

[111] J. Hertz, A. Krogh, and R. G. Palmer. *Introduction to the theory of neural computation.* Addison-Wesley, 1991.

[112] P. Peretto. *An Introduction to the modeling of neural networks.* Cambridge University Press, 1992.

[113] Y. Miyashita. Neural correlate of visual associative long-term memory in the primate temporary cortex. *Nature*, 335:817–820, 1988.

[114] K. Sakai and Y. Miyashita. Neural organization for the long-term memory of paired associates. *Nature*, 354(6349):152–155, Nov 1991.

[115] D. J. Amit. The hebbian paradigm reintegrated: local reverberations as internal representations. *Behavioral and Brain Sciences*, 18:617–657, 1995.

[116] K. Tanaka. Neuronal mechanisms of object recognition. *Science*, 262(5134): 685–688, 1993.

[117] H. Tomita, M. Ohbayashi, K. Nakahara, I. Hasegawa, and Y. Miyashita. Top-down signal originating from the prefrontal cortex for memory retrieval. *Nature*, 401:699–703, 1999.

[118] T. V. P. Bliss and G. L. Collingridge. A synaptic model of memory: long-term potentiation in the hippocampus. *Nature*, 361:31–39, 1993.

[119] R. Malenka and R. A. Nicoll. Long-term potentiation: a decade of progress? *Science*, 285:1870–1874, 1999.

[120] A. Gruart, M. D. Muñoz, and J. M. Delgado-García. Involvement of the ca3-ca1 synapse in the acquisition of associative learning in behaving mice. *J. Neurosci.*, 26:1077–1087, 2006.

[121] S. Amari. Characteristics of random nets of analog neuron-like elements. *IEEE Trans. Syst. Man. Cybern.*, 2:643–657, 1972.

[122] D. J. Amit, H. Gutfreund, and H. Sompolinsky. Statistical mechanics of neural networks near saturation. *Ann. Phys.*, 173:30–67, 1987.

[123] D. J. Amit, H. Gutfreund, and H. Sompolinsky. Spin-glass models of neural networks. *Phys. Rev. A*, 32(2):1007–1018, Aug 1985.

[124] D. J. Amit, H. Gutfreund, and H. Sompolinsky. Storing infinite numbers of patterns in a spin-glass model of neural networks. *Phys. Rev. Lett.*, 55(14): 1530–1533, Sep 1985.

[125] S. de Franciscis, J. J. Torres, and J. Marro. Unstable dynamics, nonequilibrium phases, and criticality in networked excitable media. *Phys. Rev. E*, 82 (4):041105, Oct 2010.

[126] L. F. Lago-Fernández, R. Huerta, F. Corbacho, and J. A. Sigüenza. Fast response and temporal coherent oscillations in small-world networks. *Phys. Rev. Lett.*, 84(12):2758–2761, Mar 2000.

[127] S. Pajevic and D. Plenz. Efficient network reconstruction from dynamical cascades identifies small-world topology of neuronal avalanches. *PLoS Comput Biol*, 5(1):e1000271, Jan 2009.

[128] M. D. Fox and M. E. Raichle. Spontaneous fluctuations in brain activity observed with functional magnetic resonance imaging. *Nature Reviews Neuroscience*, 8(9):700–711, 2007.

[129] W. J. Freeman, L. J. Rogers, M. D. Holmes, and D. L. Silbergeld. Spatial spectral analysis of human electrocorticograms including the alpha and gamma bands. *Journal of Neuroscience Methods*, 95(2):111 – 121, 2000.

[130] G. Buzsáki and A. Draguhn. Neuronal oscillations in cortical networks. *Science*, 304:1926–1929, jun 2004.

[131] M. D. Fox, A. Z. Snyder, J. L. Vincent, M. Corbetta, D. C. Van Essen, and M. E. Raichle. The human brain is intrinsically organized into dynamic, anticorrelated functional networks. *PNAS, Proc. Nat. Aca. Sci.*, 102(27): 9673–9678, Jul 2005.

[132] O. Kinouchi and M. Copelli. Optimal dynamical range of excitable networks at criticality. *Nature Physics*, 2(5):348–351, 2006.

[133] A. Tang, D. Jackson, J. Hobbs, W. Chen, J. L. Smith, H. Patel, A. Prieto, D. Petrusca, M. I. Grivich, A. Sher, P. Hottowy, W. Dabrowski, A. M. Litke, and J. M. Beggs. A maximum entropy model applied to spatial and temporal correlations from cortical networks in vitro. *J. Neurosci.*, 28(2): 505–518, 2008.

[134] S. N. Dorogovtsev, A. V. Goltsev, and J. F. F. Mendes. Critical phenomena in complex networks. *Rev. Mod. Phys.*, 80(4):1275–1335, Oct 2008.

[135] O. Shefi, I. Golding, R. Segev, E. Ben-Jacob, and A. Ayali. Morphological characterization of in vitro neuronal networks. *Phys. Rev. E*, 66(2):021905, Aug 2002.

[136] C. Haldeman and J. M. Beggs. Critical branching captures activity in living neural networks and maximizes the number of metastable states. *Phys. Rev. Lett.*, 94(5):058101, Feb 2005.

[137] M. V. Sanchez-Vives and D. A. McCormick. Cellular and network mechanisms of rhythmic recurrent activity in neocortex. *Nature Neuroscience*, 3: 1027–1034, 2000.

[138] R. Cossart, D. Aronov, and R. Yuste. Attractor dynamics of network up states in the neocortex. *Nature*, 423:283–288, 2003.

[139] X.-J. Wang. Synaptic reverberation underlying mnemonic persistent activity. *Trends in Neurosciences*, 24(8):455–463, 2001.

[140] D. A. McCormick. Neuronal networks: Flip-flops in thebrain. *Current Biology*, 15(8):R294–R296, 2005.

[141] H. R. Wilson and J. D. Cowan. Excitatory and inhibitory interactions in localized populations of model neurons. *Biophysical Journal*, 12(1):1–24, 1972. ISSN 0006-3495.

[142] A. Compte, M. V. Sanchez-Vives, D. A. McCormick, and X.-J. Wang. Cellular and network mechanisms of slow oscillatory activity (¡1 hz) and wave propagations in a cortical network model. *Journal of Neural Physiology*, 89 (5):2707–2725, 2003.

[143] S. H. Strogatz. *Nonlinear Dynamics and Chaos: With Applications to Physics, Biology, Chemistry, and Engineering*. Perseus Books, 2002.

[144] S. Amari. Learning patterns and pattern sequences by self-organizing nets of threshold elements. *Computers, IEEE Transactions on*, C-21(11):1197–1206, 1972.

[145] D. A. Wagenaar, Z. Nadasdy, and S. M. Potter. Persistent dynamic attractors in activity patterns of cultured neuronal networks. *Phys. Rev. E*, 73(5): 051907, May 2006.

[146] O. Mazor and V. Laurent. Transient dynamics versus fixed points in odor representations by locust antennal lobe projection neurons. *Neuron*, 48(4): 661–673, 2005.

[147] M. Shen, G. Chang, S. Wang, and P. Beadle. *Nonlinear Dynamics of EEG Signal Based on Coupled Network Lattice Model*, volume 3973 of *Lecture Notes in Computer Science*. Springer Berlin / Heidelberg, 2006.

[148] H. Sompolinsky, A. Crisanti, and H. J. Sommers. Chaos in random neural networks. *Phys. Rev. Lett.*, 61(3):259–262, 1988.

[149] W.-Z. Huang and Y. Huang. Chaos of a new class of hopfield neural networks. *Applied Mathematics and Computation*, 206(1):1–11, 2008.

[150] J. Marro, J. J. Torres, and J. M. Cortes. Complex behavior in a network with time-dependent connections and silent nodes. *J. Stat. Mech.*, page P02017, Feb 2008.

[151] J. J. Torres, J. Marro, J. M. Cortes, and B. Wemmenhove. Instabilities in attractor networks with fast synaptic fluctuations and partial updating of the neurons activity. *Neural Networks*, 21(9):1272–1277, 2008.

[152] M. O. Magnasco, O. Piro, and G. A. Cecchi. Self-tuned critical anti-hebbian networks. *Phys. Rev. Lett.*, 102(25):258102, Jun 2009.

[153] D. Plenz and D. R. Chialvo. Scaling properties of neuronal avalanches are consistent with critical dynamics. *arxiv.org/ftp/arxiv/papers/0912/0912.5369.pdf*, 2010.

[154] J. J. Hopfield. Neurons with graded response have collective computational properties like those of two-state neurons. *Proc. Natl. Acad. Sci. USA*, 81: 3088–3092, 1984.

[155] B. A. Olshausen and D. J. Field. Sparse coding of sensory inputs. *Current Opinion in Neurobiology*, 14(4):481–487, 2004.

[156] B. Cernuschi-Frias. Partial simultaneous updating in hopfield memories. *Systems, Man and Cybernetics, IEEE Transactions on*, 19(4):887–888, jul/aug 1989.

[157] J. F. Mejías, H. J. Kappen, and J. J. Torres. Irregular dynamics in up and down cortical states. *PLoS ONE*, 5:e13651, 11 2010.

[158] J. Marro, J. J. Torres, and J. M. Cortés. Chaotic hopping between attractors in neural networks. *Neural Networks*, 20(2):230–235, 2007.

[159] D. J. Amit. *Modeling brain function: The world of attractor neural networks*. Cambridge Univ. Press, 1989.

[160] N. Bertschinger and T. Natschlager. Real-time computation at the edge of chaos in recurrent neural networks. *Neural Computation*, 16(7):1413–1436, 2004.

[161] C. G. Langton. Computation at the edge of chaos: Phase transitions and emergent computation. *Physica D: Nonlinear Phenomena*, 42(1–3):12–37, 1990.

[162] D. Kaplan and L. Glass. *Understanding Nonlinear Dynamics*. Springer, New York, 1995.

[163] E. M. Izhikevich. *Dynamical Systems in Neuroscience: The Geometry of Excitability and Bursting*. MIT Press,Cambridge,Mass., 2007.

[164] S. Johnson, J. Marro, and J. J. Torres. Functional optimization in complex excitable networks. *EPL (Europhysics Letters)*, 83(4):46006, 2008.

[165] R. FitzHugh. Mathematical models of threshold phenomena in the nerve membrane. *The Bulletin Of Mathematical Biophysics*, 17(4):257–278, 1955.

[166] R. FitzHugh. Impulses and physiological states in theoretical models of nerve membrane. *Biophysical Journal*, 1(6):445–466, 1961.

[167] T. D. Rogers and D. C. Whitley. Chaos in the cubic mapping. *Mathematical Modelling*, 4(1):9 – 25, 1983.

[168] M. Griniasty, M. V. Tsodyks, and D. J. Amit. Conversion of temporal correlations between stimuli to spatial correlations between attractors. *Neural Computation*, 5(1):1–17, 1993.

[169] H. J. Jense. *Self-Organized Criticality*. Cambridge University Press, 1998., 1998.

[170] G. Grinstein. Generic scale invariance in classical nonequilibrium systems. *Journal of Applied Physics*, 69(8):5441–5446, apr 1991.

[171] D. Plenz and T. C. Thiagarajan. The organizing principles of neuronal avalanches: cell assemblies in the cortex? *Trends in Neurosciences*, 30(3): 101 – 110, 2007.

[172] J. P. Eckmann, O. Feinerman, L. Gruendlinger, E. Moses, J. Soriano, and T. Tlusty. The physics of living neural networks. *Physics Reports*, 449(1-3): 54–76, 2007.

[173] Y. Ikegaya, G. Aaron, R. Cossart, D. Aronov, I. Lampl, D. Ferster, and R. Yuste. Synfire chains and cortical songs: Temporal modules of cortical activity. *Science*, 304(5670):559–564, 2004.

[174] A. V. M. Herz and J. J. Hopfield. Earthquake cycles and neural reverberations: Collective oscillations in systems with pulse-coupled threshold elements. *Phys. Rev. Lett.*, 75(6):1222–1225, Aug 1995.

[175] H. Markram and M. Tsodyks. Redistribution of synaptic efficacy between neocortical pyramidal neurons. *Nature*, 382:759–60, 1996.

[176] T. E. Harris. *The theory of Branching Processes*. Dover, New York, 1989.

[177] R. Legenstein and W. Maass. Edge of chaos and prediction of computational performance for neural circuit models. *Neural Networks*, 20(3):323–334, 2007.

[178] C. Bédard, H. Kröger, and A. Destexhe. Does the $1/f$ frequency scaling of brain signals reflect self-organized critical states? *Phys. Rev. Lett.*, 97(11): 118102, Sep 2006.

[179] V. Pasquale, P. Massobrio, L.L. Bologna, M. Chiappalone, and S. Martinoia. Self-organization and neuronal avalanches in networks of dissociated cortical neurons. *Neuroscience*, 153(4):1354–1369, 2008.

[180] J. D. Halley and D. A. Winkler. Critical-like self-organization and natural selection: Two facets of a single evolutionary process? *Biosystems*, 92(2): 148–158, 2008.

[181] S. Royer and D. Paré. Conservation of total synaptic weight through balanced synaptic depression and potentiation. *Nature*, 422:518–522, 12003.

[182] A. Levina, J. M. Herrmann, and T. Geisel. Phase transitions towards criticality in a neural system with adaptive interactions. *Phys. Rev. Lett.*, 102 (11):118110, Mar 2009.

[183] C. W. Eurich, J. M. Herrmann, and U. A. Ernst. Finite-size effects of avalanche dynamics. *Phys. Rev. E*, 66(6):066137, Dec 2002.

[184] A. Levina, U. Ernst, and J. M. Herrmann. Criticality of avalanche dynamics in adaptive recurrent networks. *Neurocomput.*, 70:1877–1881, June 2007.

[185] G. Pruessner and H. J. Jensen. A solvable non-conservative model of self-organised criticality. *EPL (Europhysics Letters)*, 58(2):250, 2002.

[186] M. H. Hennig, C. Adams, D. Willshaw, and E. Sernagor. Early-stage waves in the retinal network emerge close to a critical state transition between local and global functional connectivity. *J. of Neuroscience*, 29:1077, 2009.

[187] A. Vespignani, R. Dickman, M. A. Muñoz, and S. Zapperi. Driving, conservation, and absorbing states in sandpiles. *Phys. Rev. Lett.*, 81(25):5676–5679, Dec 1998.

[188] A. Vespignani, R. Dickman, M. A. Muñoz, and S. Zapperi. Absorbing-state phase transitions in fixed-energy sandpiles. *Phys. Rev. E*, 62(4):4564–4582, Oct 2000.

[189] M. A. Muñoz, R. Dickman, A. Vespignani, and S. Zapperi. Avalanche and spreading exponents in systems with absorbing states. *Phys. Rev. E*, 59(5): 6175–6179, May 1999.

[190] J. A. Bonachela, J. J. Ramasco, H. Chaté, I. Dornic, and M. A. Muñoz. Sticky grains do not change the universality class of isotropic sandpiles. *Phys. Rev. E*, 74(5), Nov 2006.

[191] J. A. Bonachela and M. A. Muñoz. Confirming and extending the hypothesis of universality in sandpiles. *Phys. Rev. E*, 78(4):041102, Oct 2008.

[192] J. L. Cardy and P. Grassberger. Epidemic models and percolation. *Journal of Physics A: Mathematical and General*, 18(6):L267, 1985.

[193] T. Kotani, H. Yoshino, and H. Kawamura. Periodicity and criticality in the olami-feder-christensen model of earthquakes. *Phys. Rev. E*, 77(1):010102, Jan 2008.

[194] L. de Arcangelis, C. Perrone-Capano, and H. J. Herrmann. Self-organized criticality model for brain plasticity. *Phys. Rev. Lett.*, 96(2):028107, Jan 2006.

[195] G.M. Süel, J. Garcia-Ojalvo, L.M. Liberman, and M.B. Elowitz. An excitable gene regulatory circuit induces transient cellular differentiation. *Nature*, 440: 545–50, 2006.

[196] S. V. Buldyrev, R. Parshani, G. Paul, H. E. Stanley, and S. Havlin. Catastrophic cascade of failures in interdependent networks. *Nature*, 464:1025–8, 2010.

[197] M. Boguñá, F. Papadopoulos, and D. Krioukov. Sustaining the internet with hyperbolic mapping. *Nature Communications*, 1(62), 2010.

[198] L. F. Abbott and T. B. Kepler. *From Hodgkin-Huxley to Hopfield, in Statistical mechanics of neural networks*. Springer-Verlag, Berlin, 1990.

[199] T. P. Vogels, K. Rajan, and L. F. Abbott. Neural network dynamics. *Annu. Rev. Neurosci.*, 28:357–76, 2005.

[200] J. J. Torres, J. M. Cortes, J. Marro, and H. J. Kappen. Competition between synaptic depression and facilitation in attractor neural networks. *Neural Computation*, 19:2739–55, 2007.

[201] J. F. Mejías and J. J. Torres. Maximum memory capacity on neural networks with short-term synaptic depression and facilitation. *Neural Comput.*, 21: 851–71, 2009.

[202] A. L. Barabási and Z. N. Oltvai. Network biology: understanding the cell's functional organization. *Nature Reviews Genetics*, 5:101–3, 2004.

[203] M. Barahona and L. M. Pecora. Synchronization in small-world systems. *Phys. Rev. Lett.*, 89:054101, 2002.

[204] R. Pastor-Satorras, A. Vázquez, and A. Vespignani. Dynamical and correlation properties of the internet. *Phys. Rev. Lett.*, 87:258701, 2001.

[205] M. E. J. Newman. Assortative mixing in networks. *Phys. Rev. Lett.*, 89: 208701, 2002.

[206] M. Brede and S. Sinha. Assortative mixing by degree makes a network more unstable. *arXiv:cond-mat/0507710*, 2005.

[207] S. Maslov, K. Sneppen, and A. Zaliznyak. Pattern detection in complex networks: correlation profile of the internet. *Physica A*, 333:529–40, 2004.

[208] G. Caldarelli, A. Capocci, P. De Los Rios, and M. A. Muñoz. Scale-free networks from varying vertex intrinsic fitness. *Phys. Rev. Lett.*, 89:258702, 2002.

[209] B. Söderberg. General formalism for inhomogeneous random graphs. *Phys. Rev. E*, 66:066121, 2002.

[210] M. Boguñá and R. Pastor-Satorras. Class of correlated random networks with hidden variables. *Phys. Rev. E*, 68:036112, 2003.

[211] A. Fronczak and P. Fronczak. Networks with given two-point correlations: hidden correlations from degree correlations. *Phys. Rev. E*, 74:026121, 2006.

[212] R. J. Morgan and I. Soltesz. Nonrandom connectivity of the epileptic dentate gyrus predicts a major role for neuronal hubs in seizures. *Proc. Nat. Acad. Sci. USA*, 105:6179, 2008.

[213] P. Bonifazi, M. Goldin, M. A. Picardo, I. Jorquera, A. Cattani, G. Bianconi, A. Represa, Y. Ben-Ari, and R. Cossart. Gabaergic hub neurons orchestrate synchrony in developing hippocampal networks. *Science*, 326:1419, 2009.

[214] O. Paulsen and T. J. Sejnowski. Natural patterns of activity and long-term synaptic plasticity. *Current Opinion in Neurobiology*, 10(2):172–180, 2000.

[215] G. Bianconi. Mean-field solution of the Ising model on a Barabási-Albert network. *Phys. Lett. A*, 303:166–8, 2002.

[216] S. N. Dorogovtsev, A. L. Ferreira, A. V. Goltsev, and J. F. F. Mendes. Zero pearson coefficient for strongly correlated growing trees. *Phys. Rev. E*, 81: 031135, 2005.

[217] G. Bianconi. The entropy of randomized network ensembles. *EPL*, 81:28005, 2008.

[218] T. Pereira. Hub synchronization in scale-free networks. *Phys. Rev. E*, 82: 036201, 2010.

[219] K. Suchecki, V. M. Eguíluz, and M. San Miguel. Conservation laws for the voter model in complex networks. *EPL*, 69:228–34, 2005.

[220] T. P. Peixoto. Redundancy and error resilience in boolean networks. *Phys. Rev. Lett.*, 104:048701, 2010.

[221] M. Camperi and X.-J. Wang. A model of visuospatial working memory in prefrontal cortex: recurrent network and cellular bistability. *J. Comp. Neurosci.*, 5:383–405, 1998.

[222] A. Compte, C. Constantinidis, J. Tegner, S. Raghavachari, and M. V. Chafee. Temporally irregular mnemonic persistent activity in prefrontal neurons of monkeys during a delayed response task. *J. Neurophysiol.*, 90: 3441–54, 2003.

[223] B. Percha, R. Dzakpasu, and M. Zochowski. Transition from local to global phase synchrony in small world neural network and its possible implications for epilepsy. *Phys. Rev. E*, 72(3):031909, 2005.

[224] C. Zhou, L. Zemanová, G. Zamora-López, C. C. Hilgetag, and J. Kurths. Structure–function relationship in complex brain networks expressed by hierarchical synchronization. *New Journal of Physics*, 9(6):178–178, 2007.

[225] M. Müller-Linow, C. C. Hilgetag, and M.-T. Hütt. Organization of excitable dynamics in hierarchical biological networks. *PLoS Computational Biology*, 4(9):15, 2008.

[226] S. R. Campbell, D. Ll Wang, and C. Jayaprakash. Synchrony and desynchrony in integrate-and-fire oscillators. *Neural Computation*, 11(7):1595–1619, 1999.

[227] L. F. Lafuerza, P. Colet, and R. Toral. Nonuniversal results induced by diversity distribution in coupled excitable systems. *Phys. Rev. Lett.*, 105(8): 084101, Aug 2010.

[228] M. Denker, M. Timme, M. Diesmann, F. Wolf, and T. Geisel. Breaking synchrony by heterogeneity in complex networks. *Phys. Rev. Lett.*, 92(7): 074103, Feb 2004.

[229] M. Eden. A two-dimensional growth process. *Proceedings of the 4th Berkeley Symposium on Mathematics and Probability*, 4:223–239, 1961.

[230] G. A. Losa. Fractals in pathology: are they really useful? *Pathologica*, 87: 310–317, 1995.

[231] S. S. Cross. Fractals in pathology. *J. Pathol.*, 182(1):1–8, 1997.

[232] S. de Franciscis, H. Hatzikirou, and A. Deutsch. Analysis of lattice gas models of tumour growth by means of fractal scaling. *Acta Physica Polonica B*, 4(2):167–182, 2011.

[233] L. A. N. Amaral, A.-L. Barabási, and H. E. Stanley. Universality classes for interface growth with quenched disorder. *Phys. Rev. Lett.*, 73(1):62–65, Jul 1994.

[234] A. Brú and M. A. Herrero. From the physical laws of tumour growth to modelling cancer processes. *Math. Mod. and Meth. in Appl. Sc.*, 16(1): 1199–1218, 2006.

[235] R. A. Gatenby. Mathematical models of tumour-host interactions. *Cancer J.*, 11(6):289–293, 1998.

[236] N. L. Komarova. Mathematical modeling of tumorigenesis: mission possible. *Current Opinion in Oncology*, 17(1):39–43, 2005.

[237] L. Norton. Conceptual and practical implications of breast tissue geometry: Toward a more effective, less toxic therapy. *Oncologist*, 10(6):370–381, 2005.

[238] A Brú and D Casero. Anomalous scaling of multivalued interfaces. *Europhysics Letters*, 64(5):620–626, 2003.

[239] C. W. Gardiner. *Handbook of stochastic methods for physics, chemistry, and the natural sciences.* Springer, 2004.

[240] M. Plischke, J. D. Shore, M. Schroeder, M. Siegert, and D. E. Wolf. Comment on "solid-on-solid rules and models for nonequilibrium growth in 2+1 dimensions". *Phys. Rev. Lett.*, 71(15):2509, Oct 1993.

[241] J. J. Ramasco, J. M. López, and M. A. Rodríguez. Generic dynamic scaling in kinetic roughening. *Phys. Rev. Lett.*, 84(10):2199–2202, Mar 2000.

[242] S. Das Sarma, S. V. Ghaisas, and J. M. Kim. Kinetic super-roughening and anomalous dynamic scaling in nonequilibrium growth models. *Phys. Rev. E*, 49(1):122–125, Jan 1994.

[243] J. Krug, M. Plischke, and M. Siegert. Surface diffusion currents and the universality classes of growth. *Phys. Rev. Lett.*, 70(21):3271–3274, May 1993.

[244] W. W. Mullins. Flattening of a nearly plane solid surface due to capillarity. *Journal of Applied Physics*, 30(1):77, 1959.

[245] M. Marsili, A. Maritan, F. Toigo, and J. R. Banavar. Stochastic growth equations and reparametrization invariance. *Rev. Mod. Phys.*, 68(4):963–983, Oct 1996.

[246] C. Escudero. Stochastic models for tumoral growth. *Phys. Rev. E*, 73(2):020902, Feb 2006.

[247] A. Maritan, F. Toigo, J. Koplik, and J. R. Banavar. Dynamics of growing interfaces. *Phys. Rev. Lett.*, 69(22):3193–3195, Nov 1992.

[248] M. Kardar, G. Parisi, and Y.-C. Zhang. Dynamic scaling of growing interfaces. *Phys. Rev. Lett.*, 56(9):889–892, Mar 1986.

[249] T. Halpin-Healy and Y.-C. Zhang. Kinetic roughening phenomena, stochastic growth, directed polymers and all that. aspects of multidisciplinary statistical mechanics. *Physics Reports*, 254(4-6):215 – 414, 1995.

[250] J. Galeano, J. Buceta, K. Juarez, B. Pumarino, J. de la Torre, and J. M. Iriondo. Dynamical scaling analysis of plant callus growth. *Europhysics Letters*, 63:83–89, 2003.

[251] VV AA. *Cancer Modelling and Simulation.* L. Preziosi, CRC Press, 2003.

[252] VV AA. *Selected Topics on Cancer Modelling Genesis - Evolution - Immune Competition - Therapy.* Bellomo, N., Birkhäuser-Springer, 2008.

[253] N. Bellomo, N. K. Li, and P. K. Maini. On the foundations of cancer modelling: selected topics, speculations, & perspectives. *Mathematical Models and Methods in Applied Sciences*, 18(04):593, 2010.

[254] B. P. Norbury J. Marchant and A. J. Perumpanani. Traveling shock waves arising in a model of malignant invasion. *SIAM. J. Appl. Math.*, 60(2): 263–276, 2000.

[255] A. J. Perumpanani, J. A. Sherratt, J. Norbury, and H. M. Byrne. A two parameter family of travelling waves with a singular barrier arising from the modelling of extracellular matrix mediated cellular invasion. *Physica D: Nonlinear Phenomena*, 126(3-4):145–159, 1999.

[256] J. A. Sherratt and M. A. J. Chaplain. A new mathematical model for avascular tumour growth. *Journal of Mathematical Biology*, 43:291–312, 2001.

[257] M. Marusić, Z. Bajzer, J. P. Freyer, and S. Vuk-Pavlović. Analysis of growth of multicellular tumour spheroids by mathematical models. *Cell Proliferation*, 27(2):73–94, 1994.

[258] M. Block, E. Schöll, and D. Drasdo. Classifying the expansion kinetics and critical surface dynamics of growing cell populations. *Phys. Rev. Lett.*, 99 (24):248101, Dec 2007.

[259] B. Chopardt, M. Drozt, and M. Kolb. Cellular automata approach to non-equilibrium diffusion and gradient percolation. *J. Phys. A: Math. Gen.*, 22: 1609–1619, 1989.

[260] H. Hatzikirou, S. de Franciscis, and F. Peruani. A stochastic jump process of cellular adhesion. *in preparation*, 2011.